

**SPACE VECTOR PWM TECHNIQUES FOR  
SIX-PHASE THREE-LEVEL  
INVERTER-FED DRIVES**

**ENGKU AHMAD RAFIQI BIN ENGKU ARIFF**

**A thesis submitted in partial fulfilment of the requirements of  
Liverpool John Moores University for the degree of  
Doctor of Philosophy**

**December 2017**



## ABSTRACT

In recent years, research in the area of multiphase drives has increased significantly. Having higher number of machine phases allows the current to be shared between the phases, thus reducing the current rating of power semiconductors used in the power converter. Additionally, if a multilevel inverter is used to drive the machine, the output voltage waveforms are going to be approximated closer toward sinusoidal waveforms, thus resulting in lower total harmonic distortion. Therefore, the combination of multiphase and multilevel technologies gives considerable benefits compared to conventional two-level three-phase drives.

Unlike a carrier-based approach, which can be easily expanded to any number of converter voltage levels and any number of machine phases, the development of space vector algorithms is also reliant on the machine's configuration. In other words, different drive topologies require their own unique space vector algorithms. In fact, the complexity of developing a space vector algorithm will dramatically increase with the increase of number of levels and/or number of phases. This thesis presents pulse width modulation techniques for two- and three-level asymmetrical and symmetrical six-phase drives with a single or two isolated neutral points configuration. However, since the modulation techniques for the drives with two isolated neutral points are based on the well-established modulation techniques for three-phase drives, more emphasis is given towards the development of modulation techniques for single neutral point case, particularly those that are based on space vector algorithm principles. In order to realise sinusoidal output phase voltage waveforms, several requirements and conditions have to be met. The requirements revolve around ensuring that the low order harmonics, which contribute to the machine losses, will not exist. Meanwhile, the conditions are more towards minimising the switching losses.

All modulation techniques are verified through simulation, while those for three-level case are validated experimentally as well. Comparison and discussion of obtained simulation and experimental results, performance and complexity in terms of execution time of the developed modulation techniques, are presented. The equivalence between corresponding modulation techniques, which are based on the space vector algorithm and carrier-based approach are also established.

## ACKNOWLEDGEMENT

In the name of Allah, the Most Gracious and the Most Merciful.

First and foremost, I would like to gratefully acknowledge Universiti Malaysia Perlis, UniMAP and Ministry of Higher Education Malaysia, for the opportunities and financial supports given to me to pursue my PhD studies here at Liverpool John Moores University.

My deepest gratitude goes to my supervisors, Dr Obrad Dordevic and Dr Martin Jones for their great supervision, insightful point of views and undivided attention given during the course of my PhD studies. I also would like to express my gratitude to Prof Emil Levi for the guidance and support given along with overseeing the whole progress of my studies. Having them as my supervision team is a blessing. It is a great privilege for me to have had the opportunity to work with them.

I also wish to express my sincere appreciation to my colleague, Ivan Zoric for his support, as well as his persistence in optimising the codes and synchronising the equipment used in the laboratory. It significantly reduced the complexity and the required time for me to do and complete the experiments.

My sincere thanks also go to other members of the group, Ahmad Abdullallah, Marko Slunjski and Dr Ivan Subotic as well as the visiting members, Sandro Rubino, Dr Ignacio G. Prieto and Prof Mario J. Duran. They always make me smile and laugh with their jokes and sharp discussion about everything. A cheerful working environment, surrounded by great people, I could not ask for a better place to do my PhD studies.

Last but not least, I would like to express my special appreciation to my parents, Engku Ariff and Rasuna Zakey for their endless prayers, advices and encouragements throughout all these years. I also want to express my endless gratitude to my beloved wife, Sakinah for her love, understanding and support in taking care of our lovely children, Engku Hana Safiya, Engku Aina Batrisyia and Engku Arif Zafri, especially during the last year of my PhD studies. Your love, laughter and company through my ups and downs, became my strength to finally reach the end of this journey.

## CONTENTS

<b>ABSTRACT .....</b>	<b>I</b>
<b>ACKNOWLEDGEMENT.....</b>	<b>II</b>
<b>CONTENTS .....</b>	<b>III</b>
<b>LIST OF PRINCIPAL SYMBOLS .....</b>	<b>VI</b>
<b>LIST OF USED ABBREVIATIONS.....</b>	<b>VIII</b>
<b>CHAPTER 1 INTRODUCTION.....</b>	<b>1</b>
1.1    PRELIMINARY REMARKS.....	1
1.2    AIM AND OBJECTIVES .....	3
1.3    CONTRIBUTIONS TO THE KNOWLEDGE.....	3
1.4    THESIS OUTLINE .....	4
<b>CHAPTER 2 LITERATURE REVIEW.....</b>	<b>7</b>
2.1    INTRODUCTION.....	7
2.2    MULTILEVEL THREE-PHASE DRIVES.....	7
2.3    TWO-LEVEL MULTIPHASE DRIVES.....	11
2.4    MULTILEVEL MULTIPHASE DRIVES .....	14
2.5    SUMMARY .....	18
<b>CHAPTER 3 PWM TECHNIQUES FOR TWO-LEVEL SYMMETRICAL SIX-PHASE DRIVES .....</b>	<b>21</b>
3.1    INTRODUCTION.....	21
3.2    POWER CIRCUIT TOPOLOGIES AND GENERAL EQUATIONS .....	21
3.3    DRIVE WITH SINGLE NEUTRAL POINT CONFIGURATION .....	24
3.3.1    Space vector PWM algorithm .....	24
3.3.2    Carrier-based PWM technique .....	31
3.3.3    Simulation results.....	31
3.4    DRIVE WITH TWO ISOLATED NEUTRAL POINTS CONFIGURATION .....	38
3.4.1    Space vector PWM algorithm .....	38
3.4.2    Carrier-based PWM technique .....	39
3.4.3    Simulation results.....	39
3.5    PERFORMANCE COMPARISON BETWEEN THE MODULATION TECHNIQUES WITH BOTH NEUTRAL POINT CONFIGURATIONS .....	40
3.6    SUMMARY .....	45
<b>CHAPTER 4 PWM TECHNIQUES FOR THREE-LEVEL SYMMETRICAL SIX-PHASE DRIVES ....</b>	<b>47</b>
4.1    INTRODUCTION.....	47
4.2    POWER CIRCUIT TOPOLOGIES.....	47
4.3    DRIVE WITH SINGLE NEUTRAL POINT CONFIGURATION .....	49
4.3.1    Space vector PWM algorithm .....	49

4.3.2	Carrier-based PWM technique .....	69
4.3.3	Simulation and experimental results .....	69
4.4	DRIVE WITH TWO ISOLATED NEUTRAL POINTS CONFIGURATION .....	77
4.4.1	Space vector PWM algorithm .....	77
4.4.2	Carrier-based PWM technique .....	78
4.4.3	Simulation and experimental results .....	79
4.5	PERFORMANCE COMPARISON BETWEEN THE MODULATION TECHNIQUES OF BOTH NEUTRAL POINT CONFIGURATIONS .....	84
4.6	SUMMARY .....	86
<b>CHAPTER 5 PWM TECHNIQUES FOR TWO-LEVEL ASYMMETRICAL SIX-PHASE DRIVES.....</b>		<b>89</b>
5.1	INTRODUCTION .....	89
5.2	POWER CIRCUIT TOPOLOGIES AND GENERAL EQUATIONS .....	89
5.3	DRIVE WITH SINGLE NEUTRAL POINT CONFIGURATION .....	90
5.3.1	Space vector PWM algorithm .....	91
5.3.2	Carrier-based PWM technique .....	100
5.3.3	Simulation results.....	101
5.4	DRIVE WITH TWO ISOLATED NEUTRAL POINTS CONFIGURATION .....	109
5.4.1	Space vector PWM algorithm .....	109
5.4.2	Carrier-based PWM technique .....	110
5.4.3	Simulation results.....	110
5.5	PERFORMANCE COMPARISON BETWEEN THE MODULATION TECHNIQUES WITH BOTH NEUTRAL POINT CONFIGURATIONS .....	116
5.6	SUMMARY .....	118
<b>CHAPTER 6 PWM TECHNIQUES FOR THREE-LEVEL ASYMMETRICAL SIX-PHASE DRIVES</b>		<b>121</b>
6.1	INTRODUCTION .....	121
6.2	POWER CIRCUIT TOPOLOGIES.....	121
6.3	DRIVE WITH SINGLE NEUTRAL POINT CONFIGURATION .....	121
6.3.1	Space vector PWM algorithm .....	122
6.3.2	Carrier-based PWM technique .....	135
6.3.3	Simulation and experimental results .....	136
6.4	DRIVE WITH TWO ISOLATED NEUTRAL POINTS CONFIGURATION .....	142
6.4.1	Space vector PWM algorithm .....	142
6.4.2	Carrier-based PWM technique .....	143
6.4.3	Simulation and experimental results .....	143
6.5	Performance comparison between the modulation techniques of both neutral point configurations.....	148
6.6	Summary .....	150

---

<b>CHAPTER 7 CONCLUSION.....</b>	<b>153</b>
7.1 CONCLUSION.....	153
7.2 FUTURE WORK.....	157
<b>CHAPTER 8 REFERENCES.....</b>	<b>159</b>
<b>LIST OF POTENTIAL SWITCHING SEQUENCES – 3L6PSYMSV .....</b>	<b>167</b>
<b>DESCRIPTION OF EXPERIMENTAL SETUP.....</b>	<b>169</b>
B.1 COMPUTER WITH REQUIRED SOFTWARE .....	169
B.2 REAL-TIME PLATFORM .....	170
B.3 CUSTOM-BUILT INVERTER .....	170
B.4 DC POWER SUPPLY .....	171
B.5 INDUCTION MACHINES.....	171
B.6 MEASUREMENT DEVICES .....	171
<b>PUBLICATIONS FROM THE THESIS .....</b>	<b>172</b>
C.1 JOURNAL PAPER.....	172
C.2 CONFERENCE PAPERS .....	172

## LIST OF PRINCIPAL SYMBOLS

$k, i$	General index
$n$	Number of phases of machine or inverter
$l$	Number of output voltage levels of the inverter
$dv/dt$	Instantaneous rate of voltage change
$m_f$	Frequency modulation index
$m_i$	Modulation index
$s_{ph}$	Number of sub-phases
$s_{ws}$	Number of winding sets
$s_{mm}$	Number of motors that can be controlled simultaneously
$\alpha$	Spatial displacement between the stator phase windings in radian or degree
$\alpha, \beta, x, y, 0^+, 0^-, 0_1, 0_2$	Components or axes after decoupling transformation
$V_{dc}$	Constant dc voltage source
$P_{dc}$	Positive dc rail
$N_{dc}$	Negative dc rail
$M_p$	Middle point of neutral-point clamped inverter
$A_k, B_k, C_k, \dots, F_k$	Inverter legs. An added sub-script, $k$ identifies association with particular stator winding set
$a_k, b_k, c_k, \dots, f_k$	Machine phases. An added sub-script, $k$ identifies association with particular stator winding set
$n_p, n_{p1}, n_{p2}$	Isolated neutral point. Indices 1 and 2 refer to particular stator winding set
$S_{xk}, S_{xk}'$	Upper and lower switches of $x$ inverter leg. An added sub-script, $k$ is for the indices of the switches e.g. $S_{A11}, S_{A12}$
$D_{xk}, D_{xk}'$	Upper and lower diodes of $x$ inverter leg. An added sub-script, $k$ is for the indices of the switches e.g. $D_{A11}, D_{A12}$

$v_{LEG}, v_{LEG,1}, v_{LEG,2}$	Leg voltages. Indices 1 and 2 refer to particular stator winding set
$v_{ph}, v_{ph,1}, v_{ph,2}$	Phase voltages. Indices 1 and 2 refer to particular stator winding set
$v_{nN}, v_{n1N}, v_{n2N}$	Common mode voltage. Indices 1 and 2 refer to particular stator winding set
$v_x$	Voltage of $x$ inverter leg, machine phase or component e.g. $v_A, v_{A1}, v_a, v_{a1}, v_a, v_\beta$
$i_x$	Current of $x$ inverter leg or machine phase e.g. $i_A, i_{A1}, i_a, i_{a1}$

## LIST OF USED ABBREVIATIONS

ac	Alternating current
dc	Direct current
VSI	Voltage source inverter
CHB	Cascaded H-bridge
FC	Flying capacitor
NPC	Neutral point clamped
OeW	Open-end winding
MMC	Modular multilevel converter
PWM	Pulse width modulation
CBPWM	Carrier-based pulse width modulation
SVPWM	Space vector pulse width modulation
POD	Phase opposition disposition
APOD	Alternative phase opposition disposition
PD	In-phase disposition
CMV	Common mode voltage
CMI	Common mode voltage injection (zero sequence or min-max injection)
VSD	Vector space decomposition
THD	Total harmonic distortion

*Two-level modulation methods:*

$\rho 2/3SV$	Two-level symmetrical six-phase drive space vector algorithm using derived analytical equation for dwell times calculation
2L6PSymSV	Two-level symmetrical six-phase drive space vector algorithm (single neutral point)
2L6PAsymSV	Two-level asymmetrical six-phase drive space vector algorithm (single neutral point)
CBSin	Sinusoidal carrier-based modulation for symmetrical drive (single neutral point)
SinCMI	Sinusoidal carrier-based modulation with common mode voltage injection for asymmetrical drive (single neutral point)

D2L3PSV	Dual two-level three-phase space vector modulation (two neutral points)
DSinCMI	Dual sinusoidal carrier-based modulation with common mode voltage injection (two neutral points)

*Three-level modulation methods:*

3L6PSymSV	Three-level symmetrical six-phase space vector algorithm (single neutral point)
3L6PAsymSV	Three-level asymmetrical six-phase space vector algorithm (single neutral point)
PDSin	Sinusoidal carrier-based modulation with PD-PWM for symmetrical drive (single neutral point)
PD2CMI	Sinusoidal carrier-based modulation with PD-PWM with double common mode voltage injection for asymmetrical drive (single neutral point)
D3L3PSV	Dual three-level three-phase space vector modulation (two neutral points)
D3P2CMI	Dual sinusoidal three-phase carrier-based modulation with double common mode voltage injection (two neutral points)



---

# CHAPTER 1

## Introduction

---

### 1.1 Preliminary remarks

Control of electric ac motors has changed significantly since the invention of the power semiconductors. Initially, ac motors were connected directly to the grid and thus they could only operate at a constant speed i.e. fixed operating speed, which is determined by the frequency of the grid, the load, and the construction of the motor. However, thanks to the ability of power electronic converters which can vary the amplitude and frequency of the supply according to the desired application, it is possible to drive an ac motor at variable operating speed. Hence, the term variable speed ac drives emerged. The penetration of variable speed drives is high in low voltage applications but in medium voltage applications it is only 3% (Bose, 2009). Still, according to an investigation conducted in (Schmitt and Sommer, 2001), replacement of fixed speed systems with variable speed drives may be beneficial, as the payback time of investment is one to two and a half years due to the power saving.

The ability of power electronic converters to drive conventional three-phase machines for medium and high power applications is limited by the rating of power semiconductors. One of the methods to overcome this limitation is by redistributing the current which flows into a machine, i.e. by increasing the number of inverter legs to a higher number, thus reducing the required rating of power semiconductors used in power electronic converters (Levi et al., 2007). As a result, instead of a conventional three-phase machine, multiphase machine is used. The usage of multiphase machines can lead to better machine performance since the losses in the machine, particularly the losses in the rotor and stator of the machine, are lower (Williamson and Smith, 2003). A multiphase machine also has the capability to tolerate faults, henceforth improving system reliability. Even though a fault occurs, e.g. the machine phases are open-circuited, it is still able to operate, as long as there are at least three healthy phases (Levi, 2008).

The common configuration of multiphase motors is with the number of machine phases,  $n$ , equal to 5, 6, 7, 9, etc. However, five- and seven-phase machines are rare in practice, as they have to be custom made; specific design with corresponding number of slots has to be utilised. Another option for obtaining a multiphase motor is by simple reconfiguration or by rewinding of a standard three-phase machine, thus utilising the original frame of the three-phase machine

and converting it into a multiphase (e.g. six-phase) machine. This yields a simple to manufacture and a cost effective multiphase machine. In addition, multiphase machines with a composite number of phases can be constructed in two different ways, using asymmetrical or symmetrical distribution of stator winding phases. Furthermore, they can also be configured with one or more isolated neutral points,  $n_p$  (Levi, 2008).

Another method to overcome the power limitation of the inverter is by increasing the number of output voltage levels ( $l$ ), to more than two- i.e. multilevel using different types of power electronic converters, typically a variety of voltage source inverter (VSI) topologies. For example cascaded H-bridge (CHB), flying capacitor (FC), neutral point clamped (NPC) topologies for single-sided supply (Gopakumar, 2011) as well as modular multilevel inverter (Espinoza et al., 2017, Karwatzki and Mertens, 2018), or open-end winding (OeW) topology (Somasekhar et al., 2001). These topologies are able to sustain a higher dc-link voltage than two-level inverter while using power semiconductors with the same rating. As the number of output voltage levels increases, the shape of output phase voltage waveforms, which looks like a staircase, attains more and more steps. In other words, the waveforms become closer to sinusoidal, thus subsequently reducing the distortion caused by harmonics. In addition, the switches in a multilevel converter are not switching all the time (during the fundamental period), hence reducing the effective switching frequency per device. As a result, the drive performance can be significantly improved.

It therefore seems reasonable to increase both the number of motor phases, where structures with multiple three-phase windings (e.g. six-phase) are desirable, as explained, and to increase the number of inverter output voltage levels, in order to make the most of the benefits of both approaches. However, it should be emphasised that this increases the complexity in terms of control.

This research is the continuation of previous research done by (Dordevic, 2013) which covers pulse width modulation (PWM) strategies for single-sided multilevel inverter supply for induction machine drives with odd number of phases. Likewise, the research on OeW for the odd number of phases can be found in (Bodo, 2013) whilst, for even number of phases, it can be found in (Patkar, 2013). The scope of this research will cover the PWM strategies of both carrier-based (CBPWM), and space vector (SVPWM) PWM techniques, for single-sided multilevel supplied symmetrical and asymmetrical six-phase induction machines with single or two isolated neutral points. It should be noted that the PWM techniques will be developed for the multiphase machines with sinusoidal stator winding distribution, where it is desirable for

output phase voltages waveforms to be sinusoidal. In other words, the PWM techniques are developed with the aim to obtain sinusoidal output phase voltages.

## 1.2 Aim and objectives

The main purpose of this research is to develop novel PWM techniques for single-sided multilevel inverter supplied six-phase (symmetrical and asymmetrical with both single and two isolated neutral points) drives. Thus, in order to achieve the goal of this research, several objectives have been specified, as follows:

- a. To investigate the rules required for the most appropriate selection of the space vectors and switching sequences for the space vector algorithm. A novel SVPWM technique will be developed for multilevel asymmetrical and symmetrical six-phase drives with single neutral point configuration. Simulation models will be developed and extensive simulations will be performed.
- b. To develop the equivalent carrier-based PWM techniques and compare the results and performances with the developed SVPWM techniques.
- c. To implement the developed PWM techniques in the experimental rig and prove theoretical concepts by means of experimental investigation.

## 1.3 Contributions to the knowledge

Since the space vector algorithm is unique with respect to the number of inverter output leg voltage levels, number of machine phases as well as machine's neutral point configuration, the development of space vector algorithm for a specific configuration always represents a problem of its own. The development of new modulation methods in this thesis was accompanied by many challenges, and the solutions of those challenges represent the main contributions. The main contributions of the thesis can be summarised as follows.

- A new space vector algorithm for three-level symmetrical six-phase drive with single neutral point configuration is developed. The developed algorithm is addressing the complexity of choosing the right switching sequences using the graphical analysis. The detail description of the algorithm is presented in sub-section 4.3.1. Additionally, a journal (Engku Ariff et al., 2017a) and a conference (Engku Ariff et al., 2016) paper have been published related to this algorithm.
- A modified transformation matrix, for asymmetrical six-phase machine with single neutral point configuration, is proposed (as presented in sub-section 5.3.1.3). The new

transformation solves the problem of dependency between  $0^+$  and  $0^-$  axis and establishes the links between the projections of the leg voltage and phase voltage space vectors. The dependency of  $0^+$  and  $0^-$  axis made the process of choosing the right switching sequences and developing space vector algorithm not possible. The new established links are now similar to those that commonly exist in the other space vector algorithms e.g. three-, five-, six- (symmetrical) and seven-phase machine. Therefore, the process of choosing the right switching sequences and calculating their dwell times is enabled. As a result of this work, a conference paper presenting the development of new space vector algorithm for a two-level asymmetrical six-phase drive with single neutral point configuration has been published (Engku Ariff et al., 2018).

- A new permutation method, for dealing with large number of space vectors and with numerous possible combinations for switching sequences that need to be considered, is developed (sub-section 6.3.1.3). This method is particularly useful for asymmetrical six-phase machine with single neutral point configuration where it is shown that the space vectors of a switching sequence are not necessarily located within the intended sector (as commonly is the case in other symmetrical multiphase drives). Therefore, with the developed algorithm all space vectors are considered in the process of choosing the right switching sequences. The developed algorithm is general and valid for any other drive with any number of inverter levels and machine phases. This method is presented in (Engku Ariff et al., 2017b).

#### **1.4 Thesis outline**

This thesis is organised in eight chapters and two appendices.

Chapter 1 contains an overview of the reasons of why multilevel multiphase drives are gaining the interest of researchers in recent years. It also points out the advantages of multilevel drives and multiphase machines and these advantages can be utilised by combining both topologies, into multilevel multiphase drives. The scope, aim and objectives of the research are also stated.

Chapter 2 presents a literature review related to the area of research. Literature related to conventional multilevel three-phase drives is reviewed first, particularly that which addresses PWM techniques for multilevel drives. Then, literature related to two-level multiphase drives is reviewed. The emphasis here is on modelling approaches of multiphase machines. This is

followed by literature related to multilevel multiphase drives. Reviews related to available PWM techniques for single-sided supplied and OeW topologies are included.

Chapter 3 discusses space vector model of a two-level symmetrical six-phase drive. The SVPWM techniques based on (Correa et al., 2003, Dujic et al., 2007a) are investigated and compared with the equivalent CBPWM techniques. Those modulation techniques are simulated in Matlab/Simulink for single and two isolated neutral points configurations running at no load. The obtained simulation results are analysed and their performances, in terms of phase voltage and current total harmonic distortion ( $THD_v$  and  $THD_i$ ), are determined.

Chapter 4 introduces the development of space vector algorithm for three-level symmetrical six-phase drives with single neutral point configurations. The switching states selection processes and switching sequence optimisation are elaborated in detail and this leads to the construction of the new SVPWM technique for single neutral point case. The developed SVPWM technique is simulated in Matlab/Simulink and further validated in experimental testing. The performance of the modulation techniques is compared with the carrier-based equivalent.

Chapter 5 presents the development of space vector and carrier-based PWM techniques for two-level asymmetrical six-phase drives with single and two isolated neutral point configurations. Detailed explanations regarding the development of new space vector algorithm for the drive with single neutral point configuration, where a modified VSD transformation matrix is proposed, are given. All modulation techniques are developed and verified through simulation in PLECS.

Chapter 6 presents the space vector and carrier-based PWM techniques for three-level asymmetrical six-phase drives with single and two isolated neutral point configurations. However, the development of space vector algorithm for the drive with single neutral point configuration is given more attention where a novel method of selecting the right switching sequences is proposed based on the permutation of potential starting switching states. All modulation techniques are developed and verified in open loop in PLECS. Experimental validations are also included. The performance of all presented PWM techniques is compared based on calculated phase voltage and current total harmonic distortion.

Chapter 7 summarises the conclusions of the completed work in this research and also points at further possible research directions and improvements in the future.

Finally, Chapter 8 lists the references that are referred in the thesis. Appendix A contains a table of all potential switching sequences of the first sector for a three-level symmetrical six-

phase drive. Appendix B presents detailed descriptions of the experimental rig used for validating the developed modulation techniques. Appendix C lists papers published on the basis of the research described in the thesis.

---

## CHAPTER 2

### Literature review

---

#### 2.1 Introduction

A survey of literature related to the research topic is carried out. The conducted survey by and large relates to three specific subtopics, which are multilevel three-phase drives, two-level multiphase drives and multilevel multiphase drives. Multilevel three-phase drives are addressed first, where the advantageous and disadvantageous of three-level and two-level drives are initially identified; this is followed by the discussion of the available modulation methods. For two-level multiphase drives, the emphasis is placed on the modelling approaches for multiphase machines. Correspondingly, literature reviews related to the concept of multiphase machines and available two-level PWM techniques are also conducted. Lastly, review of literature, which is mainly related to the single-sided supplied multilevel multiphase drives, is undertaken. The emphasis is mainly on the algorithms used in the PWM techniques.

#### 2.2 Multilevel three-phase drives

An inverter is called multilevel inverter when its output pole voltage has three or more voltage levels. This number of voltage levels can be synthesised using a number of available capacitor voltages or separated dc sources, depending on which topology is used. As the number of voltage levels increases, the summation of the voltage levels will produce a waveform the shape of which is like a staircase (Tolbert et al., 1999). This staircase waveform approaches a sinusoidal waveform as the number of voltage levels increases. Therefore, it can be said that the main purpose of a multilevel inverter is to synthesise an approximately sinusoidal voltage waveform via several voltage levels.

Since the output voltage of a multilevel inverter is approaching a sinusoidal waveform as the number of voltage levels increases, at the same time, the harmonic distortion decreases. In addition, assuming that it is supplied from a dc-link, the inverter can sustain a higher dc-link voltage compared to a two-level inverter using power semiconductors of the same rating. However, the total number of power semiconductors is higher. As the number of voltage levels increases, more problems will arise due to: unbalance in capacitor voltages, complexity in

controlling the huge number of power semiconductors, increase in cost, circuit layout and packaging etc. (Lai and Peng, 1996).

It is over three decades since the first multilevel inverter topology was introduced in the 1980s, followed by other topologies several years later. Since then, quite a few variants and hybrids of these topologies have emerged, as surveyed and discussed in (Kouro et al., 2010). The three classic topologies are flying capacitor (FC), cascaded H-bridge (CHB) and neutral point clamped (NPC), as noted already.

As its name implies, FC inverter uses individual capacitors to clamp the inverter voltage at the capacitors' voltage levels. As the number of output voltage levels ( $l$ ), increases, the number of the auxiliary capacitors also increases according to  $(l - 1)(l - 2)/2$  per phase, excluding dc-bus capacitors (Lai and Peng, 1996). Although FC is modular and capable of balancing the auxiliary capacitor voltages naturally (if appropriate modulation technique is implemented), it has not penetrated the industry significantly, when compared to the other two topologies. This is because in order to balance the auxiliary capacitor voltages, the switching frequency has to be high or the value of capacitors need to be large; thus it is not well suited for high-power applications. Furthermore, the capacitor voltages need to be pre-charged first (Franquelo et al., 2008).

The CHB inverter is able to produce multilevel output voltage by cascading several H-bridges with individual dc sources together. These dc sources are not necessarily set at the same voltage level and, if the levels of the dc sources are unequal, more output levels can be synthesised. In this case, the flexibility is reduced due to reduction of possible switching sequences and the rating of the each H-bridge will be different (Gopakumar, 2011). Details of various configurations and applications of CHB are discussed in (Malinowski et al., 2010).

The NPC topology was introduced in (Nabae et al., 1981). The NPC inverter was proposed with an intention to reduce the magnitude of harmonics which cause losses and pulsating torques in the motor and to allow a controllability of the output voltage fundamental. Since then, it has been gaining acceptance in medium and high voltage applications and has become the most widely used multilevel inverter in many industrial applications (Rodriguez et al., 2010). The dc-bus voltage in NPC inverter is split into the required voltage levels by a series of capacitors. The voltage across the off switches is clamped through the diodes to the points between those capacitors, i.e. middle points also known as neutral points, hence the name. However, the NPC topology also suffers from several problems. As the number of output voltage levels increases, balancing of the capacitor voltages becomes a critical issue. Another

problem is uneven loss distribution between inner and outer configuration of switching devices (Gopakumar, 2011).

Multilevel output voltage can also be realised by means of open-end winding (OeW) configuration of motor stator windings using two or more two-level inverters (Somasekhar et al., 2001). The OeW offers some advantages over the classic multilevel topologies since it does not need additional diodes or capacitors. Thus, the issue of capacitor voltage balancing can also be avoided (Levi, 2013). The total power can be shared between those inverters thus making it possible to operate with lower dc-link voltages per inverter. This topology is capable of producing multilevel output voltage using individual isolated dc sources connected to each inverter (Casadei et al., 2008b) or using a single dc source supplying both inverters (Sivakumar et al., 2009). Although in some applications, usage of isolated dc supplies creates additional challenges and increases the cost of the drive, this is not the case if battery supplies are used, e.g. in electric vehicles.

As multilevel inverter topologies are gaining their place in medium power applications, several modulation algorithms for PWM control have been developed and proposed by researchers, mainly based on CBPWM or SVPWM techniques. One of the CBPWM techniques is phase-shifted PWM where the carrier signals are shifted by  $360^\circ/(m_f \cdot l)$  ( $m_f$  is the frequency modulation index, i.e. the ratio of the switching over fundamental frequency) (Joos et al., 1998). This modulation technique, which is also known as interleaved switching (Wilkinson et al., 2006), is usually used in FC topologies since it is capable of self-balancing (at the expense of more switching) the dc-link voltages and it produces lower total harmonic distortion at the output.

Additionally, other CBPWM techniques are proposed in (Carrara et al., 1992) where the carrier signals are level-shifted. These techniques are named based on the arrangement of the carrier signals, which are: 1) phase opposition disposition (POD) – when the negative side carrier signals are in the opposite phase of positive side carriers; 2) alternative phase opposition disposition (APOD) – when the carrier signals are alternately in opposite phase to each other; and 3) in-phase disposition (PD) – when the carrier signals are in phase with each other. Out of these three techniques, PD gives the lowest line-to-line harmonic voltage distortion (Carrara et al., 1992, McGrath and Holmes, 2002) and it is usually preferred in NPC topology because each carrier signal can easily be associated to the power switches.

Alternatively, SVPWM techniques for three-level three-phase case are discussed in (Ogasawara et al., 1990) for NPC topology. Since then, other algorithms for multilevel three-

phase case were proposed using different methods to determine which sector the reference voltage vector belongs to, such as in (Dai et al., 2005, Prats et al., 2003, Sanmin et al., 2003). In addition, a fast space vector modulation algorithm, which is valid for  $l$ -level three-phase inverter, is proposed and discussed in details in (Celanovic and Boroyevich, 2001).

In case of two-level inverters, CBPWM and SVPWM techniques are already proven to be able to deliver the same performance, as discussed in (Holmes, 1996). The two-level CBPWM technique is producing the same output as two-level SVPWM technique if min-max injection is used. This method of injection also known as zero sequence injection or common mode voltage injection (CMI). The purpose of the injection is to centre the reference phase voltages at zero axis. On the contrary, for three-level three-phase inverter, this kind of injection is not valid, as discussed in (McGrath et al., 2003, Wang, 2002). Thus, in order for three-level CBPWM method to be able to deliver the same performance as three-level SVPWM technique, more than one type of common mode voltage injections need to be applied based on several conditions, as proposed in (Lee et al., 2000). However, a simpler common mode voltage injection that is easier for implementation is proposed in (Grandi and Loncarski, 2014), where the injection is generalised into one equation.

Although modulation techniques that are based on carrier-based approach are much simpler to implement, they are unable to give a detail and clear overview of what is happening inside the generation process of the switching signals. However, this is not the case in space vector approach. The latter is able to show in details the mapping of the low order harmonics (which is important in multiphase case) and how the switching signals are generated with respect to the chosen switching sequences. Furthermore, it can be shown that space vector approach inherently generates symmetrical switching signals from the chosen switching sequences. This was a reason why for long period of time space vector algorithm was considered as superior in comparison to sinusoidal carrier-based PWM. The principle of symmetrical switching was inherited from space vector approach and used for development of common mode voltage injection in carrier-based PWM approach (for two-level case). Also the same principle was used in multilevel case to develop carrier-based approach with double common mode voltage injection. In general, if one requires detail information on how the modulation technique works or how the switching signals are generated, space vector approach is the right choice. Otherwise, equivalent carrier-based PWM technique is recommended due to its simplicity for implementation.

The applications of these multilevel topologies are vast and range from renewable energy applications (photovoltaic, wind power), electric vehicles, ship propulsion and traction applications, to high voltage power systems and distribution applications (Franquelo et al., 2008, Kouro et al., 2010). Although all three mentioned topologies can be implemented in all these applications, only certain topologies are recommended for certain applications. This is because each topology has its own pros and cons in terms of performance, design and cost in different applications, as discussed in (Fazel et al., 2007, Islam et al., 2011).

### 2.3 Two-level multiphase drives

The first investigation of multiphase motors can be traced back to 1969 when an inverter-fed five-phase induction motor was investigated in order to find out if it was possible to reduce the low frequency torque ripple by increasing the number of motor phases, since the lowest frequency components of torque ripple harmonics are of the order  $2n \pm 1$ , where  $n$  is the number of machine phases. Hence, the torque ripple harmonics were shifted to higher frequency (Ward and Härer, 1969).

Still, multiphase motor topology did not attract much attention of the researchers until early 1990' when the power of the drive became limited by the rating of power semiconductors used in power converters. By means of increasing the number of phases, the current which flows through the motor can be split, thus reducing the rating of power semiconductors used in the power converter (Levi et al., 2007). However, it should be noted that this limitation could be also overcome from the converter side, i.e. by using interleaved converter topologies (Honbu et al., 1983, Ueda et al., 1995). In addition, from the machine's point of view, the efficiency increases as the number of phases increases since the losses in the stator and rotor are somewhat reduced (Williamson and Smith, 2003).

Multiphase motors also show a greater fault tolerant capability, which is an important feature to increase reliability of a system. Multiphase machines can still operate while one or more of the machines' phases are open circuited (up to  $n - 3$  phases), though at lower output power (Aroquiadassou et al., 2009) or short circuited (Apsley and Williamson, 2006). This leads to increased interest in industry in replacing the classic three-phase machines in applications where the high level of reliability is required. However, during faulted operation, some problems can occur due to parameter changes and introduction of torque-speed ripples which degrade the performance (Betin et al., 2014).

If the stator winding distribution is not sinusoidal but concentrated, it is possible to increase the developed torque by harmonic injection method. A third harmonic can be injected to increase the developed torque in a five-phase motor and in seven-phase case, the third and fifth harmonics can be injected for the same purpose (Toliyat and Lipo, 1994, Toliyat et al., 1991a, Toliyat et al., 1991b).

As noted, a motor is called multiphase when the number of stator phases is larger than three (Levi, 2011). When  $n$  is an odd prime number, e.g. 5, 7 or 11, the stator windings are connected in a star with one isolated neutral point,  $n_p$ . For the other numbers of phase, such as composite numbers of phases (e.g. 6, 9 or 15), the stator phase windings can be either connected into a star with single neutral point or into multiple stars with several isolated neutral points, such that  $n_p = s_{ph} \cdot s_{ws}$ , where  $s_{ph}$  is the possible number of sub-phases (3, 5, 7, etc.), and  $s_{ws}$  is the number of winding sets, i.e. isolated neutral points (2, 3, 4, etc.) (Levi, 2008).

Furthermore, in a machine with a composite number of phases, the spatial displacement between the stator phase windings,  $\alpha$ , can be set such that it will be equal to  $\pi/n$ , which leads to asymmetrical distribution of magnetic axis of windings, instead of  $2\pi/n$ , which leads to symmetrical distribution of magnetic axis of windings. Nevertheless, the machine configuration can be with one or more isolated neutral points. In (Patkar and Jones, 2013), performance of single and dual isolated neutral point configurations of asymmetrical six-phase induction machine is investigated. The latter configuration shows better performance with lower current THD due to the absence of zero sequence current.

Analysis and modelling of an induction motor is discussed in detail in (Nelson and Krause, 1974) where asymmetrical six-phase machine with two isolated neutral points is used as an example. This type of modelling is also discussed and referred to as dual stator approach in (Bojoi et al., 2003), where the effect of unbalanced current sharing between two winding sets of an asymmetrical six-phase machine, due to the asymmetry of the machine and the supply, is analysed.

Another modelling approach is also proposed for asymmetrical six-phase machines with two isolated neutral points, which is known as vector space decomposition (VSD), in (Zhao and Lipo, 1995). This approach maps the voltage or current vectors into three two-dimensional orthogonal subspaces, which give three sets of decoupled vector equations. The first subspace is known as the  $d$ - $q$  plane (also commonly known as  $\alpha$ - $\beta$  plane in literature), where the fundamental component and harmonics of the order of  $12k \pm 1$ , ( $k = 1, 2, 3 \dots$ ) are mapped. The second subspace is called  $z_1$ - $z_2$  plane, where harmonics of the order of  $6k \pm 1$  ( $k = 1, 3, 5 \dots$ ) are

mapped. Another more common name for  $z_1$ - $z_2$  plane in literature is  $x$ - $y$  plane. The last subspace is  $0_1$ - $0_2$  plane, where zero sequence harmonics are mapped. However, harmonics of phase voltages mapped in the last subspace are zero when there are two isolated neutral points. Harmonics mapped in the  $x$ - $y$  plane produce losses and do not contribute to the torque development. Thus, by setting the vector reference in the second plane to zero, the performance of the machine can be improved significantly.

In (Bakhshai et al., 1998), vector classification technique is discussed as a way of developing the inverter modulation method. This technique decomposes the switching state vectors into two three-phase space vector planes where the second plane is rotated by  $30^\circ$  clockwise. It also uses four active and one zero vector in its switching states, as in VSD approach, but one of the chosen active vectors is smaller than the others. This technique does not consider the vectors mapped into the second subspace. On the contrary, a similar but better approach than (Bakhshai et al., 1998) was proposed in (Grandi et al., 2008), known as complete three-phase decomposition. This approach is capable of completely and independently controlling both planes; thus, zeroing the harmonics mapped into the second plane is also possible.

In order to control the machine modelled by above methods, PWM techniques are applied. In (Hadiouche et al., 2006), continuous and discontinuous SVPWM techniques for two-level asymmetrical six-phase drives are compared. The machine is modelled using the VSD approach. The comparison shows that the discontinuous SVPWM produces better performance than continuous SVPWM in high modulation index range, while in the low and medium modulation index range, it is the other way round. These control strategies are further improved in (Marouani et al., 2008) using the same drive type, but the number of sectors is increased from the original 12 to 24. The previous and improved continuous and discontinuous SVPWM techniques are compared. Although previous discontinuous SVPWM shows better performance compared to the others, in terms of switching losses, improved discontinuous SVPWM is better since the changes of output states per switching period are two or less, compared to four changes in the previous discontinuous SVPWM.

Furthermore, it is possible to operate and independently control multiple motors at the same time using a single multiphase inverter topology, although this applies to sinusoidally distributed winding topologies only. The number of motors that can be operated together can be determined as  $s_{mm} = (n - 2)/2$ , if  $n$  is an even number, and  $s_{mm} = (n - 1)/2$ , if  $n$  is an odd number. The possible connections of these motors are either in series or parallel connection.

The possibility and performance of operating several multiphase motors using series connection are discussed in (Levi et al., 2003); the parallel connection (which is of no practical relevance, in contrast to the series connection) is discussed in (Jones et al., 2009b). Last but not least, multiphase motors also enable realisation of integrated on-board battery charging systems in electric vehicles. The stator winding is used as a filter with zero-electromagnetic torque production during battery charging (Subotic et al., 2013).

## 2.4 Multilevel multiphase drives

The capability of multilevel inverter to sustain higher dc-link voltage using the same rating of power semiconductors used in two-level inverter, while at the same time reducing total harmonic distortion, and the ability of multiphase machines to deliver higher torque with the same stator current rating as in a three-phase machine (by distributing the stator current through more phases) has drawn interest of researchers in recent years. In (Lu and Corzine, 2005), the combination of a multilevel inverter and a multiphase motor was investigated for the first time. Since then several papers have been published discussing the modulation methods for multilevel multiphase drives, such as (Leon et al., 2010a, Leon et al., 2010b, Lopez et al., 2008b).

As noted, a multilevel multiphase drive was investigated for the first time in (Lu and Corzine, 2005) for three-level NPC inverter supplied five-phase induction motor in order to observe torque ripple and phase current harmonics. The five-phase induction motor was modelled in several planes orthogonal to each other and possible switching states for three-level five-phase inverter were determined. There are  $l^n$  switching states for a multilevel multiphase inverter. Hence for a three-level five-phase inverter there are  $3^5 = 243$  switching states. Out of these 243 switching states, 32 are redundant, which makes the total number of phase voltage space vectors equal to 211. It is shown in (Lu and Corzine, 2005) that, by using the nearest triangle space vectors (chosen from one layer before the outer-most and the outer-most layer space vectors), path and switching sequence adjustment (alternating between the one layer before and outer-most layer of space vector), the torque ripple and low frequency current harmonics in a five-phase induction motor will decrease. However, in this paper the authors do not consider the second i.e.  $x$ - $y$  plane. The harmonics in this plane are restricted only by stator resistance and leakage inductance, hence leading to large current ripple. Therefore, a reduced torque ripple is obtained at the cost of increased current ripple.

In (Qingguo et al., 2006), a different approach to determining the space vector modulation for three-level five-phase NPC inverter was used. Out of 243 space vectors, only 43 space vectors are chosen (40 active space vectors including ten redundant vectors and three zero vectors) as efficient working vectors. These efficient working vectors are divided into ten sections and each section is divided into four small triangular regions and four groups of voltage vectors. The switching sequences are determined basically by following three principles, which are: 1) only one-level transitions of the output leg voltage are allowed in order to avoid high  $dv/dt$ , 2) not more than two changes per leg per switching period are allowed in order to minimize switching losses, and 3) the selected voltage vectors should balance the neutral-point voltage since every voltage vector affects the neutral-point voltage. However, presented methods follow three-phase approach and do not consider  $x$ - $y$  plane, hence increasing current ripple and current THD.

Another multilevel multiphase SVPWM technique is proposed and discussed in (Lopez et al., 2008b) and tested using five-level CHB inverter with five-phase induction motor. This modulation algorithm is the combination of two-level multiphase SVPWM with a technique which determines the multilevel modulation using a two-level modulator. First of all, phase reference signals are normalised with dc supply voltage. Then the normalised signals are decomposed into integer and fractional part where the fractional part is sorted out in descending order. The permutation matrix (information produced to sort the fractional parts) is used to rearrange the coefficients in the matrix (upper triangular matrix) and extract the displacement vectors. Next, the integer parts of normalised signals are added to the displacement vectors to get the switching vectors. Finally, the switching times are calculated by using fractional parts of normalised signals vector. This modulation algorithm has also been applied in (Lopez et al., 2008a) for three-level three-phase inverter. The same modulation algorithm with consideration of switching state redundancy was discussed in (Lopez et al., 2009a).

Although the SVPWM technique in (Lopez et al., 2008b) is valid for any number of levels and phases, it is unable to correctly yield desired waveforms under unbalanced dc supply. Therefore, a multilevel multiphase feed-forward space vector algorithm for unbalanced dc supply was proposed and discussed in (Leon et al., 2010a) where the actual dc voltages of the inverter were measured. The algorithm uses a similar approach as in (Lopez et al., 2008b); however, the type of the multilevel inverter topology has to be taken into consideration in the algorithm. The algorithm was tested using five-level five-phase unbalanced dc supplied CHB inverter with a five-phase induction motor.

A different SVPWM technique is proposed and discussed in (Leon et al., 2010b). It is based on the modulation technique for multilevel single-phase inverter, as proposed in (Leon et al., 2008). The algorithm was tested using NPC, FC and CHB inverter topologies. Depending on the topology it is applied to, the reference voltage and the algorithm structure should be different. Nevertheless, three steps must be followed regardless of which multilevel inverter topology is used. The possible switching states and control region need to be determined first; this is then followed by normalisation of the reference voltage. Finally, the switching sequences and duty cycles are determined based on two nearest switching states corresponding to normalised reference voltage in the identified control region.

A comprehensive analytical solution for SVPWM technique for multilevel multiphase inverter is discussed in (Hu et al., 2011). A matrix which consists of inverter output voltage is decomposed by using eigenspace decomposition method. The algorithm is based on minimising the number of switchings of power semiconductors and total conduction time. This technique also uses an integer and fraction decomposition method as in (Lopez et al., 2008b) with a minor modification. In (Chen and Hu, 2014), this technique is improved using quantization method where the harmonic distortion is significantly reduced.

A VSD approach is used in (Gao and Fletcher, 2010) for a three-level five-phase NPC inverter modulation technique development, where the reference voltage components in the second  $x$ - $y$  plane, i.e.  $z_1$ - $z_2$  plane in (Zhao and Lipo, 1995), are set to zero and the vector space in the first  $\alpha$ - $\beta$  plane is further partitioned to determine the switching sequence. The number of possible switching states is significantly reduced from initial 243, to 113 switching states by following pole voltage relationship between different phases principle, i.e. order-per-sector law. In order to determine the possible switching sequence, there are three rules which need to be followed and these rules are as stated in (van der Broeck et al., 1988). Furthermore, switching sequences were optimised using additional criteria in order to provide dc-link capacitor voltage balancing.

In (Dordevic et al., 2013a, Dordevic et al., 2013b), a VSD modelling approach is applied with a modification of the modulation algorithm from (Gao and Fletcher, 2010) in the calculation of sector partitioning and determination of subsectors for selection of switching sequences. Although this modulation technique requires many tedious calculations to determine all the subsectors and switching sequences, all the calculations are done offline. The modified modulation technique is applied to three-level seven-phase NPC inverter with  $R$ - $L$  load. A comparison between this and PD modulation technique with double common mode voltage

injection was carried out in (Dordevic et al., 2013a) for three-level five-phase inverter drive. It is shown that both modulation techniques produce the same waveform although the execution time for the latter one is slightly lower than for the former technique.

Two schemes of space vector modulation for three-level five-phase open-end winding configuration were proposed in (Jones et al., 2010), which are named as equal and unequal reference sharing schemes. When compared, the latter scheme is better in terms of output voltage quality with lower value of THD. Since then, this scheme has been further studied in (Levi et al., 2012) and applied even in seven-phase OeW drives (Bodo et al., 2011). A further investigation of this scheme was conducted in (Jones et al., 2012) by decomposing three-level space vector decagon into several two-level decagons. The CBPWM techniques for three-level five-phase OeW drive were investigated in (Bodo et al., 2013). It is demonstrated that PD-PWM shows better performance, in terms of output voltage quality, compared to the other carrier-based techniques. A comparison in terms of performance between PD-PWM for OeW topology in (Bodo et al., 2013) and PD-PWM for single-sided supplied drive in (Dordevic et al., 2013a) was investigated in (Bodo et al., 2012). Both techniques give the same results, which demonstrate that the same performance can be obtained by using single-sided supply and OeW topology.

In addition, the above scheme is also applied in (Patkar et al., 2012) for symmetrical six-phase induction motor with open-end winding configuration using two two-level inverters. Unlike the five-phase machine with open-end winding configuration, negative zero-axis has to be taken into consideration since the mapped space vectors onto this axis are not zero. However, by using two isolated dc supplies, this issue can be avoided. Meanwhile, a comparison between the performance of phase-shifted PWM i.e. APOD-PWM and PD-PWM modulation in an asymmetrical six-phase drive with open-end winding configuration has been discussed in (Jones et al., 2013). Clearly, PD-PWM technique gives a better performance compared to the other techniques, based on the voltage THD. However, the situation is the opposite when looking at the performance based on the current THD. Performance and modulation techniques used for symmetrical and asymmetrical six-phase drive with OeW configuration are discussed in detail in (Patkar, 2013). Meanwhile, a five-phase OeW configuration is investigated in (Darijevic et al., 2013a). Two two-level inverters with isolated and unequal dc-link voltages with a ratio of 2:1 are used to synthesise four-level output voltage. Detailed investigation of glitches caused by a dead-time effect in this topology and a solution of the problem is presented in (Darijevic et al., 2013b).

A structure with four two-level three-phase inverters for driving an asymmetrical six-phase induction machine with open-end winding configuration is proposed in (Grandi et al., 2010a, Grandi et al., 2010b). The structure uses isolated dc supplies in order to avoid the negative zero sequence current component flow in the system. It also adopted the nearest three vectors control strategy approach, as introduced in (Celanovic and Boroyevich, 2001). On the contrary, in (Oleschuk et al., 2013), four three-level NPC three-phase inverters with four isolated dc supplies (equal dc voltages) are used to drive an asymmetrical six-phase induction machine with OeW configuration. A weighted THD is used as an indicator to compare the performance between synchronous SVPWM technique and discontinuous scheme for different modulation indices. The former scheme shows far better performance than the latter scheme.

In (Duran et al., 2010, Duran et al., 2011), restrained search predictive control technique is applied to a three-level NPC inverter fed asymmetrical six-phase induction machine with two isolated neutral points. The feasibility of using this control technique to drive the system is investigated using simulations. Its performance, based on several performance parameters, is also compared to optimal standard predictive control. Although the total number of commutations is greatly reduced using the restrained search predictive control technique, in terms of THD, optimal standard predictive control technique is far better.

## 2.5 Summary

In this chapter, numerous papers related to the research topic are reviewed. At first, the basic concept and topologies of multilevel three-phase drive are introduced. The available control methods, i.e. SVPWM and CBPWM, for multilevel three-phase drive are also surveyed and identified. Then, two-level multiphase drives are discussed where more focus is placed on the modelling techniques for multiphase machines, particularly six-phase symmetrical and asymmetrical induction machines. Last but not least, literature related to multilevel multiphase drives with emphasis on the PWM techniques for single-sided supplied and open-end winding topologies is reviewed. Although most of the references on multilevel multiphase drives are related to machines with odd number of phases, special attention during literature survey was paid to gather all those references which are related to multilevel six-phase drives, since this is the main topic of this research.

The literature discussing space vector modulation techniques for single-sided supplied multiphase drives is listed in Table 2.1. As already mentioned, space vector algorithms are unique and tightly related to the analysed drive topology, i.e. highly dependent on number of

Table 2.1: List of literature discussing space vector PWM techniques for single-sided supplied multiphase drives with single neutral point configuration.

No. of machine phases	Space vector algorithm	
	2-level	3-level
5	(Dujic et al., 2007b) (Dujic, 2008) (Iqbal and Moinuddin, 2009)	(Gao and Fletcher, 2010) (Dordevic et al., 2013a) (Dordevic, 2013)
6 (Symmetrical)	(Correa et al., 2003) (Dujic et al., 2007a)	
6 (Asymmetrical)	(Zhao, 1995) ** (Zhao and Lipo, 1995) **	
7	(Dujic et al., 2007d) (Dujic, 2008) (Casadei et al., 2008a)	(Dordevic et al., 2013b) (Dordevic, 2013)
9	(Dujic et al., 2007c) (Dujic, 2008) (Grandi et al., 2007)	
11	(Moinoddin et al., 2015)	

\*\* Introduced the derivation of vector space decomposition matrix, which is valid for both single and two isolated neutral points configuration. However, modification of the matrix is proposed later on in the thesis (see sub-section 5.3.1.3) for new space vector algorithm for this drive topology.

inverter output leg voltage levels, number of machine phases and the spatial distribution of the machine (symmetrical or asymmetrical). However, space vector PWM techniques for multiphase machines with multiple neutral points configuration are excluded in this list. This is because well-established three-phase SVPWM techniques are commonly used for these cases when separately applied to each three-phase winding set. In addition, carrier-based PWM techniques are also not listed since they can easily be expanded to any number of phases.

It can be clearly seen that the development of space vector PWM techniques for single-sided supplied two- and three-level asymmetrical and three-level symmetrical six-phase drives with single neutral point are not yet addressed in the literature. Hence, it can be said the novelties of this research is in focusing in closing these gaps. The gaps for development of space vector algorithms for three-level nine- and eleven-phase, are considered as potential continuations of this research.



---

## CHAPTER 3

### PWM techniques for two-level symmetrical six-phase drives

---

#### 3.1 Introduction

This chapter discusses modulation strategies based on space vector and carrier-based approaches for two-level symmetrical six-phase drives with single and two isolated neutral points. In the discussed space vector algorithm, the derivation of the equations for calculating the dwell times is shown. The discussion of this space vector algorithm is necessary as it serves as a foundation for the development of space vector algorithms for the three-level case. Additionally, another method for calculating the dwell times through time matrix approach is also presented. Unlike the derived equations, which are valid only for its particular drive topology, the time matrix approach is more general and can be applied to other drive topologies with simple adaptation. The developed modulation techniques are verified through simulations using Matlab/Simulink and their performances compared.

#### 3.2 Power circuit topologies and general equations

In a symmetrical six-phase machine, the stator phase windings are spatially shifted by  $60^\circ$  and the windings can be connected into star, either with a single or with two isolated neutral points. Furthermore, the distribution of the machine windings is assumed to be sinusoidal. The power circuit topology of a two-level symmetrical six-phase drive with single neutral point is shown in Figure 3.1. The inverter is assumed to be supplied from a constant dc voltage source ( $V_{dc}$ ). Each leg of the inverter consists of a pair of switches (the upper and the lower switch) and the inverter legs are denoted by  $A, B, C$ , etc. while the phases are denoted by  $a, b, c$ , etc. The upper and lower switches are assumed to be ideal and they are complementary to each other. In other words, when the upper switch is on, the lower switch should be off and vice versa.

From Figure 3.1, one gets that the inverter output leg voltages ( $v_{LEG}$ ), when referred to the negative dc rail ( $N_{dc}$ ), can be defined as:

$$[v_{LEG}] = [v_{ph}] + [1 \ 1 \ \dots \ 1]^T \cdot v_{nN} \quad (3.1)$$

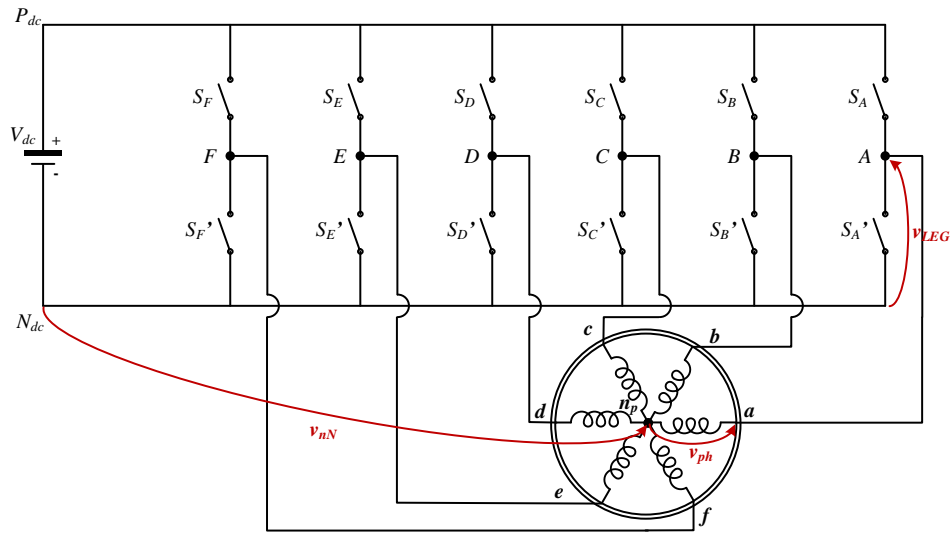


Figure 3.1: Power circuit topology of two-level symmetrical six-phase drive with single neutral point.

where  $v_{ph}$  are output phase voltages of the machine, while  $v_{nN}$  is the voltage between the neutral point and  $N_{dc}$ . This voltage is known as the common mode voltage (CMV). Since the stator windings of the machine are star connected, the sum of  $v_{ph}$  must be zero. Hence,  $v_{nN}$  can be defined as:

$$v_{nN} = \frac{1}{6} \cdot [1 \ 1 \ 1 \ 1 \ 1 \ 1] \times [v_{LEG}] \quad (3.2)$$

Therefore, by substituting (3.2) into (3.1), the relationship between  $v_{ph}$  and  $v_{LEG}$  can be obtained as in:

$$[v_{ph}] = \left( \begin{bmatrix} 1 & 0 & \cdots & 0 \\ 0 & 1 & & 0 \\ \vdots & & \ddots & \vdots \\ 0 & 0 & \cdots & 1 \end{bmatrix} - \frac{1}{6} \cdot \begin{bmatrix} 1 & 1 & \cdots & 1 \\ 1 & 1 & & 1 \\ \vdots & & \ddots & \vdots \\ 1 & 1 & \cdots & 1 \end{bmatrix} \right) \times [v_{LEG}] \quad (3.3)$$

The power circuit topology for a two-level symmetrical six-phase drive with two isolated neutral points is as shown in Figure 3.2. Since the stator windings are connected as two three-phase winding sets, additional numbering (in subscript) is added into the notations used for the inverter legs and the machine phases. From Figure 3.2, the output leg voltages of each winding set ( $v_{LEG,1}$  and  $v_{LEG,2}$ ), when referred to  $N_{dc}$ , can be defined as:

$$\begin{aligned} [v_{LEG,1}] &= [v_{ph,1}] + [1 \ 1 \ 1]^T \cdot v_{n1N} \\ [v_{LEG,2}] &= [v_{ph,2}] + [1 \ 1 \ 1]^T \cdot v_{n2N} \end{aligned} \quad (3.4)$$

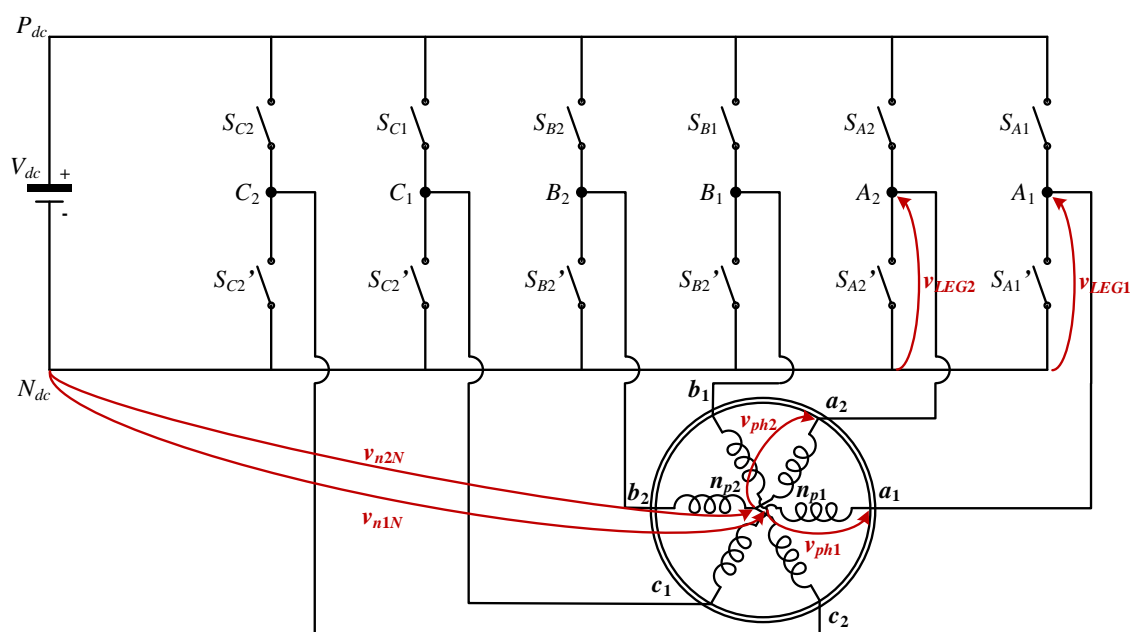


Figure 3.2: Power circuit topology of two-level symmetrical six-phase drive with two isolated neutral points.

As both of the winding sets are star connected, the sum of the output phase voltages of each winding set ( $v_{ph,1}$  and  $v_{ph,2}$ ) should be zero. Hence, the CMV of both winding sets can be defined as:

$$\begin{aligned} v_{n1N} &= \frac{1}{3} \cdot [1 \ 1 \ 1] \times [v_{LEG,1}] \\ v_{n2N} &= \frac{1}{3} \cdot [1 \ 1 \ 1] \times [v_{LEG,2}] \end{aligned} \quad (3.5)$$

Finally, by substituting (3.5) into (3.4), the relationship between  $v_{ph}$  and  $v_{LEG}$  can be obtained as:

$$\begin{aligned} [v_{ph,1}] &= \left( \begin{bmatrix} 1 & 0 & 0 \\ 0 & 1 & 0 \\ 0 & 0 & 1 \end{bmatrix} - \frac{1}{3} \cdot \begin{bmatrix} 1 & 1 & 1 \\ 1 & 1 & 1 \\ 1 & 1 & 1 \end{bmatrix} \right) \times [v_{LEG,1}] \\ [v_{ph,2}] &= \left( \begin{bmatrix} 1 & 0 & 0 \\ 0 & 1 & 0 \\ 0 & 0 & 1 \end{bmatrix} - \frac{1}{3} \cdot \begin{bmatrix} 1 & 1 & 1 \\ 1 & 1 & 1 \\ 1 & 1 & 1 \end{bmatrix} \right) \times [v_{LEG,2}] \end{aligned} \quad (3.6)$$

Since (3.3) and (3.6) represent general relationships between  $v_{ph}$  and  $v_{LEG}$  for a six-phase machine, these equations are also valid for either two- or multilevel symmetrical and asymmetrical six-phase drives, and hence will be used in the chapters to follow.

### 3.3 Drive with single neutral point configuration

In this section, a space vector PWM algorithm and carrier-based PWM technique for a two-level symmetrical six-phase drive with a single neutral point are discussed. The process of choosing the switching sequences and the derivation of equations for dwell times calculation, for space vector algorithm, are shown. In addition, another approach of calculating the dwell times is also presented. For the carrier-based approach, due to symmetry of the reference waveforms, it is adequate to implement the conventional sinusoidal modulation technique without any common mode voltage injection. Both PWM techniques are implemented and simulated in Matlab/Simulink for ideal case and when built-in inverter dead time is included.

#### 3.3.1 Space vector PWM algorithm

The development of two-level six-phase space vector algorithm (2L6PSymSV) is based on (Correa et al., 2003, Dujic et al., 2007a). In addition, a different approach of calculating the dwell times, based on dwell time matrix, is also presented. This approach does not require any derivations of the equations to calculate the dwell times. Thus, it offers the capability to calculate dwell times for any chosen switching sequence and it is easily adaptable to any number of machine phases.

##### 3.3.1.1 Projection of space vectors

In two-level symmetrical six-phase drives, there are  $2^6 = 64$  (denoted as 0 to 63) possible switching states. By normalising the output leg voltage levels by  $V_{dc}$ , they can be represented as six-digit binary system i.e. as 000000 to 111111. As an example, switching state 110011 is  $1 \cdot 2^5 + 1 \cdot 2^4 + 0 \cdot 2^3 + 0 \cdot 2^2 + 1 \cdot 2^1 + 1 \cdot 2^0 = 51$  in decimal. These switching states also correspond to  $v_{LEG}$  space vectors. In other words, by multiplying the switching states (in normalised representation) with transformation matrix, the projections of  $v_{LEG}$  space vectors onto three mutually orthogonal two-dimensional planes ( $\alpha$ - $\beta$ ,  $x$ - $y$  and  $0^+$ - $0^-$ ) can be obtained as shown in Figure 3.3. The transformation matrix for six-phase drive is defined as (Dordevic, 2013, Dujic et al., 2007a):

$$\begin{bmatrix} v_\alpha \\ v_\beta \\ v_x \\ v_y \\ v_{0^+} \\ v_{0^-} \end{bmatrix} = \frac{2}{6} \cdot \begin{bmatrix} 1 & \cos(\alpha) & \cos(2\alpha) & \cos(3\alpha) & \cos(4\alpha) & \cos(5\alpha) \\ 0 & \sin(\alpha) & \sin(2\alpha) & \sin(3\alpha) & \sin(4\alpha) & \sin(5\alpha) \\ 1 & \cos(2\alpha) & \cos(4\alpha) & \cos(6\alpha) & \cos(8\alpha) & \cos(10\alpha) \\ 0 & \sin(2\alpha) & \sin(4\alpha) & \sin(6\alpha) & \sin(8\alpha) & \sin(10\alpha) \\ 1/2 & 1/2 & 1/2 & 1/2 & 1/2 & 1/2 \\ 1/2 & -1/2 & 1/2 & -1/2 & 1/2 & -1/2 \end{bmatrix} \times \begin{bmatrix} v_a \\ v_b \\ v_c \\ v_d \\ v_e \\ v_f \end{bmatrix} \quad (3.7)$$

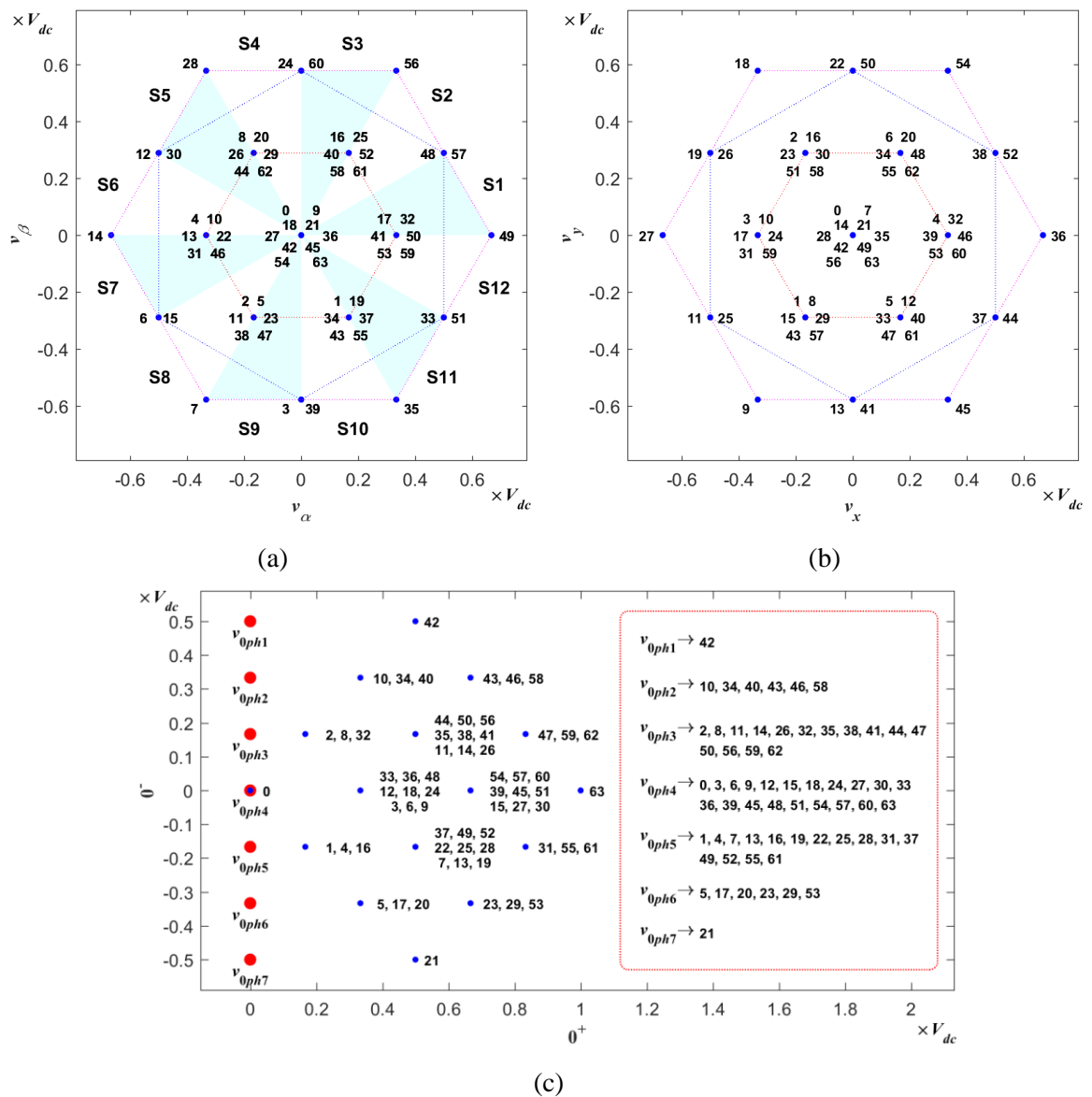


Figure 3.3: Projection of  $v_{LEG}$  and  $v_{ph}$  (dots in red) space vectors of the analysed two-level symmetrical six-phase drive with single neutral point in the: (a)  $\alpha$ - $\beta$  (b)  $x$ - $y$  and (c)  $0^+$ - $0^-$  planes.

In addition, each of the planes can be associated with the mapping of low order harmonics. The low order harmonics of the order of  $6k \pm 1$  ( $k = 0, 1, 2, 3 \dots$ ) which also contribute to the torque production in the machine map into  $\alpha$ - $\beta$  plane. As for  $x$ - $y$  plane, it maps the low order harmonics of the order of  $6k \pm 2$  ( $k = 0, 1, 2, 3 \dots$ ), i.e. even order harmonics, while for the  $0^+$ - $0^-$  plane, it maps low order harmonics of the order of  $3k$  ( $k = 1, 3, 5, \dots$ ) (Dordevic, 2013). Since these low order harmonics contribute to the machine losses, their existence is not desired. However, it will be shown later that by ensuring the space vector components of these two planes to be zero in average, sinusoidal  $v_{ph}$  waveforms can be realised.

The projections of  $v_{ph}$  space vectors into those three planes can be obtained in a similar way by substituting (3.3) into (3.7). Note that the switching states in normalised form are used in (3.3). One finds that the projections of  $v_{ph}$  space vectors in  $\alpha$ - $\beta$  and  $x$ - $y$  planes are actually the same as the projections of  $v_{LEG}$  space vectors. However, they are different in the  $0^+$ - $0^-$  plane (denoted as red dots) as shown in Figure 3.3(c). It can be seen that the projections of  $v_{ph}$  space vectors with respect to  $0^+$  axis are zero. This is because the  $0^+$  axis represents CMV and thus, it is expected that the  $v_{ph}$  space vector components for  $0^+$  axis to be zero. In addition, by not considering CMV in the development of the space vector algorithm, the sinusoidal  $v_{ph}$  waveforms can be realised through application of  $v_{LEG}$  space vectors. Nonetheless, due to the existence of switching state redundancy (switching state 0 and 63 yield identical  $v_{ph}$  space vector projection in all three planes), the number of projected  $v_{ph}$  space vectors is 63.

### 3.3.1.2 Determination of potential switching sequences

As mentioned previously, the machine is assumed to have sinusoidal distribution windings. Hence, it is desirable that the reference phase voltage ( $v_{ph}^*$ ) waveforms are also sinusoidal. The  $v_{ph}^*$  for symmetrical six-phase drive can be defined as:

$$v_{ph}^* = V_f^* \cos(\omega t - i \cdot \pi/3) \quad (3.8)$$

where  $i = 0, 1, 2, 3, 4$  and  $5$  whilst  $V_f^*$  is the desired fundamental of  $v_{ph}^*$ . The  $v_{ph}^*$  waveforms are as shown in Figure 3.4 and it can be seen that  $v_{ph}^*$  change their mutual order in terms of amplitude at  $0^\circ, 30^\circ, 60^\circ$  etc. In fact, these angles also correspond to the sector angles in the  $\alpha$ - $\beta$  plane (see Figure 3.3(a)). Furthermore, by substituting (3.8) into (3.7), one finds that only in  $\alpha$ - $\beta$  plane the  $v_{ph}^*$  space vector has the same magnitude as  $V_f^*$ , while in  $x$ - $y$  and  $0^+$ - $0^-$  planes,  $v_{ph}^*$

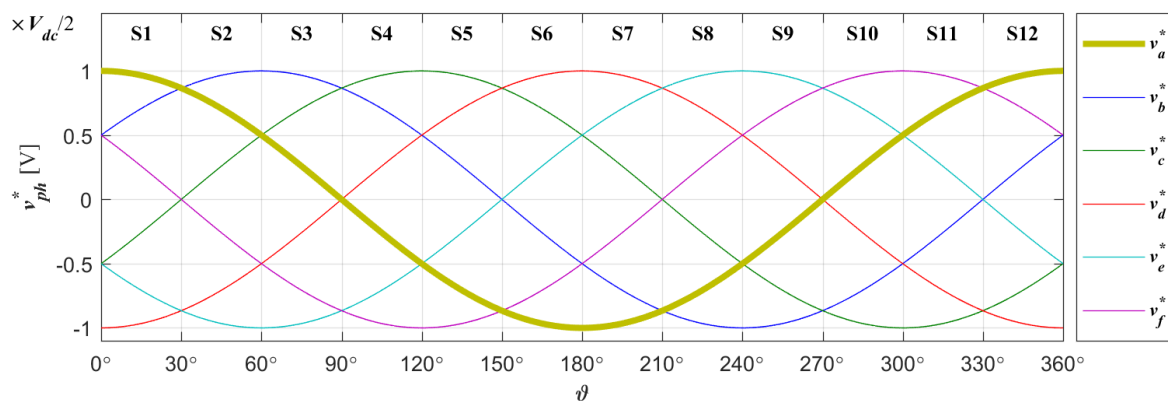


Figure 3.4: Sinusoidal reference phase voltage ( $v_{ph}^*$ ) waveforms for symmetrical six-phase drive.

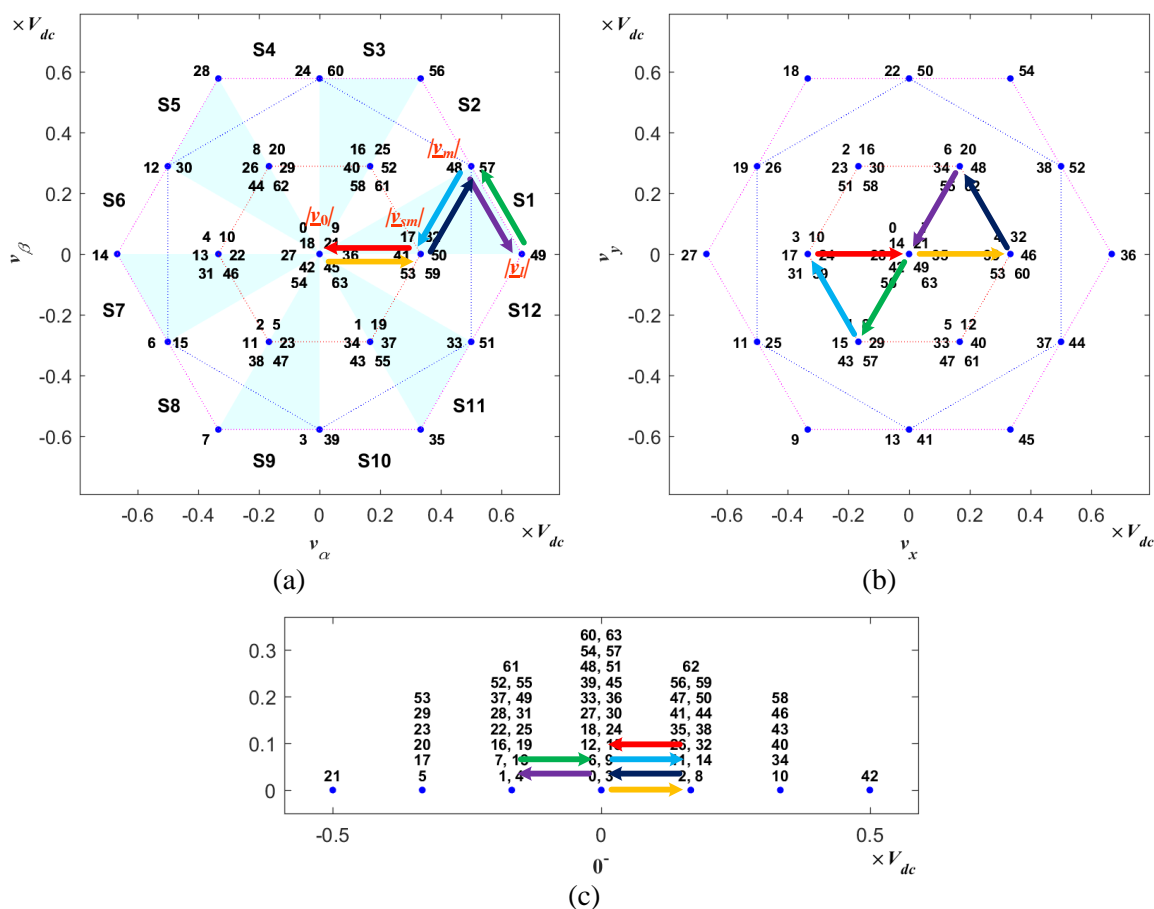


Figure 3.5: Space vector transitions of S1 switching sequence [0 32 48 49 57 59 63] in: (a)  $\alpha$ - $\beta$  (b)  $x$ - $y$  and (c)  $0^+$ - $0^-$  plane.

space vector is zero i.e. is projected at the origin. Therefore, in order to realise sinusoidal  $v_{ph}$  waveforms, the space vector components of these two planes should be zero.

As a result, the potential switching sequences should be chosen such that their  $x$ ,  $y$  and  $0^-$  space vector components are zero on average in each switching period. Note that  $0^+$  axis is no longer considered here, as commonly done in space vector practice. This axis represents CMV of the machine, and hence CMV is normally not controlled in space vector algorithms. An example of switching sequences that satisfies the previous rules is [0 32 48 49 57 59 63] i.e. 000000-100000-110000-110001-111001-111011-111111. Its space vector transition pattern in  $\alpha$ - $\beta$  and  $x$ - $y$  planes as well as  $0^-$  axis is shown in Figure 3.5. Since  $0^+$  axis is not being considered, for easier illustration purposes,  $0^-$  axis is now shown as horizontal axis. Since the transition pattern is within the first sector (S1) (see Figure 3.5(a)), it can be said that this switching sequence belongs to S1. It should be noted that although there are seven switching states per switching sequence, the first and the last switching state are in fact corresponding to the same space vector.

One gets that this switching sequence comprises one zero (0 and 63), two small (32 and 59), two medium (48 and 57) and one large (49) space vectors. These space vectors are denoted as  $\underline{v}_0$ ,  $\underline{v}_{sm}$ ,  $\underline{v}_m$  and  $\underline{v}_l$  whilst their magnitude in  $\alpha$ - $\beta$  plane are  $|\underline{v}_0| = 0$ ,  $|\underline{v}_{sm}| = 1/3V_{dc}$ ,  $|\underline{v}_m| = 1/\sqrt{3}V_{dc}$  and  $|\underline{v}_l| = 2/3V_{dc}$ , respectively (in red in Figure 3.5(a)). Due to symmetry between odd and even sectors, the switching sequences for the rest of the sectors can also be determined in a similar way. The chosen switching sequences of all twelve sectors are shown in Figure 3.6.

### 3.3.1.3 Calculation of dwell times

By applying the volt-second balance principle and time balancing equation, the equations for dwell times calculation of the applied space vectors, in one switching period, can be derived (Correa et al., 2003). Generally, the dwell times determine how long the chosen space vectors should be applied in one switching period. In other words, by applying the chosen space vectors i.e. switching sequence according to their respective calculated dwell times, desired  $v_{ph}$  waveforms can be realised. The volt-second balance principle and time balancing equation based on the chosen space vectors can be written as:

$$\underline{v}_{ph}^* T_s = \underline{v}_0 T_0 + \underline{v}_{sm} T_{sm} + \underline{v}_m T_m + \underline{v}_l T_l \quad (3.9)$$

$$T_s = T_0 + T_{sm} + T_m + T_l \quad (3.10)$$

where  $\underline{v}_{ph}^*$  is the reference  $v_{ph}$  space vector,  $T_s$  is a switching period whilst  $T_0$ ,  $T_{sm}$ ,  $T_m$  and  $T_l$  are the dwell times for the zero, small, medium and large space vectors respectively.

In  $\alpha$ - $\beta$  plane,  $\underline{v}_{ph}^*$  and the chosen space vectors comprise of two components ( $\alpha$  and  $\beta$  component). Furthermore,  $|\underline{v}_{sm}|$  is half of  $|\underline{v}_l|$  whilst  $|\underline{v}_0|$  is obviously zero. Therefore, by separating those space vectors in (3.9) into two components, one gets:

$$T_m = \frac{v_\beta^* v_l^\alpha - v_\alpha^* v_l^\beta}{v_l^\alpha v_m^\beta - v_l^\beta v_m^\alpha} T_s \quad (3.11)$$

$$T_l + \frac{T_{sm}}{2} = \frac{v_\alpha^* v_m^\beta - v_\beta^* v_m^\alpha}{v_l^\alpha v_m^\beta - v_l^\beta v_m^\alpha} T_s \quad (3.12)$$

where the  $\alpha$  and  $\beta$  superscript denote which axes the space vector components correspond to (e.g.  $\underline{v}_l = v_l^\alpha + jv_l^\beta$ ). Yet, it can be seen that in (3.12),  $T_l$  and  $T_{sm}$  are dependent on each other. In order to overcome this, a control variable ( $\rho$ ) is introduced and it is defined as:

$$\rho = \frac{T_l}{T_l + \frac{T_{sm}}{2}} \quad (3.13)$$

Sector	S1 (0° → 30°) (0 → π/6)							S2 (30° → 60°) (π/6 → 2π/6)							S3 (60° → 90°) (2π/6 → 3π/6)						
SwSt	0	32	48	49	57	59	63	0	16	48	56	57	61	63	0	16	24	56	60	61	63
A	0	1	1	1	1	1	1	0	0	1	1	1	1	1	0	0	0	1	1	1	1
B	0	0	1	1	1	1	1	0	1	1	1	1	1	1	0	1	1	1	1	1	1
C	0	0	0	0	1	1	1	0	0	0	1	1	1	1	0	0	1	1	1	1	1
D	0	0	0	0	0	0	1	0	0	0	0	0	1	1	0	0	0	0	1	1	1
E	0	0	0	0	0	1	1	0	0	0	0	0	0	1	0	0	0	0	0	0	1
F	0	0	0	1	1	1	1	0	0	0	0	1	1	1	0	0	0	0	0	1	1
δ	δ <sub>0</sub> /4	δ <sub>sm</sub> /4	δ <sub>m</sub> /4	δ <sub>1</sub> /2	δ <sub>m</sub> /4	δ <sub>sm</sub> /4	δ <sub>0</sub> /4	δ <sub>0</sub> /4	δ <sub>sm</sub> /4	δ <sub>m</sub> /4	δ <sub>1</sub> /2	δ <sub>m</sub> /4	δ <sub>sm</sub> /4	δ <sub>0</sub> /4	δ <sub>0</sub> /4	δ <sub>sm</sub> /4	δ <sub>m</sub> /4	δ <sub>1</sub> /2	δ <sub>m</sub> /4	δ <sub>sm</sub> /4	δ <sub>0</sub> /4
Sector	S4 (90° → 120°) (3π/6 → 4π/6)							S5 (120° → 150°) (4π/6 → 5π/6)							S6 (150° → 180°) (5π/6 → π)						
SwSt	0	8	24	28	60	62	63	0	8	12	28	30	62	63	0	4	12	14	30	31	63
A	0	0	0	0	1	1	1	0	0	0	0	0	1	1	0	0	0	0	0	0	1
B	0	0	1	1	1	1	1	0	0	0	1	1	1	1	0	0	0	0	1	1	1
C	0	1	1	1	1	1	1	0	1	1	1	1	1	1	0	0	1	1	1	1	1
D	0	0	0	1	1	1	1	0	0	1	1	1	1	1	0	1	1	1	1	1	1
E	0	0	0	0	0	1	1	0	0	0	0	1	1	1	0	0	0	1	1	1	1
F	0	0	0	0	0	0	1	0	0	0	0	0	0	1	0	0	0	0	0	0	1
δ	δ <sub>0</sub> /4	δ <sub>sm</sub> /4	δ <sub>m</sub> /4	δ <sub>1</sub> /2	δ <sub>m</sub> /4	δ <sub>sm</sub> /4	δ <sub>0</sub> /4	δ <sub>0</sub> /4	δ <sub>sm</sub> /4	δ <sub>m</sub> /4	δ <sub>1</sub> /2	δ <sub>m</sub> /4	δ <sub>sm</sub> /4	δ <sub>0</sub> /4	δ <sub>0</sub> /4	δ <sub>sm</sub> /4	δ <sub>m</sub> /4	δ <sub>1</sub> /2	δ <sub>m</sub> /4	δ <sub>sm</sub> /4	δ <sub>0</sub> /4
Sector	S7 (180° → 210°) (-π → -5π/6)							S8 (210° → 240°) (-5π/6 → -4π/6)							S9 (240° → 270°) (-4π/6 → -3π/6)						
SwSt	0	4	6	14	15	31	63	0	2	6	7	15	47	63	0	2	3	7	39	47	63
A	0	0	0	0	0	0	1	0	0	0	0	0	1	1	0	0	0	0	1	1	1
B	0	0	0	0	0	1	1	0	0	0	0	0	0	1	0	0	0	0	0	0	1
C	0	0	0	1	1	1	1	0	0	0	0	1	1	1	0	0	0	0	0	1	1
D	0	1	1	1	1	1	1	0	0	1	1	1	1	1	0	0	0	1	1	1	1
E	0	0	1	1	1	1	1	0	1	1	1	1	1	1	0	1	1	1	1	1	1
F	0	0	0	0	1	1	1	0	0	0	1	1	1	1	0	0	1	1	1	1	1
δ	δ <sub>0</sub> /4	δ <sub>sm</sub> /4	δ <sub>m</sub> /4	δ <sub>1</sub> /2	δ <sub>m</sub> /4	δ <sub>sm</sub> /4	δ <sub>0</sub> /4	δ <sub>0</sub> /4	δ <sub>sm</sub> /4	δ <sub>m</sub> /4	δ <sub>1</sub> /2	δ <sub>m</sub> /4	δ <sub>sm</sub> /4	δ <sub>0</sub> /4	δ <sub>0</sub> /4	δ <sub>sm</sub> /4	δ <sub>m</sub> /4	δ <sub>1</sub> /2	δ <sub>m</sub> /4	δ <sub>sm</sub> /4	δ <sub>0</sub> /4
Sector	S10 (270° → 300°) (-3π/6 → -2π/6)							S11 (300° → 330°) (-2π/6 → -π/6)							S12 (330° → 360°) (-π/6 → 0)						
SwSt	0	1	3	35	39	55	63	0	1	33	35	51	55	63	0	32	33	49	51	59	63
A	0	0	0	1	1	1	1	0	0	1	1	1	1	1	0	1	1	1	1	1	1
B	0	0	0	0	0	1	1	0	0	0	0	1	1	1	0	0	0	1	1	1	1
C	0	0	0	0	0	0	1	0	0	0	0	0	0	1	0	0	0	0	0	1	1
D	0	0	0	0	0	1	1	0	0	0	0	0	1	1	0	0	0	0	0	0	1
E	0	0	1	1	1	1	1	0	0	0	1	1	1	1	0	0	0	0	1	1	1
F	0	1	1	1	1	1	1	0	1	1	1	1	1	1	0	0	1	1	1	1	1
δ	δ <sub>0</sub> /4	δ <sub>sm</sub> /4	δ <sub>m</sub> /4	δ <sub>1</sub> /2	δ <sub>m</sub> /4	δ <sub>sm</sub> /4	δ <sub>0</sub> /4	δ <sub>0</sub> /4	δ <sub>sm</sub> /4	δ <sub>m</sub> /4	δ <sub>1</sub> /2	δ <sub>m</sub> /4	δ <sub>sm</sub> /4	δ <sub>0</sub> /4	δ <sub>0</sub> /4	δ <sub>sm</sub> /4	δ <sub>m</sub> /4	δ <sub>1</sub> /2	δ <sub>m</sub> /4	δ <sub>sm</sub> /4	δ <sub>0</sub> /4

Figure 3.6: Chosen switching sequences for the two-level symmetrical six-phase drive with one isolated neutral point (only the first half of the switching period is shown).

where  $\rho$  can be any value from zero to one i.e. in the range of  $0 \leq \rho \leq 1$  (Correa et al., 2003).

Thus, by substituting (3.13) into (3.12), both  $T_{sm}$  and  $T_l$  can be expressed as:

$$T_{sm} = 2(1 - \rho) \frac{v_\alpha^* v_m^\beta - v_\beta^* v_m^\alpha}{v_l^\alpha v_m^\beta - v_l^\beta v_m^\alpha} T_s \quad (3.14)$$

$$T_l = \rho \frac{v_\alpha^* v_m^\beta - v_\beta^* v_m^\alpha}{v_l^\alpha v_m^\beta - v_l^\beta v_m^\alpha} T_s \quad (3.15)$$

and from (3.10),  $T_0$  can then be defined as:

$$T_0 = T_s - (T_{sm} + T_m + T_l) \quad (3.16)$$

However, only  $\rho = 2/3$  gives sinusoidal  $v_{ph}$  waveforms (Correa et al., 2003).

The reason for this lays in the transition pattern of the chosen space vector on  $0^-$  axis (see Figure 3.5(c)). It can be seen that only space vectors which correspond to switching state 32 and 59 i.e.  $\underline{v}_{sm}$  as well as switching state 49 i.e.  $\underline{v}_l$  are not projected at zero, with respect to  $0^-$  axis. As a result, in order for the space vector components on the  $0^-$  axis to be zero on average in one switching period and consequently satisfy one of the requirements for realising sinusoidal  $v_{ph}$  waveforms, the dwell times of both space vectors should be equal. Therefore, according to (3.13), this can be achieved only when  $\rho = 2/3$ .

In addition,  $T_{sm}$  and  $T_m$  should also be equally distributed between their respective space vectors in order to obtain sinusoidal  $v_{ph}$  waveforms (Correa et al., 2003). By distributing  $T_{sm}$  and  $T_m$  in this manner, the space vector components in  $x$ - $y$  plane become zero on average (see Figure 3.5(b)). Dwell time  $T_0$  is equally distributed between the two switching states (Correa et al., 2003). Last but not least, the duty cycle of each dwell time (the ratio between the dwell time with respect to the switching period,  $T_s$ ) can be defined as:

$$\delta_0 = \frac{T_0}{T_s} \quad \delta_{sm} = \frac{T_{sm}}{T_s} \quad \delta_m = \frac{T_m}{T_s} \quad \delta_l = \frac{T_l}{T_s} \quad (3.17)$$

The dwell times for each switching sequence are also shown in Figure 3.6. Note that only the first half of the switching period is shown, thus the duty cycles are divided by 2.

Another approach to calculate the dwell times of the chosen switching sequence is by arranging the volt-second balance principle and time balancing equation i.e. (3.9) and (3.10) in a matrix form as in (Dordevic, 2013):

$$\begin{bmatrix} T_1 \\ T_2 \\ T_3 \\ T_4 \\ T_5 \\ T_6 \end{bmatrix} = \begin{bmatrix} v_{\alpha,1} & v_{\alpha,2} & v_{\alpha,3} & v_{\alpha,4} & v_{\alpha,5} & v_{\alpha,6} \\ v_{\beta,1} & v_{\beta,2} & v_{\beta,3} & v_{\beta,4} & v_{\beta,5} & v_{\beta,6} \\ v_{x,1} & v_{x,2} & v_{x,3} & v_{x,4} & v_{x,5} & v_{x,6} \\ v_{y,1} & v_{y,2} & v_{y,3} & v_{y,4} & v_{y,5} & v_{y,6} \\ 1 & 1 & 1 & 1 & 1 & 1 \\ v_{0^-,1} & v_{0^-,2} & v_{0^-,3} & v_{0^-,4} & v_{0^-,5} & v_{0^-,6} \end{bmatrix}^{-1} \times \begin{bmatrix} v_{\alpha}^* \\ v_{\beta}^* \\ v_x^* \\ v_y^* \\ 1 \\ v_{0^-}^* \end{bmatrix} \cdot T_s \quad (3.18)$$

The  $T_1$  to  $T_6$  represent the dwell time of each space vector in the switching sequence instead of  $T_0$ ,  $T_{sm}$ ,  $T_m$  and  $T_l$ . Hence, the distribution of the calculated dwell times between the space vectors which have the same magnitude in  $\alpha$ - $\beta$  plane (e.g. between the small and medium space vectors) are no longer a concern. However, it should be noted that since the first and last switching state correspond to the same space vector, it is sufficient to take into account only the

first switching state in the calculation and then divide calculated  $T_1$  equally between the two later on.

Meanwhile, the six-by-six matrix in (3.18) is the inverse of  $\alpha$ ,  $\beta$ ,  $x$ ,  $y$  and  $0^-$  components of the chosen space vectors from (3.7). In addition, note that the fifth row of the inverse matrix is replaced by the time balancing equation from (3.10) since  $0^+$  axis is no longer considered (CMV is not controlled) in the space vector algorithm. As the desired  $v_{ph}$  is a purely sinusoidal waveform, the  $x$ ,  $y$  and  $0^-$  reference components ( $v_x^*$ ,  $v_y^*$  and  $v_{0^-}^*$ ) in (3.18) are set to zero. On the other hand, the  $\alpha$  and  $\beta$  reference components ( $v_\alpha^*$  and  $v_\beta^*$ ) are set to  $V_f^* \cos(\omega t)$  and  $V_f^* \sin(\omega t)$ . This is equivalent to projections of the sinusoidal  $v_{ph}^*$  waveforms in the three orthogonal planes as stated previously.

### 3.3.2 Carrier-based PWM technique

Carrier-based PWM technique is the simplest way to modulate  $v_{ph}^*$  waveforms and achieve  $v_{ph}$  waveforms as desired. However, it is not possible to define the mapping of the low order harmonics and the possibility to either individually control or eliminate them from appearing in  $v_{ph}$  waveforms using carrier-based approach. Although it offers higher dc-bus utilisation when common mode voltage injection (also commonly known as min-max injection) is implemented, this injection is not possible for two-level symmetrical six-phase drive. This is because the  $v_{ph}^*$  waveforms are symmetrical around the time axis (see Figure 3.4). Therefore, the conventional way of implementing the carrier-based PWM technique i.e. by comparing the triangle carrier waveform with sinusoidal  $v_{ph}^*$  waveforms (CBSin) is adequate in this case.

### 3.3.3 Simulation results

Modulators of the presented space vector algorithm where (3.11), (3.14) and (3.15) are used to calculate the dwell times ( $\rho_{2/3SV}$ ) as well as using dwell time matrix approach (2L6PSymSV) are developed and simulated in MATLAB/Simulink for full linear range of modulation index ( $m_i$ ) in 0.05 increments. The same is also done for CBSin. The modulation index is defined as a ratio between the magnitude of fundamental phase voltages  $v_{ph}^*$  i.e.  $V_f^*$ , and half of dc-bus voltage i.e.  $V_{dc}/2$ , as in:

$$m_i = \frac{V_f^*}{V_{dc}/2} \quad (3.19)$$

At the machine's rated frequency, 50 Hz, the chosen magnitude of  $v_{ph}^*$  waveforms is  $V_f^* = 100$  V. Since  $V_{dc} = 200$  V, according to (3.19), this means that it corresponds to  $m_i = 1$ .

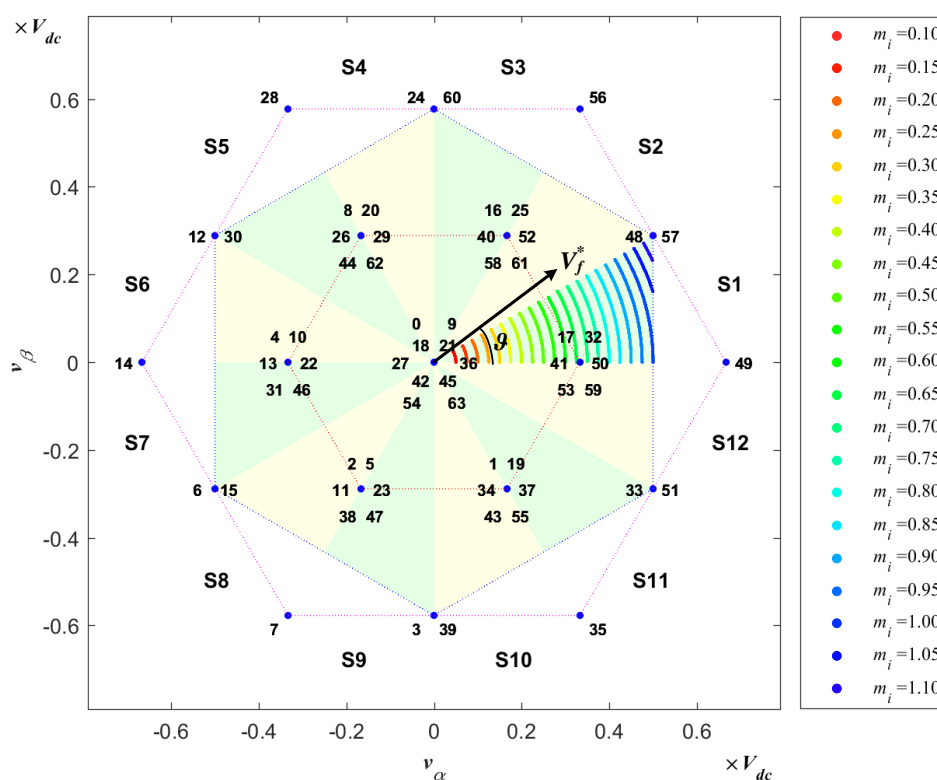


Figure 3.7: The regions of application for S1 switching sequence [0 32 48 49 57 59 63] in  $\alpha$ - $\beta$  plane.

In fact,  $m_i = 1$  is the maximum value that can be achieved for  $\rho 2/3SV$  (Correa et al., 2003). Obviously, this is the same for CBSin. As for 2L6PSymSV, it can be shown that the maximum achievable  $m_i$  is also  $m_i = 1$ . One of the methods for determining the maximum achievable  $m_i$  is by identifying the limit of the region of application generated by the chosen switching sequence in  $\alpha$ - $\beta$  plane (Dordevic et al., 2013b). This region of application is simply the visualisation of the locations of the applied  $v_{ph}^*$  space vector, if the solutions of calculated dwell times exist. In other words, by gradually increasing the magnitude of the applied  $v_{ph}^*$  space vector i.e.  $V_f^*$  from zero to  $2/3V_{dc}$  (the vertex of the largest polygon), the dwell times of the space vectors in the chosen switching sequence are repetitively calculated based on (3.18) using Matlab code. A dot is plotted at the current location of applied  $v_{ph}^*$  space vector if the solution for the calculated dwell times exist. As an example, the generated region of application for the chosen switching sequence of S1 is shown in Figure 3.7. It can be shown that the regions of application for all twelve sectors are all within the middle hexagon. Thus, its side is the limit for this region, which is  $1/2V_{dc}$ , i.e. equivalent to  $m_i = 1$ .

The modulation techniques are verified using an ideal inverter and inverter model with built-in dead time. The inverter drives the symmetrical six-phase induction machine model

Table 3.1: Parameters of symmetrical six-phase induction machine.

Parameter	Value	
Resistance	$R_s = 3.6 \Omega$	$R_r = 1.8 \Omega$
Leakage inductance	$L_{ls} = 8.1 \text{ mH}$	$L_{lr} = 11.5 \text{ mH}$
Mutual inductance	$L_m = 205 \text{ mH}$	
Pole-pairs	3	
Rotating mass inertia	$J = 0.03 \text{ kgm}^2$	

developed based on the machine parameters listed in Table 3.1. The inverter dead time is set to  $6 \mu\text{s}$  (the same as on the real inverters available in the laboratory) and it is not compensated. It should be noted that only results obtained from the ideal case are shown. However, obtained results when the uncompensated inverter dead time is taken into consideration are included later on at the end of the chapter for the sake of comparison. As mentioned, the dc-bus of the inverter is set to  $V_{dc} = 200 \text{ V}$  while the switching frequency is set to be  $f_s = 2 \text{ kHz}$ . The simulation is run for  $T_{sim} = 2 \text{ s}$  (long enough to reach steady state speed) using constant  $V/f$  control in open loop without any load.

The performances of all developed modulation techniques are determined from the calculated phase voltage and current total harmonic distortions ( $\text{THD}_v$  and  $\text{THD}_i$ ) using (Dordevic et al., 2015):

$$\text{THD}_v = \sqrt{\sum_{k=2}^h V_k^2 / V_1^2} \times 100\% \quad \text{THD}_i = \sqrt{\sum_{k=2}^h I_k^2 / I_1^2} \times 100\% \quad (3.20)$$

where  $V_k$  and  $I_k$  represent the  $k$ -th components of voltage and current in the spectrum, while  $V_1$  and  $I_1$  are the fundamental values of the phase voltage and the current, respectively. Harmonic components from the first  $h$  harmonic up to a value of  $h$  that corresponds to 21 kHz i.e. the first ten sidebands of the used switching frequency are included in both THD calculations.

Unlike the carrier-based approach where the switching signals are generated by comparing the triangle carrier waveform with the  $v_{ph}^*$  waveforms, for space vector algorithm, the switching signals are generated by applying the chosen switching sequence according to its corresponding dwell times. One gets that it is inaccurate to simply compare the applied  $v_{ph}^*$  waveforms between the modulation techniques. As an example, in the three-phase case where the  $v_{ph}^*$  waveforms for space vector algorithm are sinusoidal, the  $v_{ph}^*$  waveforms for carrier-based approach are sinusoidal waveforms with common mode voltage injection. Yet, both

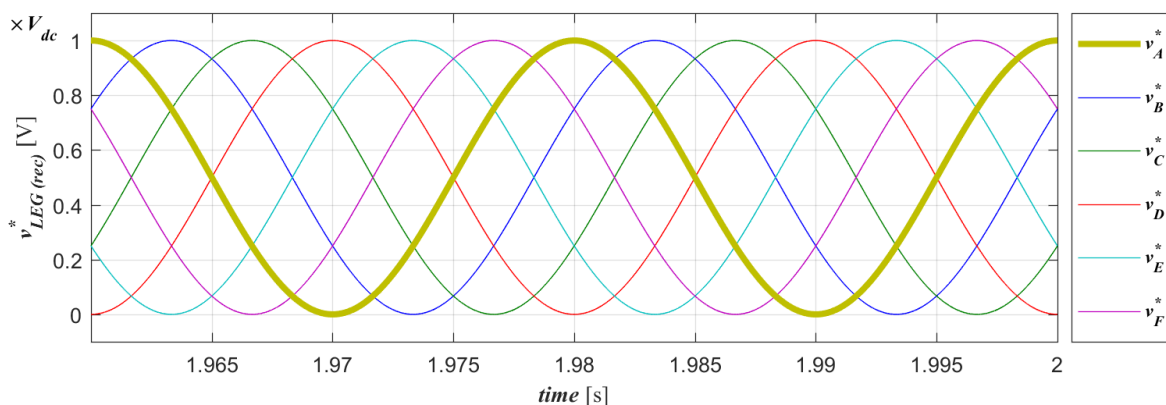


Figure 3.8: Reconstructed reference output leg voltage ( $v_{LEG,rec}^*$ ) waveforms of  $\rho2/3SV$  at  $m_i = 1$ .

modulation techniques yield identical results. This is because in the space vector algorithm, common mode voltage is naturally injected into the  $v_{ph}^*$  waveforms (Wang, 2002). Therefore, for the visual comparison of the algorithms the reconstructed reference leg voltage waveforms ( $v_{LEG,rec}^*$ ) are used instead. The  $v_{LEG,rec}^*$  waveforms are obtained from the product of applied switching sequence and its corresponding dwell times. It should be noted that  $v_{LEG,rec}^*$  is not a part of the space vector algorithm but is only used for the visual comparison purposes.

The  $v_{LEG,rec}^*$  waveforms for  $\rho2/3SV$  when  $m_i = 1$  are shown in Figure 3.8. The same waveforms are obtained for 2L6PSymSV. It can be said the obtained  $v_{LEG,rec}^*$  waveforms are the same as the  $v_{ph}^*$  waveforms shown in Figure 3.4. However, note that the magnitudes of  $v_{LEG,rec}^*$  waveforms vary between 0 to  $V_{dc}$ . Additionally, one can also obtain the reconstructed phase reference voltage waveforms ( $v_{ph,rec}^*$ ) by using (3.3). In fact, they are identical to Figure 3.4. The removal of CMV from the  $v_{LEG,rec}^*$  results in  $v_{ph,rec}^*$  waveforms to be shifted along the vertical axis and their magnitudes are now in a range of  $\pm V_{dc}/2$ .

The phase ‘a’ voltage, phase voltage components ( $v_\alpha$ ,  $v_\beta$ ,  $v_x$ ,  $v_y$ ,  $v_0^+$  and  $v_0^-$ ), and phase ‘a’ current waveforms of the machine driven by the ideal inverter, as well as their corresponding spectra for the  $\rho2/3SV$ , 2L6PSymSV and CBSin are shown in Figure 3.9, 3.10 and 3.11, respectively. It can be seen that obtained results for the three modulation techniques are roughly the same. Their fundamental phase ‘a’ voltage ( $|v_a|_{fund}$ ) and current ( $|i_a|_{fund}$ ) are 99.96 V and 1.49 A whilst  $THD_v$  and  $THD_i$  are 72.32% and 32.13%, respectively. In addition, the obtained  $|v_a|_{fund}$  is in agreement to (3.19) at  $m_i = 1$ . It can be seen in Figure 3.9 and 3.10 that the low order harmonics, which map onto  $x$ ,  $y$  and  $0^-$  axes are indeed zero (do not exist), as set out during the development of the algorithm.

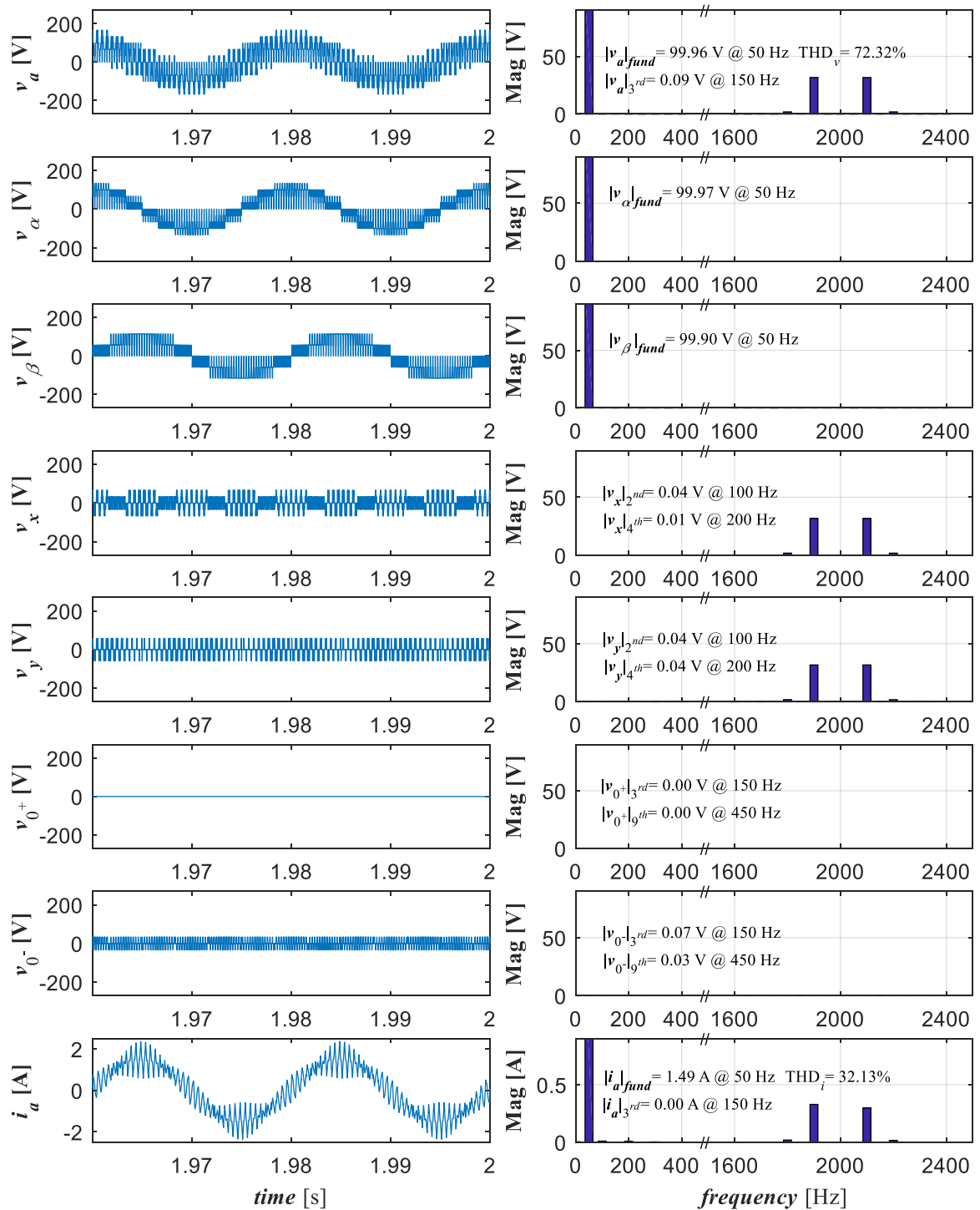


Figure 3.9: Phase ‘a’ voltage, phase voltage components ( $v_\alpha$ ,  $v_\beta$ ,  $v_x$ ,  $v_y$ ,  $v_{0^+}$  and  $v_{0^-}$ ), phase ‘a’ current and corresponding spectra of  $\rho 2/3\text{SV}$  for the machine driven by ideal inverter at  $m_i = 1$ .

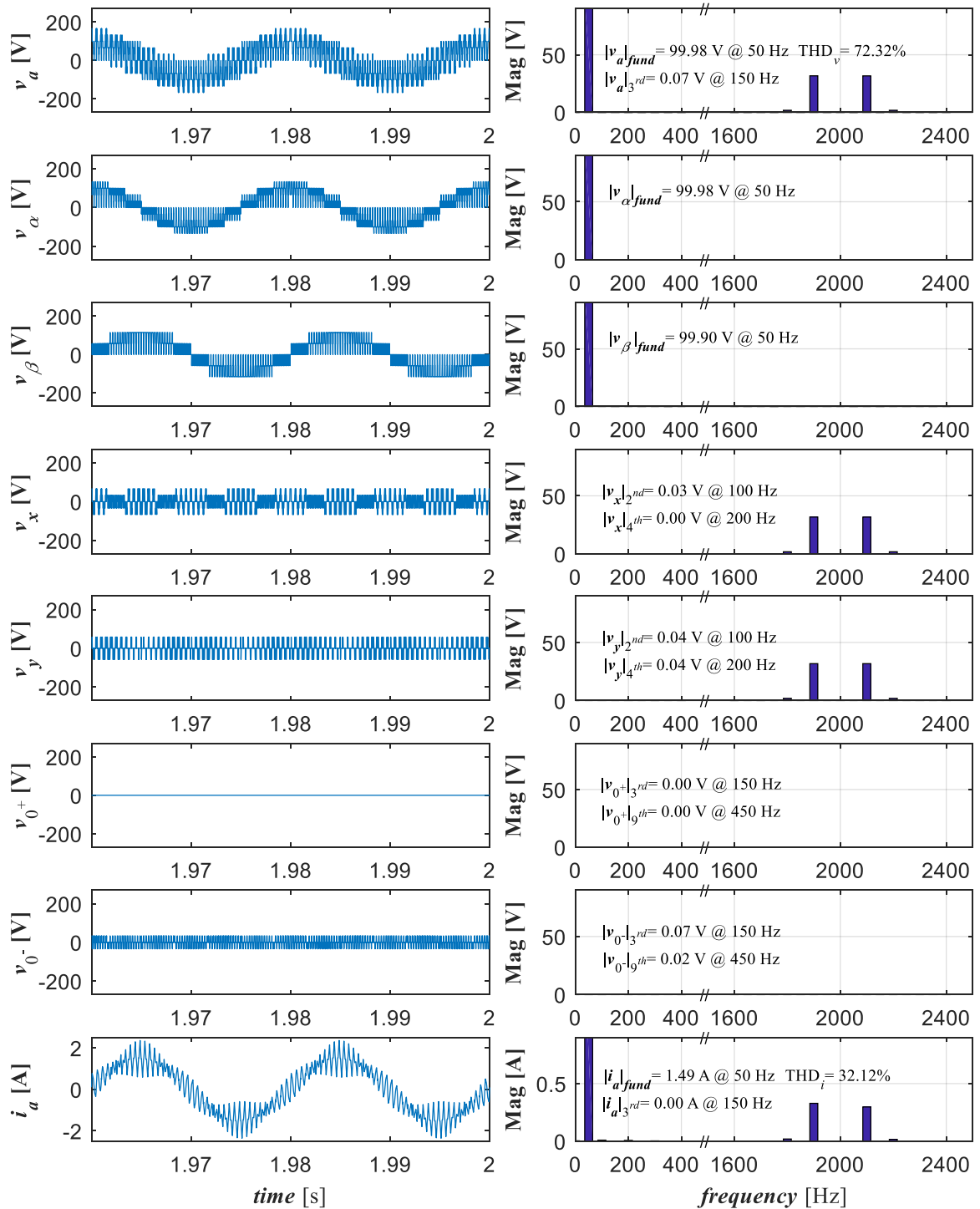


Figure 3.10: Phase 'a' voltage, phase voltage components ( $v_a$ ,  $v_\beta$ ,  $v_x$ ,  $v_y$ ,  $v_0^+$  and  $v_0^-$ ), phase 'a' current and corresponding spectra of 2L6PSymSV for the machine driven by ideal inverter

at  $m_i = 1$ .

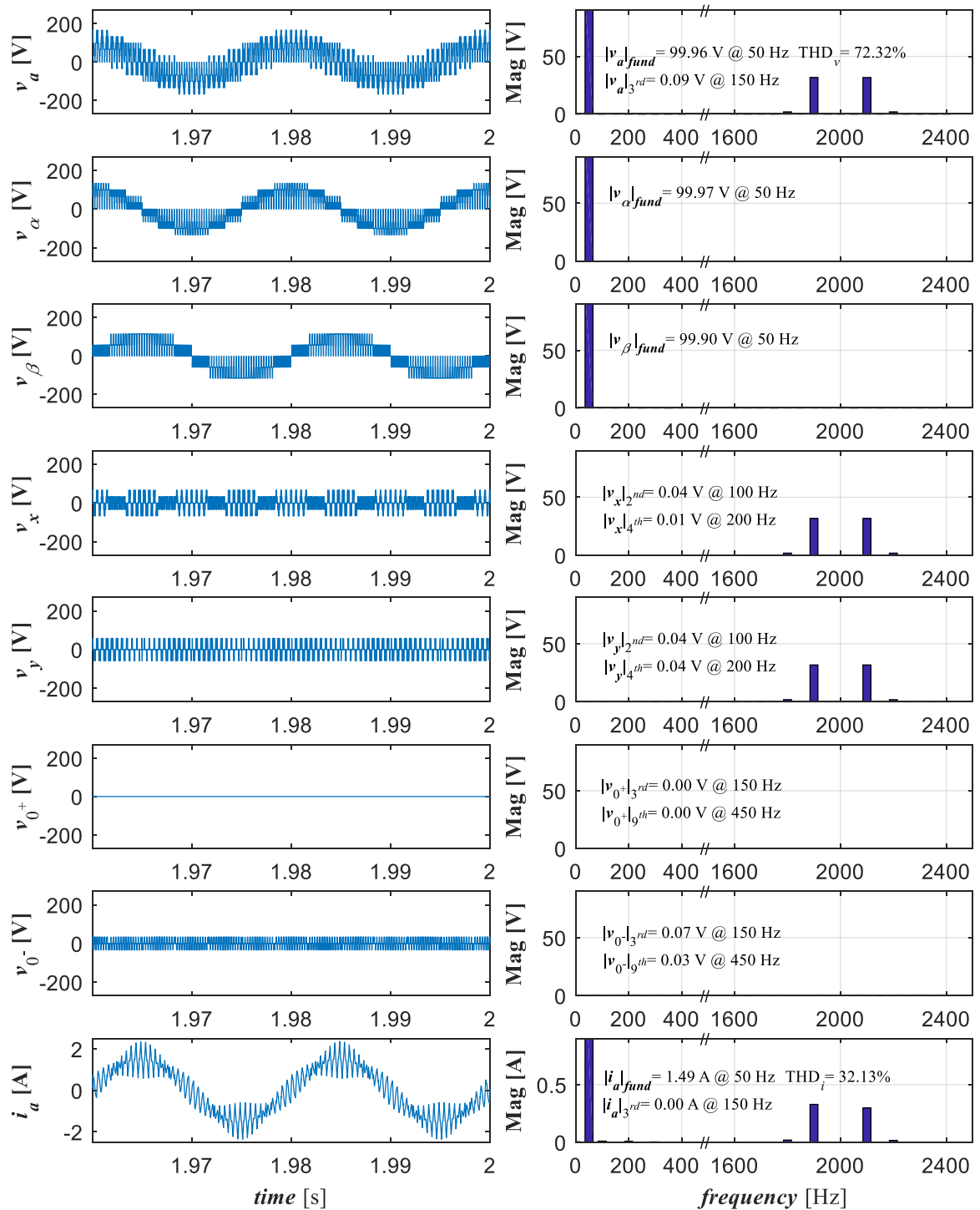


Figure 3.11: Phase ‘a’ voltage, phase voltage components ( $v_\alpha$ ,  $v_\beta$ ,  $v_x$ ,  $v_y$ ,  $v_{0^+}$  and  $v_{0^-}$ ), phase ‘a’ current and corresponding spectra of CBSin for the machine driven by ideal inverter at  $m_i = 1$ .

### 3.4 Drive with two isolated neutral points configuration

In this section, a space vector PWM algorithm and carrier-based PWM technique with min-max injection, for the two-level symmetrical six-phase drive with two isolated neutral points configuration are discussed. Since the neutral points are isolated, the modulation techniques are based on two-level three-phase PWM techniques. In other words, there are two modulators for each modulation technique with the reference waveforms for each modulator shifted accordingly. These modulation techniques are simulated in Matlab/Simulink for an ideal inverter and an inverter with dead time included.

#### 3.4.1 Space vector PWM algorithm

The number of switching states for a two-level symmetrical six-phase drive with two isolated neutral points configuration is the same as the single neutral point case, namely 64, because the same inverter topology is used. However, the transformation matrix now becomes:

$$\begin{bmatrix} v_\alpha \\ v_\beta \\ v_x \\ v_y \\ v_{0_1} \\ v_{0_2} \end{bmatrix} = \frac{2}{6} \cdot \begin{bmatrix} 1 & \cos(\alpha) & \cos(2\alpha) & \cos(3\alpha) & \cos(4\alpha) & \cos(5\alpha) \\ 0 & \sin(\alpha) & \sin(2\alpha) & \sin(3\alpha) & \sin(4\alpha) & \sin(5\alpha) \\ 1 & \cos(2\alpha) & \cos(4\alpha) & \cos(6\alpha) & \cos(8\alpha) & \cos(10\alpha) \\ 0 & \sin(2\alpha) & \sin(4\alpha) & \sin(6\alpha) & \sin(8\alpha) & \sin(10\alpha) \\ 1 & 0 & 1 & 0 & 1 & 0 \\ 0 & 1 & 0 & 1 & 0 & 1 \end{bmatrix} \times \begin{bmatrix} v_a \\ v_b \\ v_c \\ v_d \\ v_e \\ v_f \end{bmatrix} \quad (3.21)$$

Notice that the coefficients of the fifth and sixth row are different from those in (3.7). In fact, they represent the CMV of each winding set (denoted by the numbers in the subscript). Therefore the projection of the voltage space vectors remains the same in  $\alpha$ - $\beta$  and  $x$ - $y$  planes as in the single neutral point case (see Figure 3.3(a) and 3.3(b)). However, for the  $0_1$ - $0_2$  plane, the projections are different, and they are shown in Figure 3.12.

As the neutral points are isolated, each of the winding sets can be controlled independently. Therefore, dual two-level three-phase space vector (D2L3PSV) PWM modulators are used. However, the reference waveforms for these two modulators must be shifted by  $60^\circ$ , which is in accordance to the spatial angle between the winding sets. The maximum  $m_i$  for linear range of operation that can be achieved using D2L3PSV is 1.154, which is equivalent to the three-phase case.

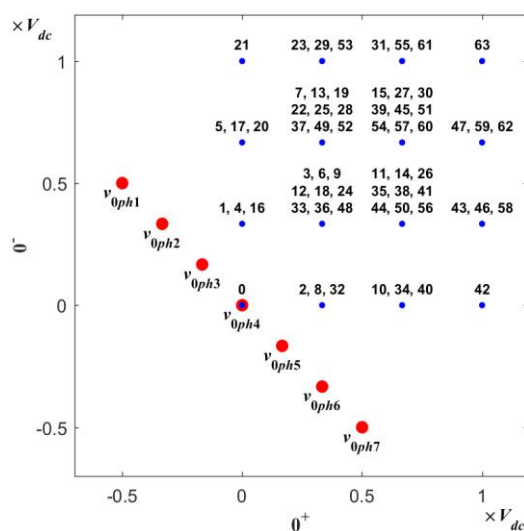


Figure 3.12: Projection of  $v_{LEG}$  and  $v_{ph}$  (in red) space vectors for two-level symmetrical six-phase drive with two isolated neutral points in  $0_1$ - $0_2$  plane.

### 3.4.2 Carrier-based PWM technique

Similarly, two PWM modulators based on the conventional two-level three-phase PWM technique with common mode voltage injection (DSinCMI) are developed to control each winding set. By injecting the common mode voltage into the reference waveforms, utilisation of the dc-bus can be increased by 15.4%. Therefore, the maximum modulation index ( $m_i$ ) for the linear range of operation becomes 1.154. The reference phase voltage waveforms with common mode voltage injection ( $v_{ph,DSinCMI}^*$ ) for the developed dual PWM modulators at  $m_i = 1.154$  are as shown in Figure 3.13.

### 3.4.3 Simulation results

The modulation techniques, D2L3PSV and DSinCMI, are developed and verified through simulation in Matlab/Simulink for full linear range of  $m_i$  up to  $m_i = 1.154$ . The  $v_{LEG,rec}^*$  for D2L3PSV when  $m_i = 1.154$  are shown in Figure 3.14. One can see that the obtained  $v_{LEG,rec}^*$  waveforms are identical to  $v_{ph,DSinCMI}^*$  shown in Figure 3.13. This shows that the space vector algorithm does naturally introduce the common mode voltage into the reference waveforms. However, from (3.6), by removing the common mode voltage, the  $v_{ph,rec}^*$  waveforms become sinusoidal as shown in Figure 3.15. Although it can be seen that the amplitude of  $v_{ph,rec}^*$  waveforms is much higher than  $\pm V_{dc}$ , it does agree with (3.19), where at  $m_i = 1.154$ ,  $V_f^*$  is  $0.577V_{dc}$ .

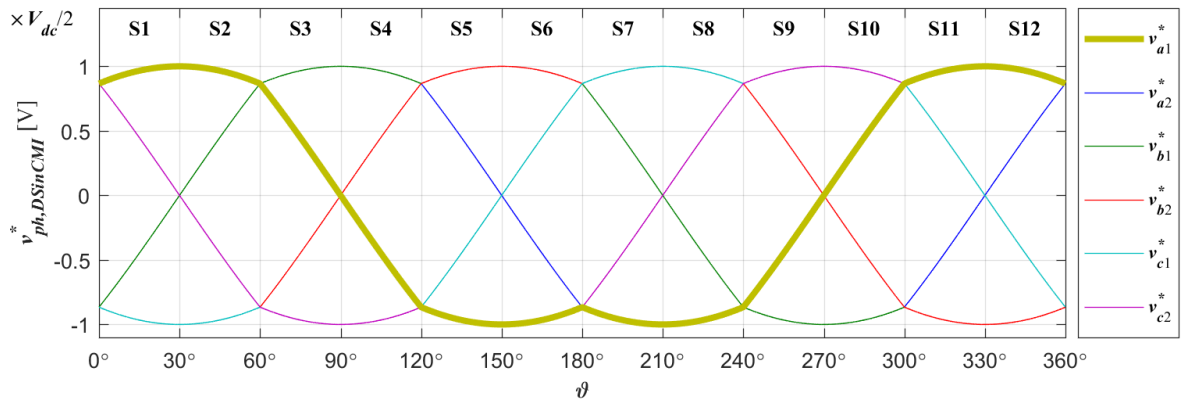


Figure 3.13: Sinusoidal reference phase voltage waveforms with dual common mode voltage injection ( $v_{ph,DSinCMI}^*$ ) for two-level symmetrical six-phase drive at  $m_i = 1.154$ .

The phase ‘ $a_1$ ’ voltage,  $v_\alpha$ ,  $v_\beta$ ,  $v_x$ ,  $v_y$ ,  $v_{01}$ ,  $v_{02}$ , and phase ‘ $a_1$ ’ current waveforms of the machine driven by the ideal inverter, as well as their corresponding spectra for the D2L3PSV and DSinCMI, are shown in Figure 3.16 and 3.17, respectively. One can see that both modulation techniques yield the same results. Their fundamental phase ‘ $a_1$ ’ voltage ( $|v_{a1}|_{fund}$ ) and current ( $|i_{a1}|_{fund}$ ) are 115.59 V and 1.5 A whilst  $THD_v$  and  $THD_i$  are 48.89% and 28.53%, respectively. In addition, it can be seen that although low order harmonics, which are mapped onto  $x$  and  $y$  axis, do exist they are negligible. Furthermore, since  $0_1$  and  $0_2$  axes correspond to CMV of each winding set, their phase voltage components are zero. Consequently, this results in the absence of their corresponding low order harmonics.

### 3.5 Performance comparison between the modulation techniques with both neutral point configurations

The obtained  $|v_{ph}|_{fund}$ , the magnitudes of the obtained fundamental output phase current ( $|i_{ph}|_{fund}$ ), the calculated  $THD_v$  and  $THD_i$ , for the full linear range of  $m_i$ , of all discussed modulation strategies, are shown in Figure 3.18. In order to confirm the validity of the modulation strategies, the correlation between the  $|v_{ph}|_{fund}$  with respect to  $m_i$  is observed. One can see that the  $|v_{ph}|_{fund}$  increases linearly with respect to  $m_i$  which is in accordance with (3.19). An uncompensated inverter dead time will cause  $|v_{ph}|_{fund}$  to be lower (Jae Hyeong et al., 2001, Jones et al., 2009a). However, from Figure 3.18(a) one can see that the influence of the dead time on  $|v_{ph}|_{fund}$  is negligible. On the other hand, one can see its impact is more pronounced in  $THD_v$  and  $THD_i$  (Figure 3.18(b) and 3.18(d)). This is because inverter dead time also contributes to the existence of low odd order harmonics (Jae Hyeong et al., 2001, Jones et al.,

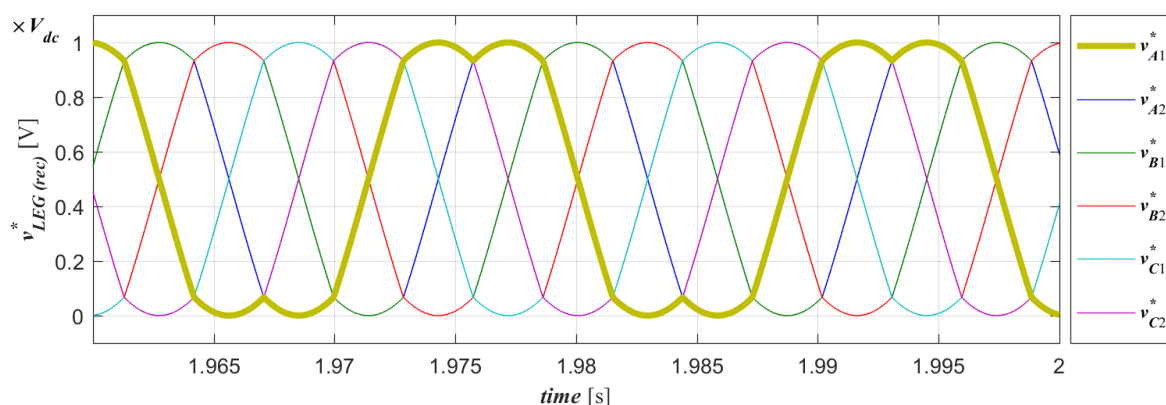


Figure 3.14: Reconstructed reference output leg voltage ( $v_{LEG,rec}^*$ ) waveforms of D2L3PSV at  $m_i = 1.154$ .

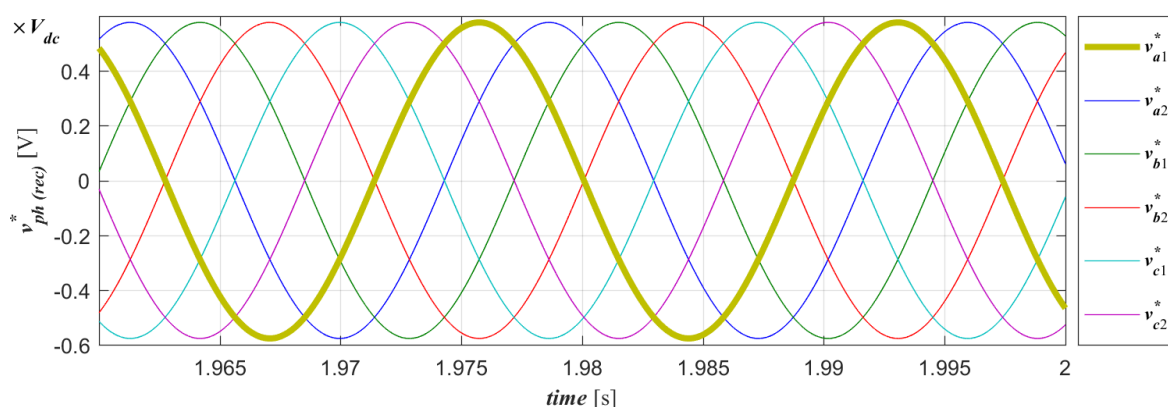


Figure 3.15: Reconstructed reference output leg voltage ( $v_{ph,rec}^*$ ) waveforms of D2L3PSV at  $m_i = 1.154$ .

2009a). The magnitude of these low odd order harmonics (particularly the 3<sup>rd</sup> harmonic) increases as  $m_i$  decreases and this relationship can clearly be observed in  $THD_i$  characteristic that corresponds to the modulation techniques for the drive with a single neutral point i.e.  $\rho 2/3SV$ , 2L6PSymSV and CBSin. Recall that the 3<sup>rd</sup> harmonic maps onto  $0^-$  axis (Dordevic, 2013). Furthermore, the  $0^-$  axis impedance is much lower than the  $\alpha$ - $\beta$  plane impedance where the fundamental harmonic components are mapped. Since the neutral points of the winding sets are connected, current can freely flow between the two winding sets and thus result in higher 3<sup>rd</sup> harmonic current. The value of the current fundamental,  $|i_{ph}|_{fund}$ , is practically constant for the full linear range of  $m_i$  since constant  $V/f$  control is used. Exception to this is at lower values of  $m_i$  because no voltage boost has been implemented.

Comparing the performances of the applied modulation techniques for the single and two isolated neutral points configurations, one can see that the modulation techniques for the

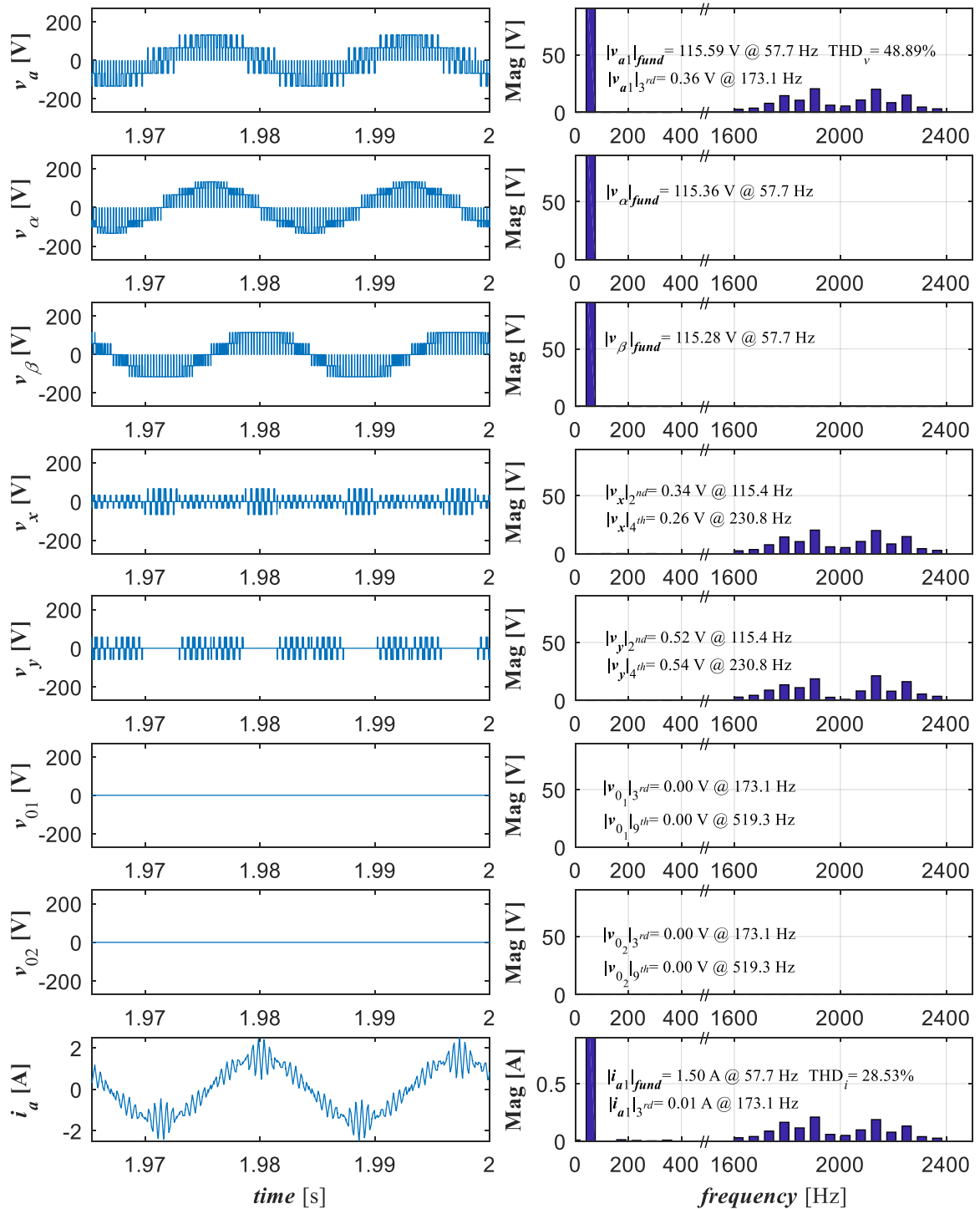


Figure 3.16: Phase 'a' voltage, phase voltage components ( $v_\alpha$ ,  $v_\beta$ ,  $v_x$ ,  $v_y$ ,  $v_0^+$  and  $v_0^-$ ), phase 'a' current and corresponding spectra of D2L3PSV for the machine driven by an ideal inverter at  $m_i = 1.154$ .

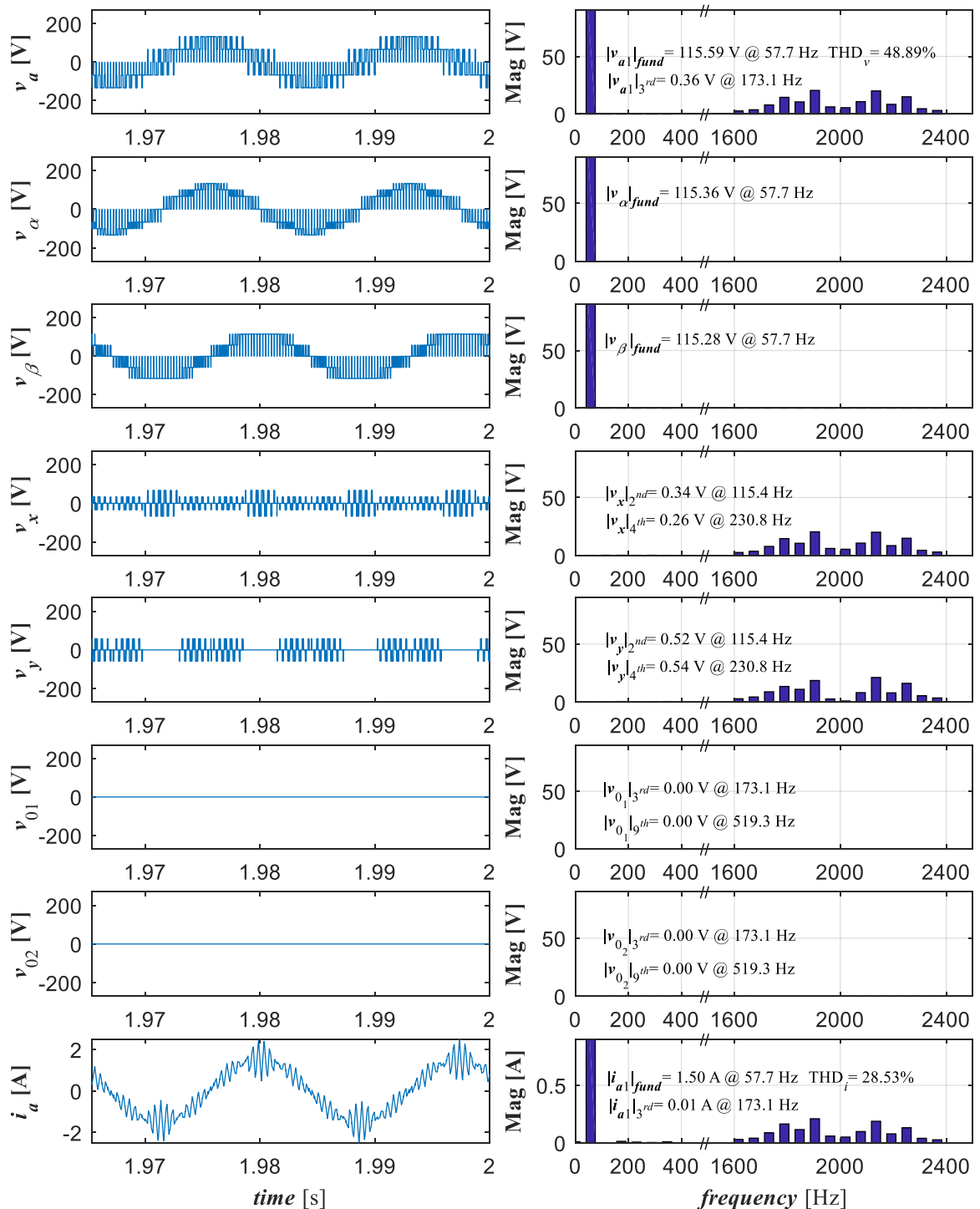
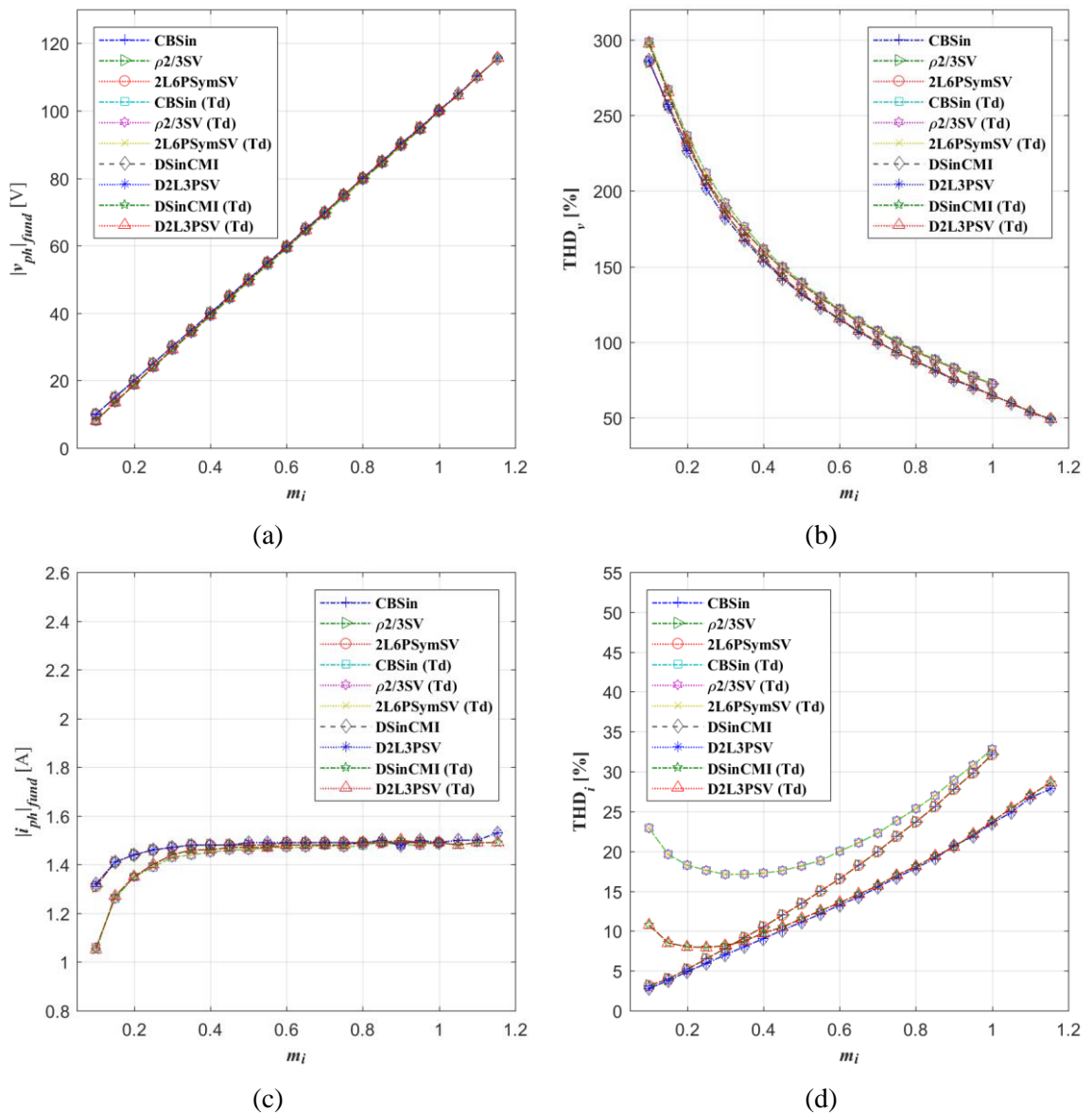


Figure 3.17: Phase ‘a’ voltage, phase voltage components ( $v_\alpha$ ,  $v_\beta$ ,  $v_x$ ,  $v_y$ ,  $v_0^+$  and  $v_0^-$ ), phase ‘a’ current and corresponding spectra of DSinCMI for the machine driven by an ideal inverter at  $m_i = 1.154$ .



Applied PWM techniques for single neutral point case:

CBSin	Sinusoidal PWM
$\rho2/3SV$	Space vector algorithm based on (Correa et al., 2003, Dujic et al., 2007a)
2L6PSymSV	Space vector algorithm using time matrix approach

Applied PWM techniques for two neutral points case:

DSinCMI	Sinusoidal with common mode voltage injection (dual three-phase modulators)
D2L3PSV	Two-level three-phase space vector algorithm (dual modulators)

Note: Td – denotes that the inverter dead-time is considered in the simulation

Figure 3.18: The performance of applied modulation strategies for full linear range of  $m_i$  based on:

(a) obtained  $|v_{ph}|_{fund}$  (b) calculated  $THD_v$  (c) obtained  $|i_{ph}|_{fund}$  and (d) calculated  $THD_i$ .

latter configuration (D2L3PSV and DSinCMI) are slightly better. This is largely because these modulation techniques are able to offer better dc-bus utilisation. In addition, since the neutral points are isolated, the low odd order harmonics due to the uncompensated inverter dead time, the 3<sup>rd</sup> harmonic in particular, simply cannot exist and this helps to lower the THD.

### 3.6 Summary

Modulation techniques based on the space vector algorithm and the carrier-based approach for two-level symmetrical six-phase drives with a single ( $\rho 2/3$ SV, 2L6PSymSV and CBSin) and two (D2L3PSV and DSinCMI) isolated neutral points configuration are presented in this chapter. Discussions regarding derivation of the equations to calculate the dwell times for  $\rho 2/3$ SV and dwell time matrix approach used in 2L6PSymSV are presented in detail. In general, they revolve around ensuring that the  $x$ ,  $y$  and  $0$  components are zero on average in one switching period, thus obtaining sinusoidal  $v_{ph}$  waveforms. All discussed modulation techniques are verified through simulation in open loop for full linear range of  $m_i$  using Matlab/Simulink. Although the obtained simulation results show that the modulation techniques based on the space vector algorithm yield the same performance as their equivalent carrier-based approach, D2L3PSV and DSinCMI offer slightly better performance than  $\rho 2/3$ SV, 2L6PSymSV and CBSin. However, this is largely due to the absence of the neutral point connection between the winding sets, where the low order harmonics of the order of  $3k$  ( $k = 1, 3, 5 \dots$ ) simply cannot exist. This is allowing to those winding sets to be controlled by two separate PWM modulators, in this case by using dual two-level three-phase modulators. Consequently, the dc-bus voltage can be utilised around 15% better than in the case of single neutral point. All in all, for better performance and higher dc-bus utilisation, drive with two isolated neutral points configuration is recommended. Additionally, if simple implementation is desired, modulation technique based on carrier-based approach should be chosen.



---

## CHAPTER 4

### PWM techniques for three-level symmetrical six-phase drives

---

#### 4.1 Introduction

Space vector algorithms based on time matrix approach and carrier-based modulation technique, with in-phase disposition method (PD), for three-level symmetrical six-phase drive with single and two isolated neutral points, are presented in this chapter. The steps regarding the potential switching sequence selection, such that the output phase voltages should not contain low order harmonics for the drive with single neutral point configuration, are described in detail. Furthermore, since the potential switching sequences in each sector generate their own respective region of application, the conditions for accurate determination of sub-sector to which the reference belongs and the corresponding switching sequence that should be applied are also derived. All presented modulation methods are verified through simulation in Matlab/Simulink and this is followed by experimental validation. The performance of the modulation methods is compared in terms of phase voltage and current total harmonic distortions as well as their execution time.

Original contribution of this chapter, in particular of sub-section 4.3.1 where novel space vector algorithm for three-level symmetrical six-phase drive with single neutral point configuration, has been presented in a conference paper (Engku Ariff et al., 2016) and published in a journal paper (Engku Ariff et al., 2017a).

#### 4.2 Power circuit topologies

Unlike the two-level inverter, the three-level diode-clamped or neutral-point clamped (NPC) inverter has two pairs of switches per leg, as shown in Figure 4.1 and 4.2 for single and two isolated neutral point configurations, respectively. Previously introduced notations for inverter output legs and phases in Chapter 3 are also applicable here. The switches are assumed to be ideal and upper and the lower switch pairs are complimentary to each other. In other words, when the upper switch is 'on', the corresponding lower switch must be 'off' and vice versa. Those switches are differentiated by additional number notation (in subscript) to indicate which pair they belong to. As an example,  $S_{A1}$  and  $S_{A1}'$  is the first pair and  $S_{A2}$  and  $S_{A2}'$  is the second pair for the first inverter leg. Moreover, there are two additional diodes, i.e.  $D_{A1}$  and

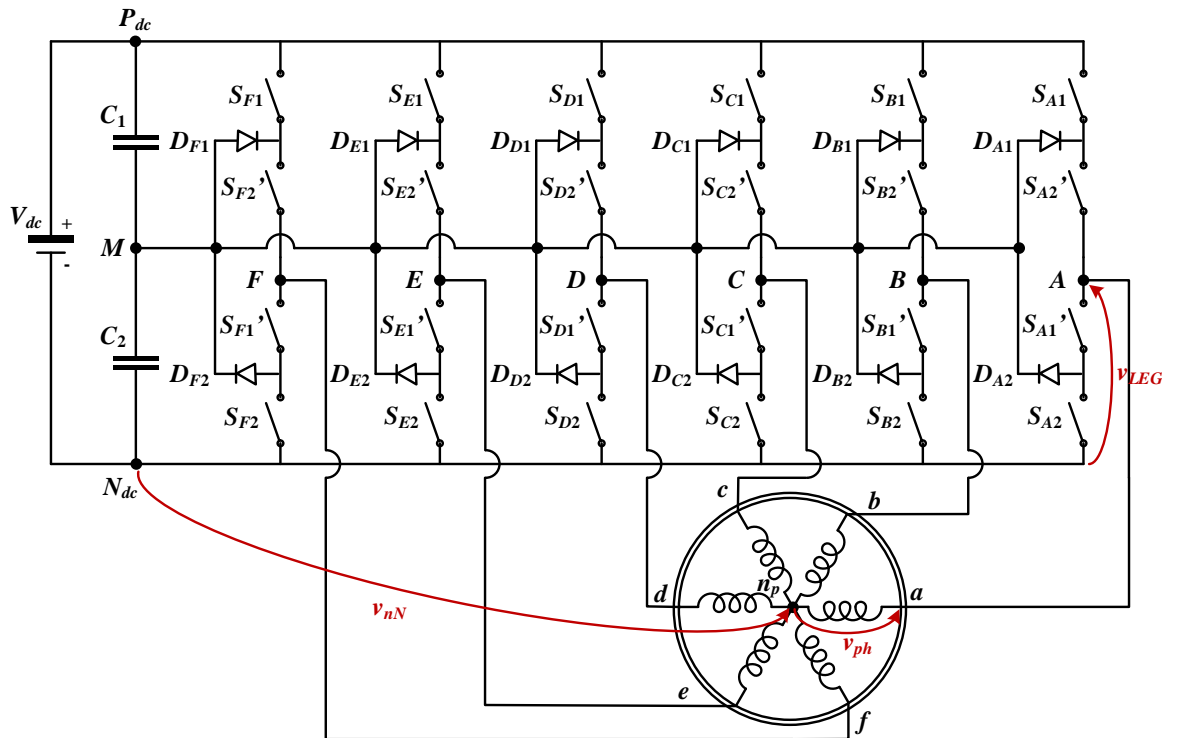


Figure 4.1: Power circuit topology of three-level symmetrical six-phase drive with single neutral point.

$D_{A2}$ , which are connected to the node  $M$  between two capacitors,  $C_1$  and  $C_2$ . These capacitors equally distribute the dc-bus voltage ( $V_{dc}$ ). Hence the midpoint of those capacitors is equivalent to the midpoint of dc-bus, which is also known as inverter neutral-point. To put it simply, the diodes are used to clamp the output leg voltage to half of  $V_{dc}$ .

Based on the switching state of the two pairs of the inverter switches, four possible output leg voltage levels could be possible. However, one of them is a floating (uncontrolled) output leg voltage and hence this state is not taken into account in the development of modulation techniques. The relationships between the switching states of the inverter switches of the first inverter leg and their possible output leg voltage levels are tabulated in Table 4.1.

Table 4.1: Relationship between switching states and  $v_{LEG}$ .

Switching States				Output leg voltage, $V_A$	Normalised leg voltage
$S_{A1}$	$S_{A2}'$	$S_{A1}'$	$S_{A2}$		
off	off	on	on	0	0
off	on	on	off	$V_{dc}/2$	1
on	on	off	off	$V_{dc}$	2
on	off	off	on	High impedance	-

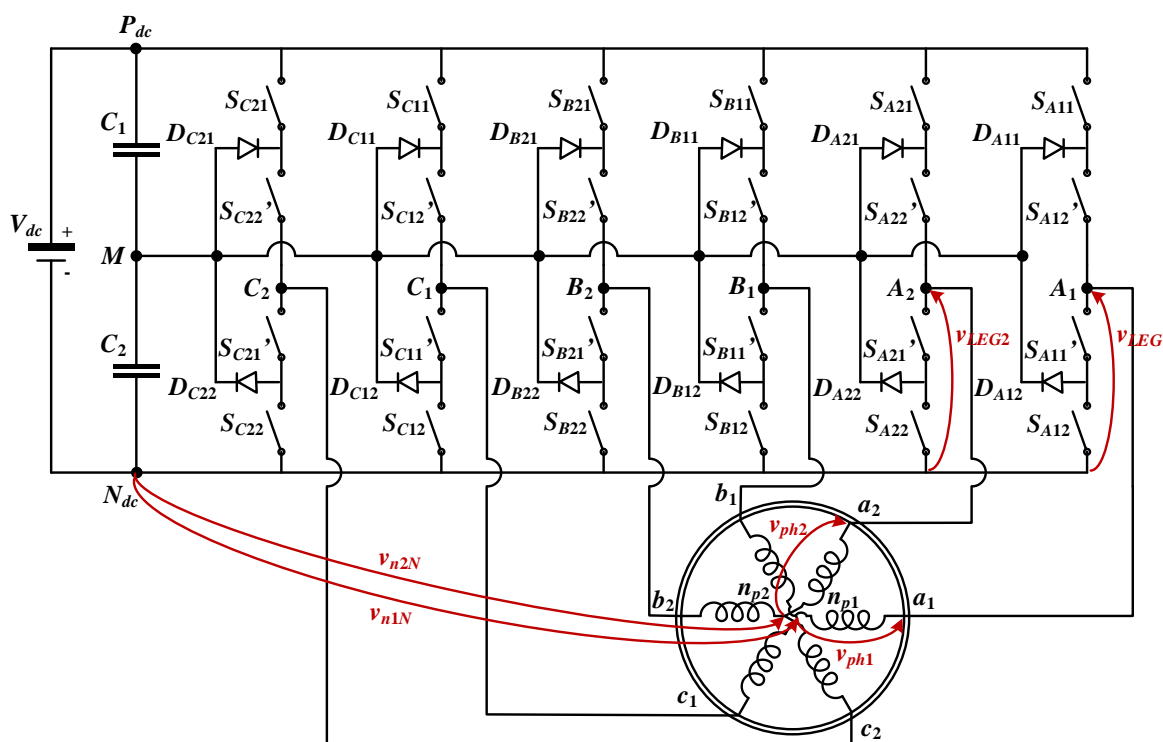


Figure 4.2: Power circuit topology of three-level symmetrical six-phase drive with two isolated neutral points.

Furthermore, it should be noted that the relationships between output leg voltages ( $v_{LEG}$ ), common mode voltage (CMV) and output phase voltages ( $v_{ph}$ ), as in (3.1) to (3.6), remain valid for the three-level case as well.

### 4.3 Drive with single neutral point configuration

A space vector PWM technique (3L6PSymSV) and its corresponding carrier-based approach, using in-phase disposition (PDSin) technique, for three-level symmetrical six-phase drive with single neutral point, are presented in this section. More emphasis is put on the development of 3L6PSymSV where the processes of selecting the switching sequences and determination of sub-sectors are explained in details. Both modulation techniques are verified and validated through simulation as well as experimental testing in the open loop.

#### 4.3.1 Space vector PWM algorithm

A process of developing new space vector algorithm for three-level symmetrical six-phase drive with single neutral point configuration is presented in this sub-section. The switching sequences are chosen by following several requirements and conditions such that the sinusoidal  $v_{ph}$  waveforms are realised. In general, the selection of the switching sequences is

performed through analysing all possible transition patterns in each sector in the two mutually orthogonal planes and one of the zero component axis graphically. Corresponding sub-sectors are then determined using visualisation of numerical solutions of the calculated dwell times.

#### 4.3.1.1 Projection of space vectors

Since there are three possible  $v_{LEG}$  levels, there are  $3^6 = 729$  possible switching states, which also define  $3^6 - 2^6 = 665$  phase voltage,  $v_{ph}$ , space vectors (Lopez et al., 2009b). Similarly as in Chapter 3, by implementing VSD approach, these space vectors can be projected into three mutually orthogonal two-dimensional planes, i.e.  $\alpha$ - $\beta$ ,  $x$ - $y$  and  $0^+$ - $0^-$  plane, where corresponding low order harmonics are also mapped. The mapping of the low order harmonics is the same as in two-level case i.e. harmonics of order  $6k \pm 1$  ( $k = 0, 1, 2, 3 \dots$ ) are mapping to  $\alpha$ - $\beta$  plane,  $6k \pm 2$  ( $k = 0, 1, 2, 3 \dots$ ) to  $x$ - $y$  plane and  $3k$  ( $k = 1, 3, 5, \dots$ ) to  $0^+$ - $0^-$  plane. This is so since the mapping of the low order harmonics does not depend on the number of levels of the inverter.

By normalising the three possible  $v_{LEG}$  levels (as listed in Table 4.1) by  $V_{dc}/2$ , all 729 possible switching states (0 to 728) can be represented by six-digit ternary numbers (000000 to 222222). Therefore, from (3.8), the projections of the normalised leg voltage space vectors can be obtained as shown in Figure 4.3. The projections of  $v_{LEG}$  and  $v_{ph}$  space vectors onto  $\alpha$ - $\beta$  and  $x$ - $y$  planes are identical. One can see that all possible switching states are projected onto 61 different locations in the planes and those locations can be clustered into nine groups based on the distance of the location to the origin, i.e. the magnitude of the mapped space vectors. These nine groups are illustrated in  $\alpha$ - $\beta$  and  $x$ - $y$  planes as: six hexagons with magnitudes of  $1/6V_{dc}$ ,  $1/(2\sqrt{3})V_{dc}$ ,  $1/3V_{dc}$ ,  $1/2V_{dc}$ ,  $1/\sqrt{3}V_{dc}$  and  $2/3V_{dc}$ ; two dodecagons with magnitudes of  $\sqrt{7}/6V_{dc}$  and  $\sqrt{13}/6V_{dc}$ ; and a dot at the origin, i.e. zero in magnitude.

The projections of  $v_{LEG}$  and  $v_{ph}$  space vectors into  $0^+$ - $0^-$  plane are different, as can be seen from Figure 4.3(c) where the projected  $v_{ph}$  space vectors are denoted as red dots. One can see that all projected  $v_{ph}$  space vectors are zero with respect to  $0^+$  axis, which is expected since  $0^+$  axis actually represents CMV. Therefore, by not considering the  $0^+$  axis in the development of space vector algorithm, one can see that the projections of  $v_{LEG}$  and  $v_{ph}$  space vectors become identical. Hence, it is possible to realise  $v_{ph}$  waveforms by applying the switching sequences that are based on  $v_{LEG}$  space vectors, i.e. corresponding switching states. Since there is much higher number of switching states than the projected locations in  $\alpha$ - $\beta$ ,  $x$ - $y$  and  $0^+$ - $0^-$  planes, existence of  $v_{ph}$  space vector redundancies should be expected.

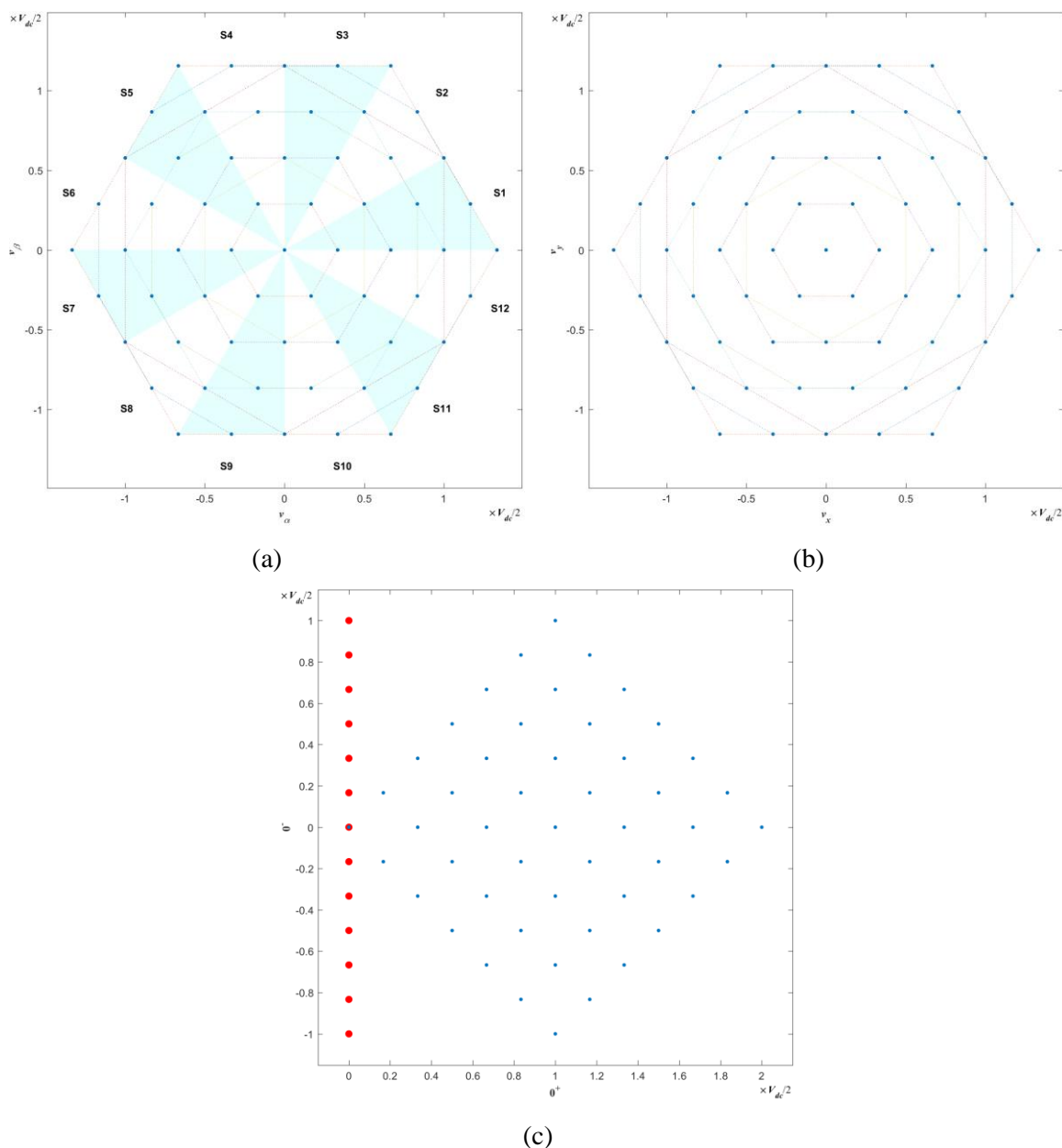


Figure 4.3: Projections of  $v_{LEG}$  and  $v_{ph}$  (dots in red) space vectors of the analysed three-level symmetrical six-phase drive with single neutral point in the: (a)  $\alpha$ - $\beta$  (b)  $x$ - $y$  and (c)  $0^+$ - $0^-$  planes.

The aim of the space vector algorithm here is to synthesise the desired sinusoidal reference phase voltage ( $v_{ph}^*$ ) waveforms. In order to achieve that, the switching sequence that consists of a set of space vectors should be chosen in such a way that the average value of the phase voltage components in  $x$ - $y$  plane and  $0^-$  axis are zero. The number of the chosen space vectors in each switching sequence should be the same as the number of machine phases (Kelly et al., 2003), i.e. six in this case. For each sector shown in Figure 4.3(a) (each sector span is  $30^\circ$ ), there is a total of 147 switching states, including those which are located at the sector

borders and at the origin. Therefore, it can be said that the process of choosing the right switching sequence becomes more difficult. Thus, a simple method of reducing the number of switching states by selecting only the switching states that meet the requirement of the order-per-sector law, is applied first.

#### 4.3.1.2 Reduction of the number of space vectors

The order-per-sector law method is introduced in (Gao and Fletcher, 2010) to reduce the number of switching states in order to improve the process of selecting the right switching sequences. The principle of this method is based on the general equation which defines the relationship between  $v_{ph}$  and  $v_{LEG}$  (3.3). The subtracted CMV (the second term) is in fact a scalar value and behaves like an offset for  $v_{ph}$ . Therefore, one can say that the order of the desired  $v_{ph}^*$  waveforms should be the same as the order of the desired reference output leg voltage ( $v_{LEG}^*$ ) waveforms. According to (3.8), the desired  $v_{ph}^*$  waveforms for the analysed symmetrical six-phase drives are sinusoidal and they change their mutual order after every  $30^\circ$  in one period (see Figure 3.4). Note that this  $30^\circ$  angle also corresponds to the sector angle in  $\alpha$ - $\beta$  plane, hence the name of ‘order-per-sector law’.

The changes of the order of  $v_{LEG}^*$  waveforms (which also correspond to the order of the desired  $v_{ph}^*$  waveforms) are tabulated in Table 4.2. The order of  $v_{LEG}^*$  in the first row must be greater than or equal to the order of  $v_{LEG}^*$  in the second row, then the order of  $v_{LEG}^*$  in second row must be greater than or equal to the order of  $v_{LEG}^*$  in third row, etc. As an example, the order of  $v_{LEG}^*$  waveforms in the first sector (S1) is  $v_A^* \geq v_B^* \geq v_F^* \geq v_C^* \geq v_E^* \geq v_D^*$ . Nevertheless, it can be said that the implementation of the order-per-sector law is simply identifying whether the projected space vectors satisfy the condition of the order-per-sector law of their corresponding

Table 4.2: Order-per-sector law of symmetrical six-phase drive.

		Sector											
		S1	S2	S3	S4	S5	S6	S7	S8	S9	S10	S11	S12
Order of $v_{LEG}^*$	$v_A^*$	$v_B^*$	$v_C^*$	$v_D^*$	$v_E^*$	$v_F^*$	$v_A^*$	$v_B^*$	$v_C^*$	$v_D^*$	$v_E^*$	$v_F^*$	$v_A^*$
	$v_B^*$	$v_A^*$	$v_C^*$	$v_D^*$	$v_E^*$	$v_F^*$	$v_B^*$	$v_C^*$	$v_D^*$	$v_E^*$	$v_F^*$	$v_A^*$	$v_B^*$
	$v_C^*$	$v_A^*$	$v_B^*$	$v_D^*$	$v_E^*$	$v_F^*$	$v_C^*$	$v_D^*$	$v_E^*$	$v_F^*$	$v_A^*$	$v_B^*$	$v_C^*$
	$v_D^*$	$v_A^*$	$v_B^*$	$v_C^*$	$v_E^*$	$v_F^*$	$v_D^*$	$v_E^*$	$v_F^*$	$v_A^*$	$v_B^*$	$v_C^*$	$v_D^*$
	$v_E^*$	$v_A^*$	$v_B^*$	$v_C^*$	$v_D^*$	$v_F^*$	$v_E^*$	$v_A^*$	$v_B^*$	$v_C^*$	$v_D^*$	$v_E^*$	$v_F^*$
	$v_F^*$	$v_A^*$	$v_B^*$	$v_C^*$	$v_D^*$	$v_E^*$	$v_F^*$	$v_A^*$	$v_B^*$	$v_C^*$	$v_D^*$	$v_E^*$	$v_F^*$

sector. To put it differently, the reduction of the number of space vectors can simply be done by comparing the states of  $v_{LEG}$  (or the switching states in six-digit ternary number representation) with the stated condition of the order-per-sector law.

Therefore, by comparing each possible switching state with the order-per-sector law listed in Table 4.2, those that do not meet the requirement will be discarded. As an example, switching state 407 (120002) is projected in S1 in  $\alpha$ - $\beta$  plane; however, it does not meet the requirement of the order-per-sector law of S1. This is because its  $v_A^*$  is less than  $v_B^*$ , while the order-per-sector law requires  $v_A^*$  to be greater than or equal to  $v_B^*$  (see the first column of Table 4.2). Hence, switching state 407 is discarded. The implementation of this method significantly reduces the total number of possible switching states and space vectors from 729 to 189 and from 665 to 157, respectively. The projections of these remaining space vectors, i.e. corresponding switching states, onto  $\alpha$ - $\beta$ ,  $x$ - $y$  and  $0^+$ - $0^-$  planes are shown in Figure 4.4. The decimal representation is used in Figure 4.4, and if switching state of each  $v_{LEG}$  is required, the conversion into six digit ternary representation should be done accordingly (e.g.  $110001_3 = 1 \cdot 3^5 + 1 \cdot 3^4 + 0 \cdot 3^3 + 0 \cdot 3^2 + 0 \cdot 3^1 + 1 \cdot 3^0 = 325_{10}$ ).

As can be seen in Figure 4.4(a), the remaining switching states are still being projected onto 61 locations. However, the possible switching states (including those which are located at the sector border line and origin) that need to be considered for switching sequences selection in each sector have decreased from 147 to 28 switching states. As a result, the process of choosing the right switching sequences becomes more feasible. On the other hand, the remaining switching states are projected into only nineteen locations in the  $x$ - $y$  plane, as shown in Figure 4.4(b). Note that the axis scale end values are smaller than in Figure 4.3(b). By comparing these two figures, one can see that the remaining hexagons in Figure 4.4(b) are actually the first three inner hexagons of Figure 4.3(b). As for  $0^+$ - $0^-$  plane, the number of locations of the projected switching states has also reduced significantly (see Figure 4.4(c)).

### 4.3.1.3 Determination of potential switching sequences

In order to obtain sinusoidal  $v_{ph}$  waveforms, the potential switching sequences are chosen such that the average values of  $x$ - $y$  and  $0^-$  components are zero. Recall that  $0^+$  component is not considered in the development of space vector algorithms. Moreover, as mentioned previously, the number of the chosen space vectors ought to be the same as the number of machine phases. In addition, to minimise the losses and reduce  $dv/dt$ , the transition of  $v_{LEG}$  also needs to be taken into consideration. The desirable number of transitions is one, either

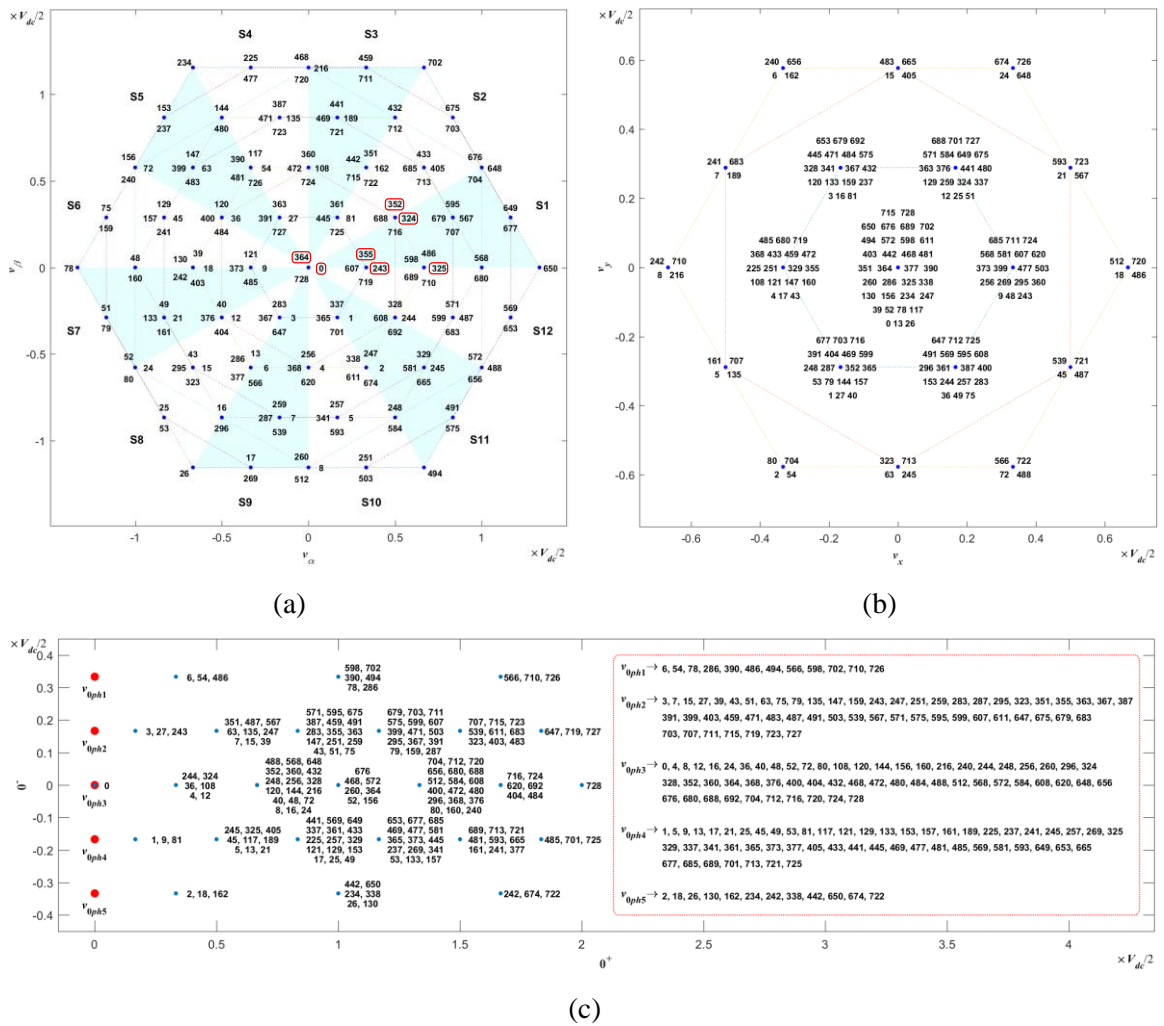


Figure 4.4: Projections of  $v_{LEG}$  and  $v_{ph}$  space vectors of the analysed three-level symmetrical six-phase drive with single neutral point after order-per-sector law implementation in the: (a)  $\alpha$ - $\beta$  (b)  $x$ - $y$  and (c)  $0^+ - 0^-$  planes.

increasing or decreasing. In addition, it is desirable that the transition of  $v_{LEG}$  in one switching period is symmetrical. In other words, the  $v_{LEG}$  transitions increase in the first half of the switching period while they decrease in the other half. Hence, the order of the chosen space vectors is simply reversed in the second half of the switching period (van der Broeck et al., 1988).

The process of determining the potential switching sequences begins by choosing the potential starting switching states. The potential starting switching states should only consist of either ‘ones’ or ‘zeros’, or combination of both when represented as a six-digit ternary number. This is because, in the first half of the switching period, the transition of the leg voltages causes the  $v_{LEG}$  level to increase by one. Thus, having ‘twos’ in the starting switching states is not

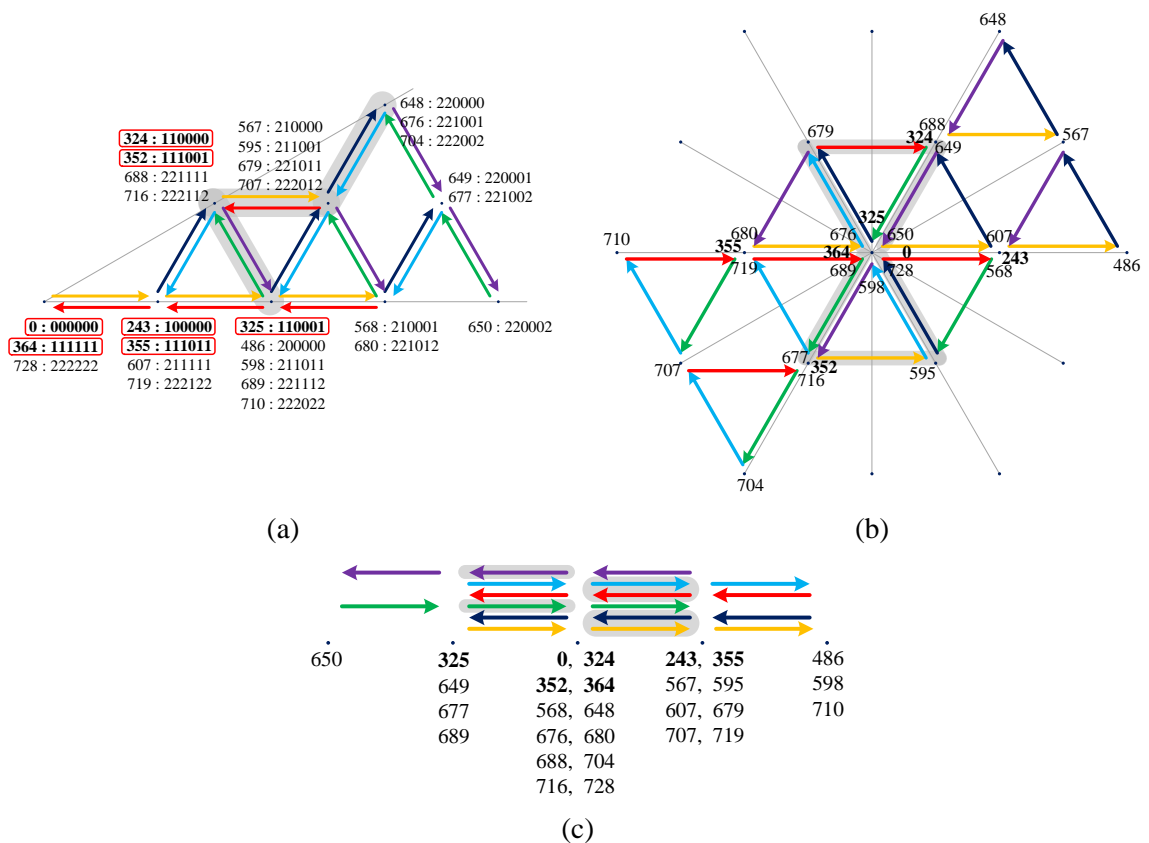


Figure 4.5: Possible transitions of voltage space vectors for the S1 in: (a)  $\alpha$ - $\beta$ , (b)  $x$ - $y$  plane and (c)  $0^-$  axis. The starting switching states are encircled in red.

possible since the maximum achievable  $v_{LEG}$  level is two, i.e. equal to  $V_{dc}$ . Therefore, out of 28 possible switching states in the sector, only seven can be chosen as the potential starting switching states. In fact, this is also true for the other sectors. As an example, the potential starting switching states for S1 are shown within the red boxes in Figure 4.4(a).

Each increment of a certain  $v_{LEG}$  in a switching sequence corresponds to a certain transition of the space vector in  $\alpha$ - $\beta$ ,  $x$ - $y$  plane as well as on  $0^-$  axis. As an example, all possible transitions of  $v_{LEG}$  space vectors in S1 are illustrated with different colour arrows in Figure 4.5. Note that  $0^-$  axis is now shown as horizontal axis for easier illustration purpose. When all possible switching state transitions are identified, one should be able to determine the possible switching sequences next.

As already mentioned, each switching sequence should satisfy the requirement that each  $v_{LEG}$  level increases by one level in the first half of a switching period. Hence, starting from a potential starting switching state, those six transitions of  $v_{LEG}$  levels will graphically form a pattern that comprises six different colour arrows in  $\alpha$ - $\beta$  and  $x$ - $y$  planes, as well as on  $0^-$  axis. In

addition, these six transitions also result in seven switching states per switching sequence. However, only six space vectors are required in order to obtain the desired sinusoidal  $v_{ph}$ . This means that two of the switching states yield identical space vector projection in  $\alpha$ - $\beta$ ,  $x$ - $y$  plane and on  $0^-$  axis. In other words, they are subjected to redundancy of switching states. The redundant switching states are the first, i.e. the starting, and the seventh switching state. As an example, the potential starting switching states and their redundant (the seventh) switching states of S1 are: 0, 364 and 728; 243 and 607; 324 and 688; 325 and 689; 352 and 716; and finally 355 and 719.

On the basis of all these considerations one finds that there are 64 potential switching sequences in each sector. The list of the potential switching sequences of S1 is given in Appendix A. These 64 switching sequences can be further categorised based on the formed space vector transition patterns. One finds that there are 32 different space vector transition patterns, which correspond to the originally determined 64 potential switching sequences. These patterns are illustrated in  $\alpha$ - $\beta$ ,  $x$ - $y$  plane, and  $0^-$  axis, as shown in Figure 4.6, 4.7 and 4.8, respectively. The number of mapped switching sequences together with their assigned reference numbers (see Table A1) are also incorporated below their corresponding patterns. Furthermore, it can be seen that some transition patterns encompass several potential starting switching states, which indicates the existence of redundancy in the switching sequences. As an example, one can see that the switching sequences 110001-111001-211001-221001-221011-221111-221112 and 110000-110001-111001-211001-221001-221011-221111 of S1 are clearly different, but they produce an identical space vector transition pattern (highlighted in grey in Figure 4.5) in the  $\alpha$ - $\beta$  and  $x$ - $y$  planes, as well as in  $0^-$  axis (this pattern is denoted with D in Figure 4.6, 4.7 and 4.8). Hence, this example confirms the existence of switching sequence redundancies.

Although there are 32 space vector transition patterns in each sector, not all of them meet the requirement that the average values of  $x$ ,  $y$  and  $0^-$  components are zero. In order to single out those transition patterns (and hence corresponding switching sequences), a graphical method of analysing the transition patterns of those potential switching sequences (Dordevic et al., 2013b, Gao and Fletcher, 2010) is implemented. The graphical method for the elimination considers the projections of the states in  $x$ - $y$  plane and on  $0^-$  axis: if all states are located at one side of the line crossing the origin and on one side of  $0^-$  axis, that space vector transition pattern cannot lead to zero on average in that plane and axis. Hence, those patterns and corresponding sequences can be eliminated

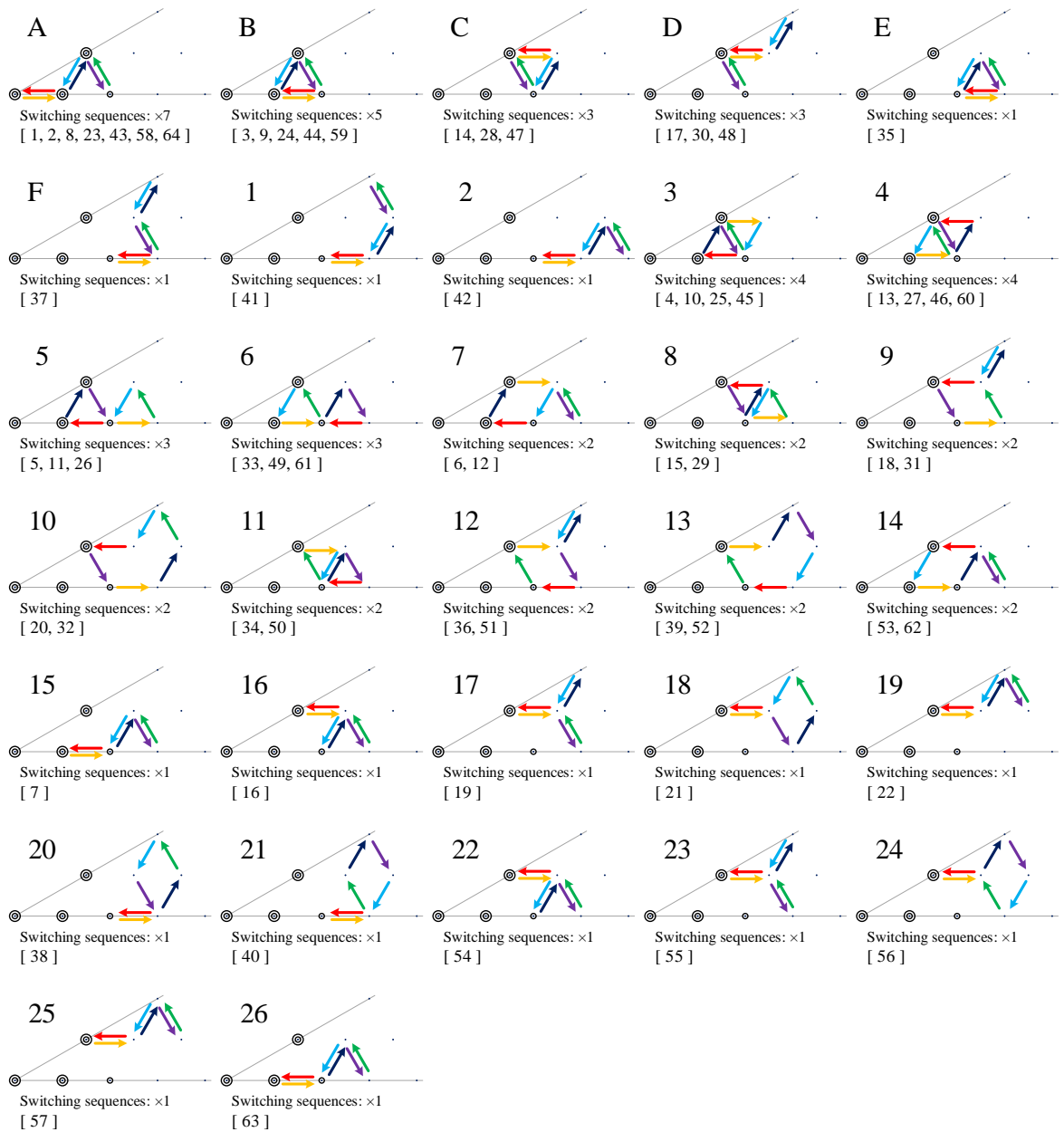


Figure 4.6: Patterns representing leg voltage transitions of the potential switching sequences for S1 in  $\alpha$ - $\beta$  plane and the number of corresponding potential switching sequence redundancies (full list of switching sequences, with corresponding sequence numbers in the square brackets, is given in Appendix A). Letters A to F stand for patterns that will be selected while numbers 1 to 26 stand for those that will be eliminated later.

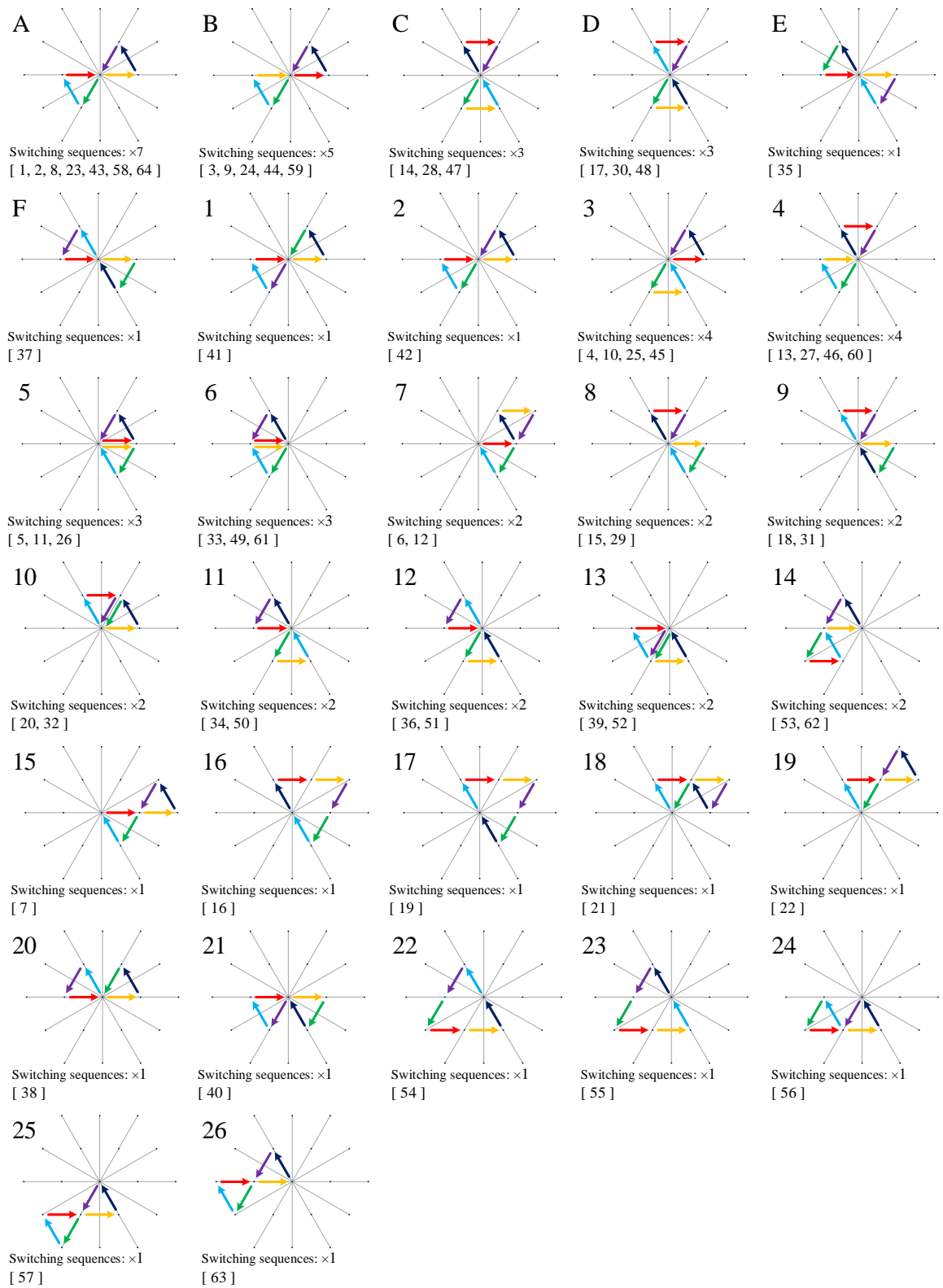


Figure 4.7: Patterns representing leg voltage transitions of the potential switching sequences for S1 in the x-y plane.

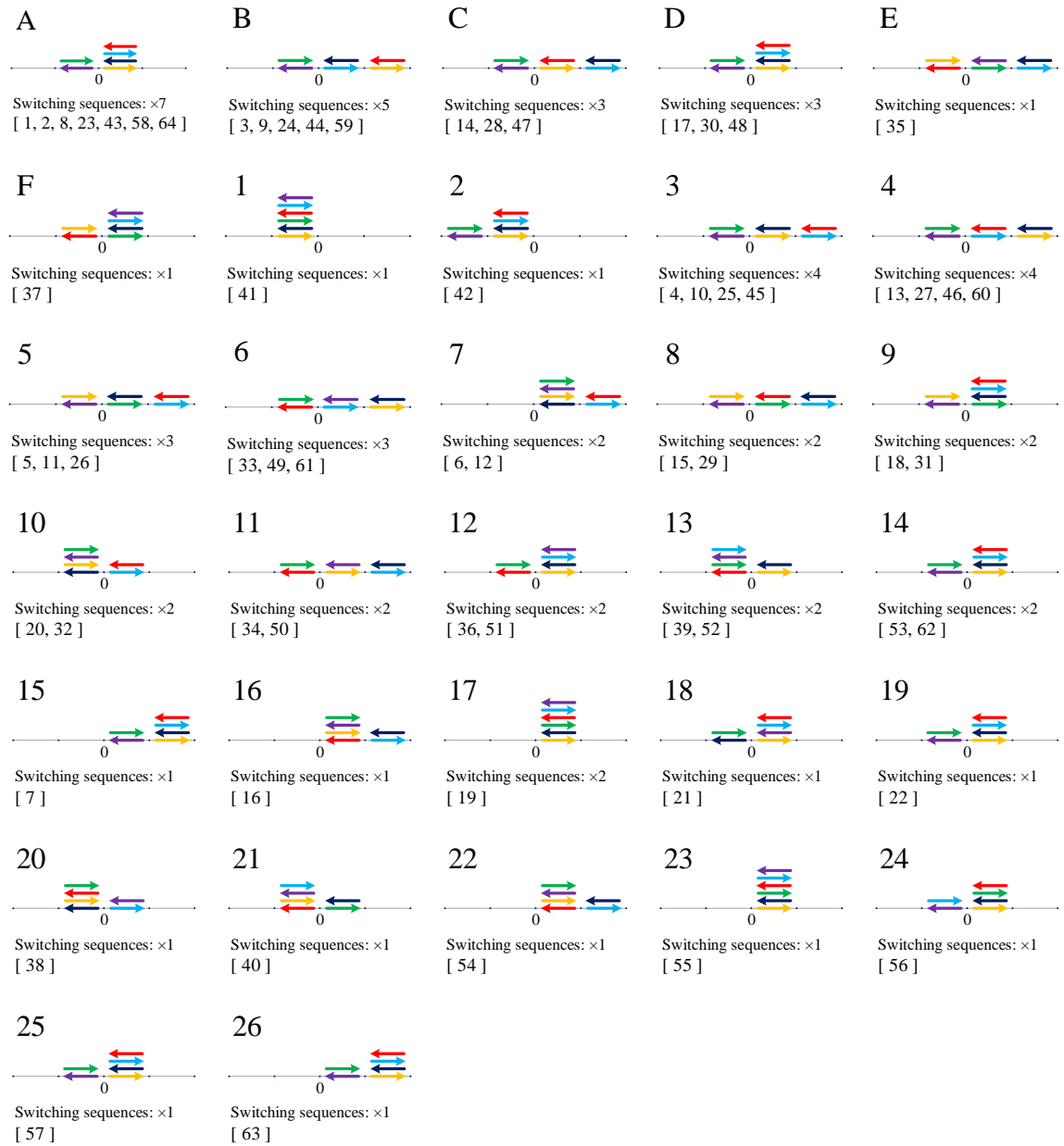


Figure 4.8: Patterns representing leg voltage transitions of the potential switching sequences for S1 on 0- axis.

Table 4.3: Potential switching sequences for S1. Switching sequences in bold denote the final selected switching sequences.

Sub-sector	Pattern in $\alpha$ - $\beta$ plane	Sequence ref. no.	Potential switching sequences (1 <sup>st</sup> half of the switching period)
$A_1$	A	1	0 - 243 - 324 - 325 - 352 - 355 - 364
		2	243 - 324 - 325 - 352 - 355 - 364 - 607
		8	324 - 325 - 352 - 355 - 364 - 607 - 688
		<b>23</b>	<b>325 - 352 - 355 - 364 - 607 - 688 - 689</b>
		43	352 - 355 - 364 - 607 - 688 - 689 - 716
		58	355 - 364 - 607 - 688 - 689 - 716 - 719
		64	364 - 607 - 688 - 689 - 716 - 719 - 728
$B_1$	B	3	243 - 324 - 325 - 352 - 355 - 598 - 607
		9	324 - 325 - 352 - 355 - 598 - 607 - 688
		<b>24</b>	<b>325 - 352 - 355 - 598 - 607 - 688 - 689</b>
		44	352 - 355 - 598 - 607 - 688 - 689 - 716
		59	355 - 598 - 607 - 688 - 689 - 716 - 719
$C_1$	C	14	324 - 325 - 352 - 595 - 598 - 679 - 688
		<b>28</b>	<b>325 - 352 - 595 - 598 - 679 - 688 - 689</b>
		47	352 - 595 - 598 - 679 - 688 - 689 - 716
$D_1$	D	17	324 - 325 - 352 - 595 - 676 - 679 - 688
		<b>30</b>	<b>325 - 352 - 595 - 676 - 679 - 688 - 689</b>
		48	352 - 595 - 676 - 679 - 688 - 689 - 716
$E_1$	E	<b>35</b>	<b>325 - 568 - 595 - 598 - 679 - 680 - 689</b>
$F_1$	F	<b>37</b>	<b>325 - 568 - 595 - 676 - 679 - 680 - 689</b>

By graphically analysing the corresponding transition patterns in  $x$ - $y$  plane, one finds that only eight (transition patterns of A to F, as well as 1 and 2) out of 32 transition patterns surround the origin, and are thus capable of achieving zero value in the  $x$ - $y$  plane on average. Likewise, on  $0^-$  axis, another two out of the eight remaining transition patterns are identified, such that the average value of  $0^-$  components cannot be zero. As a result, only six transition patterns (transition patterns A to F) remain. These transition patterns also correspond to twenty potential switching sequences. The list of the switching states associated to these remaining switching sequences in S1 is listed in Table 4.3. Note that only switching states in the first half of the switching period are listed, since the order of the switching states is reversed in the second half.

#### 4.3.1.4 Calculation of dwell times and sector division

Although all the space vector transition patterns and their corresponding potential switching sequences in each sector have been determined, the relevance of those switching sequences for the actual implementation purposes is yet to be examined. This is because each transition pattern yields different solution for dwell times calculation (Dordevic et al., 2013b). In general, the dwell times are the duration of the applied space vectors in the chosen switching sequence and they can be calculated based on the volt-second balance principle and time balancing equation, as in (3.9) and (3.10). Furthermore, depending on the magnitude of  $v_{ph}^*$  space vector ( $V_f^*$ ), the solutions of the dwell times for the transition patterns only exist in certain regions within their corresponding sector in the  $\alpha$ - $\beta$  plane. These regions are commonly known as regions of application.

The regions of application can be determined either by using analytical calculations (Gao and Fletcher, 2010), or through visualisation of numerical solutions of the calculated dwell times in the  $\alpha$ - $\beta$  plane (Dordevic et al., 2013b). The latter method is adopted here. The dwell times of each transition pattern are repetitively calculated using (3.18) by gradually increasing the value of  $V_f^*$ , of  $\alpha$  and  $\beta$  component references ( $v_\alpha^*$  and  $v_\beta^*$ ), from zero to  $2/3V_{dc}$  (governed by the largest hexagon in the  $\alpha$ - $\beta$  plane). The calculations are done using Matlab code. This ensures that the entire regions in all twelve sectors are considered as the possible regions of application. If the solution for the dwell times exists for that particular  $V_f^*$ , a dot is plotted at its coordinate in the  $\alpha$ - $\beta$  plane. Hence, the regions of application corresponding to each transition pattern can be visually determined. As an example, the space vector transition pattern D, which also corresponds to the switching sequences of 17, 30 and 48 (refer to Table 4.3), generates a region of application as shown in Figure 4.9. As a result, one finds that there are six regions of application (denoted as  $A_1$  to  $F_1$ ) per sector and there is no overlapping between them.

The regions of application divide the sector into six sub-sectors in the shape of right-angle triangles and several vertices of those triangles are located at the locations of the projected space vectors (see Figure 4.9). In addition, the borders between the right-angle triangles are straight lines. Since the locations of the projected space vectors and the angles of the right-angle triangles are known, these borders, which are basically the limits of each sub-sector, can be determined by simple trigonometric calculations. Later in the next sub-section, these limits serve as references to determine in which sub-sector the  $v_{ph}^*$  space vector is currently projected at a particular time.

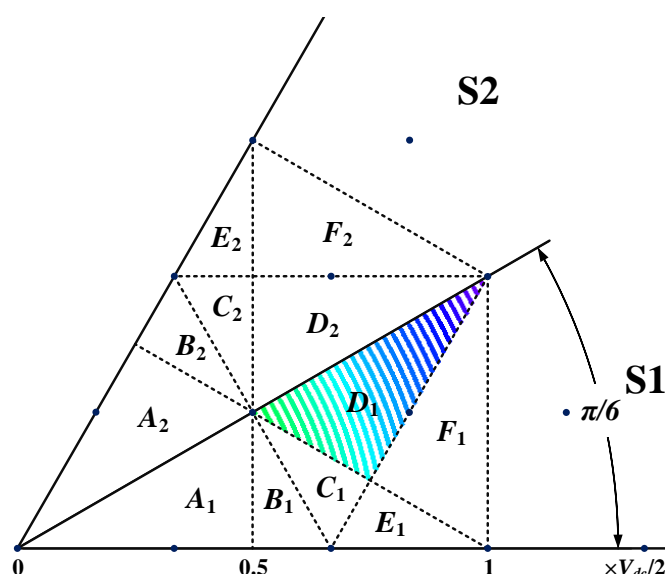


Figure 4.9: Region of application corresponding to space vector transition pattern D (shaded transition pattern in Figure 4.5 plotted by dots generated using Matlab code).

#### 4.3.1.5 Optimisation of potential switching sequences

In Table 4.3, four out of six sub-sectors have more than one potential switching sequence available. The redundancy of the available switching sequences offers flexibility in choosing the best switching sequences for the sub-sectors. The chosen switching sequences should have minimum number of  $v_{LEG}$  level transitions between the sub-sectors and thus minimise the switching losses (McGrath et al., 2003). One can see that the switching sequences which satisfy the mentioned requirement, i.e. having the same starting switching state, are switching sequences 23, 24, 28, 30, 35 and 37 (denoted in bold in Table 4.3). As a result, these six switching sequences are the ones that are going to be implemented in the space vector modulation for S1.

#### 4.3.1.6 Determination of sub-sector

Since the location of the projected  $v_{ph}^*$  space vector dictates the sub-sector and the switching sequence that is going to be applied, a method for accurately determining the sub-sector, as the projected  $v_{ph}^*$  space vector is moving through them, has to be implemented. One such method is described in (Gao and Fletcher, 2010), where the borders of the sub-sectors serve as the limits in determining the location of the projected  $v_{ph}^*$  space vector based on its magnitude and phase,  $V_f^*$ , in the  $\alpha$ - $\beta$  plane, at any given time. As an example, the illustration of how the method is implemented for S1 is shown in Figure 4.10.

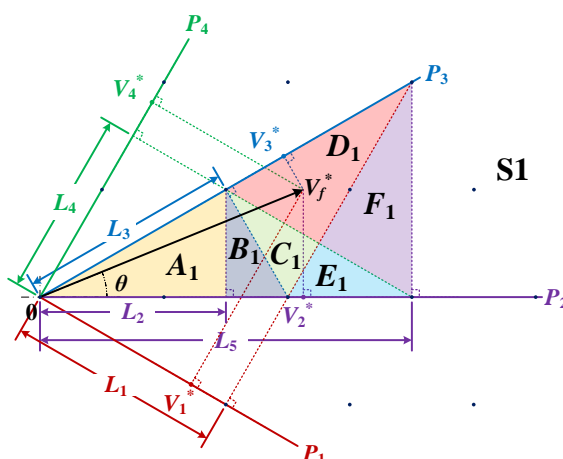


Figure 4.10: Sub-sector determination based on the location of the projected  $v_{ph}^*$  space vector in S1.

Clearly, there are five borders which divide the sub-sectors and these borders can be projected onto four perpendicular axes, which are denoted as  $P_1$  to  $P_4$ . The distances of these projected borders on the respective axes to the origin (denoted as  $L_1$  to  $L_5$ ) are then calculated using simple trigonometry calculations which result in  $L_1 = L_3 = \sqrt{3}/6V_{dc}$ ,  $L_2 = L_4 = 0.25V_{dc}$ , and  $L_5 = 0.5V_{dc}$ . Since the highest value for the limits is  $0.5V_{dc}$ , according to (3.19) the maximum achievable modulation index ( $m_i$ ) for the analysed drive topology is hence  $m_{i,max} = 1$ .

Likewise, the lengths which are associated to the projections of  $V_f^*$  onto the same perpendicular axes (denoted as  $V_1^*$  to  $V_4^*$ ), are also calculated and then compared with their respective limits (represented by the same group of colours in Figure 4.10). As an example, one can see that  $V_f^*$  is clearly located in sub-sector  $D_1$ . Thus, in order to verify that the current location of  $V_f^*$  is indeed in sub-sector  $D_1$ , the projections of  $V_f^*$  need to satisfy the conditions of  $V_1^* \leq L_1$  and  $V_4^* > L_4$ . Additionally, the necessary condition for S1, i.e.  $0 \leq \theta < \pi/6$ , must hold true as well. The conditions defining the sub-sectors in S1 are listed in Table 4.4. Therefore, by

Table 4.4: Conditions defining the sub-sectors for S1.

Projection of $V_f^*$	Sub-sector					
	$A_1$	$B_1$	$C_1$	$D_1$	$E_1$	$F_1$
$V_1^*$	-	-	$\leq L_1$	$\leq L_1$	$> L_1$	$> L_1$
$V_2^*$	$\leq L_2$	$> L_2$	-	-	-	$\leq L_5$
$V_3^*$	-	$\leq L_3$	$> L_3$	-	-	-
$V_4^*$	-	-	$\leq L_4$	$> L_4$	$\leq L_4$	$> L_4$

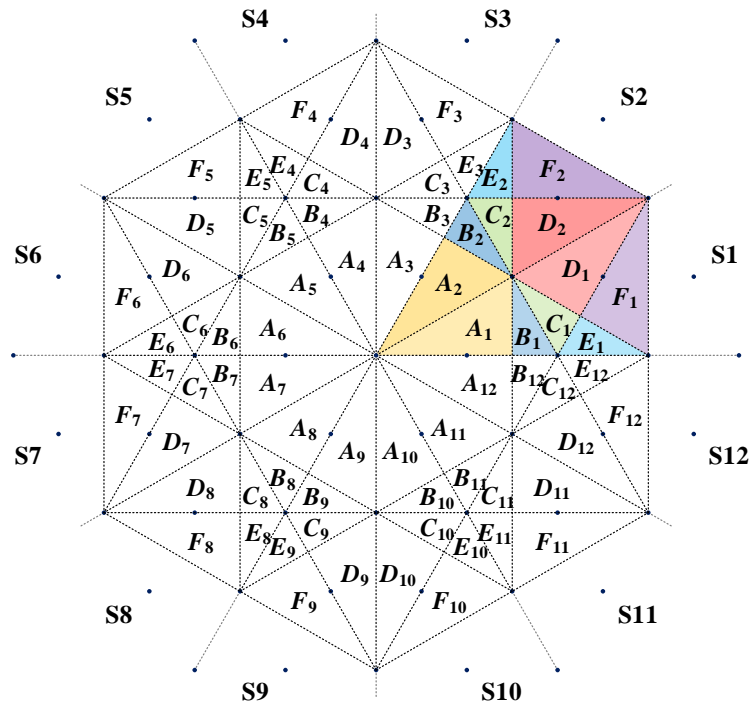


Figure 4.11: Sub-sectors of all twelve sectors in the  $\alpha$ - $\beta$  plane.

satisfying the conditions set by these limits, the right sub-sector can be identified and consequently, the corresponding switching sequence can be applied.

#### 4.3.1.7 Potential switching sequences and sub-sectors determination of other sectors

Until now, only S1 is used as an example in presenting the processes of choosing the switching sequences and determining the sub-sectors. Therefore, by following the same processes as in sub-section 4.3.1.1 till 4.3.1.6, the switching sequences and sub-sectors for the other sectors can also be determined. The list of the chosen switching sequences of the first sub-sector,  $A_k$  ( $k = 1, 2, 3 \dots 12$ ), is given in Table 4.5 while their corresponding sub-sectors as well as other sub-sectors in the  $\alpha$ - $\beta$  plane are shown in Figure 4.11.

Due to the symmetry of the sub-sector division (see Figure 4.11), it is possible to relate the switching sequences of the other sectors to those switching sequences of S1. One finds that this relationship is simply based on changing the order of the rows in the switching sequences according to the order of  $v_{LEG}^*$  in the order-per-sector law (refer to Table 4.2). As an example, the order of  $v_{LEG}^*$  of S1 is  $v_A^* \geq v_B^* \geq v_F^* \geq v_C^* \geq v_E^* \geq v_D^*$ , while for the second sector (S2) the order changes to  $v_B^* \geq v_A^* \geq v_C^* \geq v_F^* \geq v_D^* \geq v_E^*$ . This means that the first row of S1 switching sequences (which corresponds to  $v_A^*$ ) becomes the second row in S2 switching sequences (it now

Table 4.5: Chosen switching sequences for sub-sector A of all twelve sectors.

Sector	Sub-sector	Switching sequences
<b>S1</b>	<b>A<sub>1</sub></b>	<b>325 - 352 - 355 - 364 - 607 - 688 - 689</b>
<b>S2</b>	<b>A<sub>2</sub></b>	<b>351 - 352 - 361 - 364 - 445 - 688 - 715</b>
<b>S3</b>	<b>A<sub>3</sub></b>	<b>351 - 360 - 361 - 364 - 445 - 472 - 715</b>
<b>S4</b>	<b>A<sub>4</sub></b>	<b>117 - 360 - 363 - 364 - 391 - 472 - 481</b>
S5	A <sub>5</sub>	117 - 120 - 363 - 364 - 391 - 400 - 481
S6	A <sub>6</sub>	39 - 120 - 121 - 364 - 373 - 400 - 403
S7	A <sub>7</sub>	39 - 40 - 121 - 364 - 373 - 376 - 403
S8	A <sub>8</sub>	13 - 40 - 283 - 364 - 367 - 376 - 377
S9	A <sub>9</sub>	13 - 256 - 283 - 364 - 367 - 368 - 377
S10	A <sub>10</sub>	247 - 256 - 337 - 364 - 365 - 368 - 611
S11	A <sub>11</sub>	247 - 328 - 337 - 364 - 365 - 608 - 611
S12	A <sub>12</sub>	325 - 328 - 355 - 364 - 607 - 608 - 689

corresponds to  $v_B^*$ ), etc. An illustration, which demonstrates this relationship using four first sub-sector switching sequences  $A_1$  to  $A_4$  as in Table 4.5, is shown in Figure 4.12.

Based on the pattern of how the order of those switching sequences is changing in Figure 4.12, the relationship between the switching sequences of other sectors and S1 can be further simplified. One can see that the third sector (S3) switching sequence can simply be obtained by circularly shifting the S1 switching sequence by one position. Similarly, the fourth sector (S4) switching sequence can also be obtained from the S2 switching sequence through the same method. Hence, by circularly shifting either S1 or S2 switching sequences accordingly (up to five positions), other odd or even sector switching sequences can be obtained. In general, it can be said that the odd sector switching sequences can be obtained through circularly shifting the S1 switching sequences accordingly. Similarly, the even sector switching sequences can be obtained by first changing the order of the rows of the S1 switching sequences according to the order-per-sector law, so that it becomes the S2 switching sequence, and then circularly shifting the sequences accordingly.

Since switching sequence is basically a set of chosen switching states, the previously presented relationship is also true for generating the switching states corresponding to other sectors. In other words, by mapping the odd and even sectors onto S1 and S2 the switching states of other sectors can be obtained through this sector pair mapping. The S1 and S2 are grouped as the first sector pair (SP1), S3 and S4 are grouped as the second sector pair (SP2) etc. As an example, as one can see in Figure 4.4(a), switching state 153 (012200) is projected in the fifth sector (S5) and it belongs to the third sector pair (SP3). If S5 is mapped onto S1,



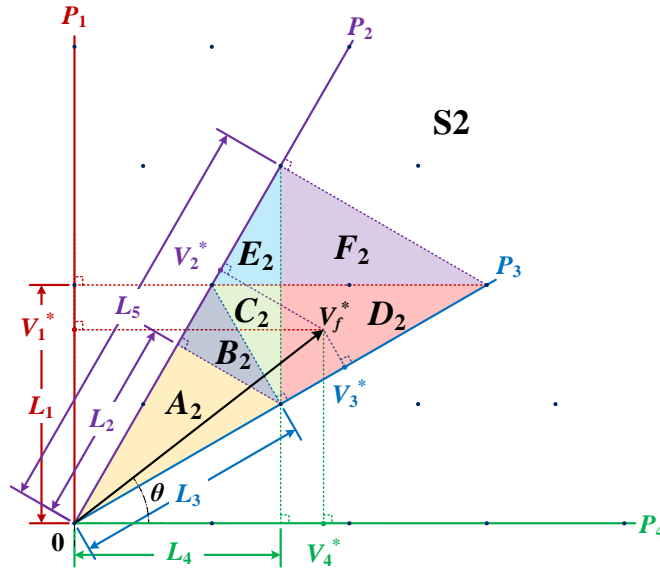


Figure 4.13: Sub-sector determination based on the location of the projected  $v_{ph}^*$  space vector in S2.

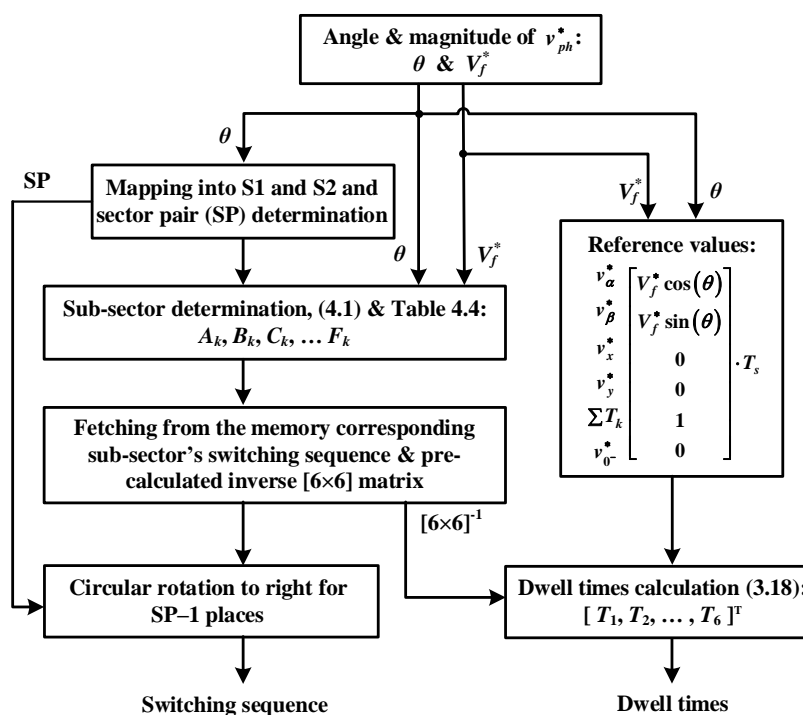
On the contrary, the projections of  $V_f^*$  in S2 will be different from those in S1 due to their dependency on the angle with respect to  $\alpha$  axis. Therefore, by mapping the odd and even sectors onto S1 and S2, one finds that the length of  $V_f^*$  projections onto their respective perpendicular axes can be generalised as:

$$\begin{aligned}
 V_i^* &= V_f^* \cos((i-2)\pi/6 - (\theta - \pi/6(k-1))) && \text{Odd sector} \\
 V_i^* &= V_f^* \cos((i-2)\pi/6 - (k\pi/6 - \theta)) && \text{Even sector}
 \end{aligned} \tag{4.1}$$

where  $k = 1, 3, 5 \dots 11$  for odd and  $k = 2, 4, 6 \dots 12$  for even sectors and  $i = 1, 2, 3, 4$ . Hence, by comparing the length of the projected  $V_f^*$  with the stated conditions in Table 4.4, the current sub-sector and its corresponding switching sequence can be accurately determined.

#### 4.3.1.8 Implementation of the presented space vector algorithm

Although the selection process of finding the optimal switching sequences is complex, the final implementation of the developed SVPWM algorithm is rather simple. By mapping the odd and even sectors onto S1 and S2 and implementing the sector pair relation, one finds that only switching sequences of S1 and S2 and their inverse matrices as in (3.18) (for dwell time calculation) are required to be stored in the memory. It should also be noted that, by simple manipulation, it is also possible to generate switching sequences of S2 and other sectors solely from S1 switching sequences.



- First, the reference voltage magnitude ( $V_f^*$ ) and angle ( $\theta$ ) of applied  $v_{ph}^*$  are determined.
- Then, the sector pair (SP) mapping and the current sub-sector in which the reference is located are obtained.
- Also, the reference values matrix for dwell times calculation is prepared based on obtained  $V_f^*$  and  $\theta$ .
- Next, the saved switching sequence and its corresponding inverse matrix are fetched from the memory based on the mapping of the current sub-sector onto S1 and S2.
- Finally, the current applied switching sequence is obtained through the circular rotation. At the same time, its corresponding applied dwell times are calculated using (3.18) based on the fetched inverse matrix and already determined reference values.

Figure 4.14: Illustration of the implementation of presented 3L6PSymSV.

Furthermore, only two components are essential for developing the modulator of the algorithm. They are: 1) the method to precisely determine the location of the reference phase voltage space vector projection and the relevant switching sequence, which is generated by mapping the corresponding sub-sector with respect to S1 and S2 sub-sectors, i.e. (4.1) and Table 4.4; and 2) the dwell time calculation of the respective switching sequences (3.18). Since the calculated dwell times are associated with the transition patterns, it is possible to use the pre-calculated inverse matrix values as in (3.18) of the switching sequences of S1 and S2. This is because the transition patterns of other sectors' switching sequences becomes identical to those from S1 and S2 after sector mapping.

In general, the implementation of the presented space vector algorithm 3L6PSymSV can be summarised as an illustration with a simple block diagram shown in Figure 4.14.

### 4.3.2 Carrier-based PWM technique

The carrier-based PWM technique, commonly used for multilevel multiphase drives, is based on in-phase disposition (PD) technique introduced in (Carrara et al., 1992) together with the application of double common mode voltage injection as in (Grandi and Loncarski, 2014, Lee et al., 2000). In addition to its capability of offering the lowest THD compared to other disposition techniques (Fukuda and Suzuki, 1997, McGrath and Holmes, 2002), the principle of how it generates its switching signals are equivalent to the SVPWM technique where  $v_{LEG}$  levels increase in the first half of the switching period and decrease in the other half (Wang, 2002). Therefore, the implementation of PD together with double common mode voltage injection yields the same results as SVPWM technique as demonstrated for three-phase, five-phase and seven-phase three-level case (Dordevic et al., 2013a, Dordevic et al., 2013b, McGrath et al., 2003).

Nevertheless, in case of a symmetrical six-phase machine, there is a symmetry of the sinusoidal  $v_{ph}^*$  waveforms (see Figure 3.4) and thus the application of double common mode voltage injection is not possible. More precisely, the application of common mode voltage (as in two-level case) or double common mode voltage injection will not change the shape of  $v_{ph}^*$  waveforms. As a result, only PD technique without any injection i.e. PDSin is implemented for the analysed drive topology. Therefore, the reference  $v_{ph}$  waveforms of PDSin ( $v_{ph,PDSin}^*$ ) at  $m_i = 1$  are identical to the desired  $v_{ph}^*$  waveforms shown in Figure 3.4. Note that the maximum achievable  $m_i$  for PDSin is  $m_{i,max} = 1$ , which is identical to 3L6PSymSV.

### 4.3.3 Simulation and experimental results

The PWM modulators of the presented 3L6PSymSV and PDSin are developed and verified through simulation in Matlab/Simulink on the model of the symmetrical six-phase machine with parameters as in Table 3.2. The machine's rated frequency is 50 Hz and the chosen  $V_f^*$  is 100 V (which, according to (3.19), corresponds to  $m_i = 1$  since  $V_{dc} = 200$  V). The simulations are run for full linear range of  $m_i$  (from 0.1 to 1) with 0.05 increments in open loop with unloaded machine. The simulation time is set to a large enough value so that the machine reaches steady state. Using (3.20), the phase voltage (THD<sub>v</sub>) and phase current (THD<sub>i</sub>) total harmonic distortions are calculated from the first  $h$  harmonics, up to value of  $h$  that corresponds to 21 kHz, i.e. the first ten sidebands.

The developed modulation techniques are also validated further through experimental testing. A real-time platform dSpace ds1006 is used and the modulation techniques are

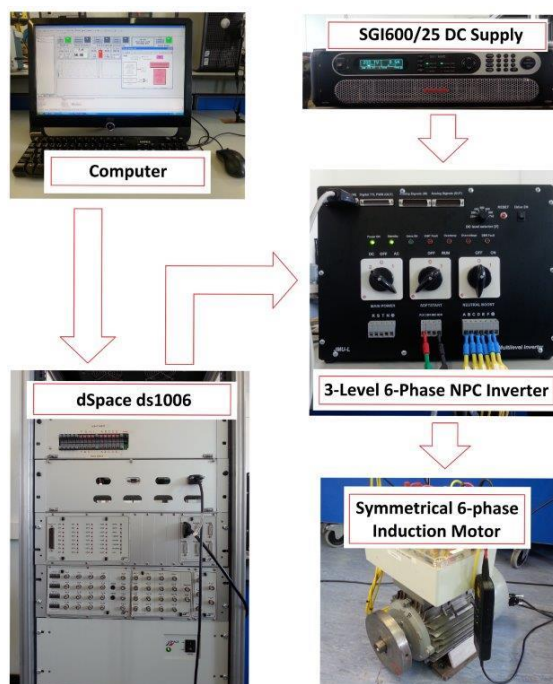


Figure 4.15: Experimental setup of three-level symmetrical six-phase drive.

programmed using Matlab/Simulink. The experimental setup is shown in Figure 4.15. Detail description of the setup is presented in Appendix B. The dc-bus voltage is set to  $V_{dc} = 200$  V using Sorensen SGI 600/25 external dc supply. There is no load attached to the machine. The machine is driven using a custom made three-level six-phase NPC inverter switching at  $f_s = 2$  kHz. The inverter dead time is  $6 \mu\text{s}$  and it is not compensated. The modulation techniques are validated in open loop for full linear range of  $m_i$ .

The reconstructed  $v_{LEG}^*$  ( $v_{LEG,rec}^*$ ) waveforms of 3L6PSymSV at  $m_i = 1$  are shown in Figure 4.16. It should be noted that  $v_{LEG,rec}^*$  are not part of space vector algorithm and they can be obtained from the product of the applied switching sequence and its calculated dwell times. However,  $v_{LEG,rec}^*$  waveforms are useful for visual comparison with carrier-based methods. As one might expect, the  $v_{LEG,rec}^*$  waveforms are identical to  $v_{ph}^*$  waveforms (see Figure 3.4). In addition, one can also obtain the reconstructed  $v_{ph}^*$  ( $v_{ph,rec}^*$ ) waveforms from (3.3). Since CMV is a scalar value and does not affect the shape of  $v_{LEG,rec}^*$  waveforms, the  $v_{ph,rec}^*$  waveforms are also sinusoidal and identical to  $v_{LEG,rec}^*$  waveforms, Figure 4.16. The amplitude of the  $v_{ph,rec}^*$  waveforms is equal to half of  $V_{dc}$ , which is in agreement with (3.19) at  $m_i = 1$ .

In Figure 4.17 and 4.18, simulation results of the phase ‘a’ voltage, phase voltage components ( $v_a$ ,  $v_\beta$ ,  $v_x$ ,  $v_y$ ,  $v_0^+$  and  $v_0^-$ ) and phase ‘a’ current waveforms (including their corresponding spectra) of the machine driven by an ideal inverter, for the 3L6PSymSV and

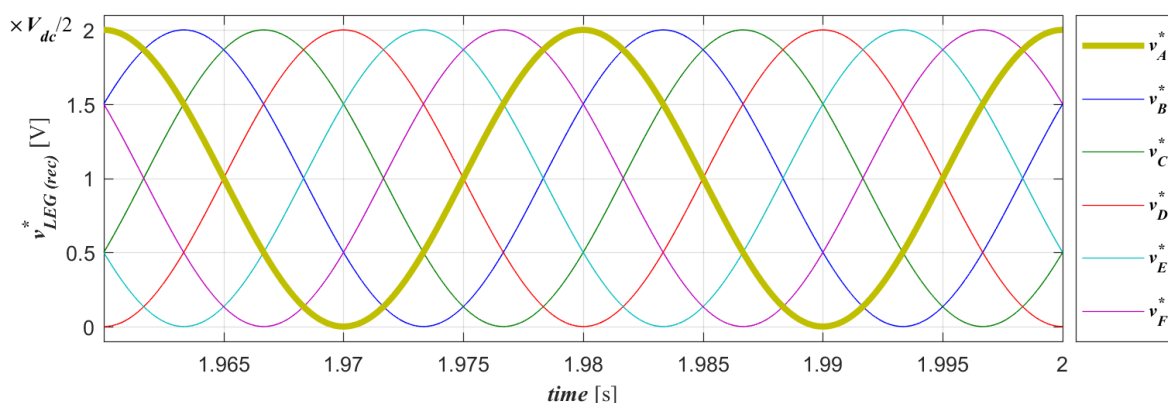


Figure 4.16: Reconstructed reference leg voltage  $v_{LEG,rec}^*$  (i.e. phase voltage  $v_{ph,rec}^*$ ) waveforms of 3L6PSymSV at  $m_i = 1$ .

PDSin, are shown. By observation of the timing waveforms and spectra one can see that both modulation techniques yield identical results. The obtained fundamental phase ‘a’ voltage ( $|v_a|_{fund}$ ) is in agreement with (3.19), with  $|v_a|_{fund} = 99.99$  V i.e. half of  $V_{dc}$ , at used value of  $m_i = 1$ . Moreover, since  $x$ ,  $y$  and  $0^-$  axes components are controlled to zero in the developed 3L6PSymSV, as one might expect, the magnitudes of low-order harmonics which correspond to  $x$ ,  $y$  and  $0^-$  axes, are practically negligible when compared to  $|v_a|_{fund}$ . Therefore, this also results in having negligible corresponding low-order harmonics in phase ‘a’ voltage and current waveforms.

For the sake of investigation of the dead-time effect, the simulations were also repeated with taking into account dead-time of  $6 \mu\text{s}$  (which corresponds to the experimental setup). Both modulation techniques again yielded identical results. The obtained  $|v_a|_{fund}$  was slightly lower than the one in ideal case, and the magnitude of the 3<sup>rd</sup> harmonic has also increased slightly, which are known and expected effects of the dead time. The obtain simulation results i.e. phase ‘a’ voltage, its components ( $v_{\alpha}$ ,  $v_{\beta}$ ,  $v_x$ ,  $v_y$ ,  $v_{0^+}$  and  $v_{0^-}$ ) and phase ‘a’ current waveforms (including their spectra) for 3L6PSymSV and PDSin, are shown in Figure 4.19 and 4.20, respectively. One can clearly see that the magnitude of the third harmonic has slightly increased in phase voltage spectra and more apparently in the current spectra, when compared to the ideal case.

The measured phase ‘a’ leg voltage, phase voltage and current waveforms (labelled as  $V_A$ ,  $V_a$  and  $i_a$ , respectively, in the oscilloscope screen captures) and corresponding spectra when  $m_i = 0.4$  and  $m_i = 1$  for both modulation techniques are shown in Figure 4.21 and 4.22, respectively. Clearly, both modulation techniques yield the same results. One can see that  $|v_a|_{fund}$  obtained using the developed 3L6PSymSV is very close to  $V_f^*$ , i.e. 40 V and 100 V, as

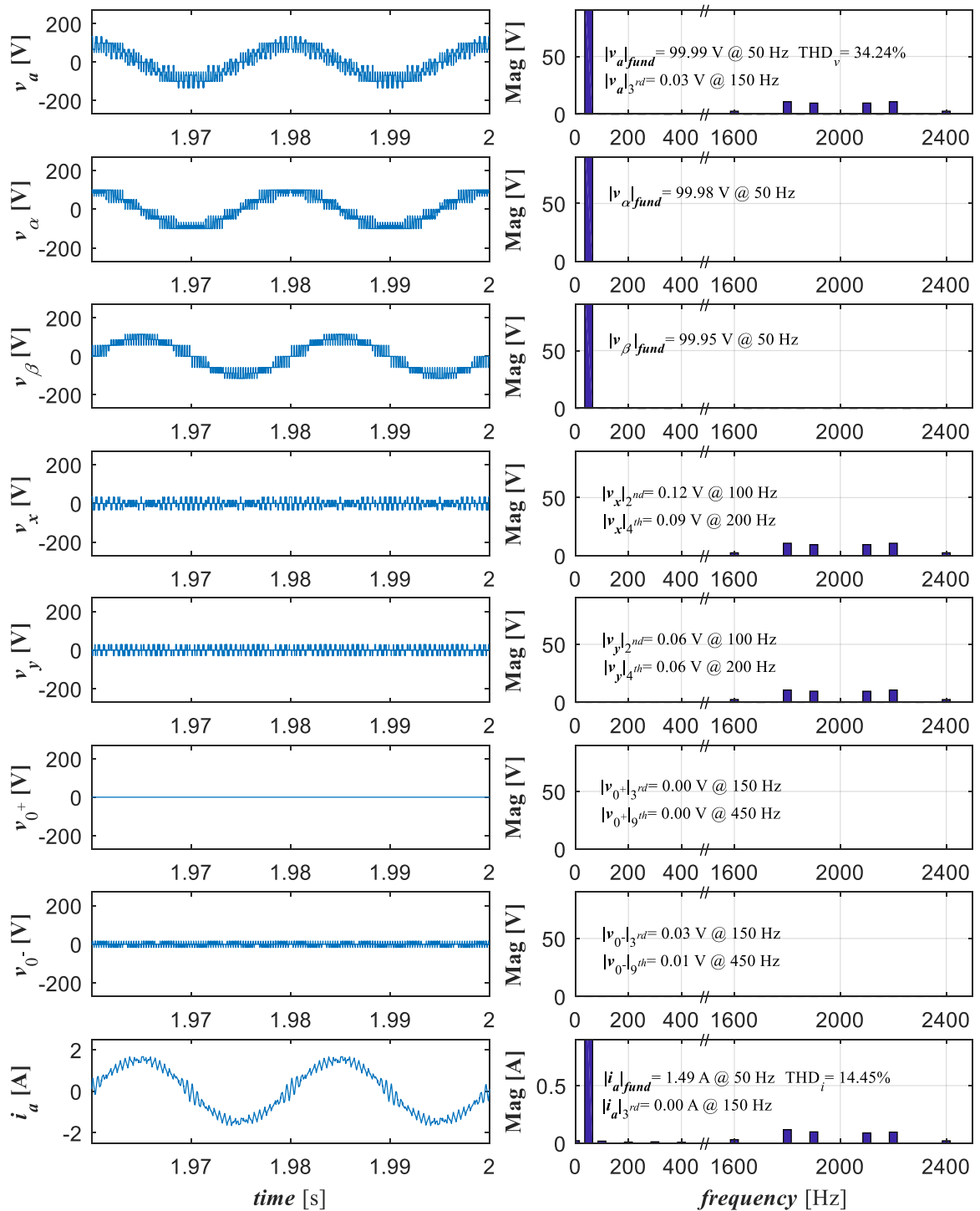


Figure 4.17: Phase 'a' voltage, phase voltage components ( $v_\alpha$ ,  $v_\beta$ ,  $v_x$ ,  $v_y$ ,  $v_{0+}$  and  $v_{0-}$ ), phase 'a' current and corresponding spectra of 3L6PSymSV for the machine driven by an ideal inverter

at  $m_i = 1$ .

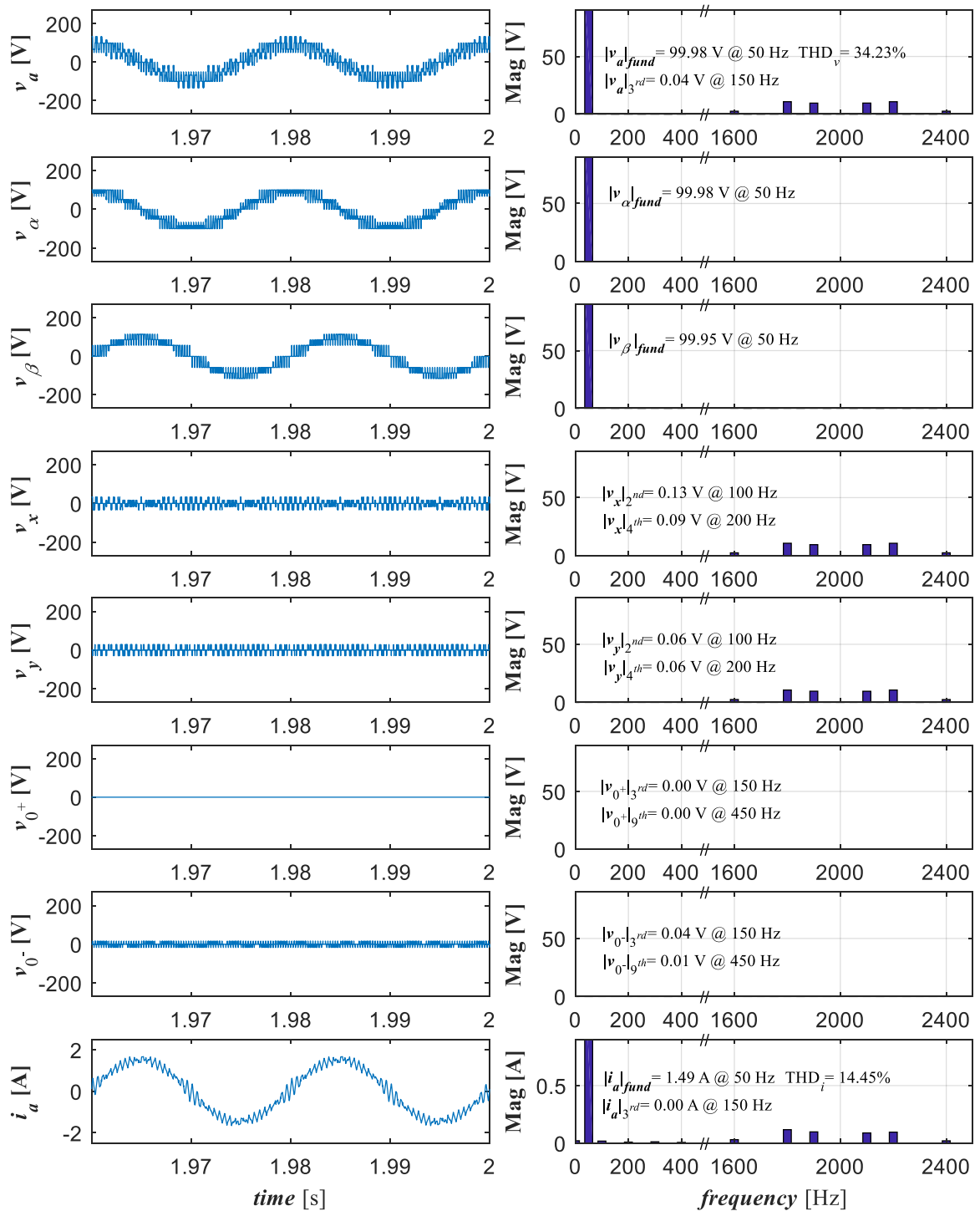


Figure 4.18: Phase ‘a’ voltage, phase voltage components ( $v_\alpha$ ,  $v_\beta$ ,  $v_x$ ,  $v_y$ ,  $v_{0+}$  and  $v_{0-}$ ), phase ‘a’ current and corresponding spectra of PDSin for the machine driven by an ideal inverter at  $m_i = 1$ .

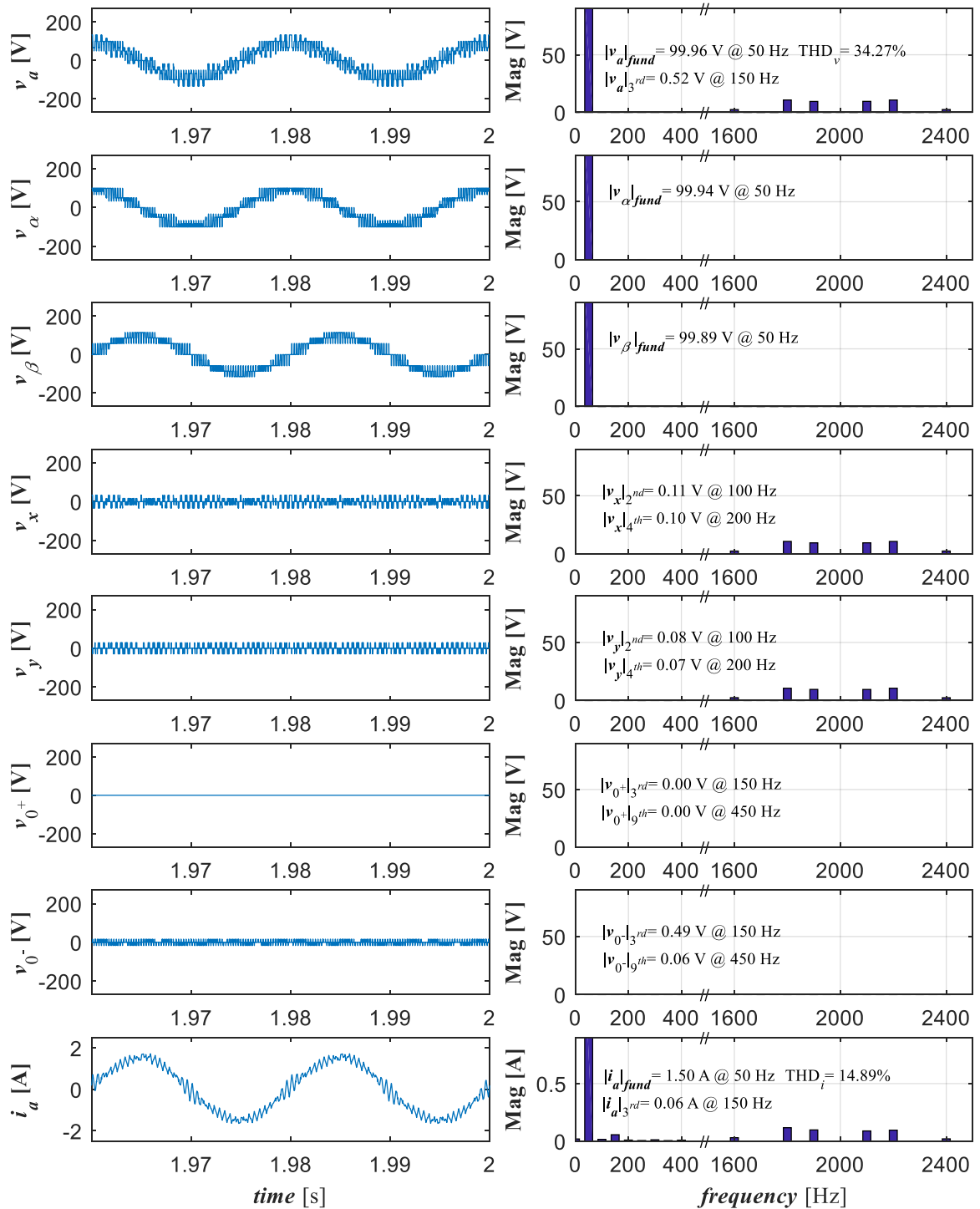


Figure 4.19: Phase 'a' voltage, phase voltage components ( $v_{\alpha}$ ,  $v_{\beta}$ ,  $v_x$ ,  $v_y$ ,  $v_0^+$  and  $v_0^-$ ), phase 'a' current and corresponding spectra of 3L6PSymSV for the machine driven by inverter with built-in dead time at  $m_i = 1$ .

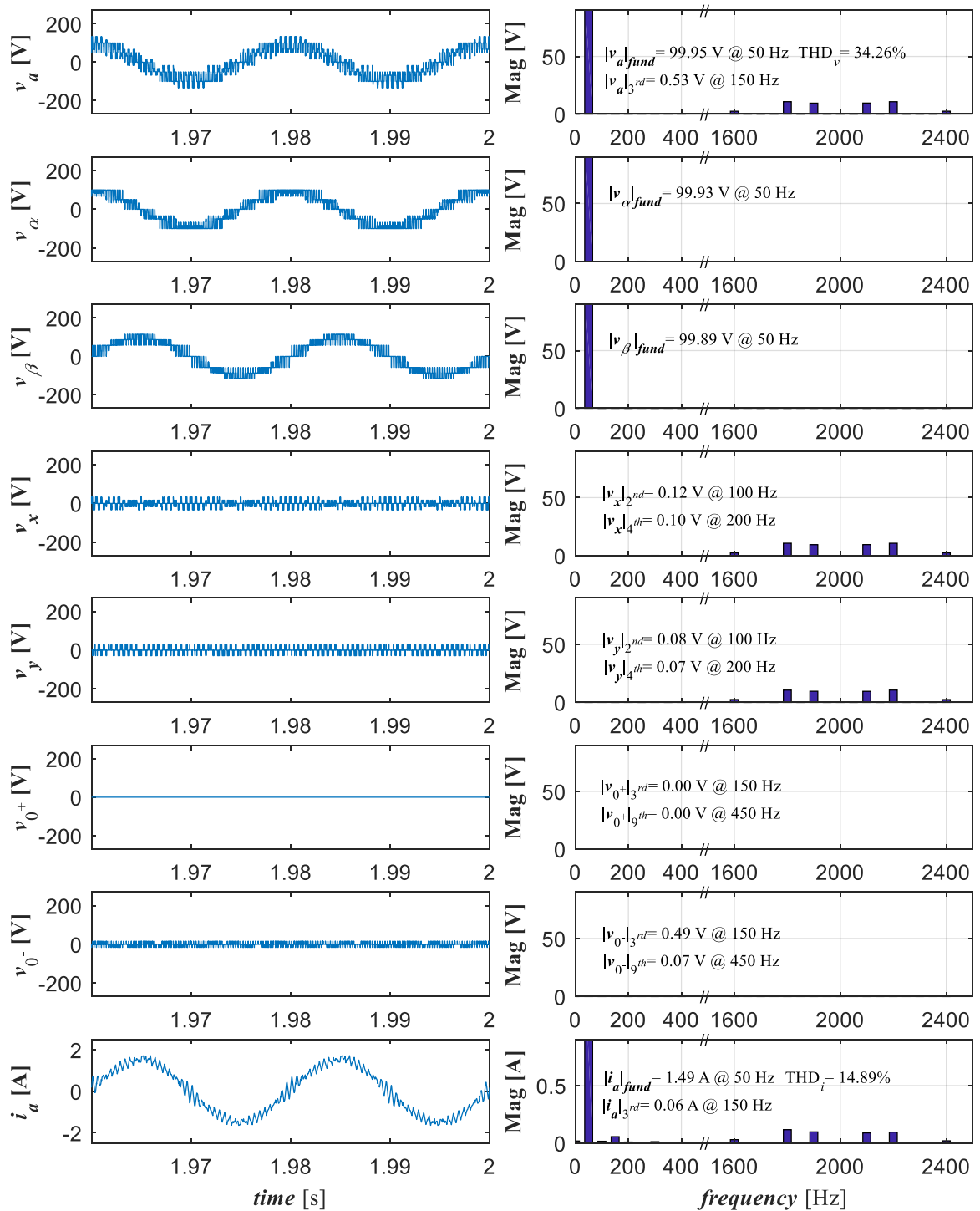


Figure 4.20: Phase 'a' voltage, phase voltage components ( $v_a$ ,  $v_\beta$ ,  $v_x$ ,  $v_y$ ,  $v_0^+$  and  $v_0^-$ ), phase 'a' current and corresponding spectra of PDSin for the machine driven by inverter with built-in dead time at  $m_i = 1$ .

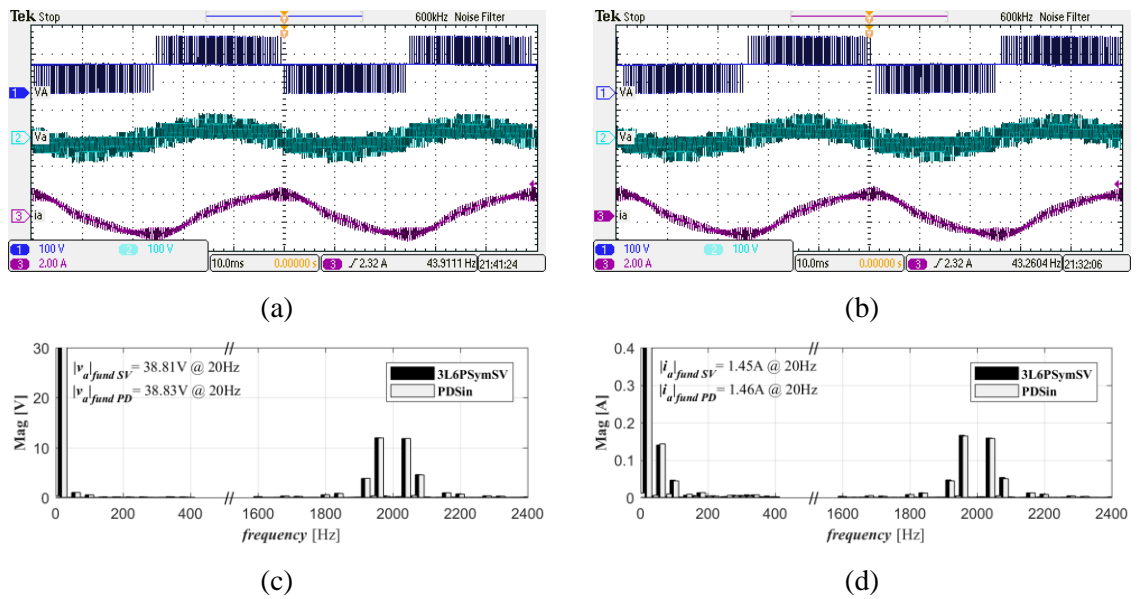


Figure 4.21: Oscilloscope capture of phase ‘a’ leg and phase voltage and current at  $m_i=0.4$  for (a) 3L6PSymSV, (b) PDSin, with corresponding (c) voltage and (d) current spectra.

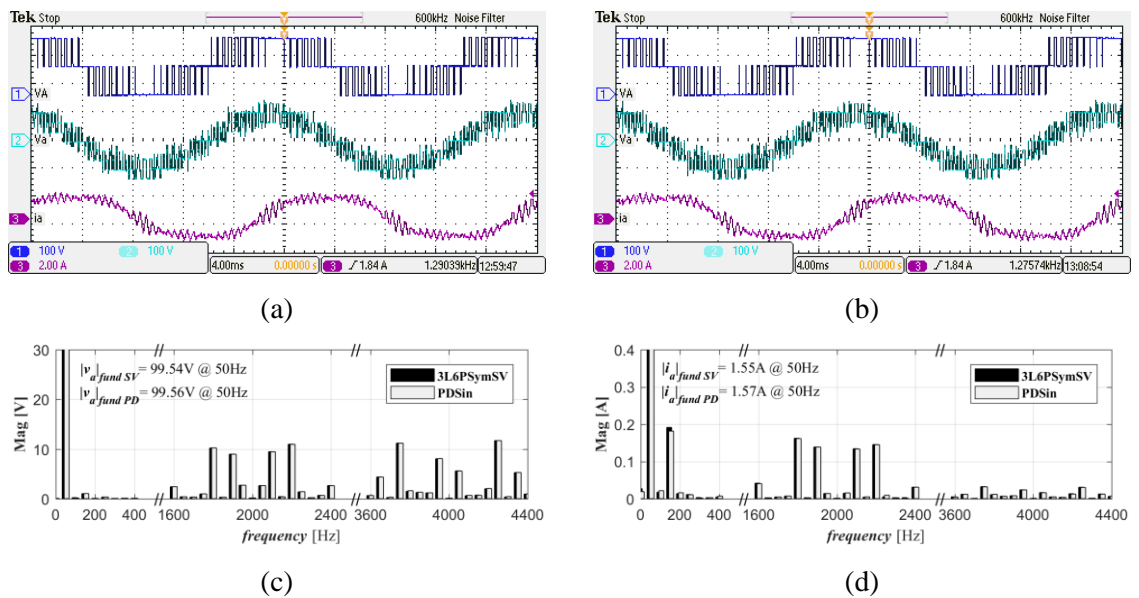


Figure 4.22: Oscilloscope capture of phase ‘a’ leg and phase voltage and current at  $m_i=1$  for (a) 3L6PSymSV, (b) PDSin, with corresponding (c) voltage and (d) current spectra.

shown in Figure 4.21(c) and 4.22(c), respectively. In addition, one can also see that the influence of the dead time on the value of the fundamental is more pronounced in the lower modulation index region, as there are more switching periods within a fundamental period. Recall that the inverter dead time is not compensated at all.

Furthermore, although it can be seen that the low order harmonics are present in both phase voltage and current harmonic spectra, they are relatively small. Ideally, the low order harmonics should not exist. In reality, this is not the case. The dominant low order harmonics are the 3<sup>rd</sup>, 5<sup>th</sup> and 9<sup>th</sup> harmonics. This is expected since the dead time is not compensated and it leads to the appearance of low order odd harmonics in  $v_{ph}$  waveform (Jeong and Park, 1991, Jones et al., 2009a). Moreover, the largest odd harmonic caused by the dead time, the 3<sup>rd</sup> harmonic, is mapped onto the 0° axis where the impedance is very low. This is because it consists of only stator resistance and leakage inductance while the impedance in the  $\alpha$ - $\beta$  plane, where the 5<sup>th</sup> harmonic maps is much higher. As a result, this contributes to larger 3<sup>rd</sup> harmonic in stator current, as can be seen from the phase current harmonic spectra (see Figure 4.21(d) and 4.22(d)). However, it should be noted that the difference of these low order harmonics (in terms of magnitude) between the simulation and experimental results is due to the influence of non-adequate parameter estimation of the used machine.

#### 4.4 Drive with two isolated neutral points configuration

In this section, PWM techniques for three-level symmetrical six-phase drive with two isolated neutral points configuration are presented. Due to isolation of the neutral points, each winding set can be controlled independently by using two identical three-phase PWM modulators which are developed based on the established space vector algorithm and carrier-based technique for three-level three-phase drives. The PWM techniques are verified through simulation in Matlab/Simulink and validated through laboratory experiment.

##### 4.4.1 Space vector PWM algorithm

Although the neutral point configuration is changed, the numbers of possible switching states and  $v_{ph}$  space vectors remain the same, i.e. 729 and 665, respectively. This is because they are only dependent on the topology of the inverter itself. However, in case of the drive with two isolated neutral points, the VSD transformation matrix becomes as in (3.21). The two zero sequence axes are now denoted as  $0_1$  and  $0_2$ , where the sub-script indicates the winding set they are representing. The projections of  $v_{ph}$  space vectors onto these axes are shown in

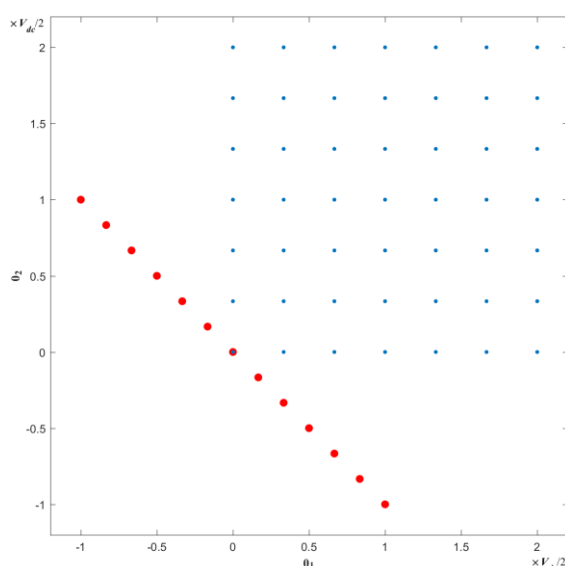


Figure 4.23: Projection of  $v_{LEG}$  and  $v_{ph}$  space vectors of the analysed three-level symmetrical six-phase drive with two isolated neutral points in the  $0_1$ - $0_2$  plane.

Figure 4.23. Note that the projections into the other planes ( $\alpha$ - $\beta$  and  $x$ - $y$ ) remain as in Figure 4.3, i.e. 4.4. Further, each zero axis also represents CMV of the corresponding winding set. Consequently, the low order harmonics of the order of  $3k$  ( $k = 1, 3, 5 \dots$ ) ideally will not exist.

Still, due to the isolation of the neutral points, each stator winding set can be controlled independently using dual three-level three-phase space vector PWM modulators (D3L3PSV). However, the reference waveforms between the two modulators should be spatially shifted by  $60^\circ$ . The modulators are developed based on space vector algorithm presented in (McGrath et al., 2003) and the maximum achievable  $m_i$  for linear range operation is 1.154 (which is the same as for three-phase case).

#### 4.4.2 Carrier-based PWM technique

The same idea also applies to the carrier-based PWM technique. The winding sets are also controlled separately using dual three-level three-phase modulators. The modulators are developed based on (Grandi and Loncarski, 2014, Lee et al., 2000) where three-phase  $v_{ph}^*$  waveforms with double common mode voltage injection are compared to carrier waveforms based on PD technique (D3P2CMI). However, the reference waveforms of the modulators are spatially shifted by  $60^\circ$ . The  $v_{ph}^*$  waveforms of these modulators ( $v_{ph,D3P2CMI}^*$ ) at  $m_i = 1$  are shown in Figure 4.24. The maximum achievable  $m_i$  for linear range operation of D3P2CMI is also 1.154.

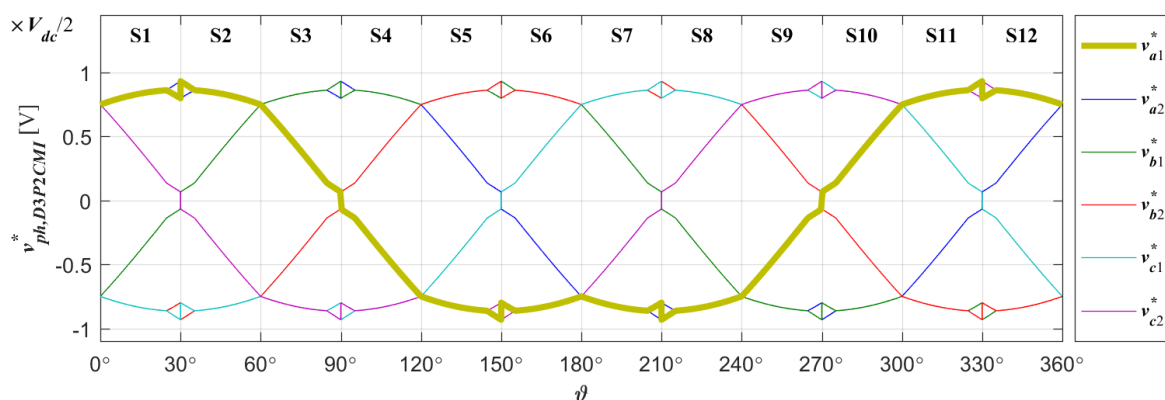


Figure 4.24: Sinusoidal reference phase voltage waveforms with dual double common mode voltage injection ( $v_{ph,D3P2CMI}^*$ ) for three-level symmetrical six-phase drive at  $m_i = 1$ .

### 4.4.3 Simulation and experimental results

Based on the D3L3PSV and D3P2CMI, two sets of PWM modulators are developed and verified through simulation in Matlab/Simulink. In addition, they are validated further in laboratory experiments for the full linear range of  $m_i$ , from  $m_i = 0.1$  to  $m_i = 1.154$ , with 0.05 increment. The same setup as in the single neutral point configuration is used.

The  $v_{LEG,rec}^*$  waveforms of D3L3PSV at  $m_i = 1$  are shown in Figure 4.25. As one might expect, the obtained  $v_{LEG,rec}^*$  waveforms are identical to  $v_{ph,D3P2CMI}^*$  waveforms shown in Figure 4.24. Also, the  $v_{ph,rec}^*$  waveforms, obtained from (3.6), are shown in Figure 4.26. Clearly, the obtained waveforms are sinusoidal. Meanwhile, the simulation results of D3L3PSV (phase ‘ $a_1$ ’ voltage, phase voltage components ( $v_\alpha, v_\beta, v_x, v_y, v_{01}$  and  $v_{02}$ ) and phase ‘ $a_1$ ’ current waveforms as well as their corresponding spectra) when the machine is driven by the ideal

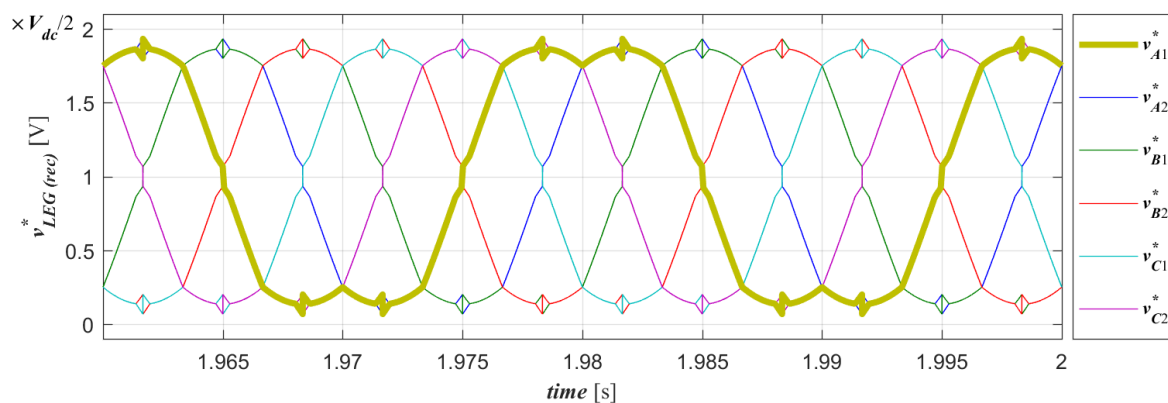


Figure 4.25: Reconstructed reference output leg voltage ( $v_{LEG,rec}^*$ ) waveforms of D3L3PSV at  $m_i = 1$ .

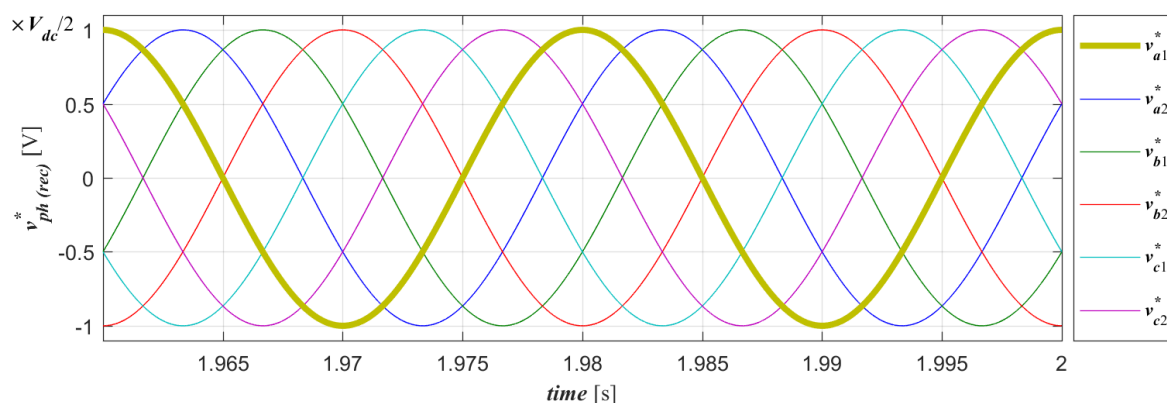


Figure 4.26: Reconstructed reference output phase voltage ( $v_{ph,rec}^*$ ) waveforms of D3L3PSV at  $m_i = 1$ .

inverter are shown in Figure 4.27. As for the results of D3P2CMI, they are shown in Figure 4.28. Clearly, both results are, as expected, identical. Once again, the influence of the dead time was examined. So, the simulations were repeated with dead time included. Both modulation techniques still performed the same and the effects were as before.

The oscilloscope captures of phase ‘ $a_1$ ’ leg voltage, phase voltage and current waveforms, as well as their corresponding spectra for D3L3PSV and D3P2CMI, when  $m_i = 0.4$  and  $m_i = 1$ , are shown in Figure 4.29 and 4.30, respectively. Not only that the waveforms for both modulation techniques are identical, even their fundamental phase voltage and current are practically the same. The magnitudes of the measured fundamental phase voltage ( $|v_{a1}|_{fund}$ ), for both modulation methods, are very close to the expected values of 40 V and 100 V, for  $m_i = 0.4$  and  $m_i = 1$ , respectively. Finally, as the consequence of uncompensated dead time the low order odd harmonics can be observed. However, they are of very low value in both phase voltage and current spectra.

Unlike in single neutral point case, the third voltage harmonic which maps into  $0_1$ - $0_2$  plane theoretically does not exist, since this plane now represents CMVs of the winding sets. Moreover, the third current harmonic is simply unable to flow between the two winding set due to the absence of the connection between the neutral points. As a result, the magnitudes of the third voltage and current harmonics are significantly lower in this case as can be seen in Figure 4.29(c)-(d) and 4.30(c)-(d) when compared to Figure 4.21(c)-(d) and 4.22(c)-(d).

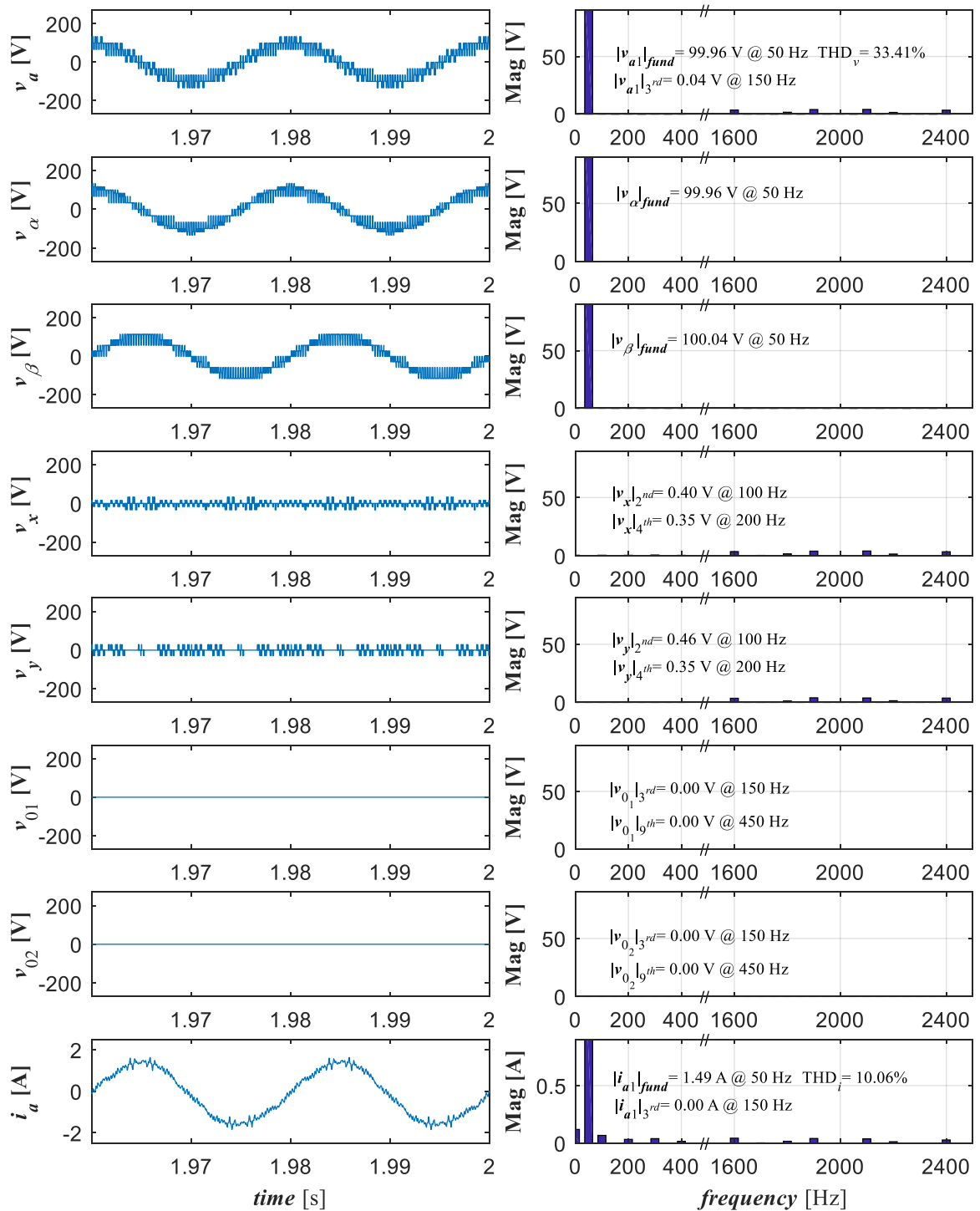


Figure 4.27: Phase ‘ $a_1$ ’ voltage, phase voltage components ( $v_a$ ,  $v_\beta$ ,  $v_x$ ,  $v_y$ ,  $v_{01}$  and  $v_{02}$ ), phase ‘ $a_1$ ’ current and corresponding spectra of D3L3PSV for the machine driven by ideal inverter at  $m_i = 1$ .

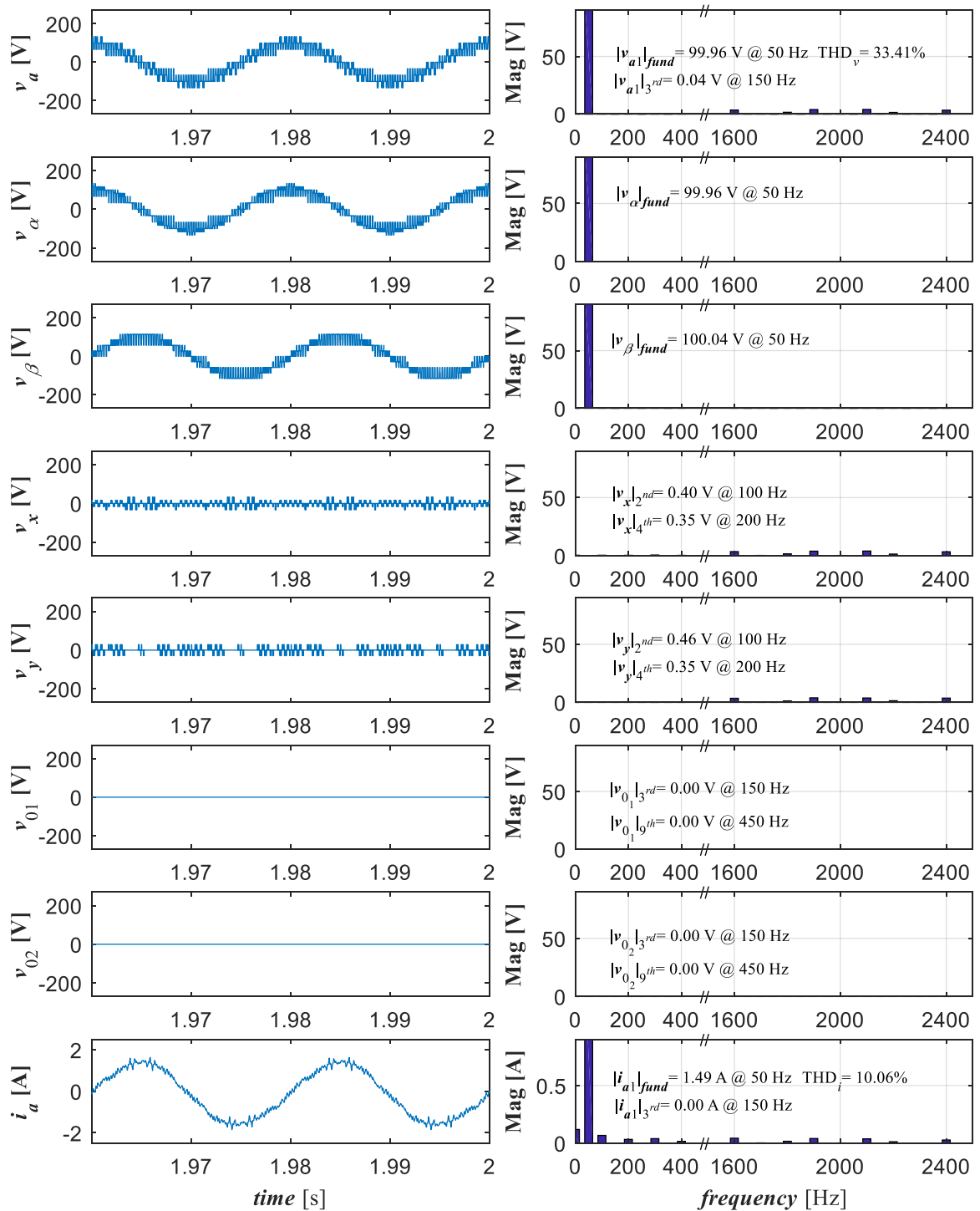


Figure 4.28: Phase 'a1' voltage, phase voltage components ( $v_a$ ,  $v_{\beta}$ ,  $v_x$ ,  $v_y$ ,  $v_{01}$  and  $v_{02}$ ), phase 'a1' current and corresponding spectra of D3P2CMI for the machine driven by ideal inverter at  $m_i = 1$ .

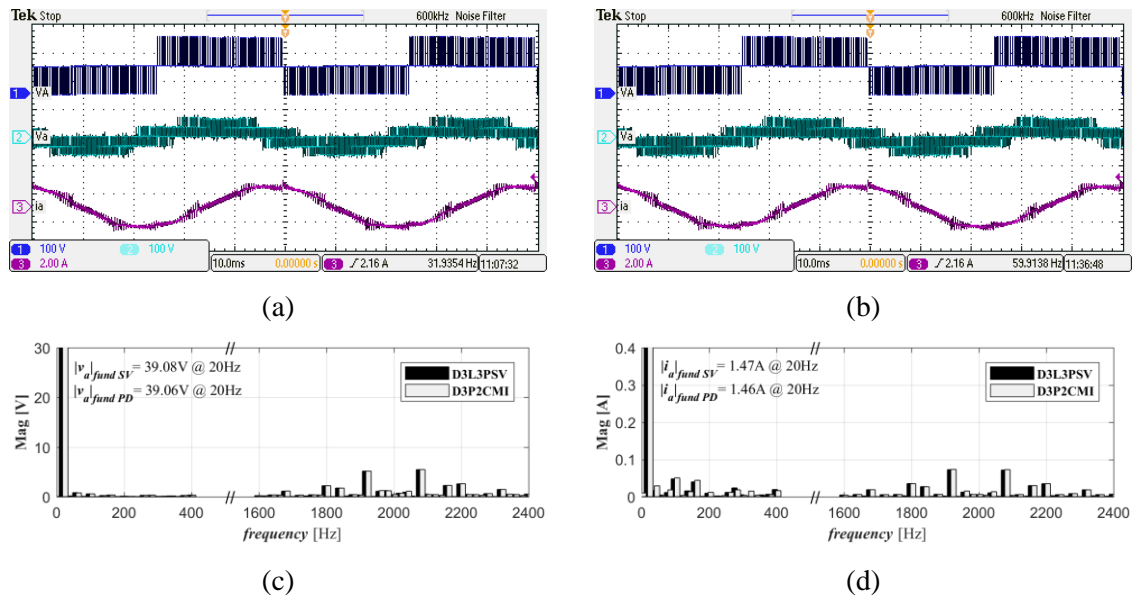


Figure 4.29: Oscilloscope capture of phase ‘ $a_1$ ’ leg and phase voltage and current at  $m_i=0.4$  for (a) D3L3PSV, (b) D3P2CMI, with corresponding (c) voltage and (d) current spectra.

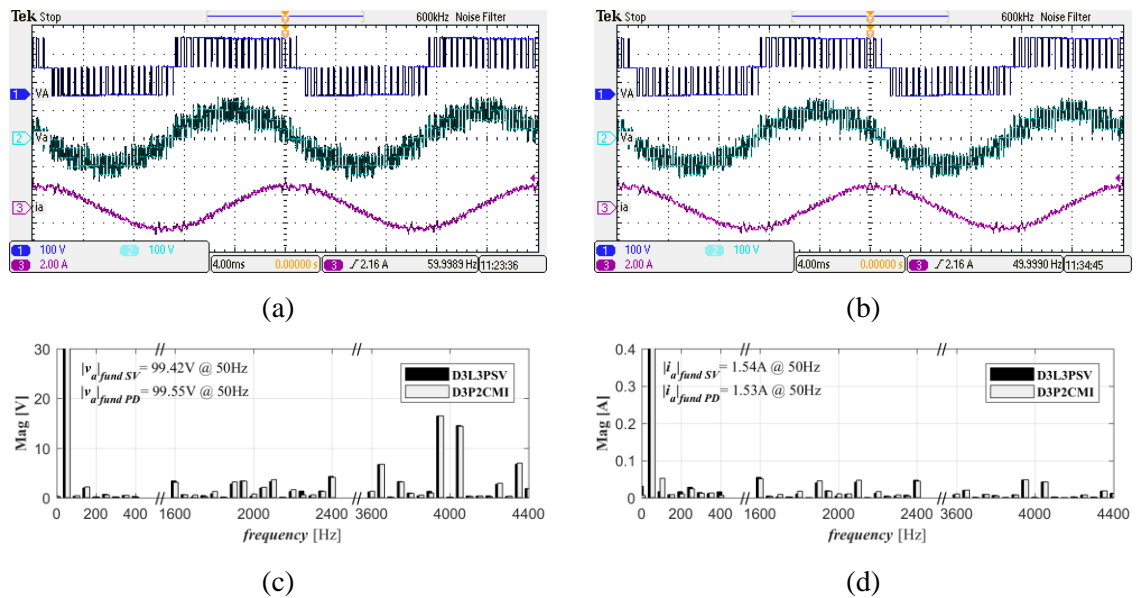


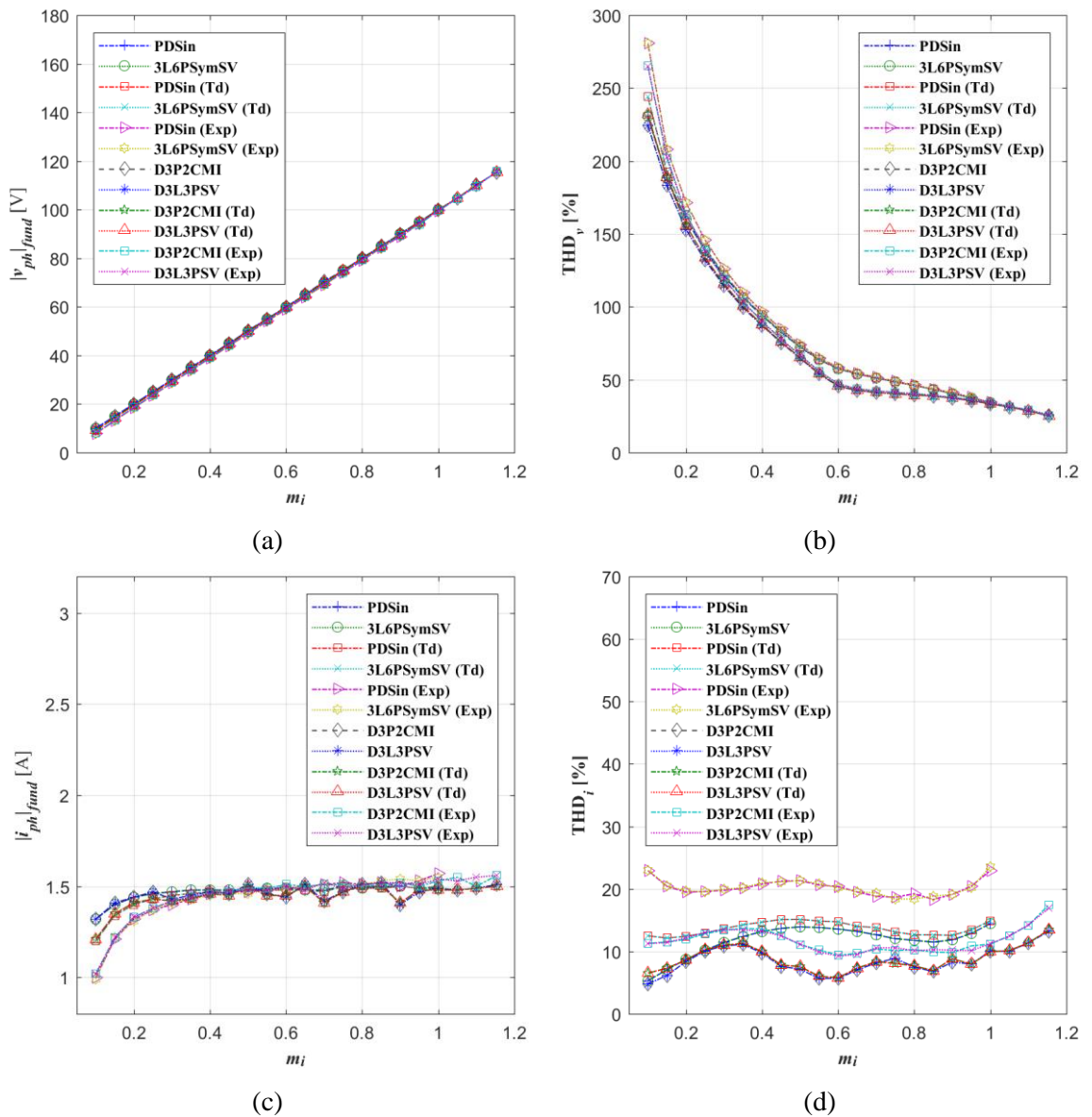
Figure 4.30: Oscilloscope capture of phase ‘ $a_1$ ’ leg and phase voltage and current at  $m_i=1$  for (a) D3L3PSV, (b) D3P2CMI, with corresponding (c) voltage and (d) current spectra.

#### 4.5 Performance comparison between the modulation techniques of both neutral point configurations

The magnitudes of the obtained fundamental output phase voltage ( $|v_{ph}|_{fund}$ ), output phase current ( $|i_{ph}|_{fund}$ ), the calculated  $THD_v$  and  $THD_i$  for full linear range of  $m_i$  of all presented modulation strategies are shown in Figure 4.31. One can see that the obtained  $|v_{ph}|_{fund}$  increases linearly with respect to  $m_i$ , in agreement with (3.19) and hence proving the validity of the presented modulation techniques (see Figure 4.31(a)). As for the obtained  $|i_{ph}|_{fund}$ , they are essentially constant throughout full linear range of  $m_i$  since constant  $V/f$  control is used (see Figure 4.31(c)). However, the lower  $|i_{ph}|_{fund}$  at low value of  $m_i$  is the consequences of not boosting the voltage to compensate the voltage drop across the stator resistance.

The  $THD_v$  and  $THD_i$  of all presented modulation techniques are calculated using (3.21). One can see that both space vector algorithm and carrier-based approach, either for single or two isolated neutral points, have yielded the identical  $THD_v$  and  $THD_i$  characteristics. In fact, the  $THD_v$  characteristic for the single neutral point case is in agreement with the analytically calculated  $THD_v$  presented in (Dordevic et al., 2015). On the other hand, although the space vector algorithm and carrier-based approach produce identical  $THD_i$  characteristics, the  $THD_i$  from the experimental results shows much higher values compared to  $THD_i$  obtained from the simulation (see Figure 4.31(d)). However, it can be seen that the shapes of both  $THD_i$  curves are similar and the experimental ones appear as having a vertical, almost constant shift with respect to the simulation ones. The difference between them is due to the assumption made in the development of the machine model where the rotor leakage inductance is assumed constant for all switching harmonics, while, in reality, this is not the case (Jones et al., 2011). In terms of the performance between the drive with single and two isolated neutral points, one can clearly see from the  $THD_v$  and  $THD_i$  curves that the performance of the latter is better than the former. Additionally, the drive with two isolated neutral points offers higher dc-bus utilisation, by 15.4%, than the drive with single neutral point configuration.

Last but not least, all presented modulation techniques are also compared in terms of the duration it takes to execute each modulation technique. The execution time is measured using dSpace Profiler Tool and the values are listed in Table 4.6. One can see that the execution time of the PDSin is significantly shorter than 3L6PSymSV, which is expected. Although the switching sequences and pre-calculated inverse matrices of S1 and S2 are stored in the memory, the calculation of dwell times and complexity in determining the corresponding sub-sector are still required in 3L6PSymSV, while in PDSin only comparison between the reference and



Applied PWM techniques for single neutral point case:

PDSin	PD sinusoidal PWM
3L6PSymSV	Space vector algorithm using time matrix approach

Applied PWM techniques for two neutral points case:

D3P2CMI	PD with double common mode voltage injection (dual three-phase modulators)
D3L3PSV	Three-level three-phase space vector algorithm (dual modulators)

Note: Td – denotes that the inverter dead-time is considered in the simulation  
 Exp – denotes experiment results

Figure 4.31: The performance of applied modulation strategies for full linear range of  $m_i$  based on:

(a) obtained  $|v_{ph}|_{fund}$  (b) calculated  $THD_v$  (c) obtained  $|i_{ph}|_{fund}$  and (d) calculated  $THD_i$ .

Table 4.6: Execution time of the applied modulation techniques.

Modulation techniques	Neutral point configuration	
	Single	Two
3L6PSymSV	3.92 $\mu$ s	-
PDSin	0.61 $\mu$ s	-
D3L3PSV	-	2.36 $\mu$ s
D3P2CMI	-	1.17 $\mu$ s

carrier waveforms is required. Hence the large difference in the execution time.

On the contrary, the difference of the execution time between the D3L3PSV and D3P2CMI is relatively small. This is because, in addition to having a lower number of switching sequences and pre-calculated inverse matrices than 3L6PSymSV, the size of each switching sequence and pre-calculated inverse matrices are reduced by half. Furthermore, the calculation of dwell times and the process to determine the corresponding sub-sector are also much simpler, hence resulting in lower execution time. Regarding D3P2CMI, the reference waveforms now have to go through two additional processes, i.e. double common mode injection. Hence, when compared to the purely sinusoidal waveforms in PDSin, the execution time is increased. As a result, the difference in the execution time between D3L3PSV and D3P2CMI becomes smaller.

#### 4.6 Summary

In this chapter, different modulation techniques based on the space vector algorithm and carrier-based approach for three-level symmetrical six-phase drive with single and two isolated neutral points configurations are presented. The emphasis is placed on the process of developing the new space vector algorithm for the three-level symmetrical six-phase drives with single neutral point configuration (3L6PSymSV).

In 3L6PSymSV, due to a large number of possible switching states, the order-per-sector law is implemented to eliminate any unnecessary space vector and hence significantly reduce their number. Therefore, it becomes feasible to analyse and choose potential switching sequences. By categorising the chosen potential switching sequences based on the transition patterns in all three planes, the switching sequences can be narrowed down further using graphical analysis of the transition patterns. Thus, only six switching sequences (which also

correspond to six sub-sectors) are left per sector. Finally, by accurately determining the location of applied reference space vector in  $\alpha$ - $\beta$  plane, the exact switching sequence can be applied. As a result, sinusoidal  $v_{ph}$  waveforms are realised.

The presented modulation techniques are verified in simulation using Matlab/Simulink and also validated in experimental testing in open loop speed controlled induction machine for the full linear range of  $m_i$ . Obtained simulation and experimental results show that the space vector algorithm based modulation techniques yield identical performance as their carrier-based equivalents. It can be noted that this is the first time that this equivalence is experimentally proved for symmetrical six-phase drive supplied by a three-level inverter case. The topology is analysed when single and two isolated neutral points are present.

Nevertheless, it is shown that D3L3PSV and D3P2CMI give better performance when compared to 3L6PSymSV and PDSin. The better performance is largely influenced by the significant reduction of the low order harmonics, particularly the third harmonic due to the absence of neutral point connection between the neutrals of the two winding sets. Moreover, by controlling the two winding sets separately using dual three-level three-phase PWM modulators, the dc-bus voltage utilisation is increased by 15.4%. Last but not least, if one only desires to use PWM technique and does not concern about the details regarding the modulation technique itself, PWM technique based on carrier based approach (e.g. D3P2CMI) is recommended. Besides, it is much simpler to implement compared to the one based on space vector approach.



---

## CHAPTER 5

### PWM techniques for two-level asymmetrical six-phase drives

---

#### 5.1 Introduction

In this chapter, space vector and carrier-based PWM techniques for two-level asymmetrical six-phase drives are presented. Special attention is paid to the development of a new space vector algorithm for a drive with a single neutral point configuration. The algorithm proposes a modified VSD transformation matrix where the rotational transformation is applied onto the  $0^+-0^-$  planes. The developed space vector algorithm is verified through simulations using PLECS software. Finally yet importantly, the performance of all presented PWM techniques is compared and the results are presented at the end of this chapter.

Original contributions from this chapter, particularly sub-section 5.3.1, where modification of VSD matrix is proposed for single neutral point case. As a result, a conference paper presenting new space vector algorithm has been published in (Engku Ariff et al., 2018).

#### 5.2 Power circuit topologies and general equations

A schematic of a two-level asymmetrical six-phase drive with single and two isolated neutral points are shown in Figure 5.1 and 5.2, respectively. The same notation introduced in

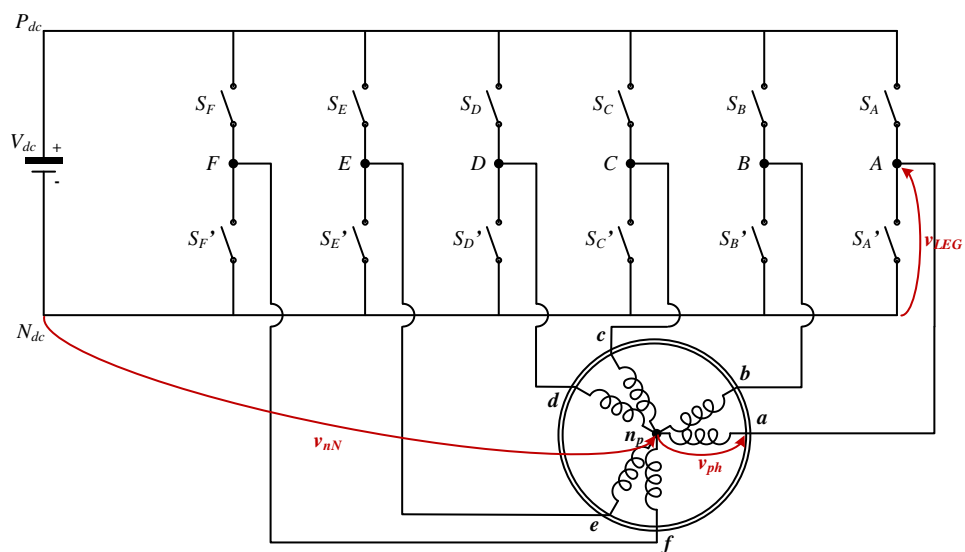


Figure 5.1: Power circuit topology of two-level asymmetrical six-phase drive with single neutral point.

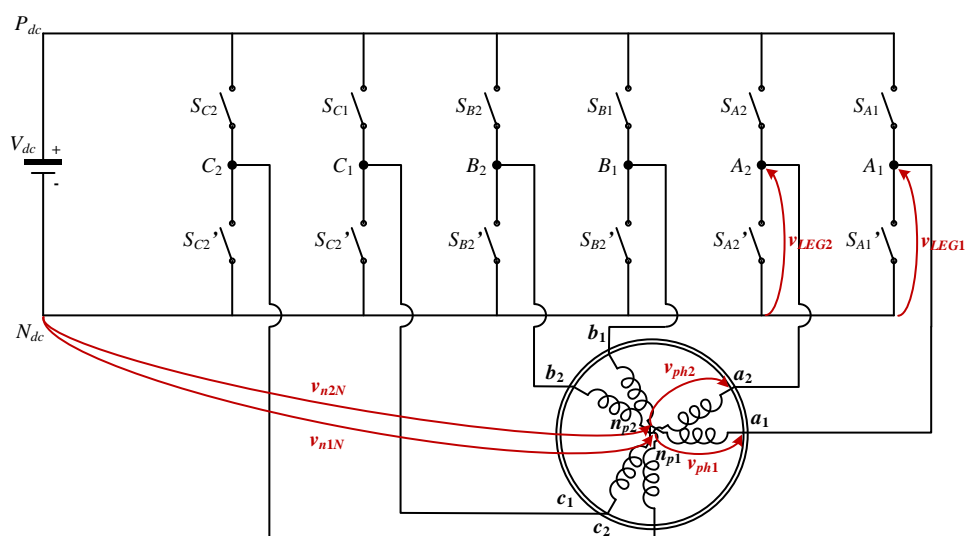


Figure 5.2: Power circuit topology of two-level asymmetrical six-phase drive with two isolated neutral points.

Chapter 3 is also used in this chapter. As can be seen in Figure 5.1 and 5.2, the stator windings are spatially shifted by  $30^\circ$  between the two winding sets, where the first winding set comprises phases  $a$ ,  $c$  and  $e$  (or phases  $a_1$ ,  $b_1$  and  $c_1$ ), while the rest belong to the second winding set. It should be noted that the stator winding is assumed to be sinusoidally distributed and hence, sinusoidal  $v_{ph}$  waveforms are desirable. Since the difference of the analysed drive topologies only lies in the displacement of the winding sets, when compared to a two-level symmetrical six-phase drive, the relationship between inverter output leg voltages ( $v_{LEG}$ ), common mode voltage (CMV) and output phase voltages ( $v_{ph}$ ) remains the same. In other words, equations (3.1) to (3.6) are also valid for the analysed two-level asymmetrical six-phase drives.

### 5.3 Drive with single neutral point configuration

In this section, a newly developed space vector PWM algorithm (2L6PAsymSV) and a carrier-based PWM technique with min-max injection (SinCMI), for two-level asymmetrical six-phase drive with single neutral point configuration, are discussed. Complete development of 2L6PAsymSV algorithm is presented, while the SinCMI (as it is a general modulation method) is just directly applied onto the considered topology. Both PWM techniques are implemented and simulated using PLECS software. This is so since more precise model of the machine based on (Che et al., 2017) is developed using this software. Finally, the simulation

results, when an ideal inverter is used and when the dead-time effect is considered, are compared at the end of this section.

### 5.3.1 Space vector PWM algorithm

The development of space vector PWM algorithm based on VSD modelling approach, for the analysed six-phase two-level single neutral point drive topology, is presented in this subsection. The aim of the algorithm is to realise sinusoidal output phase voltage waveforms. From the projection of the voltage space vectors onto  $\alpha$ - $\beta$ ,  $x$ - $y$  and  $0^+$ - $0^-$  planes, by meeting several stated requirements and conditions, all potential switching sequences are determined first. Then, the dwell times of each switching sequence are calculated using time matrix approach, which also results in identifying their respective regions of application in the  $\alpha$ - $\beta$  plane. Therefore, by properly applying the switching sequences and their corresponding calculated dwell times, the desired sinusoidal output phase voltage waveforms are realised.

#### 5.3.1.1 Projection of space vectors

For a standard two-level inverter topology, the upper and lower switches complement each other. Hence, there are two possible switching combinations per inverter leg, which lead to two possible output leg voltage ( $v_{LEG}$ ) levels, 0 and  $V_{dc}$ . Thus, there are  $2^6 = 64$  possible switching state configurations and they can be further denoted from 0 to 63. In addition, they can also be represented using a six-digit binary number system as 000000 to 111111, if normalised by  $V_{dc}$ . By implementing VSD approach, introduced in (Zhao and Lipo, 1995), these 64 switching states are projected onto three orthogonal planes ( $\alpha$ - $\beta$ ,  $x$ - $y$  and  $0^+$ - $0^-$  planes as shown in Figure 5.3(a) to 5.3(c), respectively). These represent the projections of  $v_{LEG}$  space vectors. Thus, the number of  $v_{LEG}$  space vectors is 64.

Different low order harmonics map into different planes. For example, the low order harmonics of the order  $12k \pm 1$  ( $k = 0, 1, 2, 3, \dots$ ) are mapped into the  $\alpha$ - $\beta$  plane while the low order harmonics of the order of  $12k \pm 5$  ( $k = 0, 1, 2, 3, \dots$ ) are mapped into the  $x$ - $y$  plane. Lastly, the low order harmonics of the order of  $3k$  ( $k = 1, 3, 5, \dots$ ) are mapped into the  $0^+$ - $0^-$  plane (Zhao and Lipo, 1995). Recall that only the low order harmonics that map into  $\alpha$ - $\beta$  plane contribute to the machine's torque/flux production while the low order harmonics, which map into  $x$ - $y$  and  $0^+$ - $0^-$  planes, contribute to the losses.

The VSD transformation matrix for the analysed two-level asymmetrical six-phase drive is defined as (Zhao and Lipo, 1995):

$$\begin{bmatrix} v_\alpha \\ v_\beta \\ v_x \\ v_y \\ v_{0^+} \\ v_{0^-} \end{bmatrix} = \frac{2}{6} \begin{bmatrix} 1 & \cos(\alpha) & \cos(4\alpha) & \cos(5\alpha) & \cos(8\alpha) & \cos(9\alpha) \\ 0 & \sin(\alpha) & \sin(4\alpha) & \sin(5\alpha) & \sin(8\alpha) & \sin(9\alpha) \\ 1 & \cos(5\alpha) & \cos(8\alpha) & \cos(\alpha) & \cos(4\alpha) & \cos(9\alpha) \\ 0 & \sin(5\alpha) & \sin(8\alpha) & \sin(\alpha) & \sin(4\alpha) & \sin(9\alpha) \\ 1 & 0 & 1 & 0 & 1 & 0 \\ 0 & 1 & 0 & 1 & 0 & 1 \end{bmatrix} \times \begin{bmatrix} v_a \\ v_b \\ v_c \\ v_d \\ v_e \\ v_f \end{bmatrix} \quad (5.1)$$

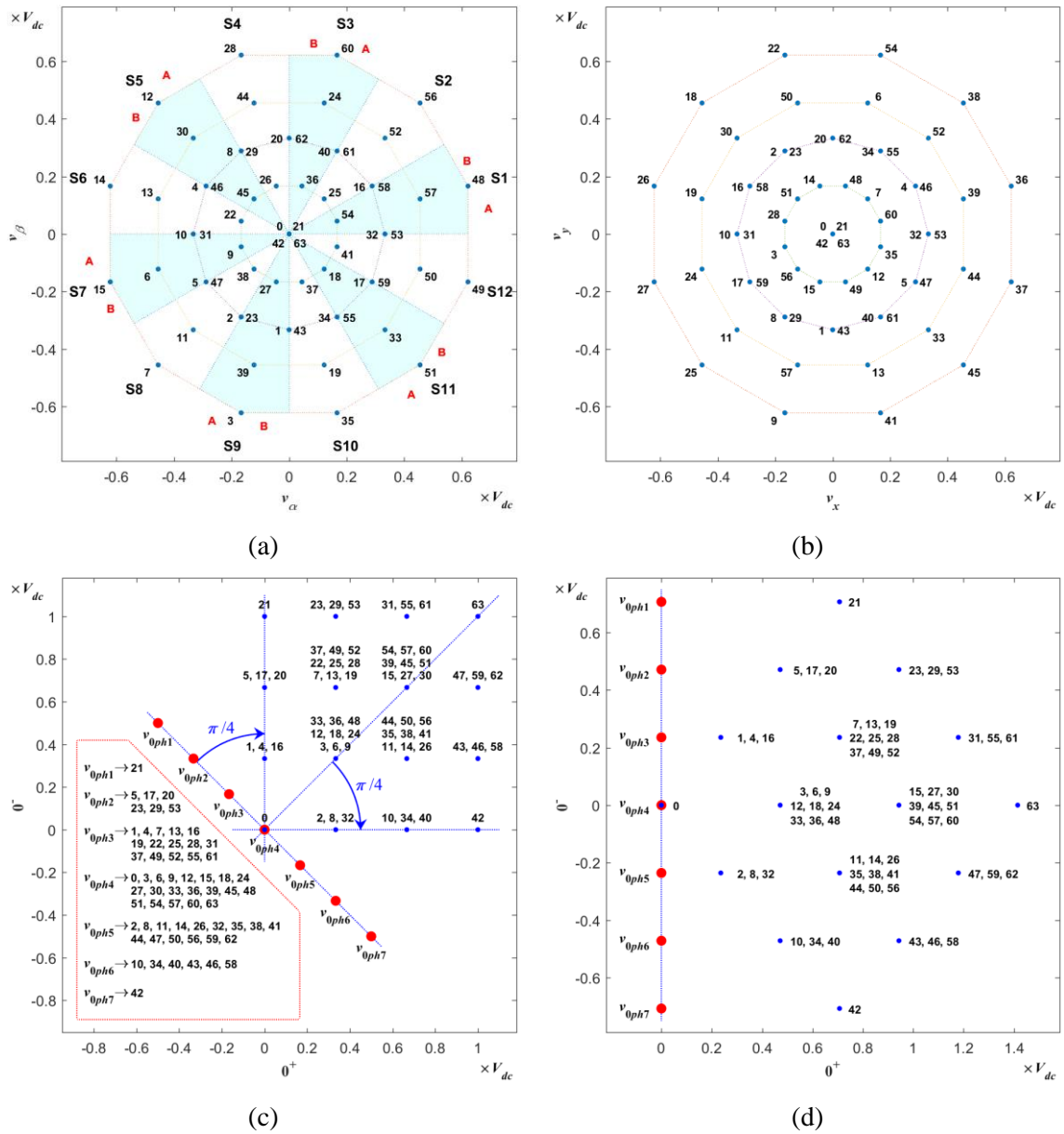


Figure 5.3: Projection of  $v_{LEG}$  and  $v_{ph}$  space vectors of the analysed two-level asymmetrical six-phase drive with single neutral point in the: (a)  $\alpha$ - $\beta$  (b)  $x$ - $y$ , (c)  $0^+$ - $0^-$  and (d)  $0^+$ - $0^-$  plane after rotational transformation of  $-\pi/4$  (will be explained later on in sub-section 5.3.1.3).

where  $\alpha = \pi/6$ . Similarly, by substituting (3.3) into (5.1), the projection of  $v_{ph}$  space vectors into  $\alpha$ - $\beta$ ,  $x$ - $y$  and  $0^+$ - $0^-$  planes can also be obtained. One finds that the projected  $v_{ph}$  space vectors are identical to the projected  $v_{LEG}$  space vectors in  $\alpha$ - $\beta$  and  $x$ - $y$  planes, but different in  $0^+$ - $0^-$  plane. The projected  $v_{ph}$  space vectors in  $0^+$ - $0^-$  plane are denoted as red dots in Figure 5.3(c). In addition, one finds that the number of  $v_{ph}$  space vectors is 63. This is because; the projections of  $v_{ph}$  space vectors corresponding to switching states 0 and 63 are identical.

### 5.3.1.2 Reduction of the number of space vectors

Since not all  $v_{ph}$  space vectors can be chosen in order to realise the sinusoidal reference phase voltage waveforms ( $v_{ph}^*$ ), the order-per-sector law is implemented to eliminate those unnecessary  $v_{ph}$  space vectors (Gao and Fletcher, 2010). The order-per-sector law states that the projected  $v_{ph}$  space vectors in each sector in  $\alpha$ - $\beta$  plane (including space vectors located on the borders of the bordering sectors, as well as at the origin) must satisfy the order of the  $v_{ph}^*$  waveforms for the corresponding sector in the time domain.

The  $v_{ph}^*$  waveforms for the two-level asymmetrical six-phase system are defined as:

$$v_{ph}^* = V_f^* \cos(\omega t - i \cdot \pi/6) \quad (5.2)$$

where  $i = 0, 1, 4, 5, 8$  and  $9$  and  $V_f^*$  is the desired fundamental of  $v_{ph}^*$ . By plotting (5.2), one finds that  $v_{ph}^*$  values change their mutual order at  $0^\circ, 15^\circ, 30^\circ, 60^\circ, 75^\circ, 90^\circ, 120^\circ$ , etc. as shown in Figure 5.4. These angles also correspond to the sector angles in  $\alpha$ - $\beta$  plane where the odd sectors are further sub-divided into two sections at  $15^\circ$ , while even sectors span the entire  $30^\circ$  (see Figure 5.3(a)).

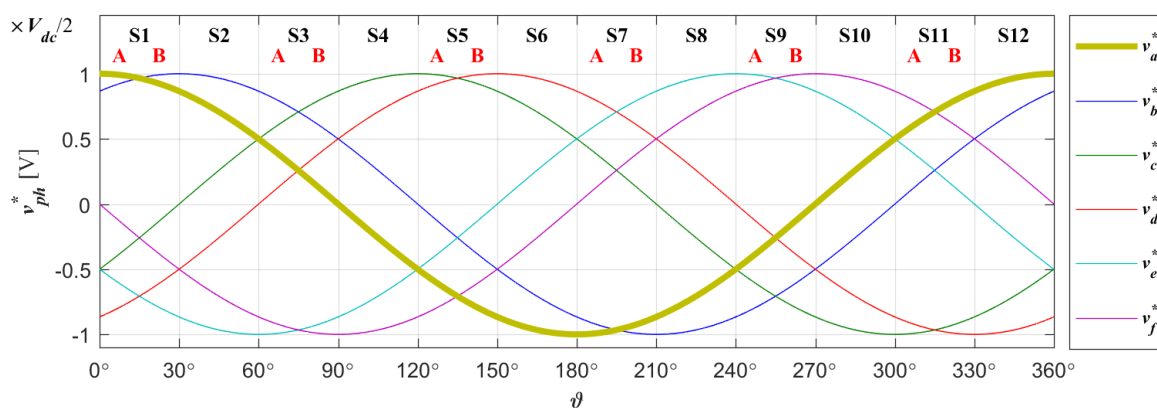


Figure 5.4: Sinusoidal reference output phase voltage ( $v_{ph}^*$ ) waveforms for two-level asymmetrical six-phase drive.

As the projected  $v_{ph}$  and  $v_{LEG}$  space vectors are identical in the  $\alpha$ - $\beta$  plane, the order-per-sector law can be implemented by simply comparing the order of the normalised  $v_{LEG}$  levels i.e. switching states represented in six-digit binary representation, with the order of  $v_{ph}^*$  in the time domain. As an example, the conditions for the order-per-sector law for both sections of the first sector (S1-A and S1-B) are:  $v_a^* \geq v_b^* \geq v_f^* \geq v_c^* \geq v_e^* \geq v_d^*$  and  $v_b^* \geq v_a^* \geq v_c^* \geq v_f^* \geq v_d^* \geq v_e^*$ , respectively. Based on this, one can see that switching state 54 (110110) which is projected on the border of S1-A and S1-B sectors does not satisfy either of these conditions. Hence, it is discarded. Meanwhile, switching state 57 (111001) which is also projected on the border of S1-A and S1-B sectors satisfies both of the stated conditions. Thus, it is kept as a potential switching state. In this way, all switching states in all sectors should be examined. One finds that the numbers of  $v_{LEG}$  and  $v_{ph}$  space vectors can be reduced by half, i.e. from 64 to 32 and from 63 to 31, respectively. The remaining projected  $v_{LEG}$  and  $v_{ph}$  space vectors in  $\alpha$ - $\beta$ ,  $x$ - $y$  and  $0^+$ - $0^-$  planes are shown in Figure 5.5(a) to 5.5(c). Note that the scaling of the axes may now be different.

### 5.3.1.3 Rotational transformation of $0^+$ - $0^-$ plane

In Figure 5.3(c) and 5.5(c), it can be seen that the projections of  $v_{ph}$  space vectors (denoted as red dots) are along a straight line in  $0^+$ - $0^-$  plane, which makes the analysed drive topology a five-dimensional system (Zhao and Lipo, 1995). Yet, both  $0^+$  and  $0^-$  axes are still dependent on each other. Therefore, in order to make it a genuine five-dimensional system, the components of one of the axes should always be zero. This can be achieved by rotating the projected  $v_{ph}$  space vectors and aligning them along  $0^-$  axis, through a rotational transformation by  $-\pi/4$  as illustrated in Figure 5.3(c) and 5.5(c). As a result, the transformation matrix of (5.1), is redefined as:

$$\begin{bmatrix} v_\alpha \\ v_\beta \\ v_x \\ v_y \\ v_{0^+} \\ v_{0^-} \end{bmatrix} = \frac{2}{6} \begin{bmatrix} 1 & \cos(\alpha) & \cos(4\alpha) & \cos(5\alpha) & \cos(8\alpha) & \cos(9\alpha) \\ 0 & \sin(\alpha) & \sin(4\alpha) & \sin(5\alpha) & \sin(8\alpha) & \sin(9\alpha) \\ 1 & \cos(5\alpha) & \cos(8\alpha) & \cos(\alpha) & \cos(4\alpha) & \cos(9\alpha) \\ 0 & \sin(5\alpha) & \sin(8\alpha) & \sin(\alpha) & \sin(4\alpha) & \sin(9\alpha) \\ 1/\sqrt{2} & 1/\sqrt{2} & 1/\sqrt{2} & 1/\sqrt{2} & 1/\sqrt{2} & 1/\sqrt{2} \\ -1/\sqrt{2} & 1/\sqrt{2} & -1/\sqrt{2} & 1/\sqrt{2} & -1/\sqrt{2} & 1/\sqrt{2} \end{bmatrix} \times \begin{bmatrix} v_a \\ v_b \\ v_c \\ v_d \\ v_e \\ v_f \end{bmatrix} \quad (5.3)$$

It should be noted that the rotational transformation of the  $0^+$ - $0^-$  plane does not affect neither the mapping of low order harmonics nor the number of  $v_{LEG}$  and  $v_{ph}$  space vectors, either before or after the order-per-sector law implementation.

The new projected  $v_{ph}$  and  $v_{LEG}$  space vectors in the  $0^+-0^-$  plane are shown in Figure 5.3(d) and 5.5(d). Although the coefficients of  $\pm 1/\sqrt{2}$  in (5.3), which correspond to  $0^+$  and  $0^-$  axes, are obtained from the application of rotational transformation, the existence of these coefficients can also be analytically proven. These coefficients appear as a scaling factor for the amplitude of  $v_{ph}$  low order harmonics of the order  $3k$  ( $k = 1, 3, 5, \dots$ ), in terms of the amplitude of the corresponding  $v_{LEG}$  low order harmonics (Zoric et al., 2016). Recall that these low order harmonics are mapped into the  $0^+-0^-$  plane.

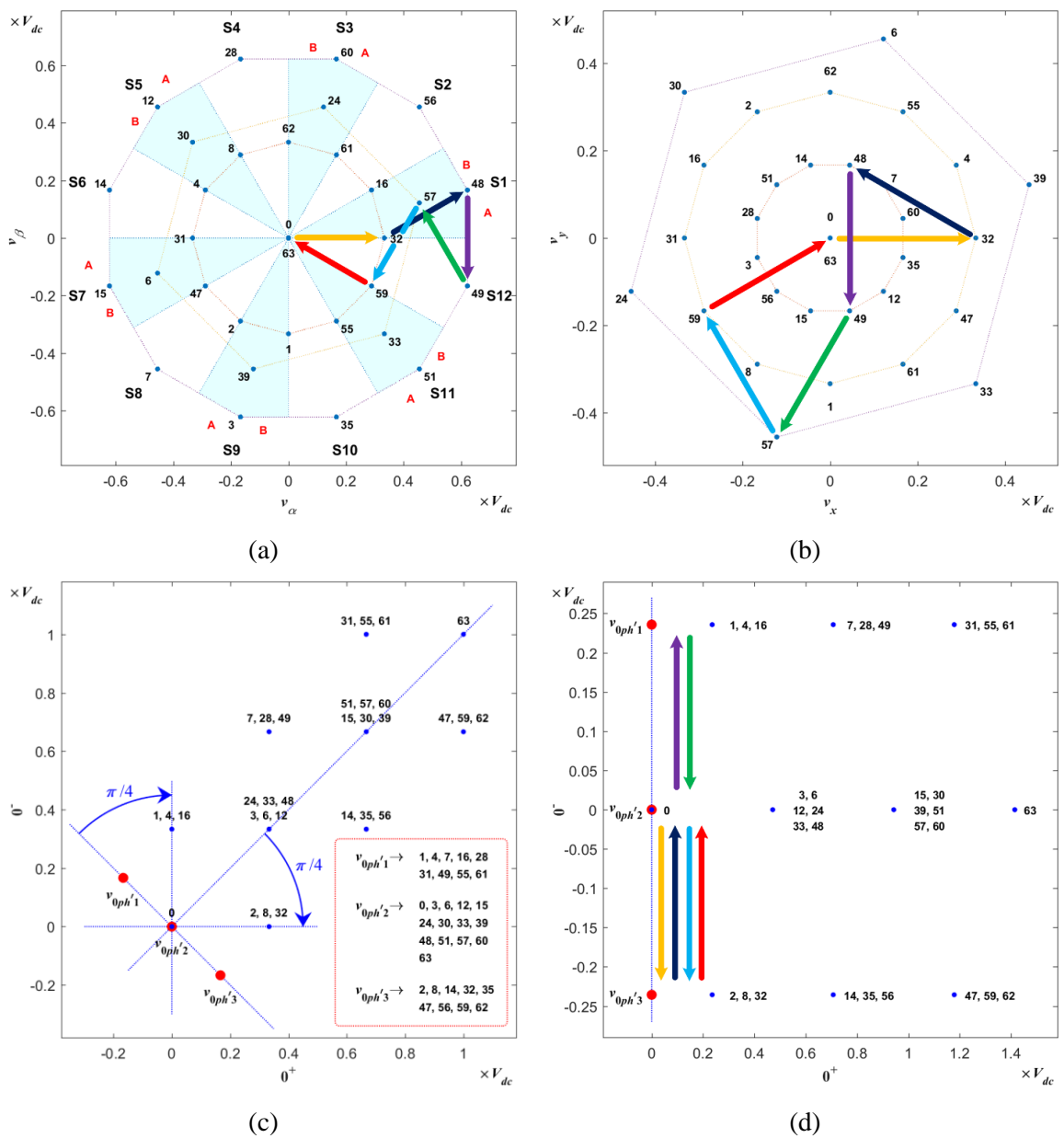


Figure 5.5: Projection of  $v_{LEG}$  and  $v_{ph}$  space vectors of the analysed two-level asymmetrical six-phase drive with single neutral point after the application of order-per-sector law in:

(a)  $\alpha$ - $\beta$  (b)  $x$ - $y$ , (c)  $0^+-0^-$  and (d)  $0^+-0^-$  plane after rotational transformation of  $-\pi/4$ .

The projection of  $v_{LEG}$  space vectors onto  $0^+$  axis can also be related to CMV (Zoric et al., 2016). Normally in practice, CMV is not considered i.e. it's not controlled in space vector algorithms. This is also the case for the analysed drive topology. Therefore, by not considering  $0^+$  axes, one finds that the projections of  $v_{LEG}$  and  $v_{ph}$  space vectors are identical on all remaining axes i.e.  $\alpha, \beta, x, y$  and  $0^-$  (of course,  $0^+$  and  $0^-$  refer to new axes after rotational transformation, i.e. to the axes shown in Figure 5.3(d), 5.5(d) and used in (5.3)). Hence, it can be said that by not considering CMV ( $0^+$  axis), the determination of the switching sequences by means of selecting  $v_{LEG}$  space vectors (i.e. corresponding switching states) will achieve the required  $v_{ph}$  waveforms.

In short, from the control point of view, it is advantageous to implement (5.3) instead of (5.1) when developing space vector algorithm for the two-level asymmetrical six-phase drive with a single neutral point configuration. Thus, any reference made to  $0^+-0^-$  plane henceforth is referring to  $0^+-0^-$  plane after the implementation of rotational transformation i.e. the plane shown in Figure 5.5(d).

#### 5.3.1.4 Determination of potential switching sequences

As stated previously, sinusoidal  $v_{ph}$  waveforms are desired for the two-level asymmetrical six-phase drive with a single neutral point configuration. The same requirements and conditions for the development of space vector algorithm stated in Chapter 4 are also valid. One of those requirements is that the average values of the chosen space vectors in the auxiliary planes need to be zero, since  $x-y$  and  $0^+-0^-$  planes are associated with machine losses. Consequently, the corresponding low order harmonics are zero as well.

It is also desirable that the transition of the inverter output leg voltages ( $v_{LEG}$ ), of the chosen space vectors, is symmetrical within a switching period. This can be achieved if, during the first half of the switching period the output leg voltages increase the level while in the other half, they decrease. When constructing the switching sequence it is important that the number of chosen space vectors in each switching sequence is equal to the number of the machine phases (Kelly et al., 2003), i.e. six in this case.

Although six space vectors are required per switching sequence, there are seven switching states per switching sequence. This is because each inverter  $v_{LEG}$  level will increase by one level. It can be easily shown that the first and the seventh switching state yield the same space vector projections in all planes (switching state redundancy), thus meeting the stated requirement. Additionally, due to the condition that each leg will have one-level increment in

the first half of the switching period, only switching state 0 (000000) can be chosen as a starting point, i.e. the first switching state, for the analysed drive topology. Its only redundant switching state is switching state 63 (111111), which therefore represents the seventh switching state in the sequence. Note that in the process of determining the potential switching sequences, it is adequate to consider the sequences only in the first half of the switching period because in the other half the sequences are reversed.

Normally, the subsequent space vectors (or switching states) for every switching sequence are chosen within their own respective sectors in  $\alpha$ - $\beta$  plane (Dujic et al., 2007a, Grandi et al., 2007, Iqbal and Moinuddin, 2009, Moinoddin et al., 2015). However, this is not the case for the analysed two-level asymmetrical six-phase drive. As an example, one can see the number of the remaining space vectors in sector S1-A in Figure 5.5(a) is only four (corresponding switching states are: 0 or 63, 32, 48 and 57). Therefore, in order to have six space vectors per switching sequence, two additional space vectors have to be chosen outside S1-A sector.

One finds that the only potential switching sequence comprising switching states 0, 32, 48, 49, 57, 59 and 63 i.e. [000000-100000-110000-110001-111001-111011-111111] is able to satisfy the previously stated requirements and desirable conditions for sector S1-A. The corresponding leg voltage transitions of the chosen space vectors for S1-A are denoted by the different colours of the arrows in Figure 5.5. The potential switching sequences for the other sectors can be similarly determined and are shown in Figure 5.6. In fact, those switching sequences are unique to their respective sectors. Thus, it can be said that there is no switching sequence redundancy for the analysed drive topology.

### 5.3.1.5 Dwell time calculation

As shown in Figure 3.5 for the two-level symmetrical six-phase case with single neutral point configuration, the dwell time of the two chosen small space vectors is equally distributed. The same distribution also applies to the medium space vectors. Since the transition of the chosen space vectors is symmetrical in the  $x$ - $y$  plane, their average value is zero. In addition, the sum of dwell times of both chosen small space vectors must be equal to the dwell time of the chosen large space vector. These conditions further simplify the derivation of the equations to calculate the dwell times of the chosen space vectors for a symmetrical six-phase case. However, it is not the case for the two-level asymmetrical six-phase drive with a single neutral point configuration.

Sector	S1-A ( $0^\circ \rightarrow 15^\circ$ ) ( $0 \rightarrow \pi/12$ )							S1-B ( $15^\circ \rightarrow 30^\circ$ ) ( $\pi/12 \rightarrow 2\pi/12$ )							S2 ( $30^\circ \rightarrow 60^\circ$ ) ( $2\pi/12 \rightarrow 4\pi/12$ )						
SwSt	0	32	48	49	57	59	63	0	16	48	56	57	61	63	0	16	48	56	60	61	63
A	0	1	1	1	1	1	1	0	0	1	1	1	1	1	0	0	1	1	1	1	1
B	0	0	1	1	1	1	1	0	1	1	1	1	1	1	0	1	1	1	1	1	1
C	0	0	0	0	1	1	1	0	0	0	1	1	1	1	0	0	0	1	1	1	1
D	0	0	0	0	0	0	1	0	0	0	0	0	1	1	0	0	0	0	1	1	1
E	0	0	0	0	0	1	1	0	0	0	0	0	0	1	0	0	0	0	0	0	1
F	0	0	0	1	1	1	1	0	0	0	0	1	1	1	0	0	0	0	0	1	1
$\delta$	$\delta_1/4$	$\delta_2/2$	$\delta_3/2$	$\delta_4/2$	$\delta_5/2$	$\delta_6/2$	$\delta_1/4$	$\delta_1/4$	$\delta_2/2$	$\delta_3/2$	$\delta_4/2$	$\delta_5/2$	$\delta_6/2$	$\delta_1/4$	$\delta_1/4$	$\delta_2/2$	$\delta_3/2$	$\delta_4/2$	$\delta_5/2$	$\delta_6/2$	$\delta_1/4$
Sector	S3-A ( $60^\circ \rightarrow 75^\circ$ ) ( $4\pi/12 \rightarrow 5\pi/12$ )							S3-B ( $75^\circ \rightarrow 90^\circ$ ) ( $5\pi/12 \rightarrow 6\pi/12$ )							S4 ( $90^\circ \rightarrow 120^\circ$ ) ( $6\pi/12 \rightarrow 8\pi/12$ )						
SwSt	0	16	24	56	60	61	63	0	8	24	28	60	62	63	0	8	12	28	60	62	63
A	0	0	0	1	1	1	1	0	0	0	0	1	1	1	0	0	0	0	1	1	1
B	0	1	1	1	1	1	1	0	0	1	1	1	1	1	0	0	0	1	1	1	1
C	0	0	1	1	1	1	1	0	1	1	1	1	1	1	0	1	1	1	1	1	1
D	0	0	0	0	1	1	1	0	0	0	1	1	1	1	0	0	1	1	1	1	1
E	0	0	0	0	0	0	1	0	0	0	0	0	1	1	0	0	0	0	0	1	1
F	0	0	0	0	0	1	1	0	0	0	0	0	0	1	0	0	0	0	0	0	1
$\delta$	$\delta_1/4$	$\delta_2/2$	$\delta_3/2$	$\delta_4/2$	$\delta_5/2$	$\delta_6/2$	$\delta_1/4$	$\delta_1/4$	$\delta_2/2$	$\delta_3/2$	$\delta_4/2$	$\delta_5/2$	$\delta_6/2$	$\delta_1/4$	$\delta_1/4$	$\delta_2/2$	$\delta_3/2$	$\delta_4/2$	$\delta_5/2$	$\delta_6/2$	$\delta_1/4$
Sector	S5-A ( $120^\circ \rightarrow 135^\circ$ ) ( $8\pi/12 \rightarrow 9\pi/12$ )							S5-B ( $135^\circ \rightarrow 150^\circ$ ) ( $9\pi/12 \rightarrow 10\pi/12$ )							S6 ( $150^\circ \rightarrow 180^\circ$ ) ( $10\pi/12 \rightarrow \pi$ )						
SwSt	0	8	12	28	30	62	63	0	4	12	14	30	31	63	0	4	12	14	15	31	63
A	0	0	0	0	0	1	1	0	0	0	0	0	0	1	0	0	0	0	0	0	1
B	0	0	0	1	1	1	1	0	0	0	0	1	1	1	0	0	0	0	0	1	1
C	0	1	1	1	1	1	1	0	0	1	1	1	1	1	0	0	1	1	1	1	1
D	0	0	1	1	1	1	1	0	1	1	1	1	1	1	0	1	1	1	1	1	1
E	0	0	0	0	1	1	1	0	0	0	1	1	1	1	0	0	0	1	1	1	1
F	0	0	0	0	0	0	1	0	0	0	0	0	1	1	0	0	0	0	1	1	1
$\delta$	$\delta_1/4$	$\delta_2/2$	$\delta_3/2$	$\delta_4/2$	$\delta_5/2$	$\delta_6/2$	$\delta_1/4$	$\delta_1/4$	$\delta_2/2$	$\delta_3/2$	$\delta_4/2$	$\delta_5/2$	$\delta_6/2$	$\delta_1/4$	$\delta_1/4$	$\delta_2/2$	$\delta_3/2$	$\delta_4/2$	$\delta_5/2$	$\delta_6/2$	$\delta_1/4$
Sector	S7-A ( $180^\circ \rightarrow 195^\circ$ ) ( $-\pi \rightarrow -11\pi/12$ )							S7-B ( $195^\circ \rightarrow 210^\circ$ ) ( $-11\pi/12 \rightarrow -10\pi/12$ )							S8 ( $210^\circ \rightarrow 240^\circ$ ) ( $-10\pi/12 \rightarrow -8\pi/12$ )						
SwSt	0	4	6	14	15	31	63	0	2	6	7	15	47	63	0	2	3	7	15	47	63
A	0	0	0	0	0	0	1	0	0	0	0	0	1	1	0	0	0	0	0	1	1
B	0	0	0	0	0	1	1	0	0	0	0	0	0	1	0	0	0	0	0	0	1
C	0	0	0	1	1	1	1	0	0	0	0	1	1	1	0	0	0	0	1	1	1
D	0	1	1	1	1	1	1	0	0	1	1	1	1	1	0	0	0	1	1	1	1
E	0	0	1	1	1	1	1	0	1	1	1	1	1	1	0	1	1	1	1	1	1
F	0	0	0	0	1	1	1	0	0	0	1	1	1	1	0	0	1	1	1	1	1
$\delta$	$\delta_1/4$	$\delta_2/2$	$\delta_3/2$	$\delta_4/2$	$\delta_5/2$	$\delta_6/2$	$\delta_1/4$	$\delta_1/4$	$\delta_2/2$	$\delta_3/2$	$\delta_4/2$	$\delta_5/2$	$\delta_6/2$	$\delta_1/4$	$\delta_1/4$	$\delta_2/2$	$\delta_3/2$	$\delta_4/2$	$\delta_5/2$	$\delta_6/2$	$\delta_1/4$
Sector	S9-A ( $240^\circ \rightarrow 255^\circ$ ) ( $-8\pi/12 \rightarrow -7\pi/12$ )							S9-B ( $255^\circ \rightarrow 270^\circ$ ) ( $-7\pi/12 \rightarrow -6\pi/12$ )							S10 ( $270^\circ \rightarrow 300^\circ$ ) ( $-6\pi/12 \rightarrow -4\pi/12$ )						
SwSt	0	2	3	7	39	47	63	0	1	3	35	39	55	63	0	1	3	35	51	55	63
A	0	0	0	0	1	1	1	0	0	0	1	1	1	1	0	0	0	1	1	1	1
B	0	0	0	0	0	0	1	0	0	0	0	0	1	1	0	0	0	0	1	1	1
C	0	0	0	0	0	1	1	0	0	0	0	0	0	1	0	0	0	0	0	0	1
D	0	0	0	1	1	1	1	0	0	0	0	1	1	1	0	0	0	0	0	1	1
E	0	1	1	1	1	1	1	0	0	1	1	1	1	1	0	0	1	1	1	1	1
F	0	0	1	1	1	1	1	0	1	1	1	1	1	1	0	1	1	1	1	1	1
$\delta$	$\delta_1/4$	$\delta_2/2$	$\delta_3/2$	$\delta_4/2$	$\delta_5/2$	$\delta_6/2$	$\delta_1/4$	$\delta_1/4$	$\delta_2/2$	$\delta_3/2$	$\delta_4/2$	$\delta_5/2$	$\delta_6/2$	$\delta_1/4$	$\delta_1/4$	$\delta_2/2$	$\delta_3/2$	$\delta_4/2$	$\delta_5/2$	$\delta_6/2$	$\delta_1/4$
Sector	S11-A ( $300^\circ \rightarrow 315^\circ$ ) ( $-4\pi/12 \rightarrow -3\pi/12$ )							S11-B ( $315^\circ \rightarrow 330^\circ$ ) ( $-3\pi/12 \rightarrow -2\pi/12$ )							S12 ( $330^\circ \rightarrow 360^\circ$ ) ( $-2\pi/12 \rightarrow 0$ )						
SwSt	0	1	33	35	51	55	63	0	32	33	49	51	59	63	0	32	48	49	51	59	63
A	0	0	1	1	1	1	1	0	1	1	1	1	1	1	0	1	1	1	1	1	1
B	0	0	0	0	1	1	1	0	0	0	1	1	1	1	0	0	1	1	1	1	1
C	0	0	0	0	0	0	1	0	0	0	0	0	1	1	0	0	0	0	0	1	1
D	0	0	0	0	0	1	1	0	0	0	0	0	0	1	0	0	0	0	0	0	1
E	0	0	0	1	1	1	1	0	0	0	0	1	1	1	0	0	0	0	1	1	1
F	0	1	1	1	1	1	1	0	0	1	1	1	1	1	0	0	0	1	1	1	1
$\delta$	$\delta_1/4$	$\delta_2/2$	$\delta_3/2$	$\delta_4/2$	$\delta_5/2$	$\delta_6/2$	$\delta_1/4$	$\delta_1/4$	$\delta_2/2$	$\delta_3/2$	$\delta_4/2$	$\delta_5/2$	$\delta_6/2$	$\delta_1/4$	$\delta_1/4$	$\delta_2/2$	$\delta_3/2$	$\delta_4/2$	$\delta_5/2$	$\delta_6/2$	$\delta_1/4$

Figure 5.6: switching sequences of the two-level asymmetrical six-phase drive with single isolated neutral point, (only the first half of the switching period is shown).

As can be seen in Figure 5.5(b), the transition of the chosen space vectors in  $x$ - $y$  plane is not symmetrical. This increases the complexity in the process of deriving the required dwell times equation. Thus, the dwell time matrix approach, i.e. (3.18) to calculate the dwell times, is adopted here as well. Note that the six-by-six matrix in (3.18) will be the inverse of the obtained projected chosen space vectors by using (5.3) rather than (5.1). Because the CMV is not controlled in the space vector algorithm (as previously mentioned),  $0^+$  axis, i.e. the fifth row, is replaced by the time balancing equation. This equation guarantees that the sum of the calculated dwell times is equal to the switching period. The  $v_{\alpha}^*$  and  $v_{\beta}^*$  are set to  $V_f^* \cdot \cos(\omega t)$  and  $V_f^* \cdot \sin(\omega t)$ , while  $v_x^*$ ,  $v_y^*$ , and  $v_{0^-}$  are set to zero, which corresponds to projections of the sinusoidal reference phase voltages, defined in (5.2), onto these axes. As an example, to calculate the dwell times for S1-A sector, (3.18) becomes:

$$\begin{bmatrix} T_1 \\ T_2 \\ T_3 \\ T_4 \\ T_5 \\ T_6 \end{bmatrix} = \begin{bmatrix} v_{\alpha,0} & v_{\alpha,32} & v_{\alpha,48} & v_{\alpha,49} & v_{\alpha,57} & v_{\alpha,59} \\ v_{\beta,0} & v_{\beta,32} & v_{\beta,48} & v_{\beta,49} & v_{\beta,57} & v_{\beta,59} \\ v_{x,0} & v_{x,32} & v_{x,48} & v_{x,49} & v_{x,57} & v_{x,59} \\ v_{y,0} & v_{y,32} & v_{y,48} & v_{y,49} & v_{y,57} & v_{y,59} \\ 1 & 1 & 1 & 1 & 1 & 1 \\ v_{0^-,0} & v_{0^-,32} & v_{0^-,48} & v_{0^-,49} & v_{0^-,57} & v_{0^-,59} \end{bmatrix}^{-1} \begin{bmatrix} V_f^* \cdot \cos(\omega t) \\ V_f^* \cdot \sin(\omega t) \\ 0 \\ 0 \\ 1 \\ 0 \end{bmatrix} \cdot T_s \quad (5.4)$$

The duty cycles of the calculated dwell times can be defined as:

$$\delta_1 = \frac{T_1}{T_s} \quad \delta_2 = \frac{T_2}{T_s} \quad \delta_3 = \frac{T_3}{T_s} \quad \delta_4 = \frac{T_4}{T_s} \quad \delta_5 = \frac{T_5}{T_s} \quad \delta_6 = \frac{T_6}{T_s} \quad (5.5)$$

where  $T_s$  is the switching period. Their order in the first half of the switching period is shown in Figure 5.6. The starting and seventh switching states correspond to the same space vector, and it is desirable to equally divide  $\delta_1$  between the two (McGrath et al., 2003). The application of those switching sequences with respect to their duty cycles will result in generation of the switching signals for the inverter switches.

### 5.3.1.6 Identification of region of application

One can see that the reference for  $\alpha$ - $\beta$  plane in (5.4) will transverse not only through S1-A sector, but also through the other sectors. Thus, by increasing  $V_f^*$  from zero up to  $\sqrt{2 + \sqrt{3}}/3 V_{dc}$  (the circumradius of the largest polygon in  $\alpha$ - $\beta$  plane), all possible solutions for the dwell time can be obtained. However, one finds that the solutions for the dwell time of each switching sequence only exist at certain value of  $V_f^*$ . Therefore, by marking the coordinates of

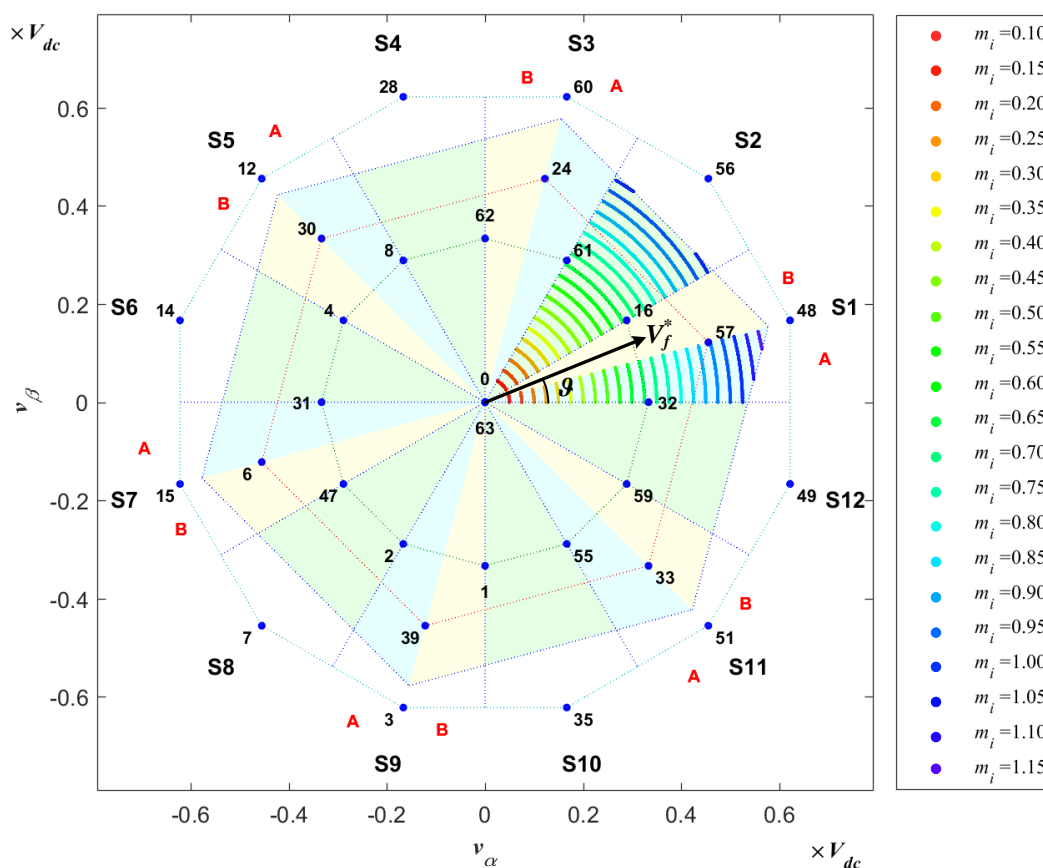


Figure 5.7: The regions of application for S1-A switching sequence [0 32 48 49 57 59 63] and S2 switching sequence [0 16 48 56 60 61 63] in  $\alpha$ - $\beta$  plane.

the applied  $V_f^*$  in  $\alpha$ - $\beta$  plane where the solutions for dwell times exist, a region of application is formed. This is done using Matlab code. As an example, the regions where there are solutions for dwell time for switching sequence [0 32 48 49 57 59 63] and [0 16 48 56 60 61 63] are within the expected S1-A and the second (S2) sectors, as shown in Figure 5.7. The regions of application correspond to other switching sequences and their respective sectors are also shown in Figure 5.7.

In addition, the maximum  $m_i$  for liner operation of the analysed drive topology can also be determined from the obtained regions of application. The  $m_i$  is defined as in (3.19). As a result, one finds that the maximum  $m_i$  for liner operation is 1.035, which is in agreement with (Dujic et al., 2010).

### 5.3.2 Carrier-based PWM technique

In an asymmetrical six-phase drive, the sinusoidal  $v_{ph}^*$  waveforms are not symmetrical around the time axis, as can be seen in Figure 5.4. Therefore, common mode injection or also

known as min-max injection technique can be implemented (Holmes, 1996, Holmes, 1998, Wang, 2002). In fact, one can see that the injection technique will make the lower and upper envelopes of the sinusoidal  $v_{ph}^*$  waveforms to be balanced. Furthermore, it is commonly known that in the two-level three-phase case, carrier-based PWM technique with common mode voltage injection yields the same performance as space vector PWM technique. In addition, it will also improve the dc-bus utilisation of the inverter where the maximum  $m_i$  for liner operation becomes 1.035. This value is equivalent to the maximum  $m_i$  for liner operation for 2L6PAsymSV as stated in sub-section 5.3.1.6.

The sinusoidal  $v_{ph}^*$  waveforms of (5.2) with min-max injection ( $v_{ph,SinCMI}^*$ ) for two-level asymmetrical six-phase system can be defined as:

$$v_{ph,SinCMI}^* = v_{ph}^* - \frac{[\min(v_{ph}^*) + \max(v_{ph}^*)]}{2} \quad (5.6)$$

The  $v_{ph,SinCMI}^*$  waveforms at  $m_i = 1.035$  are shown in Figure 5.8. Note that at  $m_i = 1.035$ , the peaks of  $v_{ph,SinCMI}^*$  waveforms reach  $1/2V_{dc}$ . Last but not least, the switching signals for the inverter switches are generated by comparing the  $v_{ph,SinCMI}^*$  waveforms with triangular carrier waveform with switching period of  $T_s$ .

### 5.3.3 Simulation results

The presented space vector PWM algorithm and carrier-based PWM with min-max injection are developed and verified through simulations in PLECS. A simulation diagram of the developed space vector algorithm is shown in Figure 5.9. A similar diagram (with the only difference being the used modulator), was used for testing the carrier-based algorithm. For

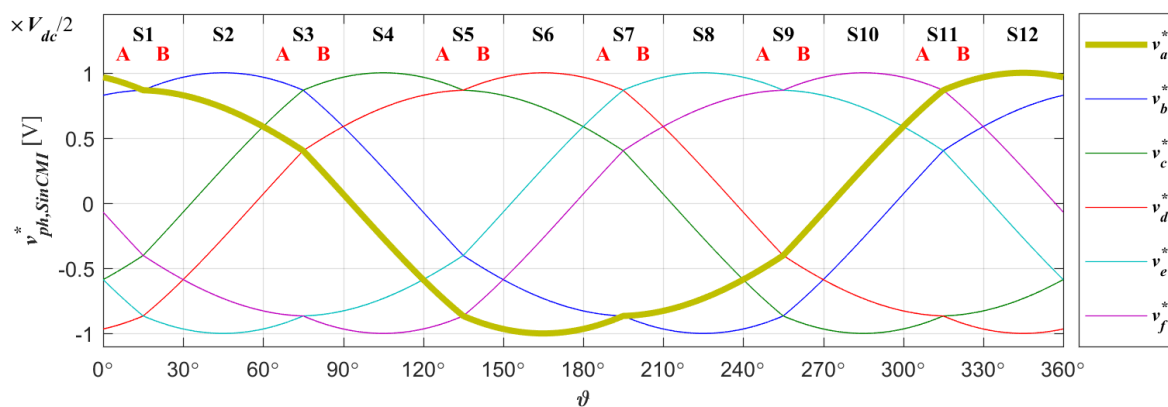


Figure 5.8: Sinusoidal reference waveforms with min-max injection ( $v_{ph,SinCMI}^*$ ) for two-level asymmetrical six-phase drive at  $m_i = 1.035$ .

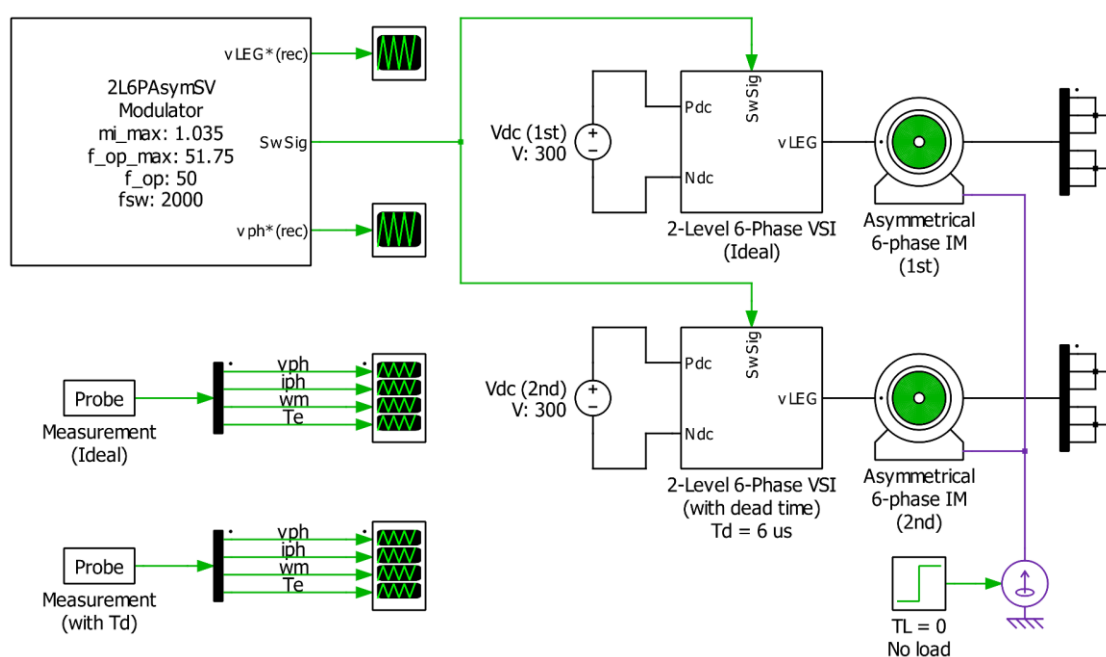


Figure 5.9: Simulation diagram of the developed space vector PWM algorithm (2L6PAsymSV) for two-level asymmetrical six-phase drive with single neutral point configuration.

consistency of graphical representation, all saved simulation data are analysed and plotted in Matlab. The sinusoidal  $v_{ph}^*$  waveforms are used as the reference waveforms for 2L6PAsymSV while  $v_{ph, SinCMI}^*$  waveforms are used for SinCMI. At 50 Hz, i.e. at the machine's rated frequency, the chosen peak value of reference phase voltage waveforms is  $V_f^* = 150$  V and according to (3.19), this corresponds to  $m_i = 1$ . Thus, when  $m_i = 1.035$ , the expected fundamental voltage is 155.25 V (at 51.75 Hz).

In order to test the influence of the inverter dead-time, the switching signals generated by PWM modulator are fed into an ideal inverter model block as well as into another inverter model block with built-in dead time of  $T_d = 6 \mu s$  (see Figure 5.9). The inverter dead time is not being compensated in any way. The dc-bus of each inverter is set to  $V_{dc} = 300$  V while its switching frequency is set to  $f_s = 2$  kHz i.e.  $T_s = 0.5$  ms. Furthermore, two asymmetrical six-phase machine models with parameters as listed in Table 5.1 are developed and each is driven by the inverter as shown in Figure 5.9. The same setup is also used for SinCMI.

The drive is in open loop for the full linear range of  $m_i$  (from  $m_i = 0.1$  to 1.035) with 0.05 increments. The simulation time is set to be  $T_{sim} = 2$  s, where the speed of the machine has reached steady state. Finally, the performances of the PWM techniques are determined by calculating the total harmonic distortion for phase 'a' voltage and current ( $THD_v$  and  $THD_i$ )

Table 5.1: Parameters of asymmetrical six-phase induction machine.

Parameter	Value	
Resistance	$R_s = 13.75 \Omega$	$R_r = 5.775 \Omega$
Leakage inductance	$L_{ls} = 5.3 \text{ mH}$	$L_{lr} = 12.7 \text{ mH}$
Mutual inductance	$L_m = 296.5 \text{ mH}$	
Pole-pairs	3	
Rotating mass inertia	$J = 0.03 \text{ kgm}^2$	

using (3.20), where the first  $h$  harmonics up to the value of  $h$  that corresponds to 21 kHz (i.e. the first ten sidebands of the used switching frequency) are taken into account.

In the space vector PWM algorithm, the switching signals are generated from the switching sequence, and the duration of switching states application is based on the calculated dwell times. In addition, one can also reconstruct the reference output leg voltage ( $v_{LEG,rec}^*$ ) waveforms from the product of the applied switching sequence and its corresponding calculated dwell times. Although  $v_{LEG,rec}^*$  is not part of the space vector PWM algorithm, this representation of  $v_{LEG,rec}^*$  is convenient for the purpose of comparison with SinCMI technique.

The  $v_{LEG,rec}^*$  waveforms when  $m_i = 1.035$  are shown in Figure 5.10. The amplitude of  $v_{LEG,rec}^*$  waveforms is in between zero and  $V_{dc}$  since the representation of the switching signals i.e. switching states are in the binary system which are normalised to  $V_{dc}$ . In fact, they are identical to  $v_{ph,SinCMI}^*$  (see Figure 5.8). In addition, one can also obtain the reconstructed reference phase voltage ( $v_{ph,rec}^*$ ) waveforms from (3.3). Removal of common mode voltage from the  $v_{LEG,rec}^*$  results in  $v_{ph,rec}^*$  which have sinusoidal waveforms albeit at slightly higher amplitude. This is expected since space vector PWM algorithm inherently injects common mode voltage into the balanced reference waveforms (Wang, 2002). Hence, it can be said that the references for output phase voltage waveforms remain sinusoidal but with higher utilisation of the dc-bus voltage. The obtained  $v_{ph,rec}^*$  waveforms at  $m_i = 1.035$  are shown in Figure 5.11.

The phase ‘a’ voltage, phase voltage components ( $v_a, v_\beta, v_x, v_y, v_0^+$  and  $v_0^-$ ), and phase ‘a’ current waveforms of the machine driven by the ideal inverter, as well as their corresponding spectra for the 2L6PAsymSV and SinCMI are shown in Figure 5.12 and 5.13, respectively. One finds that, not only the fundamental phase ‘a’ voltage ( $|v_a|_{fund}$ ) and its  $\text{THD}_v$  for both PWM techniques are identical, even the fundamental phase ‘a’ current ( $|i_a|_{fund}$ ) and  $\text{THD}_i$  are also identical. The obtained  $|v_a|_{fund}$  is 155.57 V with  $\text{THD}_v$  of 66.52%, while  $|i_a|_{fund}$  is 0.75 A with

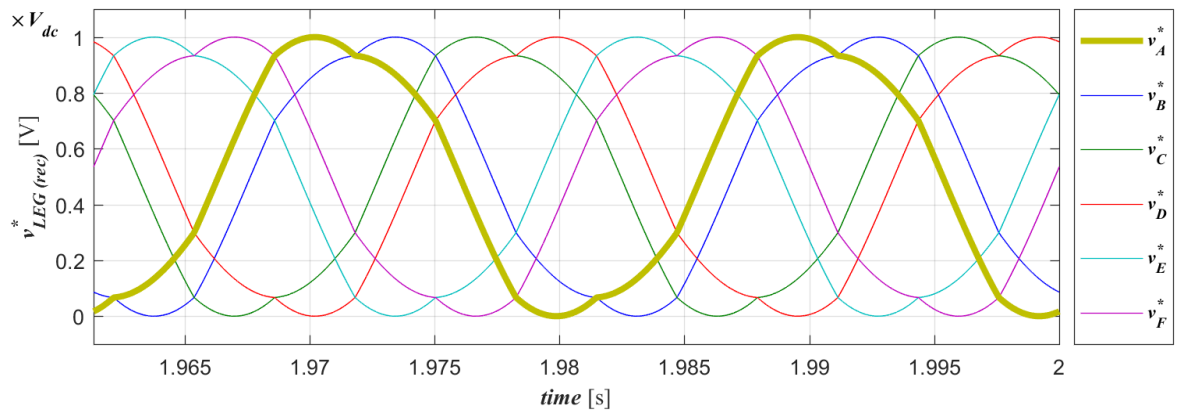


Figure 5.10: Reconstructed reference output leg voltage ( $v_{LEG,rec}^*$ ) waveforms of 2L6PASymSV at  $m_i = 1.035$ .

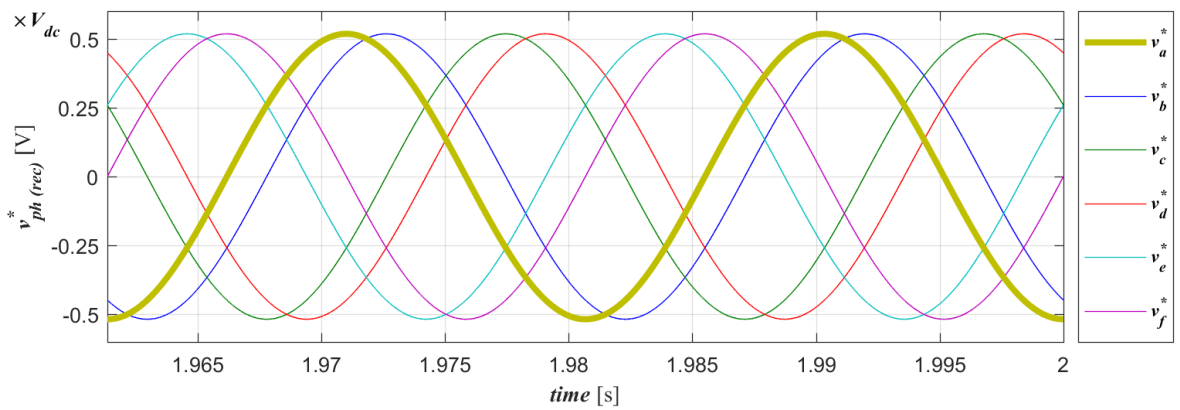


Figure 5.11: Reconstructed reference output phase voltage ( $v_{ph,rec}^*$ ) waveforms of 2L6PASymSV at  $m_i = 1.035$ .

THD<sub>*i*</sub> of 108.93%. In addition, it can be seen that the magnitude of the phase voltage low order harmonics, which map onto  $x$ ,  $y$  and  $0^-$  axis (only the magnitude of the 3<sup>rd</sup>, 5<sup>th</sup>, 7<sup>th</sup> and 9<sup>th</sup> harmonics are shown), are very low with respect to  $|v_a|_{fund}$ . This is expected since one of the requirements of 2L6PASymSV is to set the average value of  $x$ - $y$  and  $0^-$  components to zero, in order to ensure that their corresponding low order harmonics do not exist. Furthermore, one can see that the low order harmonics in the phase ‘ $a$ ’ current spectrum also do not exist. In fact, the magnitude for the 3<sup>rd</sup> harmonic is zero. Nevertheless, higher order harmonics do exist in the side-bands around multiples of the switching frequency, i.e. around  $k \cdot f_s$  ( $k = 1, 2, 3 \dots$ ).

The same sets of graphs (phase ‘ $a$ ’ voltage,  $v_a$ ,  $v_b$ ,  $v_x$ ,  $v_y$ ,  $v_{0^+}$ ,  $v_{0^-}$  and phase ‘ $a$ ’ current waveforms as well as their corresponding spectra) for the machine driven by the inverter with built-in dead time, for both PWM techniques, are shown in Figure 5.14 and 5.15, respectively. Both PWM techniques still yield identical results. The obtained  $|v_a|_{fund}$  is 153.48 V with THD<sub>*v*</sub>

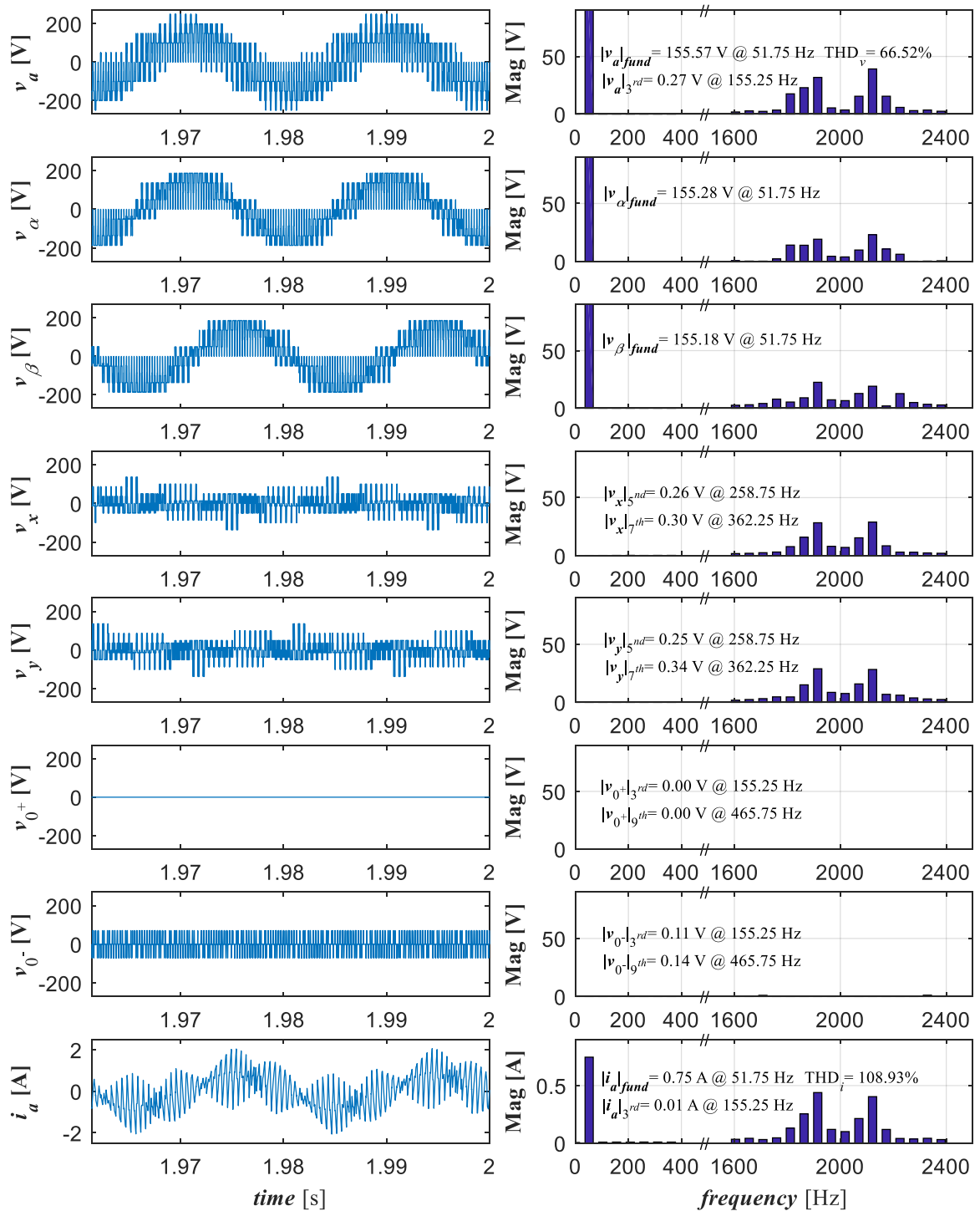


Figure 5.12: Phase ‘a’ voltage, phase voltage components ( $v_a$ ,  $v_\beta$ ,  $v_x$ ,  $v_y$ ,  $v_{0^+}$  and  $v_{0^-}$ ), phase ‘a’ current and corresponding spectra of 2L6PAsymSV for the machine driven by ideal inverter at  $m_i = 1.035$ .

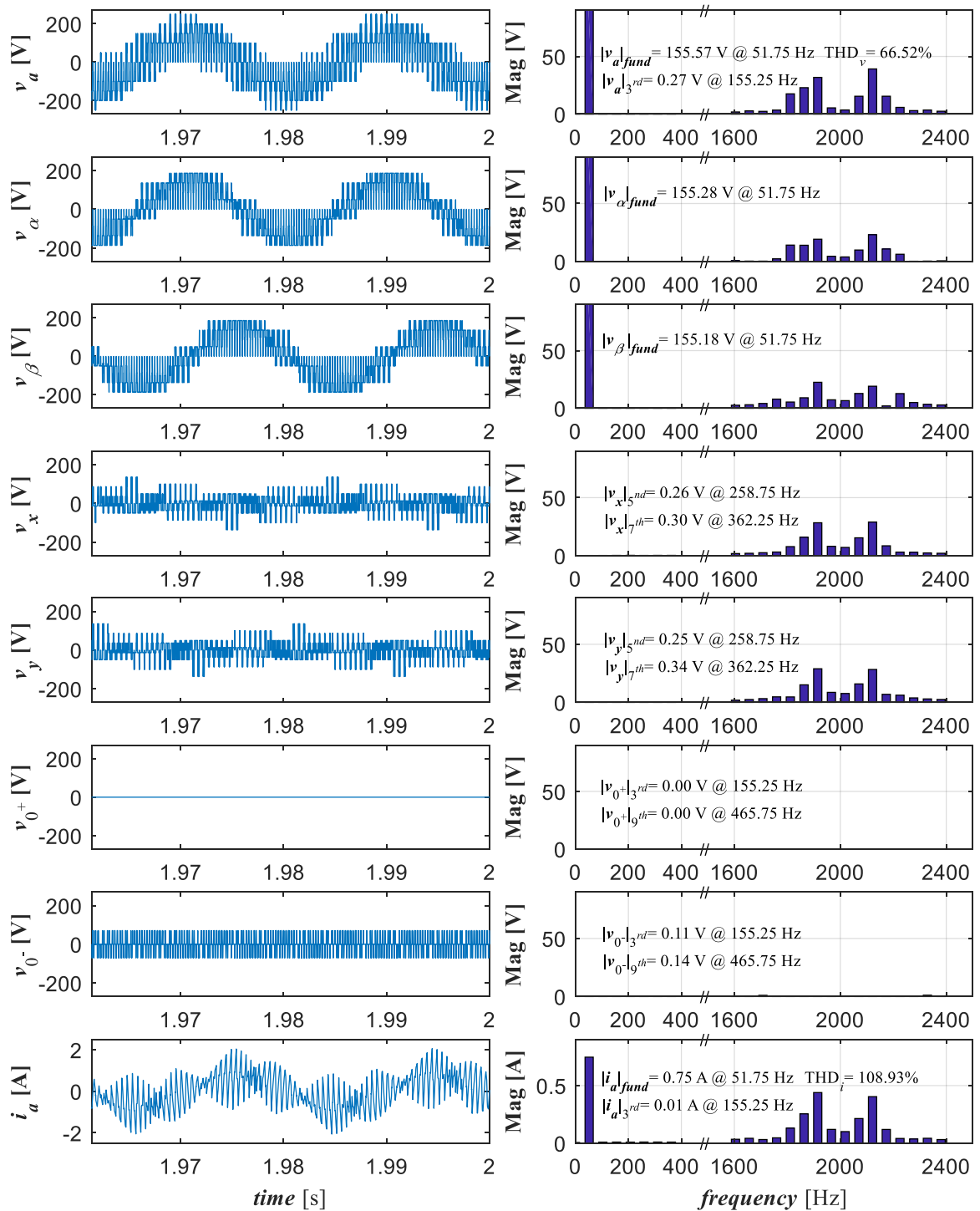


Figure 5.13: Phase 'a' voltage, phase voltage components ( $v_a$ ,  $v_{\beta}$ ,  $v_x$ ,  $v_y$ ,  $v_{0^+}$  and  $v_{0^-}$ ), phase 'a' current and corresponding spectra of SinCMI for the machine driven by ideal inverter at  $m_i = 1.035$ .

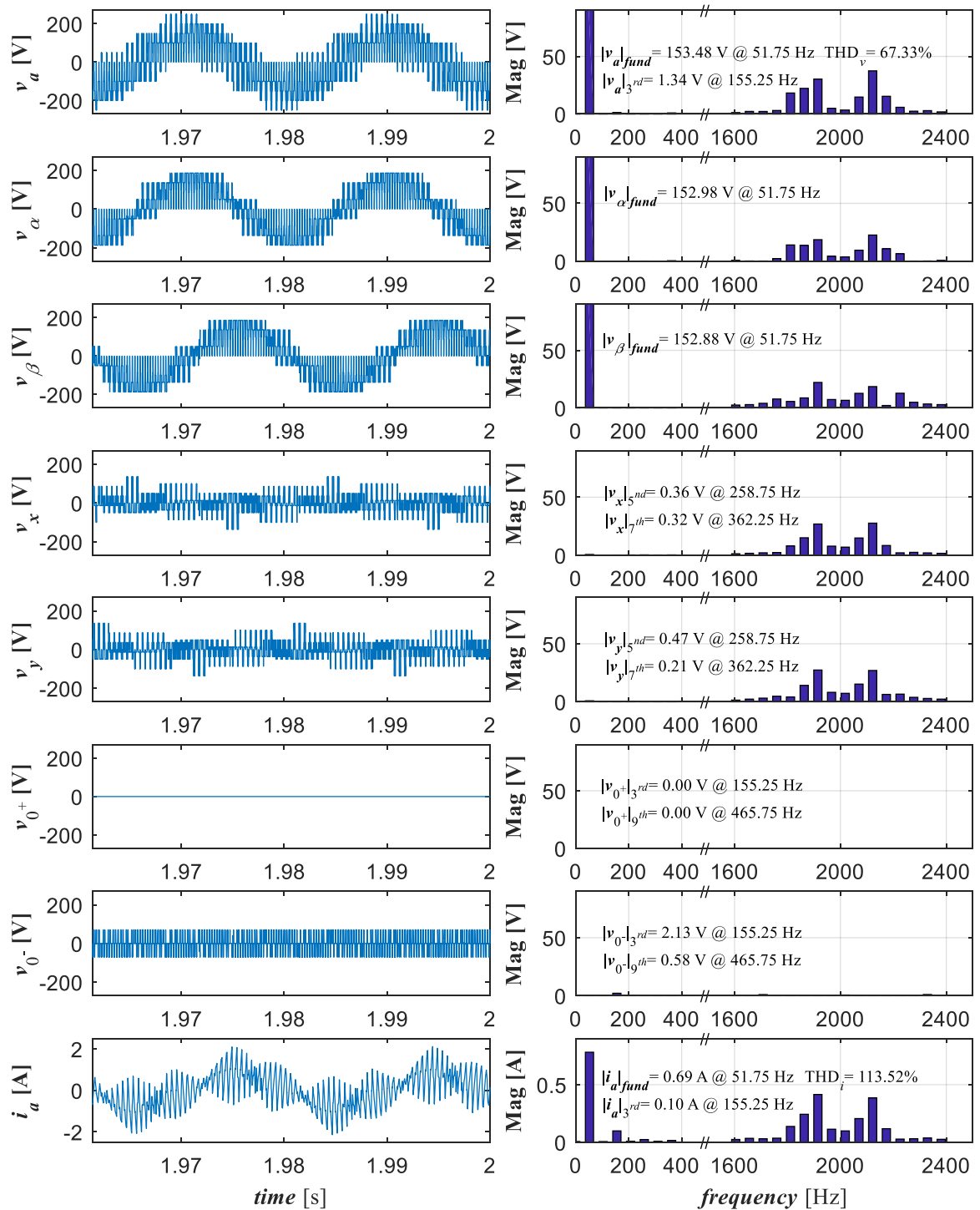


Figure 5.14: Phase ‘a’ voltage, phase voltage components ( $v_a$ ,  $v_\beta$ ,  $v_x$ ,  $v_y$ ,  $v_{0^+}$  and  $v_{0^-}$ ), phase ‘a’ current and corresponding spectra of 2L6PA<sub>sym</sub>SV for the machine driven by inverter with build-in dead time at  $m_i = 1.035$ .

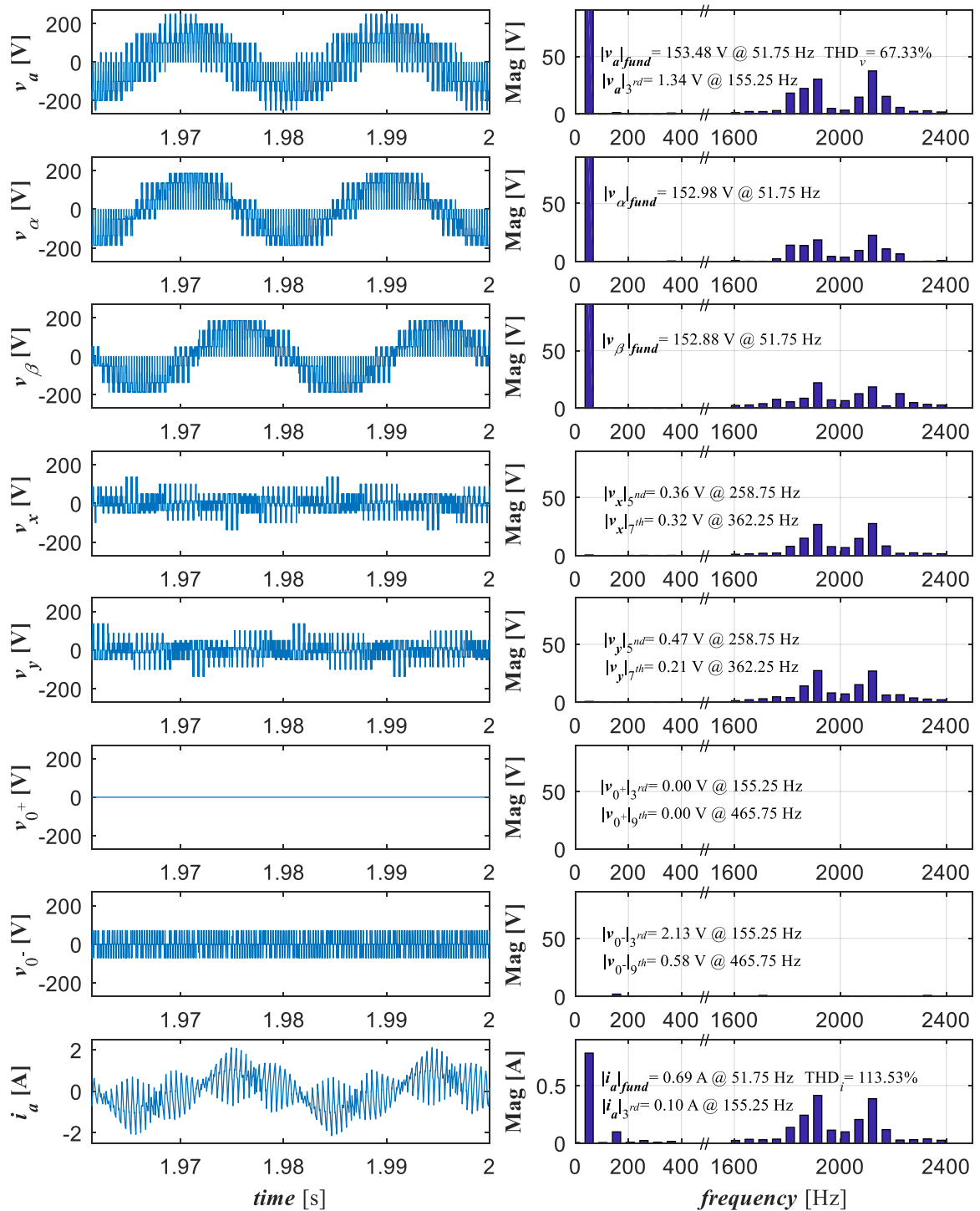


Figure 5.15: Phase 'a' voltage, phase voltage components ( $v_a$ ,  $v_\beta$ ,  $v_x$ ,  $v_y$ ,  $v_0^+$  and  $v_0^-$ ), phase 'a' current and corresponding spectra of SinCMI for the machine driven by inverter with built-in dead time at  $m_i = 1.035$ .

of 67.33%, while  $|i_a|_{fund}$  is 0.69 A with  $THD_i$  of 113.52%. Note that,  $|v_a|_{fund}$  and  $|i_a|_{fund}$  are slightly lower when compared to the previous results when the machine is driven by the ideal inverter. This is clearly due to the uncompensated inverter dead time. The resulting voltage error caused by the dead time will decrease  $|v_a|_{fund}$  and it becomes more obvious at lower values of  $m_i$ . Furthermore, it also contributes to the existence of odd harmonics in  $v_{ph}$  waveforms (Jeong and Park, 1991, Jones et al., 2009a). Recall that low order odd harmonics are mapped onto the  $x$ - $y$  and  $0^+$ - $0^-$  planes. One can see that the magnitudes of the low order harmonics corresponding to  $x$ ,  $y$  and  $0^-$  axes are higher than in ideal case. Moreover, the influence of dead time on rising of the odd harmonics is more apparent in the phase ‘ $a$ ’ voltage and current, e.g. the 3<sup>rd</sup> harmonic, which consequently results in higher  $THD_v$  and  $THD_i$ .

#### 5.4 Drive with two isolated neutral points configuration

In this section, a space vector PWM algorithm and carrier-based PWM technique with min-max injection based on dual two-level three-phase PWM modulators for a two-level asymmetrical six-phase drive with two isolated neutral points configuration, are discussed. The PWM techniques are simulated using PLECS software. Once again, the influence of the inverter dead time was investigated and hence the machine was driven by separate ideal inverter and by an inverter with built-in dead time. Obtained simulation results are presented at the end of this section.

##### 5.4.1 Space vector PWM algorithm

As the name implies, only the configuration of isolated neutral points is changed but the same inverter topology is still used. Thus, the numbers of switching states and space vectors remain the same as previously analysed drive topology i.e. 64 and 63, respectively. In fact, the VSD transformation matrix of (5.1) still holds true for the analysed two-level asymmetrical six-phase drive with two isolated neutral points configuration (Zhao and Lipo, 1995). Therefore, the space vector projections of the analysed drive topology into all three orthogonal planes are as shown in Figure 5.3(a) to 5.3(c). However, the notation of  $0^+$ - $0^-$  plane is changed to  $0_1$ - $0_2$  plane (the sub-script corresponds to the winding set numbering) and each axis of the plane represents CMV of the corresponding winding set. As a result, the low order harmonics of the order of  $3k$  ( $k = 1, 3, 5, \dots$ ) which mapped into this plane will not exist.

Nevertheless, since the neutral points are isolated, the analysed drive topology can be controlled using dual two-level three-phase space vector PWM modulators (D2L3PSV). In

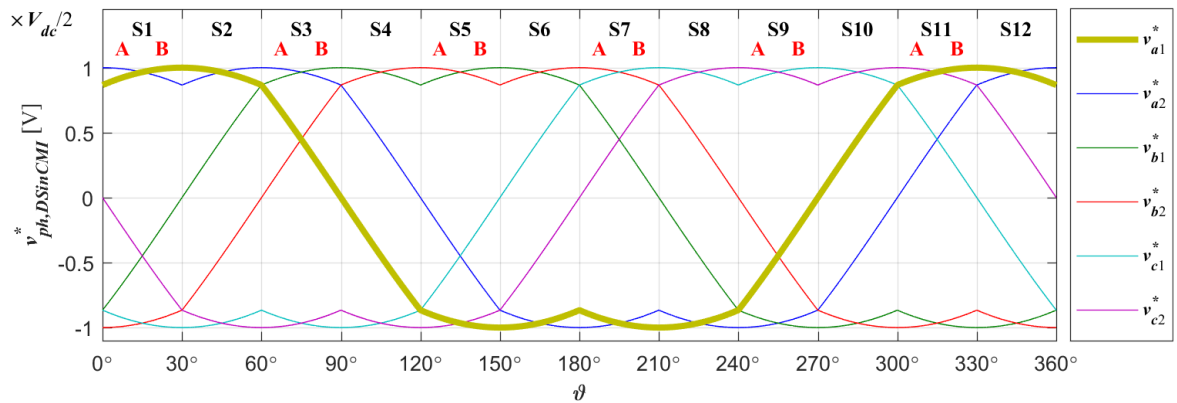


Figure 5.16: Sinusoidal reference output phase voltage waveforms with dual min-max injection ( $v_{ph,DSinCMI}^*$ ) for two-level asymmetrical six-phase drive at  $m_i = 1.154$ .

addition, note that the references for these two space vector PWM modulators have to be shifted by  $30^\circ$  with each other since the stator windings are spatially shifted by  $30^\circ$  between the two winding sets. The maximum  $m_i$  for liner range operation that can be achieved is 1.154. Generally, this indicates the dc-bus can be further utilised up to 15.4% which is also equivalent to the conventional two-level three-phase case.

#### 5.4.2 Carrier-based PWM technique

As the neutral points are isolated, two winding sets can be controlled separately using two two-level three-phase carrier-based PWM modulators (dual modulator). Additionally, a common mode voltage injection technique (DSinCMI) of (5.6) can also be applied into the sinusoidal reference waveforms (three-phase instead of six-phase), of both PWM modulators (Holmes, 1996, Holmes, 1998, Wang, 2002). This yields the maximum modulation index ( $m_i$ ) for the linear range of operation to be 1.154, which is equivalent to dual two-level three-phase SVPWM algorithm, as discussed previously. Additionally, identical performance between DSinDCMI and D2L3PSV is expected. The sinusoidal reference output phase voltage waveforms with dual common mode voltage injection ( $v_{ph,DSinCMI}^*$ ) for the analysed drive topology at  $m_i = 1.154$  are as shown in Figure 5.16.

#### 5.4.3 Simulation results

The same simulation setup as in Figure 5.9 is used to verify the developed PWM techniques for the full linear range of  $m_i$  up to  $m_i = 1.154$ . It should be noted that the same machine model is used and the parameters of the machine model remain the same. However,

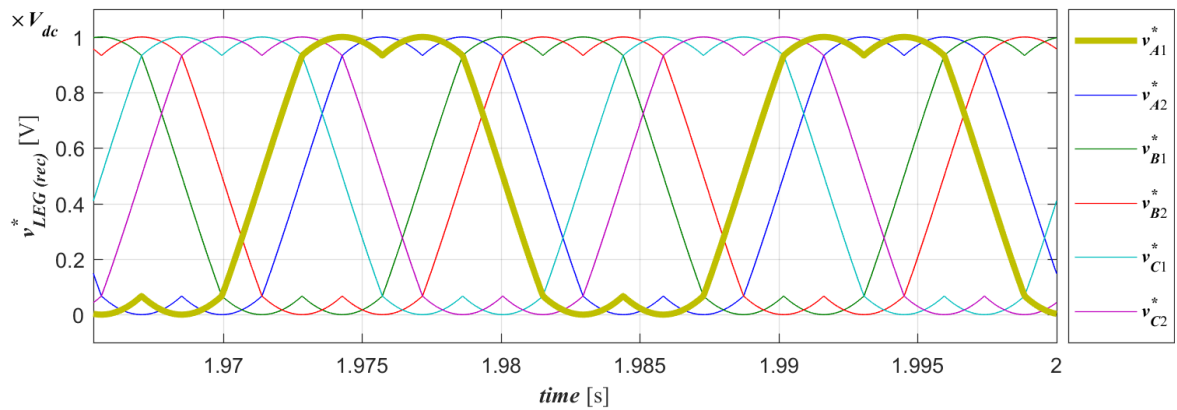


Figure 5.17: Reconstructed reference output leg voltage ( $v_{LEG,rec}^*$ ) waveforms of D2L3PSV at  $m_i = 1.154$ .

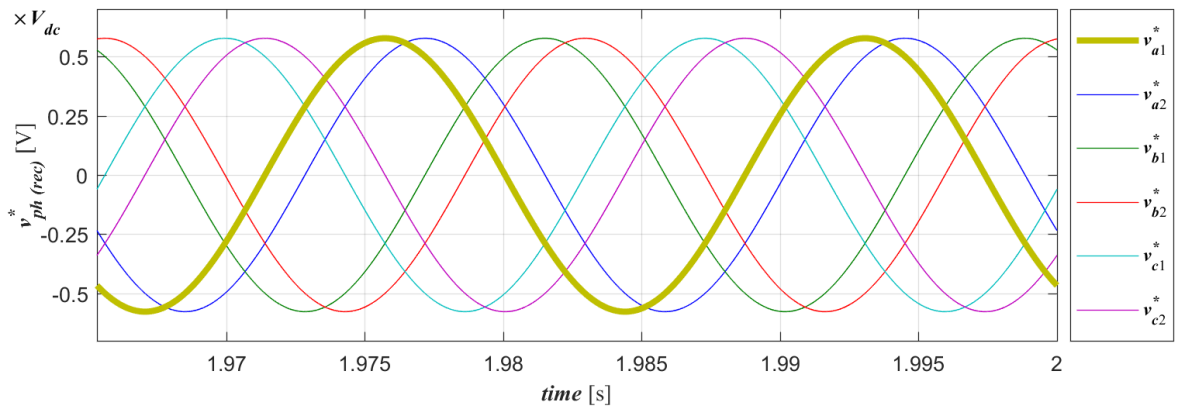


Figure 5.18: Reconstructed reference output phase voltage ( $v_{ph,rec}^*$ ) waveforms of D2L3PSV at  $m_i = 1.154$ .

the neutral point of the machine model needs to be configured as two isolated neutral points. In addition, note that the applied PWM techniques are based on well-established two-level three-phase PWM techniques, thus two identical PWM modulators are used. However, the reference waveforms of the two PWM modulators are shifted by  $30^\circ$ .

The reconstructed leg voltage waveforms ( $v_{LEG,rec}^*$ ) when  $m_i = 1.154$  for D2L3PSV are shown in Figure 5.17. As one might expect, the obtained  $v_{LEG,rec}^*$  waveforms are identical to  $v_{ph,DSinCMI}^*$  shown in Figure 5.16. Moreover,  $v_{ph,rec}^*$  waveforms obtained from (3.6) are sinusoidal as shown in Figure 5.18 and their amplitudes are  $0.577V_{dc}$ , which is in agreement with (3.19).

The phase ‘ $a_1$ ’ voltage,  $v_a$ ,  $v_\beta$ ,  $v_x$ ,  $v_y$ ,  $v_{01}$ ,  $v_{02}$ , and phase ‘ $a_1$ ’ current waveforms of the machine driven by the ideal inverter, as well as their corresponding spectra for the D2L3PSV and DSinCMI, are shown in Figure 5.19 and 5.20, respectively. One can see that both PWM

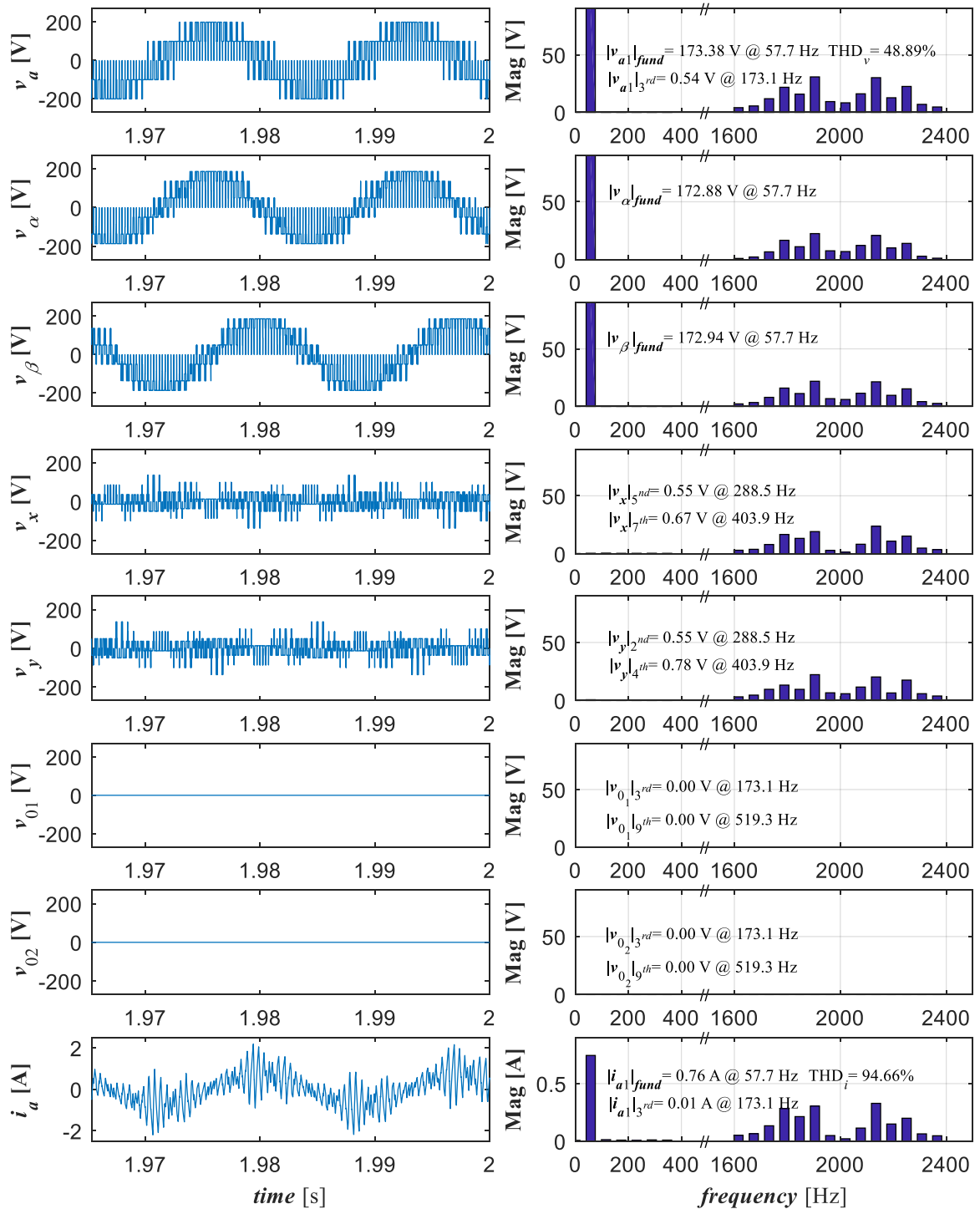


Figure 5.19: Phase 'a1' voltage, phase voltage components ( $v_a$ ,  $v_\beta$ ,  $v_x$ ,  $v_y$ ,  $v_{01}$  and  $v_{02}$ ), phase 'a1' current and corresponding spectra of D2L3PSV for the machine driven by ideal inverter at  $m_i = 1.154$ .

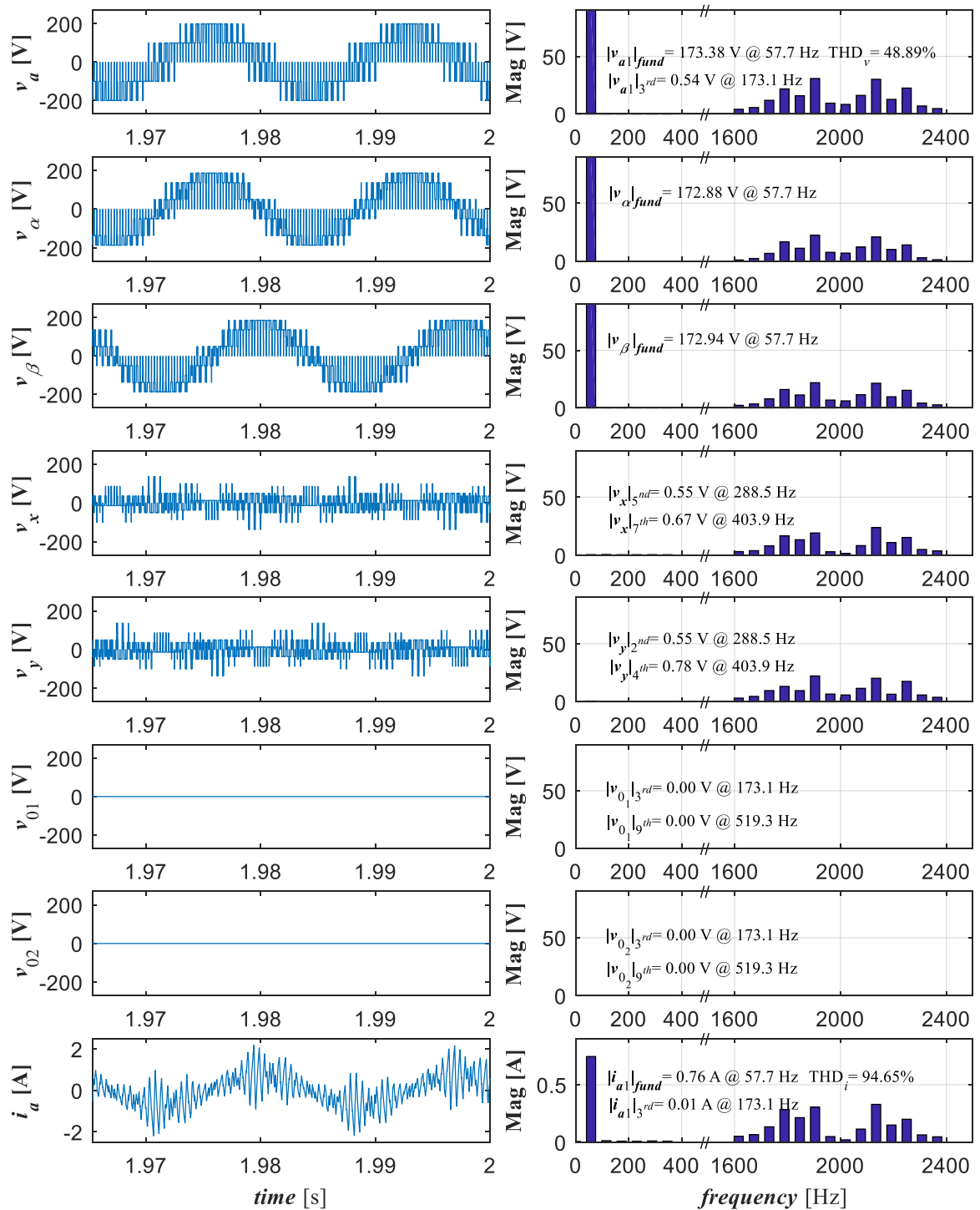


Figure 5.20: Phase ‘ $a_1$ ’ voltage, phase voltage components ( $v_a$ ,  $v_\beta$ ,  $v_x$ ,  $v_y$ ,  $v_{01}$  and  $v_{02}$ ), phase ‘ $a_1$ ’ current and corresponding spectra of DSinCMI for the machine driven by ideal inverter at  $m_i = 1.154$ .

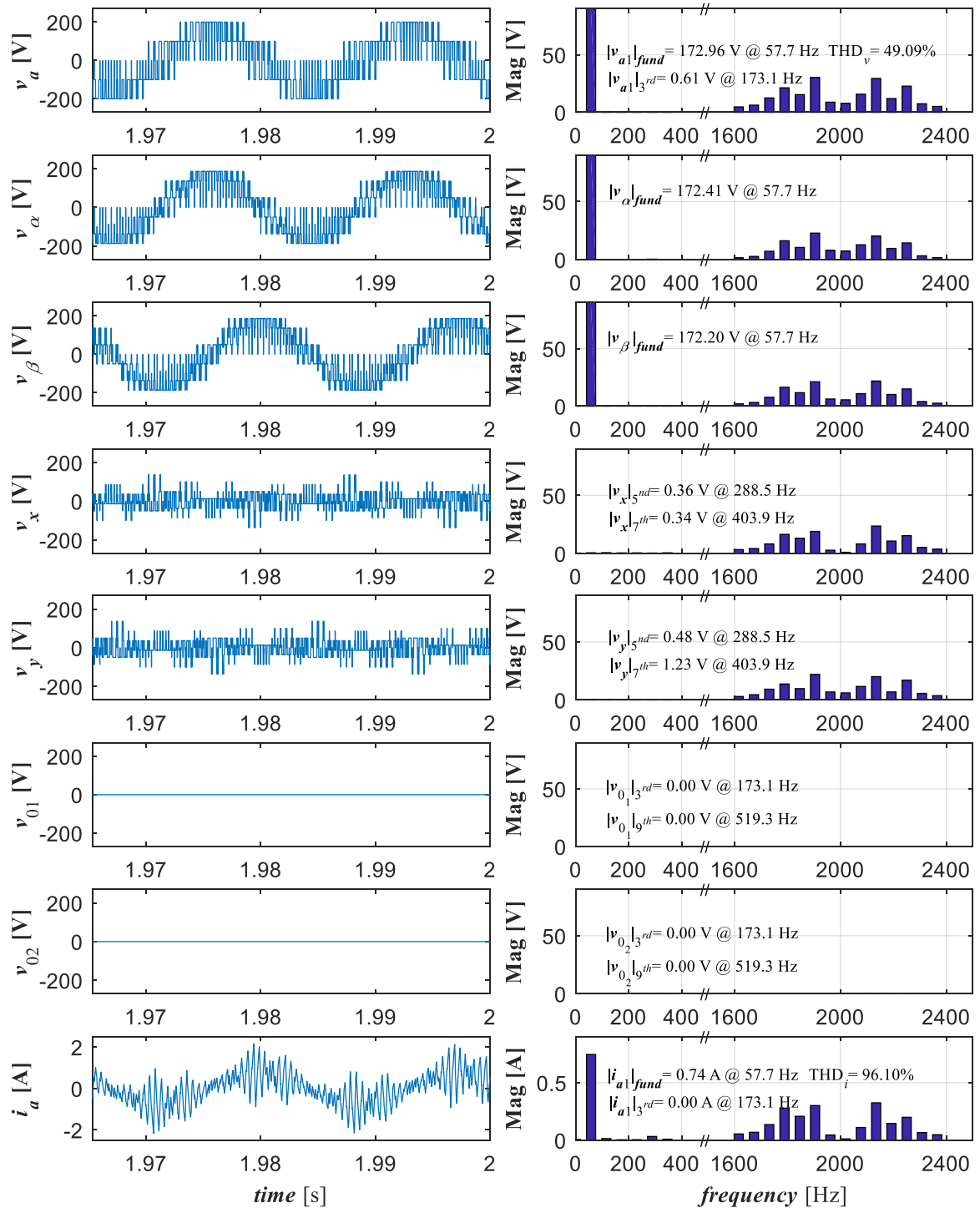


Figure 5.21: Phase 'a1' voltage, phase voltage components ( $v_a$ ,  $v_\beta$ ,  $v_x$ ,  $v_y$ ,  $v_{01}$  and  $v_{02}$ ), phase 'a1' current and corresponding spectra of the D2L3PSV for the machine driven by inverter with built-in dead time at  $m_i = 1.154$ .

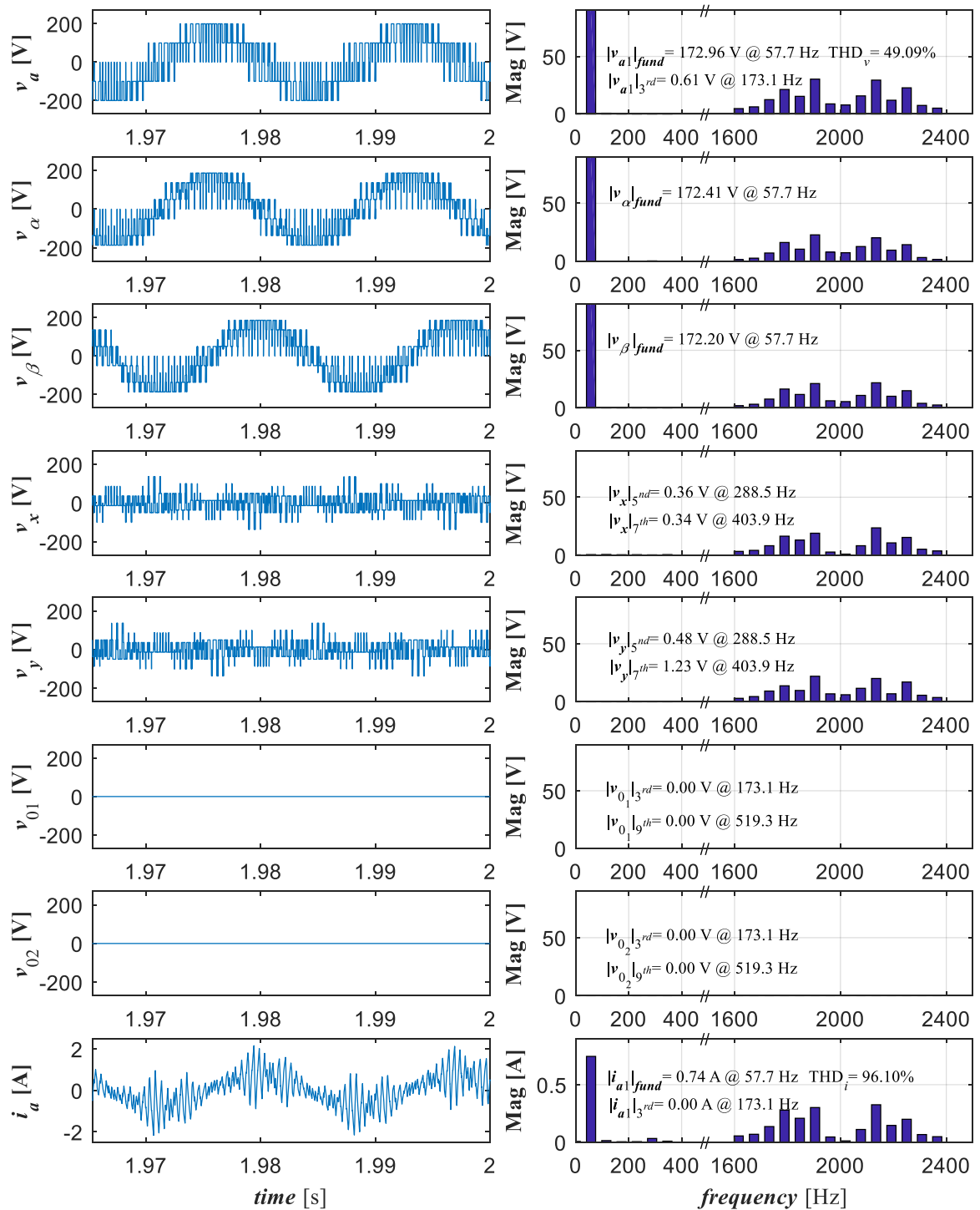


Figure 5.22: Phase 'a<sub>1</sub>' voltage, phase voltage components ( $v_a$ ,  $v_\beta$ ,  $v_x$ ,  $v_y$ ,  $v_{01}$  and  $v_{02}$ ), phase 'a<sub>1</sub>' current and corresponding spectra of the DSinCMI for the machine driven by inverter with built-in dead time at  $m_i = 1.154$ .

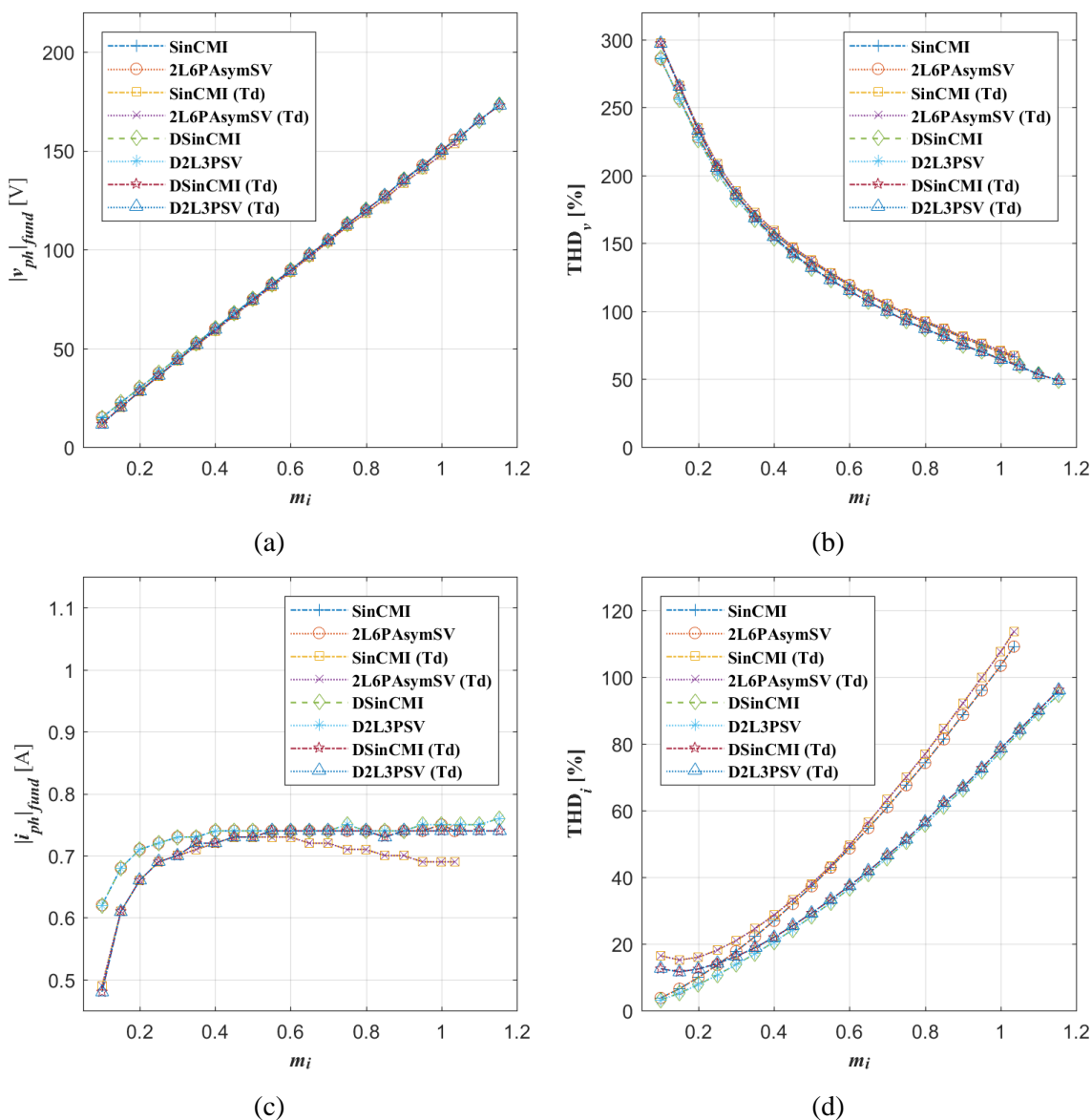
techniques have the same  $|v_{a1}|_{fund}$  of 173.38 V and  $THD_v$  of 48.89%. In fact, even  $|i_{a1}|_{fund}$  and  $THD_i$  are also the same with values of 0.76 A and 94.66%, respectively. Moreover, one can also see that the magnitude of the 5<sup>th</sup> and 7<sup>th</sup> harmonics which are mapped onto the  $x$  and  $y$ ,  $0_1$  and  $0_2$  axes are really small when compared to  $|v_{a1}|_{fund}$ . Additionally, since  $0_1$  and  $0_2$  axes correspond to CMV of each winding set, the 3<sup>rd</sup> and 9<sup>th</sup> harmonics do not exist as can be seen in Figure 5.19 as well as in Figure 5.20. Last but not least, it can be seen that although the low order harmonics in phase ‘ $a_1$ ’ voltage and current do exist, they are relatively small with respect to the corresponding fundamental values i.e.  $|v_{a1}|_{fund}$  and  $|i_{a1}|_{fund}$ .

On the other hand, the phase ‘ $a_1$ ’ voltage,  $v_a$ ,  $v_\beta$ ,  $v_x$ ,  $v_y$ ,  $v_{01}$ ,  $v_{02}$ , and phase ‘ $a_1$ ’ current waveforms including the spectra of the machine driven by the inverter with built-in dead time for both PWM techniques, at  $m_i = 1.154$ , are shown in Figure 5.21 and 5.22. When compared to the ideal case, due to the influence of dead time, the obtained  $|v_{a1}|_{fund}$  decreases slightly to 172.96 V while  $THD_v$  increases to 49.09%. The same situation can be observed for  $|i_{a1}|_{fund}$  and  $THD_i$  with values of 0.74 A and 96.10%, respectively. However, the odd order harmonics, which are produced due to the dead-time effect, especially those that are mapped into  $0_1$ - $0_2$  plane (e.g. 3<sup>rd</sup>, 9<sup>th</sup> harmonics), do not exist since the neutral points are isolated. Additionally, unlike the drive with a single neutral point where the  $0^-$  current component as well as the corresponding harmonics can flow between the two winding sets, this is not the case here. Therefore, the magnitude of the third current harmonic ( $|i_{a1}|_{3rd}$ ) remains the same as in the ideal case.

## 5.5 Performance comparison between the modulation techniques with both neutral point configurations

The performance of all modulation strategies is determined by calculating the  $THD_v$  and  $THD_i$  using (3.20). This is so since THDs are the most suitable indicators for determining the performance of modulation strategies of multiphase drives (Dordevic et al., 2015). Furthermore, in order to confirm the validity of the developed modulation strategies, the magnitudes of the obtained fundamental output phase voltages ( $|v_{ph}|_{fund}$ ) are observed and compared to the corresponding reference values ( $V_f^*$ ). The obtained  $|v_{ph}|_{fund}$ , the magnitudes of the obtained fundamental output phase current ( $|i_{ph}|_{fund}$ ), the calculated  $THD_v$  and  $THD_i$ , for the full linear range of  $m_i$ , of all discussed modulation strategies, are shown in Figure 5.23.

In Figure 5.23(a), one can see that the obtained  $|v_{ph}|_{fund}$  increases linearly as  $m_i$  increases.



Applied PWM techniques for single neutral point case:

SinCMI	Sinusoidal PWM with common mode voltage injection
2L6PAsymSV	Space vector algorithm using time matrix approach

Applied PWM techniques for two neutral points case:

DSinCMI	Dual sinusoidal PWM with common mode voltage injection
D2L3PSV	Two-level three-phase space vector algorithm (dual modulators)

Note: Td – denotes that the inverter dead-time is considered in the simulation

Figure 5.23: The performance of applied modulation strategies for full linear range of  $m_i$  based on:

(a) obtained  $|v_{ph}|_{fund}$  (b) calculated  $THD_v$  (c) obtained  $|i_{ph}|_{fund}$  and (d) calculated  $THD_i$ .

In other words, the obtained  $|v_{ph}|_{fund}$  are the same as the expected  $V_f^*$  for the full linear range of  $m_i$ , hence confirming the validity of the applied modulation strategies. In addition, one can also observe the influence of the inverter dead time over the modulation strategies. Although its influence is trivial in  $|v_{ph}|_{fund}$  and  $THD_v$  (Figure 5.23(b)), it is more obvious in  $|i_{ph}|_{fund}$  and  $THD_i$  particularly in range of lower modulation index values, as is obvious from Figure 5.23(c) and 5.23(d). From Figure 5.23(c), one can see that the current magnitude is practically constant for modulation indices over  $m_i = 0.3$ . This is expected because constant  $V/f$  control is used. However, the lower values for small modulation indices are the consequence of non-implemented boost voltage (which would compensate voltage drop across the stator resistance).

From Figure 5.23(d), one can see that the influence of the dead time on the  $THD_i$  is not so significant. However, it can be seen that when the neutral points are isolated, the  $THD_i$  is much lower. This is expected since the largest low order harmonic i.e. 3<sup>rd</sup> harmonic which mostly contributes to higher  $THD_i$  is relatively smaller in this case compared to the one in single neutral point case (comparison between Figure 5.14 and 5.15 with Figure 5.21 and 5.22). In addition, this is also due to the mapping of the 3<sup>rd</sup> harmonic onto the  $0_1-0_2$  plane, where for  $v_{ph}$ , it is zero.

All in all, by comparing the applied modulation strategies between the drive with a single (i.e. 2L6PAsymSV and SinCMI) and two (i.e. D2L3PSV and DSinCMI) isolated neutral points configurations, the D2L3PSV and DSinCMI are the best in terms of performance. This is predominantly because of the increased modulation index range, reduced influence of the dead-time effect on the magnitude of the current fundamental, lower  $THD_i$ , and finally because of simpler implementation of the modulators.

## 5.6 Summary

Several PWM techniques for two different configurations of two-level asymmetrical six-phase drive, supplied by two-level inverter, are presented in this chapter. The discussed PWM techniques are based on space vector algorithm and carrier-based approach. The development of space vector PWM algorithm, especially for the analysed drive with single neutral point configuration – 2L6PAsymSV, is discussed in detail. In order to realise the desired sinusoidal output phase voltage waveforms, the space vectors for the switching sequences are chosen through equivalent leg voltage space vector projections in the  $\alpha-\beta$ ,  $x-y$  and  $0^+-0^-$  planes. However, these projections cannot be achieved using the known VSD transformation matrix. Therefore, a new rotational transformation is applied onto  $0^+-0^-$  plane such that the  $0^+$  axis

components are always zero. In addition, the rotated  $0^+$  axis represents CMV which is normally not considered in space vector algorithms.

The 2L6PAsymSV and the other PWM techniques are verified using PLECS software for the full obtainable linear range of modulation index. The simulations are run in open loop. Obtained simulation results show that the developed space vector algorithm has the same performance as the carrier-based approach when min-max injection is used. Also, it may be concluded that, D2L3PSV and DSinCMI modulation strategies (when two neutral points are isolated) yield slightly better performance, as they offer much higher dc-bus utilisation and lower  $THD_i$ , when compared to the 2L6PAsymSV and SinCMI (when a single neutral point is used).



---

## CHAPTER 6

### PWM techniques for three-level asymmetrical six-phase drives

---

#### 6.1 Introduction

This chapter presents space vector and carrier-based PWM techniques for three-level asymmetrical six-phase drives. More attention is given towards the development of a space vector algorithm for the drive with a single neutral point where a novel method of selecting the correct switching sequences is proposed based on permutation of the potential switching states. All considered modulation techniques are developed and verified in open loop using PLECS software. Experimental validations for the drive with single and two neutral points configurations are also included. Finally, the performance of the presented PWM techniques is compared based on calculated phase voltage and current total harmonic distortion.

Original contribution of this chapter, in particular of sub-section 6.3.1, has been presented in a conference paper (Engku Ariff et al., 2017b).

#### 6.2 Power circuit topologies

The power circuit topologies of the three-level asymmetrical six-phase drive, with single and two neutral point configurations, are shown in Figure 6.1 and Figure 6.2, respectively. The notation used for the machine and the inverter in Chapter 4 is also applied here. Similarly, the equations, which describe the relationship between the output leg voltages ( $v_{LEG}$ ) and the output phase voltages ( $v_{ph}$ ) as in (3.1) to (3.6), are also valid for the corresponding drive topologies.

#### 6.3 Drive with single neutral point configuration

The development of novel space vector PWM technique (3L6PAsymSV) and its equivalent carrier-based technique, in-phase disposition with double min-max injection (PD2CMI), for a three-level asymmetrical six-phase drive with single neutral point, are presented in this section. Obtained simulation and experimental results of the two methods are shown at the end of this section confirming the validity of the developed algorithms.

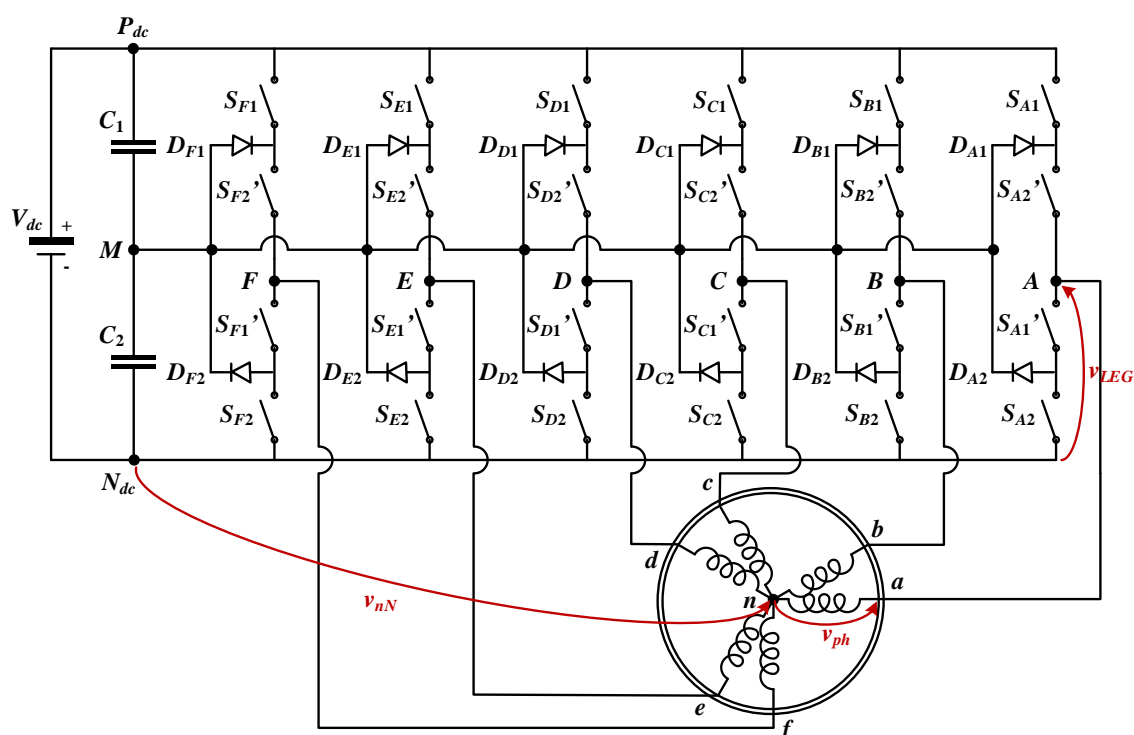


Figure 6.1: Power circuit topology of three-level asymmetrical six-phase drive with single neutral point.

### 6.3.1 Space vector PWM algorithm

In this sub-section, a process of developing a novel space vector algorithm for a three-level asymmetrical six-phase drive with a single neutral point is presented. The voltage space vectors are chosen such that the application of the resultant switching sequences, for their corresponding calculated dwell times, obtains sinusoidal output phase voltage waveforms. Due to asymmetry of the drive, the process of selecting the switching sequences becomes more difficult. Therefore, a permutation method, where all remaining space vectors are considered as potential subsequent space vectors in a switching sequence, is proposed to solve this issue.

#### 6.3.1.1 Projection of space vectors

Since the inverter topology analysed in this chapter is identical to the one in Chapter 4, the possible  $v_{LEG}$  levels and the number of possible switching states are the same. The possible  $v_{LEG}$  levels are 0,  $V_{dc}/2$ ,  $V_{dc}$  and the high impedance output. Note that the high impedance state is not considered, and hence the number of possible switching states is  $3^6 = 729$ . These switching states can be further denoted from 0 to 728. In addition, they can also be represented in ternary numeral system as 000000 to 222222 by normalising them with  $V_{dc}/2$ .

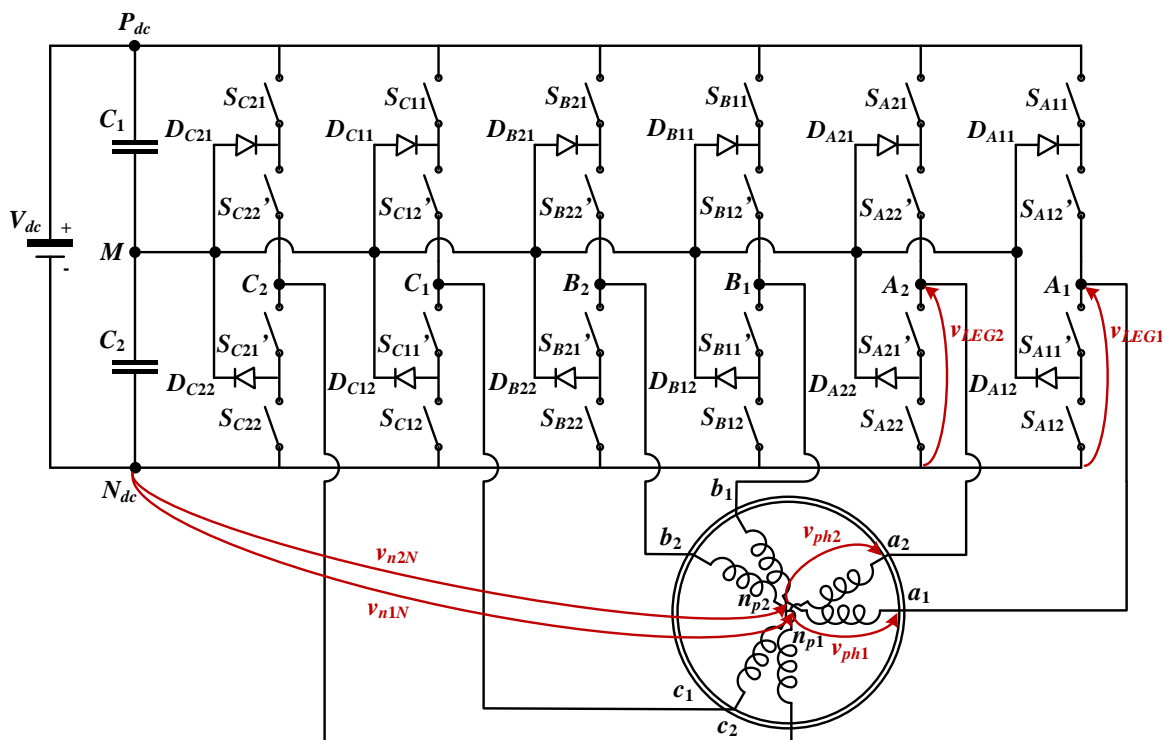


Figure 6.2: Power circuit topology of three-level asymmetrical six-phase drive with two isolated neutral points.

By substituting the normalised form of the switching states into (5.1), the projection of  $v_{LEG}$  space vectors onto the three orthogonal planes ( $\alpha$ - $\beta$ ,  $x$ - $y$  and  $0^+$ - $0^-$  planes) can be obtained (Zhao and Lipo, 1995). The projection of  $v_{ph}$  space vectors onto these planes can also be obtained in a similar way by substituting (3.3) into (5.1). The projections of these space vectors are shown in Figure 6.3(a) to 6.3(c). It should be noted that mapping of the low order harmonics into these three planes remains the same as in the two-level case presented in Chapter 5. So, the low order harmonics of the order of  $12k \pm 1$  and  $12k \pm 5$  ( $k = 0, 1, 2, 3, \dots$ ) are mapped into  $\alpha$ - $\beta$  and  $x$ - $y$  plane, respectively, while the low order harmonics of the order of  $3k$  ( $k = 1, 3, 5, \dots$ ) are mapped into  $0^+$ - $0^-$  plane. One finds that the number of  $v_{LEG}$  and  $v_{ph}$  space vectors is 729 and 665, respectively. As can be seen in Figure 6.3(c), the difference in the number of space vectors between the two lies in the  $0^+$ - $0^-$  plane, where the projections of  $v_{ph}$  space vectors are shown as red dots. Therefore, it can be said that several corresponding switching states produce identical projection of  $v_{ph}$  space vectors in those three planes. In other words, there is redundancy in the switching states.

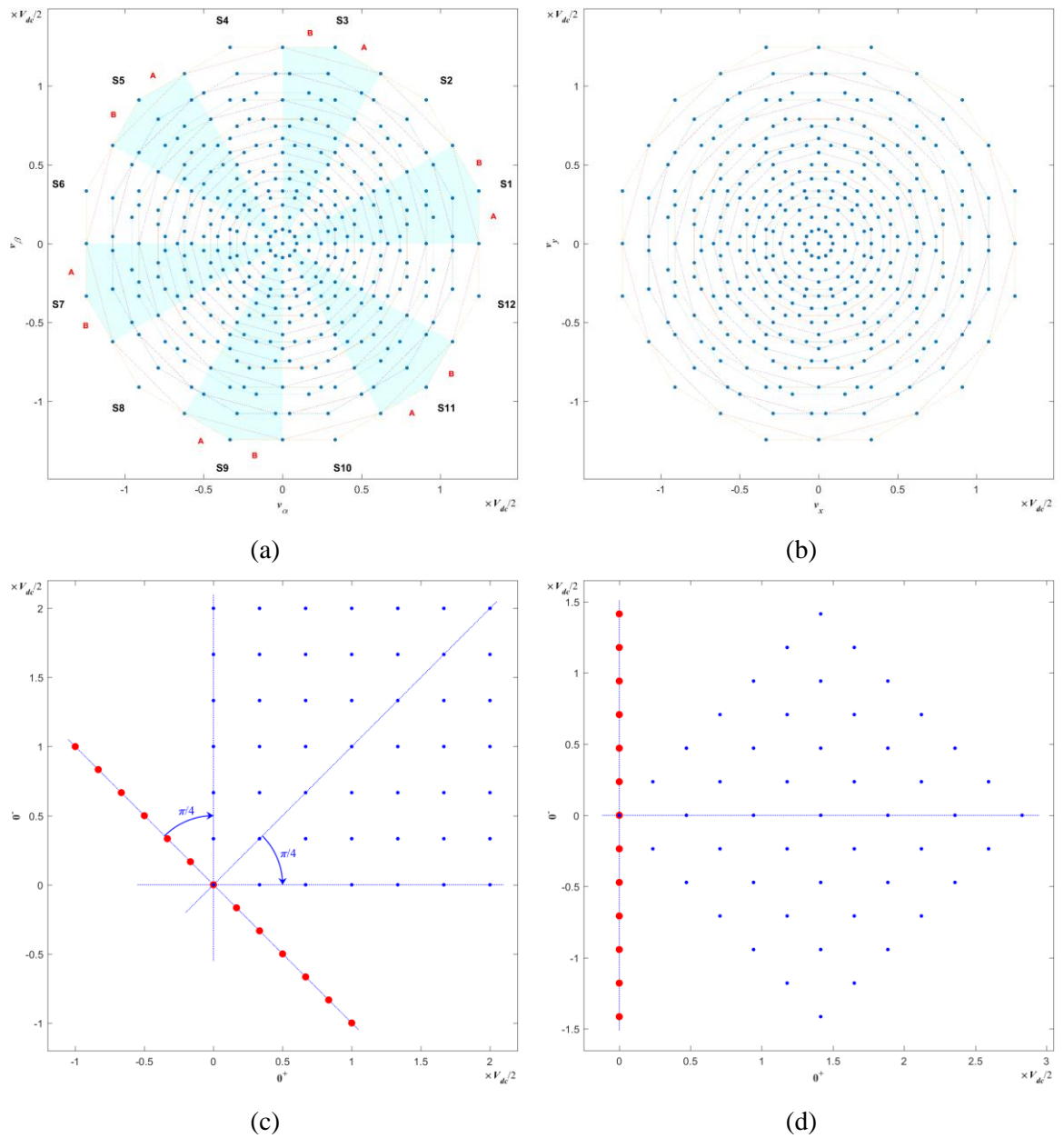


Figure 6.3: Projection of  $v_{LEG}$  and  $v_{ph}$  space vectors of the analysed three-level asymmetrical six-phase drive with single neutral point in the: (a)  $\alpha$ - $\beta$  (b)  $x$ - $y$ , (c)  $0^+-0^-$  and (d)  $0^+-0^-$  plane after rotational transformation of  $-\pi/4$ .

As explained in Chapter 5, in order to develop a space vector modulation algorithm for the analysed drive topology, it is more beneficial to use the transformation matrix of (5.3) as previously discussed in sub-section 5.3.1.3. The projection of  $v_{LEG}$  and  $v_{ph}$  space vectors onto the rotated  $0^+-0^-$  plane is shown in Figure 6.3(d). By rotating  $0^+-0^-$  plane, it reduces the analysed drive topology to a five-dimensional system and the  $0^+$  axis now represents CMV. Since CMV is normally not being considered in space vector algorithm, the realisation of sinusoidal  $v_{ph}$  waveforms can be achieved through switching sequences chosen based on  $v_{LEG}$  space vectors.

### 6.3.1.2 Reduction of the number of space vectors

Even though the total number of  $v_{ph}$  space vectors is large, not all of them can be chosen in order to achieve the desired sinusoidal  $v_{ph}$  waveforms. These  $v_{ph}$  space vectors can be identified using the order-per-sector law (Gao and Fletcher, 2010).

As the projected  $v_{ph}$  and  $v_{LEG}$  space vectors are identical in  $\alpha$ - $\beta$  plane, the order-per-sector law can be implemented by simply comparing the order of the normalised  $v_{LEG}$  levels in the switching states (when represented in six-digit ternary numeral system) with the order of  $v_{ph}^*$  in the time domain. As an example, one can see from Figure 5.4 (these references are for asymmetrical six-phase machine, and hence are valid in this chapter as well), that the order of  $v_{ph}^*$  in the first section of the first sector (S1-A) is  $v_a^* \geq v_b^* \geq v_f^* \geq v_c^* \geq v_e^* \geq v_d^*$ . Moreover, it can be shown that  $v_{ph}$  space vector corresponding to the switching state 651 (220010) is also projected within S1-A sector. Thus, by comparing the order of the normalised  $v_{LEG}$  levels of the switching state 651 with the order of  $v_{ph}^*$  in S1-A, clearly switching state 651 does not meet the condition and hence is discarded. As a result, the numbers of  $v_{LEG}$  and  $v_{ph}$  space vectors can be significantly reduced i.e. from 729 to 195 and from 665 to 163, respectively. The remaining  $v_{LEG}$  and  $v_{ph}$  space vector projections, after the order-per-sector law, in  $\alpha$ - $\beta$ ,  $x$ - $y$ ,  $0^+$ - $0^-$  and rotated  $0^+$ - $0^-$  plane are shown in Figure 6.4.

### 6.3.1.3 Determination of potential switching sequences

With the aim of realising sinusoidal  $v_{ph}$  waveforms, the selection of  $v_{LEG}$  space vectors and the corresponding switching states has to meet several general requirements and conditions. One of the main requirements is that the average value of  $x$ - $y$  plane and  $0^-$  axis component must be zero in each switching period. Furthermore, in order to minimise switching losses and  $dv/dt$ , it is desirable that the  $v_{LEG}$  levels only increase by one level per transition in the first half of the switching period and decrease by one level per transition in the second half (van der Broeck et al., 1988). This will result in having symmetrical PWM switching signals within a switching period. Since the transition of  $v_{LEG}$  levels in the second half of the switching period is just the opposite of the first half, it is adequate to consider only the first half of switching period in the selection process of the switching sequences.

On one hand, there are six  $v_{LEG}$  level transitions in the first half of the switching period, which results in having seven switching states in each switching sequence. On the other hand, the number of chosen space vectors in each switching sequence must be equal to the number of

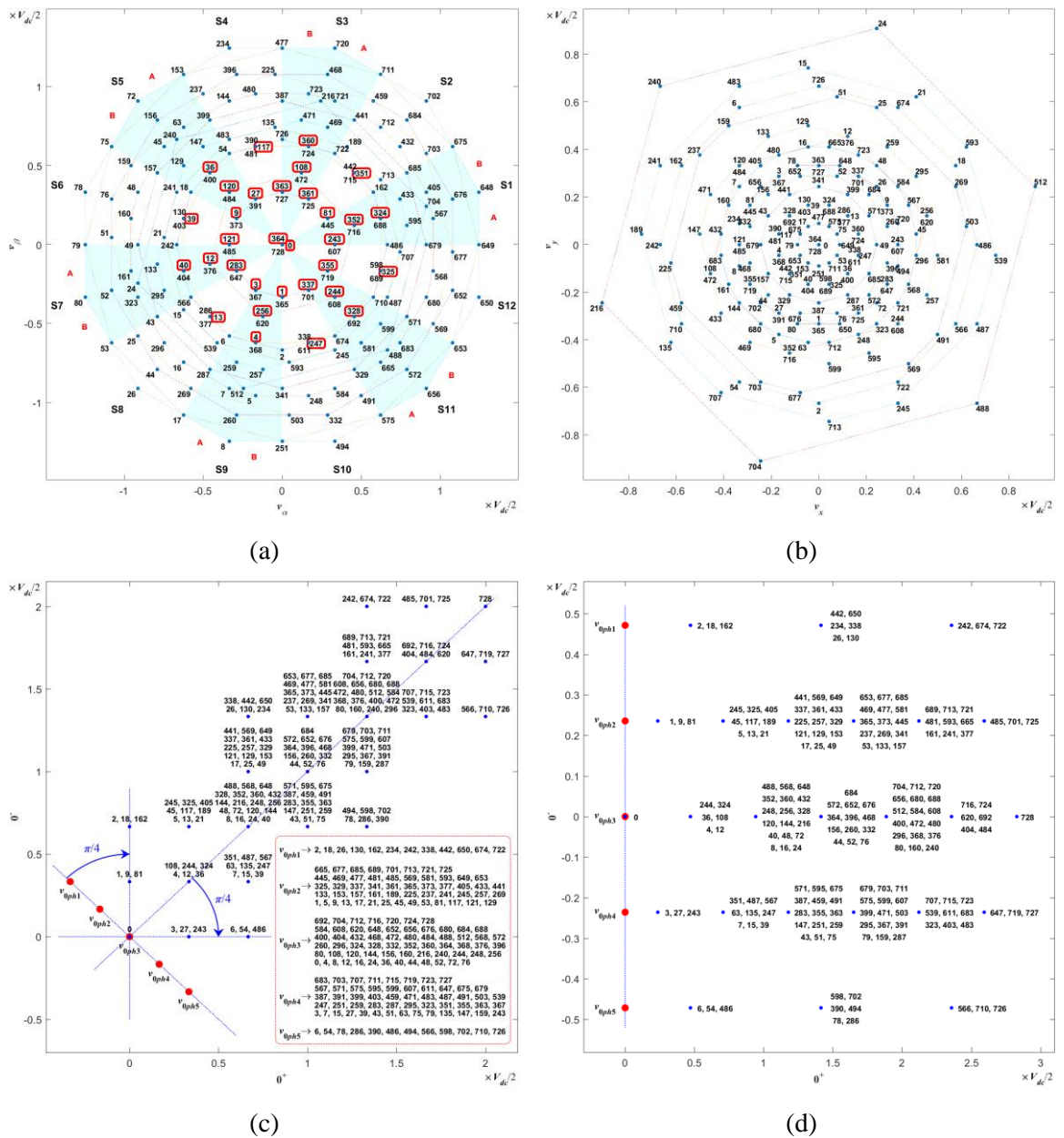


Figure 6.4: Projection of  $v_{LEG}$  and  $v_{ph}$  space vectors of the analysed three-level asymmetrical six-phase drive with single neutral point after order-per-sector in the: (a)  $\alpha\beta$  (b)  $x-y$ , (c)  $0^+-0^-$  and (d)  $0^+-0^-$  plane after rotational transformation of  $-\pi/4$ .

machine phases (Kelly et al., 2003), i.e. six in this case. This indicates that two of the chosen switching states in a switching sequence have identical space vector projections on all considered axes. In fact, these redundant switching states are the first and the last switching states. Therefore, the selection of the starting switching states should consider the existence of the redundant switching state(s). Furthermore, since each  $v_{LEG}$  level increases by one level in each transition, the potential starting switching states can only contain ‘zeros’, ‘ones’ or

combination of the two, for the analysed drive topology (Dordevic et al., 2013b). As a result, only 32 out of 195 remaining switching states (enclosed in the red boxes in Figure 6.4) satisfy the stated requirements and can be chosen as the starting switching states.

Based on the conditions that each leg voltage changes its level and that each transition represents one-level increment, one can easily determine the subsequent switching states in the sequence. Normally, space vectors corresponding to the switching sequence are projected into the same sector in  $\alpha$ - $\beta$  plane as the space vector of the starting switching state (Dordevic et al., 2013a, Dordevic et al., 2013b, Engku Ariff et al., 2017a). Yet, for the analysed asymmetrical six-phase drive topology, this is not the case. In fact, one finds that this situation can clearly be seen in Figure 5.5(a). Moreover, because the three-level drive topology can be observed as an extension of the two-level asymmetrical six-phase drive, in terms of the number of leg voltage levels, it can be shown that all of switching sequences from Figure 5.6 are also potential switching sequences for the analysed drive topology. However, they represent only a small portion of the full set of potential switching sequences available in the three-level topology. Therefore, in order to overcome this situation, a new method for switching sequence determination is proposed. In this method, all remaining space vectors i.e. corresponding switching states (regardless of their sector position) are considered as candidates for the subsequent switching state.

Since there are six  $v_{LEG}$  transition levels in a switching sequence, thus there are  $6! = 720$  possible permutations of switching sequences per selected starting switching state. In total, there are 23040 switching sequences that need to be considered as potential switching sequences. However, not all of them are suitable. Some of the switching sequences comprise switching states which have been previously eliminated by the order-per-sector law. Therefore, one gets that the number of potential switching sequences is less than 720 per starting switching state. Due to the immense number of potential switching sequences as well as the combinations of switching states that have to be considered, a permutation method is developed in Matlab, to ease the selection process.

As an example, only 102 out of 720 permutations, i.e. switching sequences, starting with switching state 324 (110000), include the remaining switching states after the order-per-sector law implementation. All possible single level  $v_{LEG}$  transitions of these 102 potential switching sequences are illustrated with different colour arrows (each colour represents one-level transition in a different inverter leg), as shown in Figure 6.5. Only transitions in  $\alpha$ - $\beta$  plane are shown although each of these 102 potential switching sequences produce unique transition

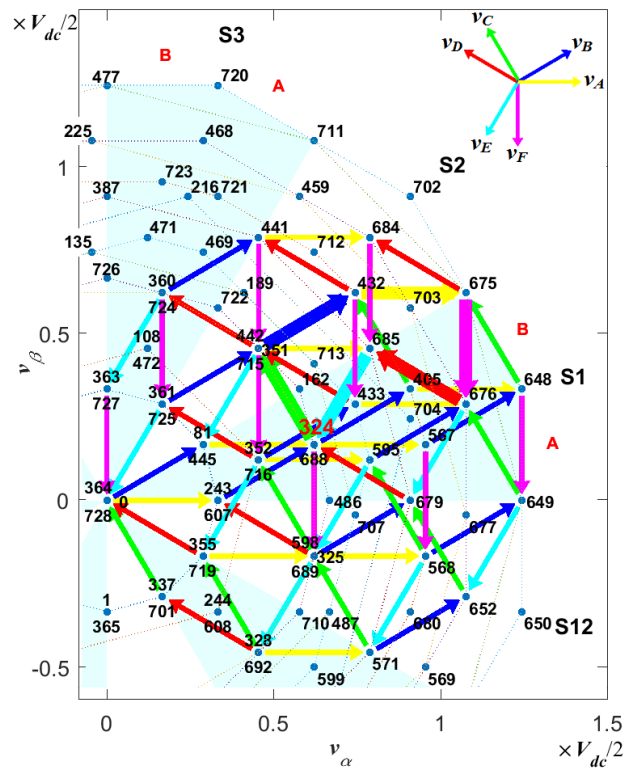


Figure 6.5: All possible single level increasing transitions of  $v_{LEG}$  for starting switching state 324 (110000).

patterns in  $\alpha$ - $\beta$ ,  $x$ - $y$  and  $0^+$ - $0^-$  plane. It should be noted that due to the numerous potential switching sequences, that could be obtained from the other starting switching states, there is a high possibility of having identical transition patterns belonging to different potential switching sequences. This causes redundancy of potential switching sequences.

One finds that not all potential switching sequences can satisfy the requirement that the values of  $x$ - $y$  and  $0^+$ - $0^-$  plane components are zero on average. By using the graphical analysis proposed in (Gao and Fletcher, 2010), and observing the location of the transition patterns in  $x$ - $y$  and  $0^+$ - $0^-$  planes (and the possibility to give zero on average), the number of potential switching sequences can be reduced further. As an example, for potential switching sequences with starting switching state 324, only 54 out of 102 satisfy the stated requirement. One can show that this graphical method is not sufficient for complete determination of the potential switching sequences for the analysed drive topology. This is because the graphical requirement for obtaining zero value on average may be satisfied in each plane ( $x$ - $y$  and  $0^+$ - $0^-$ ) independently, but the solutions do not overlap. Therefore, a method, which relies on a numerical solution, is directly applied and this method will be addressed further in the following sub-section.

Finally, it is worth that to mention, since the permutation method determines the potential switching sequences by taking into account all possible  $v_{LEG}$  single-level transitions, for each identified starting switching state, it is also valid for the other drives with any number of inverter levels and machine phases.

### 6.3.1.4 Calculation of dwell times and sector division

The dwell times typically refer to the duration of the applied space vectors in any chosen switching sequence. Thus, the calculation of the dwell times is based on space vector projections of the respective switching sequence rather than on the sequence itself. Hence, each transition pattern (which may have several corresponding redundant switching sequences) yields different value of the dwell times. Consequently, the switching sequences that correspond to the same transition patterns will have the same value of dwell times (Dordevic et al., 2013b). The dwell times can be calculated using the standard volt-second balance principle as well as time balancing equation, which can be put in matrix form as in (5.4). Note that the same conditions as in Chapter 5 remain valid for the analysed drive topology as well. Therefore, the CMV is not considered, and  $0^+$  axis is replaced with time balancing equation. The references for  $v_a^*$ ,  $v_\beta^*$ ,  $v_x^*$ ,  $v_y^*$ , and  $v_0^*$  are set to  $V_f^* \cdot \cos(\omega t)$ ,  $V_f^* \cdot \sin(\omega t)$  and zero for the rest. Lastly, the calculated dwell time for the first space vector,  $T_1$ , is equally shared between the first and the seventh switching state.

One finds that the solutions for the dwell times of some transition patterns only exist in certain regions in the  $\alpha$ - $\beta$  plane. These regions are commonly known as regions of application and can be identified either using analytical calculation (Gao and Fletcher, 2010) or by visualisation of numerical solutions of (5.4) in  $\alpha$ - $\beta$  plane (Dordevic et al., 2013b). As in the previous chapters, the latter method is adopted. The visualisation of numerical solutions is represented by consecutive dots, where the dot indicates the location of the applied  $v_a^*$  and  $v_\beta^*$  pair, if the solution of (5.4) does exist. In essence, while gradually increasing the magnitude  $V_f^*$  from zero to  $0.644V_{dc}$  (from the origin until the circumradius of the largest polygon in  $\alpha$ - $\beta$  plane), the dwell times of each transition pattern are repetitively calculated with the help of Matlab code. If a solution for dwell times exists, a dot is plotted at the current values of  $v_a^*$  and  $v_\beta^*$ . As an example, transition pattern denoted by the thick arrows in Figure 6.5, which corresponds to switching sequence [324 351 432 675 676 685 688] i.e. [110000-111000-121000-221000-221001-221101-221111], produces a region of application illustrated by dots (in gradient blue) in Figure 6.6.

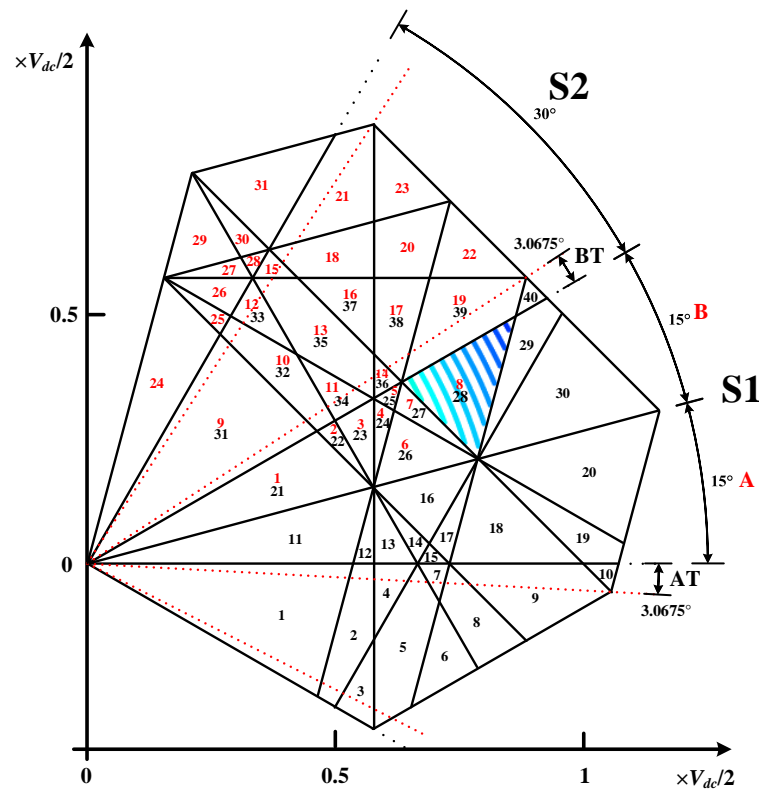


Figure 6.6: Regions of application of all possible transition patterns for starting switching state 324 (110000) and 351 (111000). The AT and BT are the additional sectors introduced later for switching sequence optimisation (see sub-section 6.3.1.5).

One finds that only 40 out of 102 potential switching sequences, i.e. transition patterns obtained from starting switching state 324, have solutions for the dwell-times calculation. This proves the inadequacy of the graphical method in determining the final set of switching sequences (where the reduction was done only up to 54 switching sequences). Besides, those 40 switching sequences also form 40 unique regions of application, as shown in Figure 6.6 (denoted from 1 to 40). In addition, they also divide the sectors into several geometrical shapes. Hence, the regions of application also represent sub-sectors. However, the regions of application can also correspond to the potential switching sequences obtained from the other starting switching states. As an example, the regions of application of the switching sequences obtained from starting switching state 351 (111000) which are identified in a similar way are also shown in Figure 6.6 (denoted from 1 to 31 in red).

It can be clearly seen that several regions of application can be associated to potential switching sequences either with starting switching state 324 or 351. Since the existence of regions of application is unique to transition patterns, this indicates that several switching

sequences form identical transition patterns in  $\alpha$ - $\beta$ ,  $x$ - $y$  and  $0^+$ - $0^-$  planes. Hence, this confirms that there are redundancies among potential switching sequences.

### 6.3.1.5 Optimisation of potential switching sequences

The existence of potential switching sequence redundancies gives more freedom in the process of the switching sequence optimisation. The optimisation process is actually based on minimisation of the switching losses, where the switching sequences of all sub-sectors within a sector should have the same starting switching state (McGrath et al., 2003). Thus, during the transition between sub-sectors, additional switching losses can be avoided. However, as can be seen in Figure 6.6, sub-sector 10 and 40 of starting switching state 324 are located outside the first sector (S1) and it can be shown that they also do not have any redundant potential switching sequences. Hence, in order to meet the stated requirement, two additional small sectors, where each consists of eight sub-sectors, are introduced at each side of odd sectors (denoted by AT and BT in Figure 6.6). Essentially, each odd sector comprises A, AT, B and BT sectors, which consequently reducing the size of even sectors.

As an example, the switching sequences of all sub-sectors denoted by A, within sector S1, are listed in Table 6.1. Note that only the switching states in the first half of the switching period are listed in Table 6.1 since the order of the switching states is reversed in the second half. Notice that the starting switching state for all four sub-sectors is the same, 324 (110000). The S1 sub-sectors as well as the other sectors' sub-sectors are shown in Figure 6.7.

In the previous sub-section, it is mentioned that the sub-sectors represent regions where the applied switching sequence and the corresponding dwell times are able to realise sinusoidal

Table 6.1: Potential switching sequences of all sub-sectors in A of S1.

Sector	Potential switching sequences (first half of the switching period)	
	Decimal	Ternary
S1-AT	324-325-328-355-364-607-688	110000-110001-110011-111011-111111-211111-221111
S1-A	324-325-352-355-364-607-688	110000-110001-111001-111011-111111-211111-221111
S1-B	324-351-352-361-364-445-688	110000-111000-111001-111101-111111-121111-221111
S1-BT	324-351-360-361-364-445-688	110000-111000-111100-111101-111111-121111-221111

$v_{ph}^*$  waveforms. Therefore, it can be said that the maximum modulation index,  $m_i$ , for the linear range operation of the analysed drive topology can be determined from the boundary of the sub-sectors in Figure 6.7. As one might expect, the maximum  $m_i$  for linear range operation is 1.035, which is identical as in two-level asymmetrical six-phase drive.

### 6.3.1.6 Determination of sub-sectors

It has been shown that the chosen switching sequences and their corresponding dwell times are highly dependent on the location of projected  $v_{ph}^*$  space vector in  $\alpha$ - $\beta$  plane. But, in time, the projected  $v_{ph}^*$  space vector travels along a circular trajectory and passes through the sectors as well as sub-sectors. Hence, the corresponding switching sequences and calculated

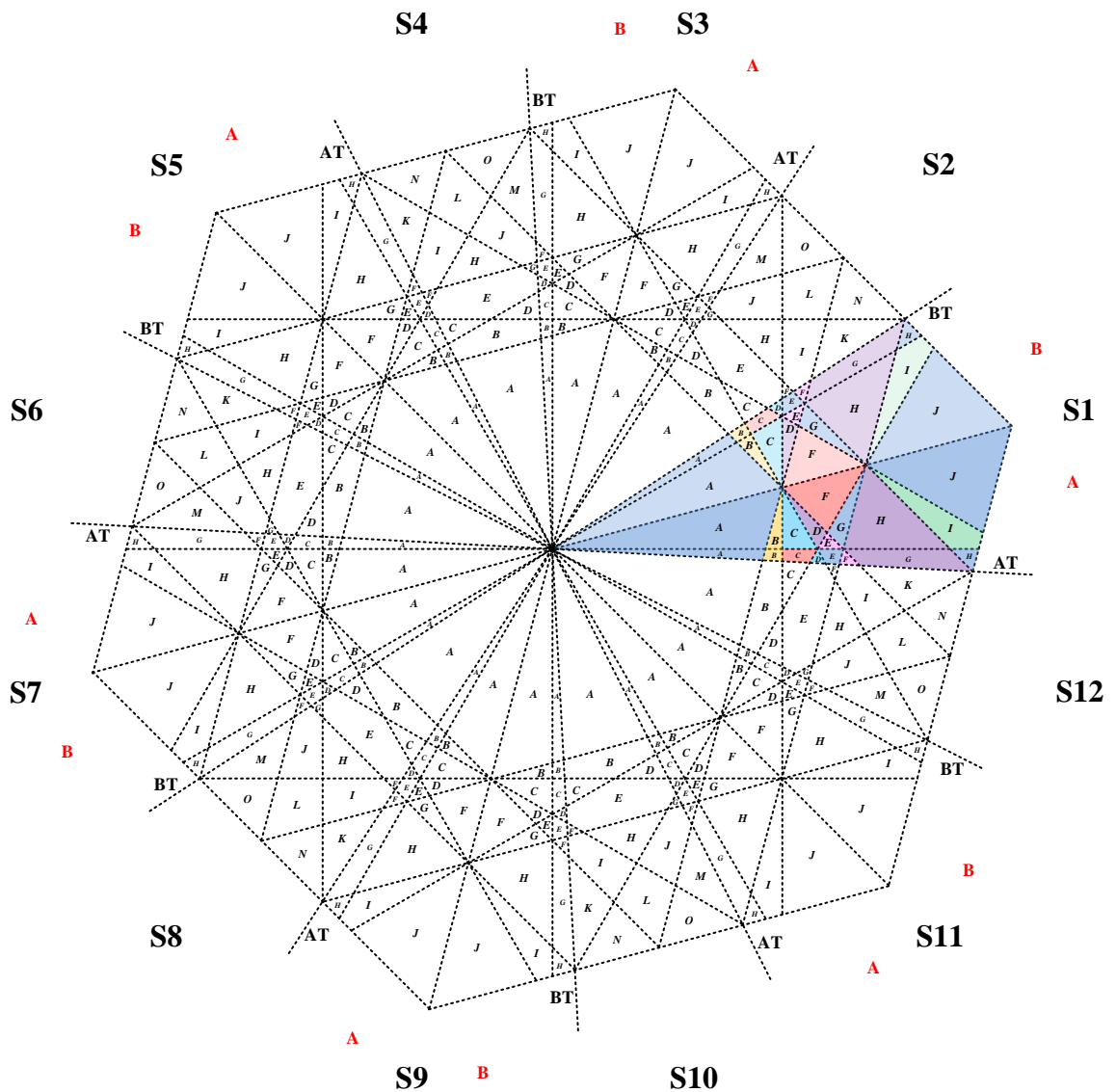


Figure 6.7: Sub-sectors of all twelve sectors in the  $\alpha$ - $\beta$  plane.

dwelling times have to be applied accordingly. In order to accommodate this, a method introduced in (Gao and Fletcher, 2010) where the borders of the sub-sectors are utilised to determine the current location of the projected  $v_{ph}^*$  space vector in the  $\alpha$ - $\beta$  plane is adopted. An illustration of how this method is applied for S1-A is shown in Figure 6.8.

There are nine borders between the sub-sectors of S1-A and these borders can be projected onto six perpendicular axes  $P_1$  to  $P_6$ , respectively. The distances from the intersection points, between the projected borders and those axes, with respect to the origin can be calculated using simple trigonometry. These distances serve as limits and are further denoted as  $L_{11}, L_{21}, L_{22} \dots L_{61}$ . Moreover, one can find that these limits can be segregated into four groups due to some of them having the same value. These four groups (limits) are  $L_{11} = L_{31} = L_{41} = L_{61} = \sqrt{3}/6 V_{dc}$ ,  $L_{21} = L_{51} = \sqrt{2}(\sqrt{3}-1)/4 V_{dc}$ ,  $L_{22} = L_{52} = \sqrt{2}/4 V_{dc}$  and  $L_{23} = \sqrt{2}(\sqrt{3}-1)/2 V_{dc}$ . They are further denoted as  $L_1, L_2, L_3$  and  $L_4$ , respectively.

Similarly, the  $\alpha$  and  $\beta$  components of the  $v_{ph}^*$  space vector can also be projected onto the same perpendicular axes,  $P_1$  to  $P_6$ . The distances between the point of intersections between the two, to the origin (denoted as  $V_1^*$  to  $V_6^*$ ) are calculated and then compared to the limits. As a result, the present location of projected  $v_{ph}^*$  space vector can be accurately determined at any given time instant and hence, the correct switching sequence and corresponding dwelling times can also be applied accordingly. The required conditions in determining the sub-sectors for S1-A are listed in Table 6.2. However, it should be noted that when this method is applied to the other sectors e.g. S1-B, S1-AT etc., the projections of the sub-sectors' borders onto their respective perpendicular axes, i.e. limits, might be different than those shown in Figure 6.8. Therefore, although the previous four limits are also applicable to the other sectors, one has to identify and denote the relevant limits as well as the required conditions accordingly.

### 6.3.1.7 Implementation of the space vector algorithm

Despite the complex selection process presented in sub-section 6.3.1.1 to sub-section 6.3.1.6, implementation of the proposed space vector algorithm is actually rather simple. In fact, only the relevant switching sequence (chosen based on the current location of  $v_{ph}^*$  space vector projections in the  $\alpha$ - $\beta$  plane) and its corresponding dwelling times are required in order to generate the switching signals. Furthermore, all the switching sequences have already been determined as discussed earlier. Based on these switching sequences, the corresponding inverse matrices (as in (5.4)) for dwelling time calculation can also be pre-calculated and stored as constants in the controller memory.

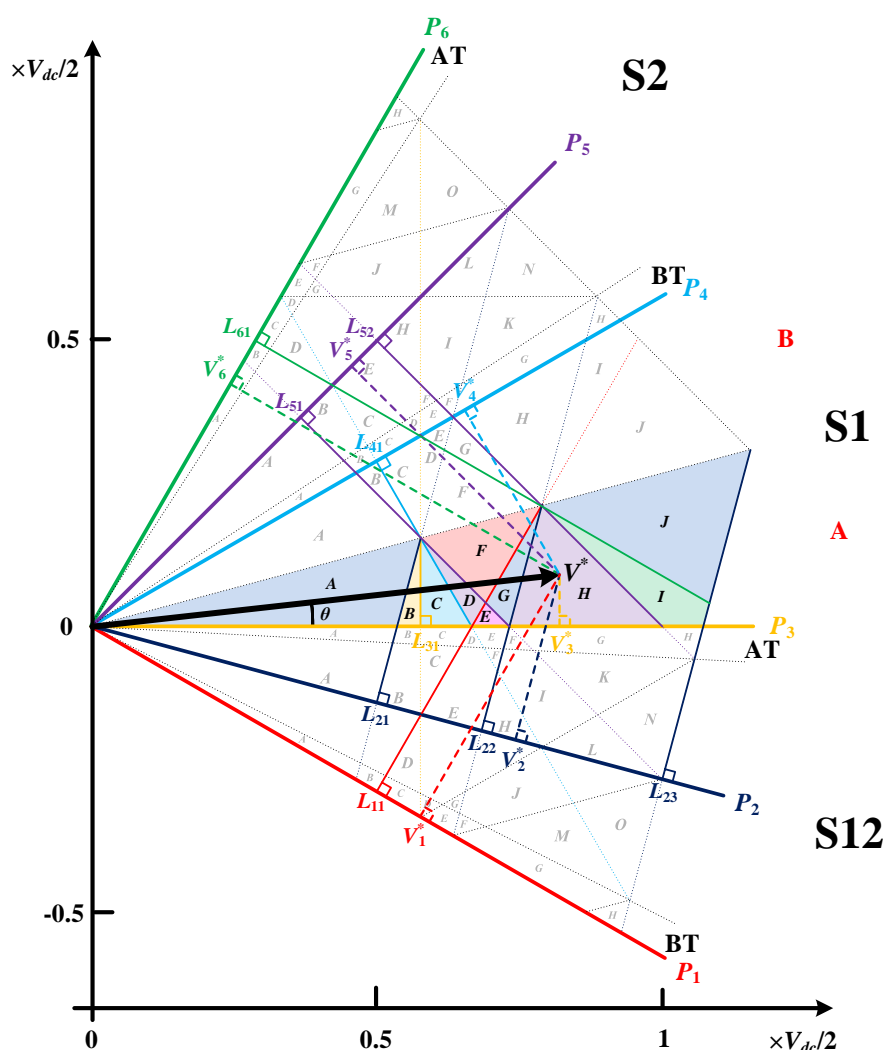


Figure 6.8: Sub-sector determination based on the location of the projected  $v_{ph}^*$  space vector in S1-A.

In addition, the total number of saved switching sequences and pre-calculated inverse matrices can be reduced further by adopting the relationship between the other sectors with the first three sectors i.e. mapping to S1 to S3 and then implementing the sector pair relation as described in (Dordevic, 2013, Engku Ariff et al., 2017a) as described in sub-section 4.3.1.7. Although the denotation of sub-sectors in S3 is identical to S1 (see Figure 6.7), it is difficult to acquire the relationship between these two sectors. This is so since the compositions of  $v_{LEG}$  levels of the switching states in S3 switching sequences are different than in S1. As an example, switching sequence for sub-sector A of S3-A is [111100-111101-111111-121111-122111-222111-222211] while [110000-110001-111001-111011-111111-211111-221111] applies for the same sub-sector in S1-A. Also, it should be noted that S4, S8 and S12 are reflections of S2,

Table 6.2: Conditions defining the sub-sectors that correspond to the location of the  $v_{ph}^*$  space vector in S1-A.

Sub-sector	Conditions	where: $V_1^* = V^* \cos(\omega t + \pi/6)$ $V_2^* = V^* \cos(\omega t + \pi/12)$ $V_3^* = V^* \cos(\omega t)$ $V_4^* = V^* \cos(\omega t - \pi/6)$ $V_5^* = V^* \cos(\omega t - \pi/4)$ $V_6^* = V^* \cos(\omega t - \pi/3)$
A	$V_2^* \leq L_2$	
B	$V_2^* > L_2, V_3^* \leq L_3$	
C	$V_3^* > L_3, V_4^* \leq L_1$	
D	$V_4^* > L_1, V_5^* \leq L_2, V_1^* \leq L_1$	
E	$V_1^* > L_1, V_5^* \leq L_2$	
F	$V_5^* > L_2, V_1^* \leq L_1$	
G	$V_1^* > L_1, V_5^* \leq L_2, V_2^* \leq L_3$	
H	$V_2^* > L_3, V_5^* \leq L_2$	
I	$V_5^* > L_3, V_6^* \leq L_1, V_2^* \leq L_4$	
J	$V_6^* > L_1, V_2^* \leq L_4$	

S6 and S10. Thus, when mapping those sectors into S2, the corresponding switching sequences for S4, S8 and S12 have to be rearranged and the corresponding dwell times are calculated accordingly.

In summary, the algorithm is implemented by accurately determining the current location of the applied  $v_{ph}^*$  in  $\alpha$ - $\beta$  plane. The corresponding sector is then mapped into the first three-sectors i.e. S1 to S3. Next, the respective switching sequence and pre-calculated inverse matrix are fetched from the controller memory. Then, the switching sequence is generated based on the sector mapping relation while the dwell times are calculated using the pre-calculated inverse matrix. A simple rearrangement of generated switching sequences and calculated dwell times should be applied accordingly for even sectors. Finally, the application of obtained switching sequence and calculated dwell times generates the switching signals for the inverter switches.

### 6.3.2 Carrier-based PWM technique

Due to the asymmetry of the  $v_{ph}^*$  waveforms, a modulation technique where CMV is injected, can be done as discussed in sub-section 5.3.2 for a two-level asymmetrical six-phase drive with a single neutral point. However, in the three-level case, CMV has to be injected twice into the reference waveforms. Then the waveforms are compared with two carrier signals that are in-phase with each other, i.e. using the in-phase disposition technique (PD), which finally

generates the switching signals for the inverter switches (Grandi and Loncarski, 2014, Lee et al., 2000). It should be noted that the implementation of double common mode voltage injections does not affect the  $m_i$  range of operation (Dordevic et al., 2013a). Thus, the maximum  $m_i$  for linear range operation remains at 1.035.

The first common mode injection is done according to (5.6), obtaining  $v_{ph,SinCMI}^*$  waveforms. Due to the usage of level shifted carriers with in-phase disposition, PD, the  $v_{ph,SinCMI}^*$  waveforms belonging to the upper carrier band can be shifted into the lower carrier band, forming a common carrier band (Dordevic et al., 2013a). Shifting of the  $v_{ph,SinCMI}^*$  waveforms into a common carrier band, in the analysed case, is achieved as in:

$$v_{ph,CCB}^* = v_{ph,SinCMI}^* - \frac{sign(v_{ph,SinCMI}^*)}{2} \quad (6.1)$$

where the second term of the equation represents half of the integer part of  $v_{ph,SinCMI}^*$  waveforms. Finally, the  $v_{ph}^*$  waveforms with second, i.e. double common mode voltage injection ( $v_{ph,PD2CMI}^*$ ), are obtained using:

$$v_{ph,PD2CMI}^* = v_{ph,SinCMI}^* - \frac{[\min(v_{ph,CCB}^*) + \max(v_{ph,CCB}^*)]}{2} \quad (6.2)$$

As an example, the  $v_{ph,PD2CMI}^*$  waveforms at  $m_i = 1$  are shown in Figure 6.9.

### 6.3.3 Simulation and experimental results

The proposed space vector algorithm and carrier-based PWM with double common mode voltage injection are verified using simulations in PLECS. The same asymmetrical six-phase machine model with parameters as in Table 5.1 is used. Hence, at the machine's rated frequency, 50 Hz, the chosen  $V_f^*$  is 150 V. Because  $V_{dc} = 300$  V and since  $m_i$  is defined as in

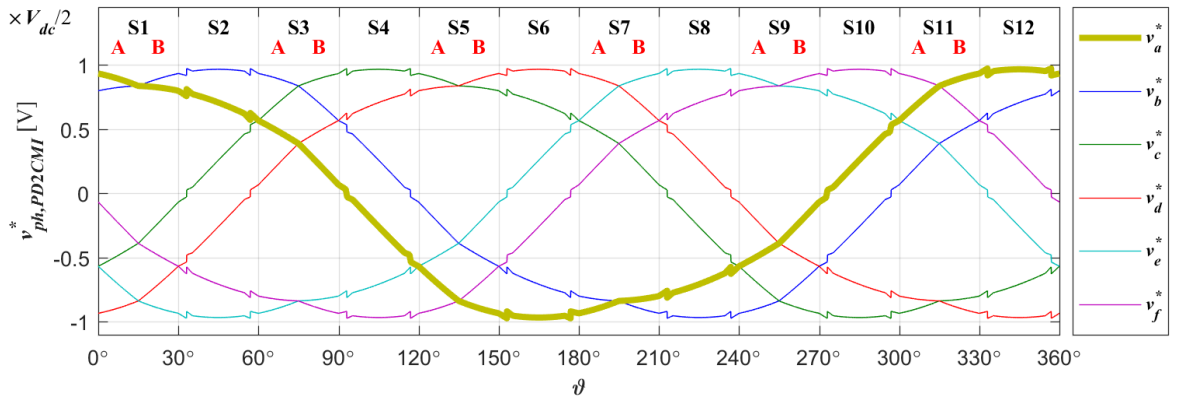


Figure 6.9: Sinusoidal reference phase voltage waveforms with double common mode voltage injection ( $v_{ph,PD2CMI}^*$ ) for three-level asymmetrical six-phase drive at  $m_i = 1$ .

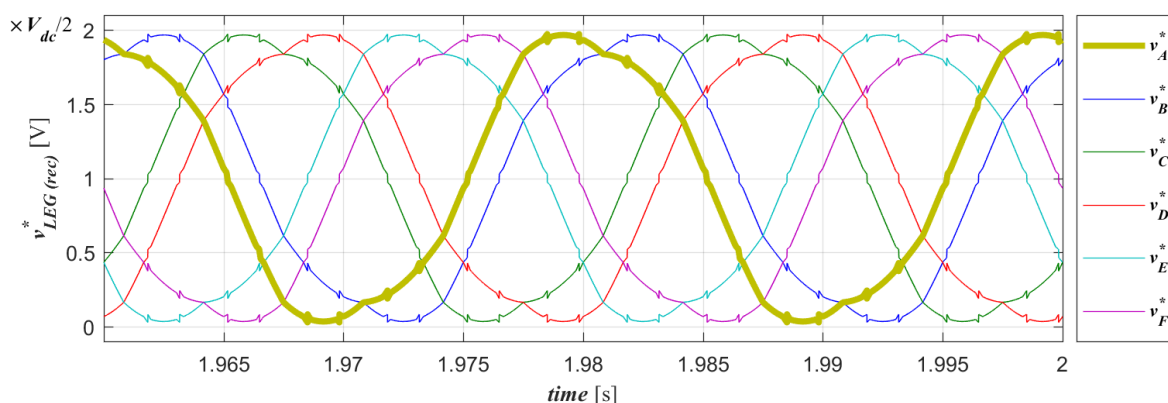


Figure 6.10: Reconstructed reference output leg voltage ( $v_{LEG,rec}^*$ ) waveforms of 3L6PAsymSV at  $m_i = 1$ .

(3.19), this is equivalent to  $m_i = 1$ . The simulations are run for the full linear range of  $m_i$  with 0.05 increments, in open loop and at no load, up to  $m_i = 1.035$ . The performance of both modulation techniques is determined by means of the phase voltage (THD<sub>v</sub>) and phase current (THD<sub>i</sub>) total harmonic distortions using (3.20). The first  $h$  harmonics, up to the value of  $h$  that corresponds to 21 kHz, i.e. the first ten sidebands, are included in the THD<sub>v</sub> and THD<sub>i</sub> calculations.

The developed modulation techniques are validated through experimental testing. The experimental setup is as shown in Figure 4.15 but using asymmetrical six-phase machine (see Appendix 2 for more details). The modulation techniques are programmed into a real-time platform dSpace ds1006 using Matlab/Simulink. The dc-bus voltage is set to be  $V_{dc} = 300$  V using Sorensen SGI 600/25 external dc supply. The asymmetrical six-phase induction machine is operated under no-load condition and driven using a custom made three-level six-phase NPC inverter, which switches at  $f_s = 2$  kHz. The inverter dead time is 6  $\mu$ s and is not compensated in any way. As in the simulations, both modulation techniques are tested in open loop for full linear operating range of  $m_i$ .

The reconstructed  $v_{LEG}^*$  waveforms ( $v_{LEG,rec}^*$ ) of the developed space vector algorithm at  $m_i = 1$  are shown in Figure 6.10. These waveforms are obtained from the product of the applied switching sequence and its calculated dwell times. As one might expect, the  $v_{LEG,rec}^*$  waveforms are identical to  $v_{ph,PD2CMI}^*$  waveforms (see Figure 6.9). Although the  $v_{LEG,rec}^*$  waveforms clearly have ‘distortions’ in them, it can be shown that the reconstructed  $v_{ph}^*$  waveforms ( $v_{ph,rec}^*$ ) remain sinusoidal. The  $v_{ph,rec}^*$  waveforms can be obtained from (3.3) and they are shown in Figure 6.11.

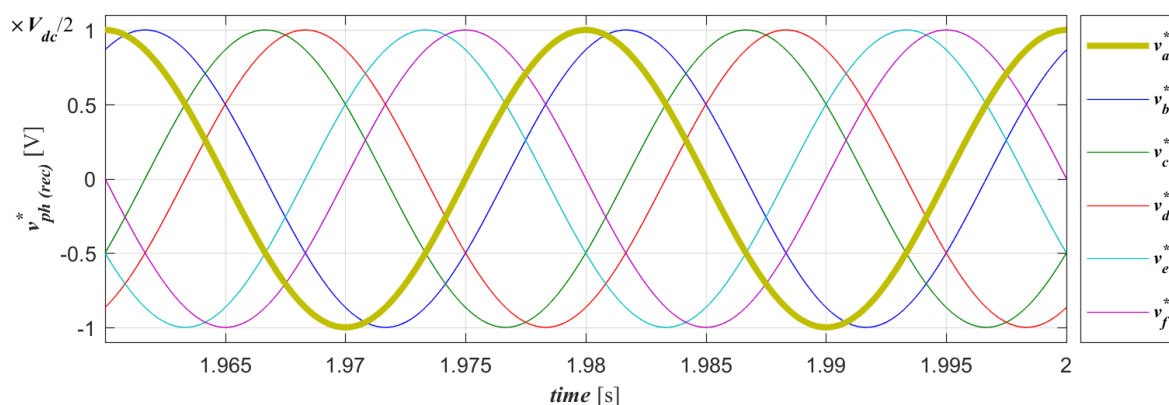


Figure 6.11: Reconstructed reference output phase voltage ( $v_{ph,rec}^*$ ) waveforms of 3L6PA symSV at  $m_i = 1$ .

Note that, the amplitude of the  $v_{ph,rec}^*$  waveforms is equal to half  $V_{dc}$  which is in agreement with (3.19) at  $m_i = 1$ .

In Figure 6.12 and 6.13, the phase ‘a’ voltage, phase voltage components ( $v_{\alpha}$ ,  $v_{\beta}$ ,  $v_x$ ,  $v_y$ ,  $v_0^+$  and  $v_0^-$ ) and phase ‘a’ current waveforms (including their corresponding spectra) of the machine driven by the ideal inverter in simulation, for the 3L6PA symSV and PD2CMI are shown. The fundamental phase ‘a’ voltage ( $|v_a|_{fund}$ ) is 149.94 V which is in agreement with (3.19) at  $m_i = 1$ . It can be seen that the magnitudes of low-order harmonics which correspond to  $x$ ,  $y$  and  $0^-$  axes are negligible when compared to  $|v_a|_{fund}$ . This is so since one of the main requirements of the developed 3LSVA symSV is that the  $x$ ,  $y$  and  $0^-$  axes components are to be controlled to zero. In this way, it is ensured that the low-order harmonics of the corresponding axes do not exist.

The measured phase ‘a’ leg voltage, phase voltage and current waveforms (labelled as  $V_A$ ,  $V_a$  and  $i_a$  respectively in the oscilloscope screen captures) and corresponding spectra when  $m_i = 0.4$  and  $m_i = 1$ , for 3L6PA symSV as well as PD2CMI, are shown in Figure 6.14 and 6.15, respectively. One can see that the waveforms obtained by both modulation techniques are practically the same. In addition, the values of the measured fundamental phase voltage are approximately the same as the reference values of  $V_f^*$  which are obtained from (3.19), i.e. 60 V and 150 V, at  $m_i = 0.4$  and  $m_i = 1$ , respectively. Although  $v_x^*$ ,  $v_y^*$  and  $v_0^-$  are set to zero in 3L6PA symSV to ensure that the low order harmonics of the order of  $12k \pm 5$  ( $k = 0, 1, 2, 3, \dots$ ) and  $3k$  ( $k = 1, 3, 5, \dots$ ) do not exist, they are still present in both phase voltage and current spectra (see Figure 6.14(c) and 6.14(d) as well as Figure 6.15(c) and 6.15(d)). However, the magnitudes of these harmonics are relatively small. The appearance of these low odd order

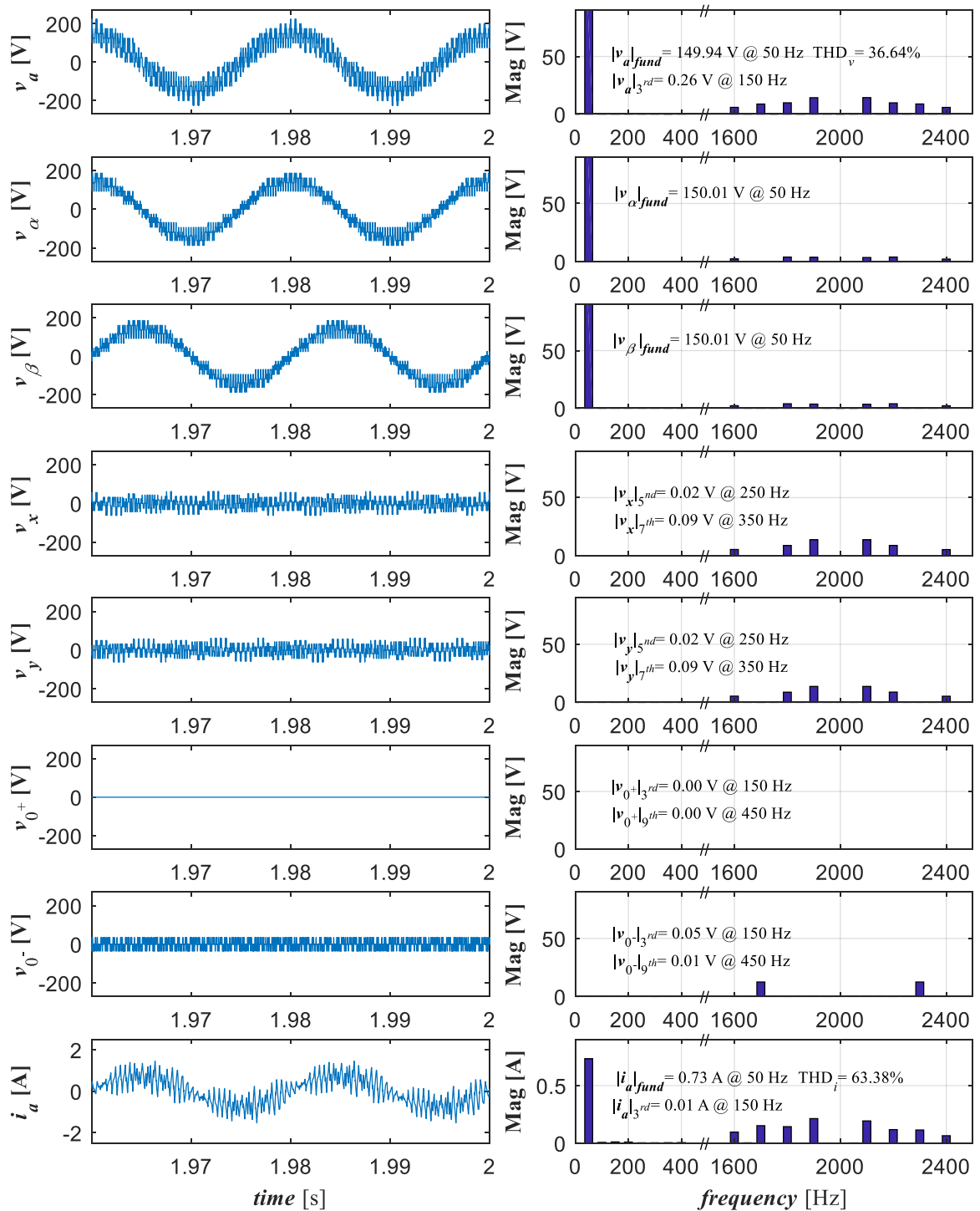


Figure 6.12: Phase 'a' voltage, phase voltage components ( $v_a$ ,  $v_\beta$ ,  $v_x$ ,  $v_y$ ,  $v_0^+$  and  $v_0^-$ ), phase 'a' current and corresponding spectra of 3L6PAsymSV for the machine driven by ideal inverter

at  $m_i = 1$ .

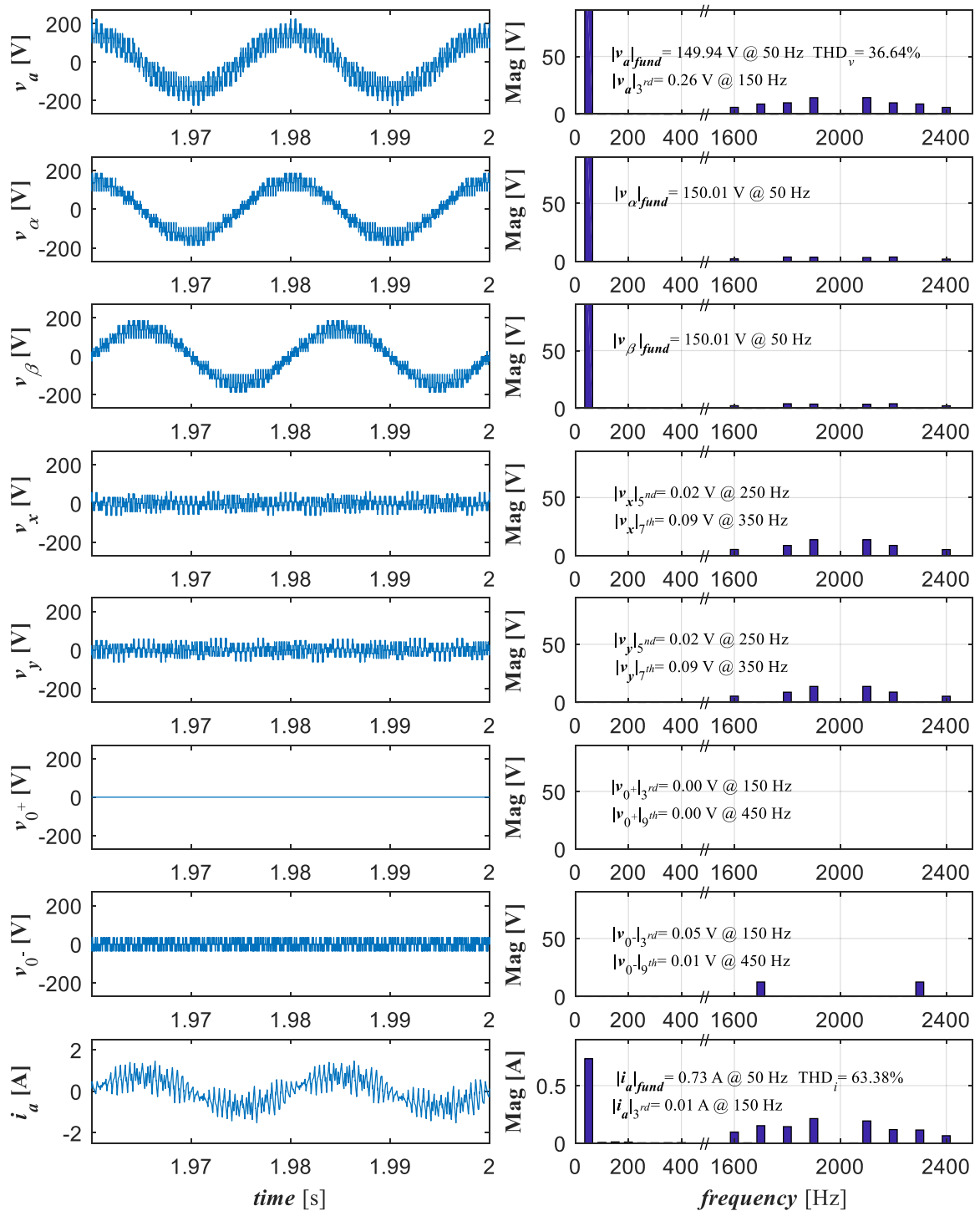


Figure 6.13: Phase 'a' voltage, phase voltage components ( $v_a$ ,  $v_\beta$ ,  $v_x$ ,  $v_y$ ,  $v_0^+$  and  $v_0^-$ ), phase 'a' current and corresponding spectra of PD2CMI for the machine driven by ideal inverter at  $m_i = 1$ .

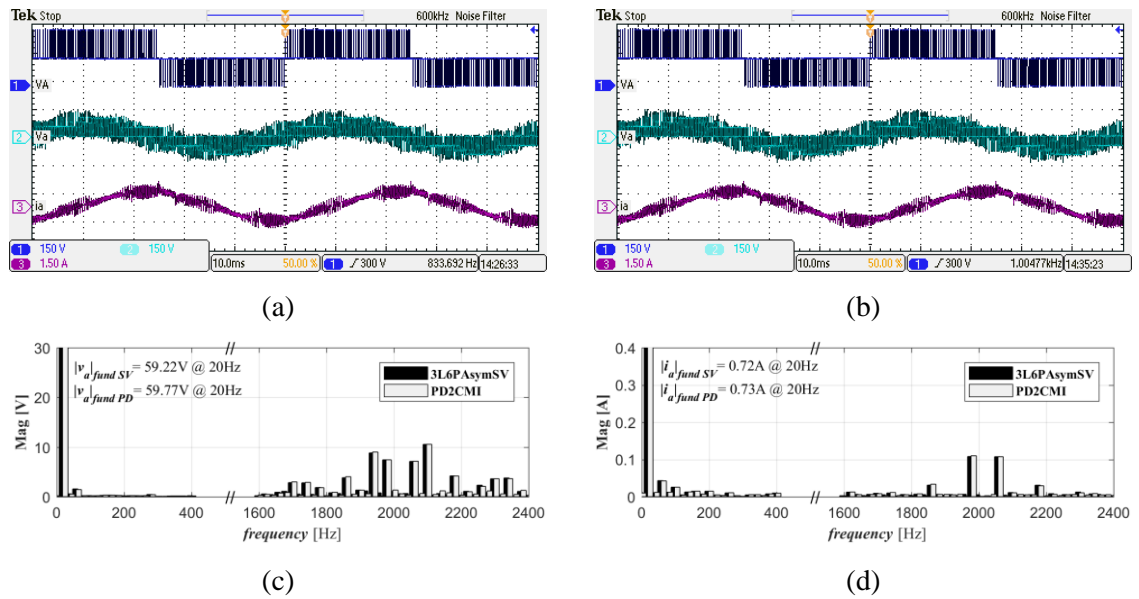


Figure 6.14: Oscilloscope capture of phase ‘a’ leg and phase voltage and current at  $m_i = 0.4$  for (a) 3L6PAsymSV, (b) PD2CMI, with corresponding (c) voltage and (d) current spectra.

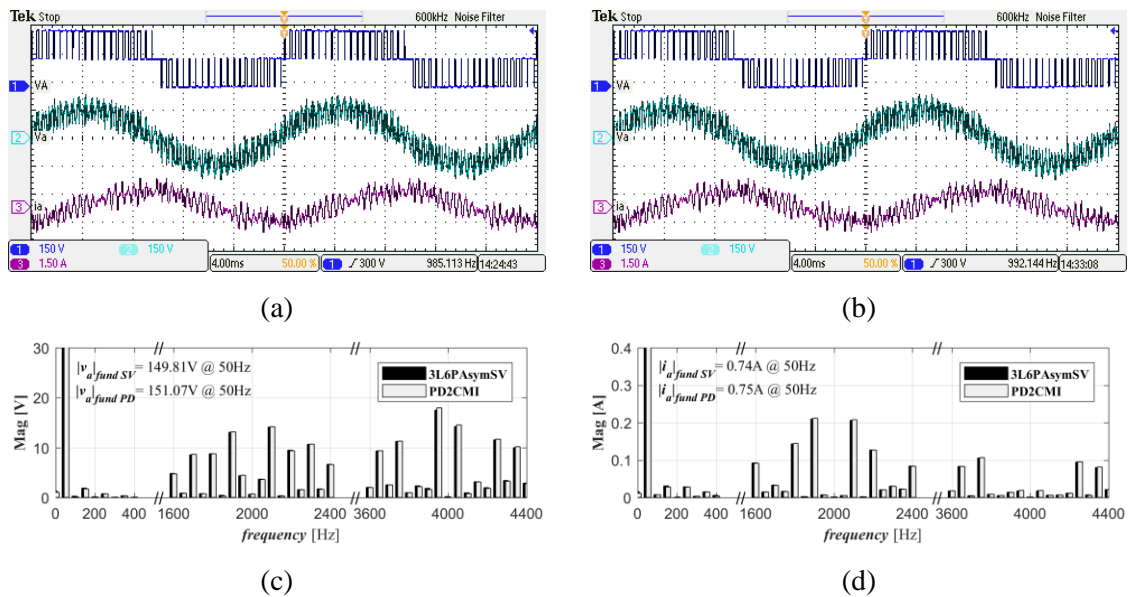


Figure 6.15: Oscilloscope capture of phase ‘a’ leg and phase voltage and current at  $m_i = 1$  for (a) 3L6PAsymSV, (b) PD2CMI, with corresponding (c) voltage and (d) current spectra.

harmonics is a consequence of the uncompensated inverter dead time (Jeong and Park, 1991, Jones et al., 2009a) as demonstrated in Chapter 5 for two-level system.

Furthermore, notice that the magnitude of the third current harmonic of the analysed drive topology is significantly lower than in symmetrical six-phase drive (see Figure 4.21(d) and 4.22(d)). This is largely due to the former having a much larger impedance in 0- axis equivalent circuit ( $33.7 \Omega$  at 150 Hz obtained based on the improved zero-sequence model in (Che et al., 2017)) compared to the latter ( $8.44 \Omega$  at 150 Hz, where zero-axis circuit comprises of stator resistance and stator leakage inductance only). Hence, although the magnitudes of the third voltage harmonics for both drive topologies are similar, the magnitudes of the third current harmonics will differ greatly.

## 6.4 Drive with two isolated neutral points configuration

In this section, PWM techniques for a three-level asymmetrical six-phase drive with two isolated neutral points are presented. The switching signals of the drive are generated using two identical PWM modulators that are developed based on the established space vector algorithm and carrier-based technique for three-level three-phase drives. The applied PWM techniques are verified using simulations in PLECS and experimental testing.

### 6.4.1 Space vector PWM algorithm

The number of switching states and  $v_{ph}$  space vectors of the analysed drive topology are 729 and 665 respectively i.e. the same as in the single neutral point configuration. This is because the number of switching states and  $v_{ph}$  space vectors are dependent on the topology of the inverter itself. Similarly, the space vector projections of the analysed drive topology onto the three orthogonal planes can also be obtained from (5.1) (Zhao and Lipo, 1995) and they are identical to those shown in Figure 6.3(a) to 6.3(c). However, the denotation of the  $0^+-0^-$  plane as in Figure 6.3(c) is changed to  $0_1-0_2$  plane. Due to the existence of two isolated neutral points, now each axis represents CMV of the winding set ( $0_1$  axis represents CMV of the first and  $0_2$  of the second winding set). Thus, low order harmonics, which mapped onto this plane, i.e. low order harmonics of the order of  $3k$  ( $k = 1, 3, 5 \dots$ ), do not exist anymore.

The isolated neutral points also mean that each stator winding set can be controlled using a dual three-level three-phase space vector PWM modulator (D3L3PSV). The reference waveforms of the modulators are shifted spatially by  $30^\circ$  and the modulators are developed based on the space vector algorithm presented in (McGrath et al., 2003). Finally yet importantly,

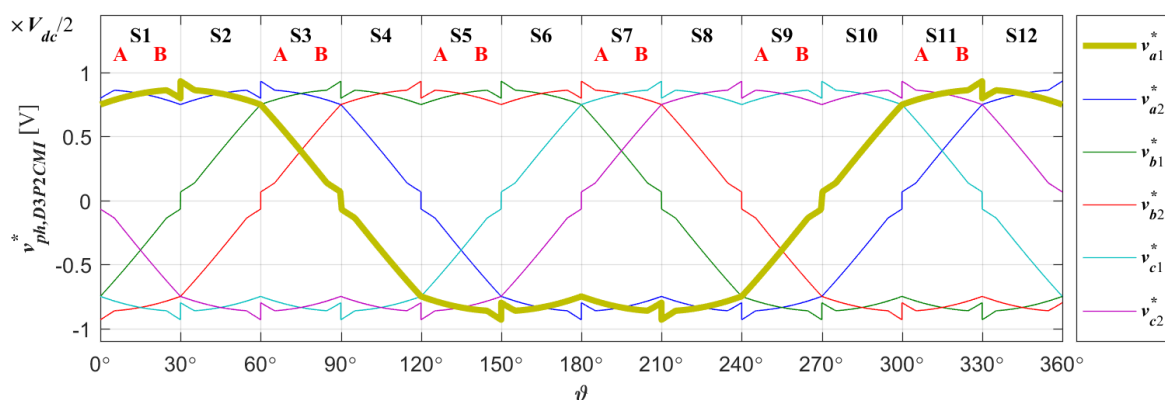


Figure 6.16: Sinusoidal reference phase voltage waveforms with dual double common mode voltage injection ( $v_{ph,D3P2CMI}^*$ ) for three-level asymmetrical six-phase drive at  $m_i = 1$ .

the maximum  $m_i$  for linear range operation, using D3L3PSV, is 1.154, which is the same as in the standard three-phase case.

#### 6.4.2 Carrier-based PWM technique

As for the carrier-based PWM technique, the winding sets are also controlled separately through dual three-level three-phase carrier-based PWM (D3P2CMI) modulators with the reference waveforms spatially shifted by  $30^\circ$ . The modulators are developed in a similar way as in sub-section 6.3.2, by using double common mode voltage injection, as in (6.1) and (6.2), which is applied to each set individually. The resultant reference phase voltage waveforms ( $v_{ph,D3P2CMI}^*$ ) for the analysed drive topology at  $m_i = 1$  are as shown in Figure 6.16. The maximum  $m_i$  for linear range of operation, that can be achieved using D3P2CMI, is 1.154.

#### 6.4.3 Simulation and experimental results

PWM modulators based on the D3L3PSV and D3P2CMI are developed and verified through simulations in PLECS using the same settings as for the drive with a single neutral point. Additionally, the modulation techniques are further validated through experimental testing for the full linear range of  $m_i$  i.e. from  $m_i = 0.1$  to  $m_i = 1.154$  with 0.05 increments.

The  $v_{LEG,rec}^*$  waveforms of D2L3PSV that are obtained through simulation at  $m_i = 1$  are shown in Figure 6.17. It can be seen that the obtained  $v_{LEG,rec}^*$  waveforms are the same as  $v_{ph,D3P2CMI}^*$  waveforms shown in Figure 6.16. Furthermore, from (3.6), the reconstructed reference phase voltage waveforms ( $v_{ph,rec}^*$ ) can also be obtained and, as expected, they are sinusoidal, as shown in Figure 6.18.

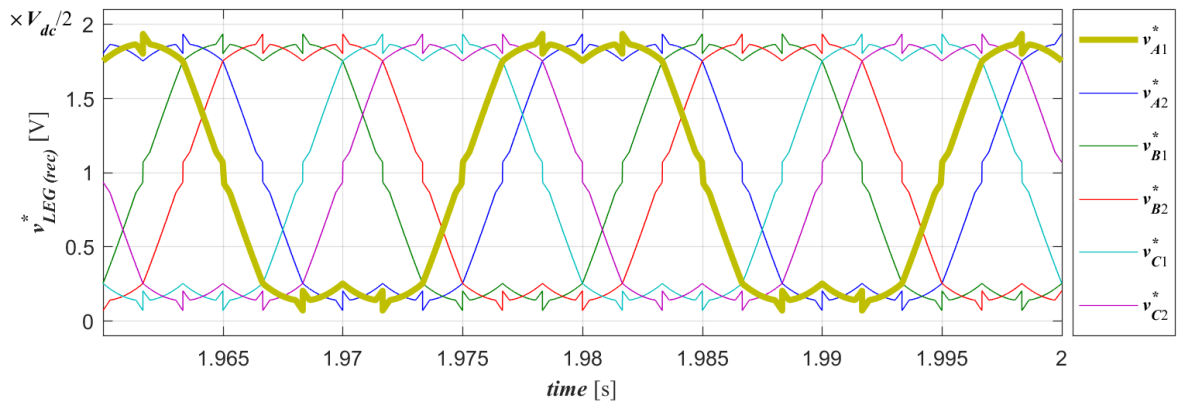


Figure 6.17: Reconstructed reference output leg voltage ( $v_{LEG,rec}^*$ ) waveforms of D3L3PSV at  $m_i = 1$ .

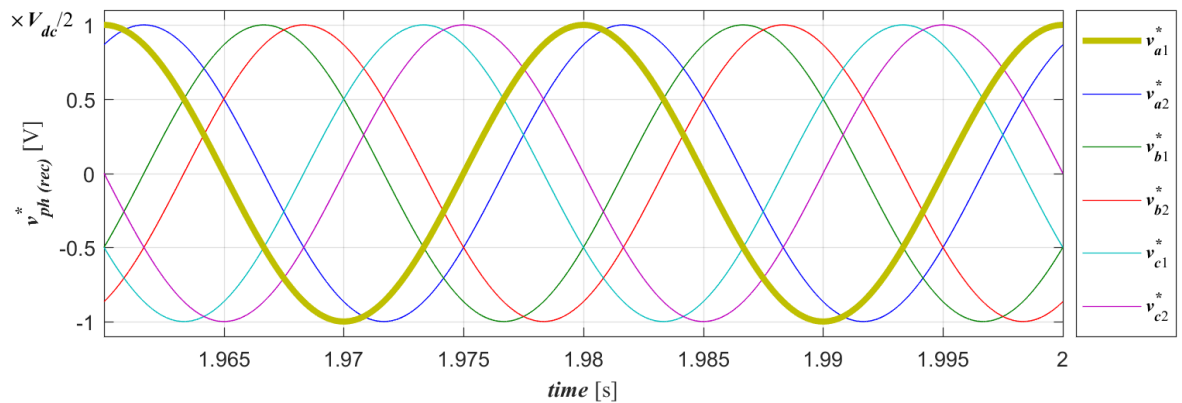


Figure 6.18: Reconstructed reference output phase voltage ( $v_{ph,rec}^*$ ) waveforms of D3L3PSV at  $m_i = 1$ .

The obtained simulation results for D3L3PSV and D3P2CMI (phase ‘ $a_1$ ’ voltage, phase voltage components:  $v_\alpha$ ,  $v_\beta$ ,  $v_x$ ,  $v_y$ ,  $v_{01}$  and  $v_{02}$ , and phase ‘ $a_1$ ’ current waveform, as well as their corresponding spectra), for the machine driven by an ideal inverter are shown in Figure 6.19 and 6.20, respectively. One can see that both modulation techniques yield identical performance. Since  $0_1$  and  $0_2$  axis correspond to CMV of each winding set, as one might expect, the corresponding phase voltage components are zero.

The measured experimental results are shown in Figure 6.21 and 6.22 for the case when  $m_i = 0.4$  and  $m_i = 1$ , respectively. The oscilloscope captures show the measured phase ‘ $a_1$ ’ leg voltage, phase voltage and current waveforms for D3L3PSV and D3P2CMI modulation strategies. One can see that the measured waveforms for both modulation techniques are the same. In fact, one can clearly see that the values of the measured fundamental phase voltage and phase current of both modulation techniques, denoted in corresponding phase voltage and

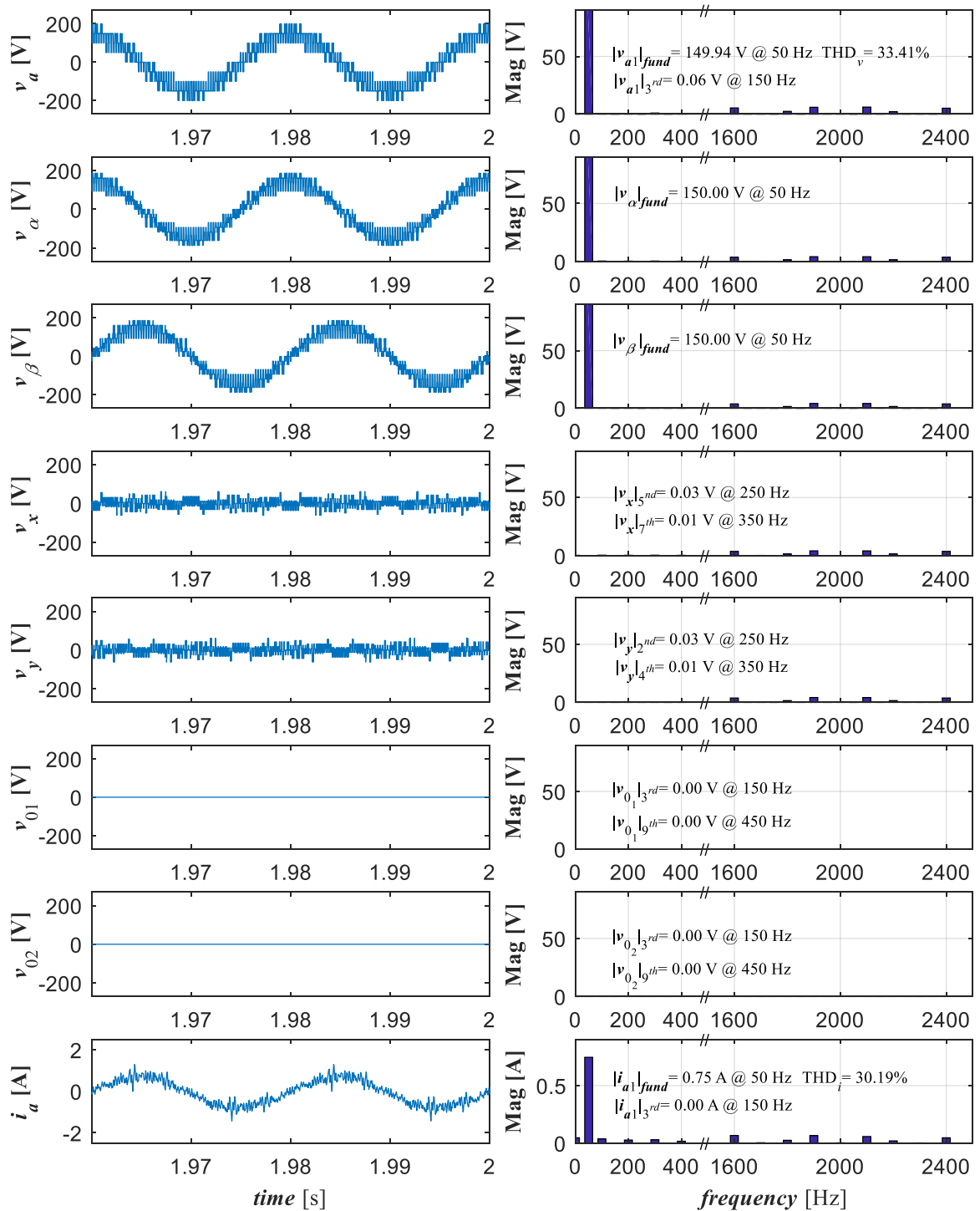


Figure 6.19: Phase ‘a<sub>1</sub>’ voltage, phase voltage components ( $v_a, v_\beta, v_x, v_y, v_{01}$  and  $v_{02}$ ), phase ‘a<sub>1</sub>’ current and corresponding spectra of D3L3PSV for the machine driven by ideal inverter at  $m_i = 1$ .

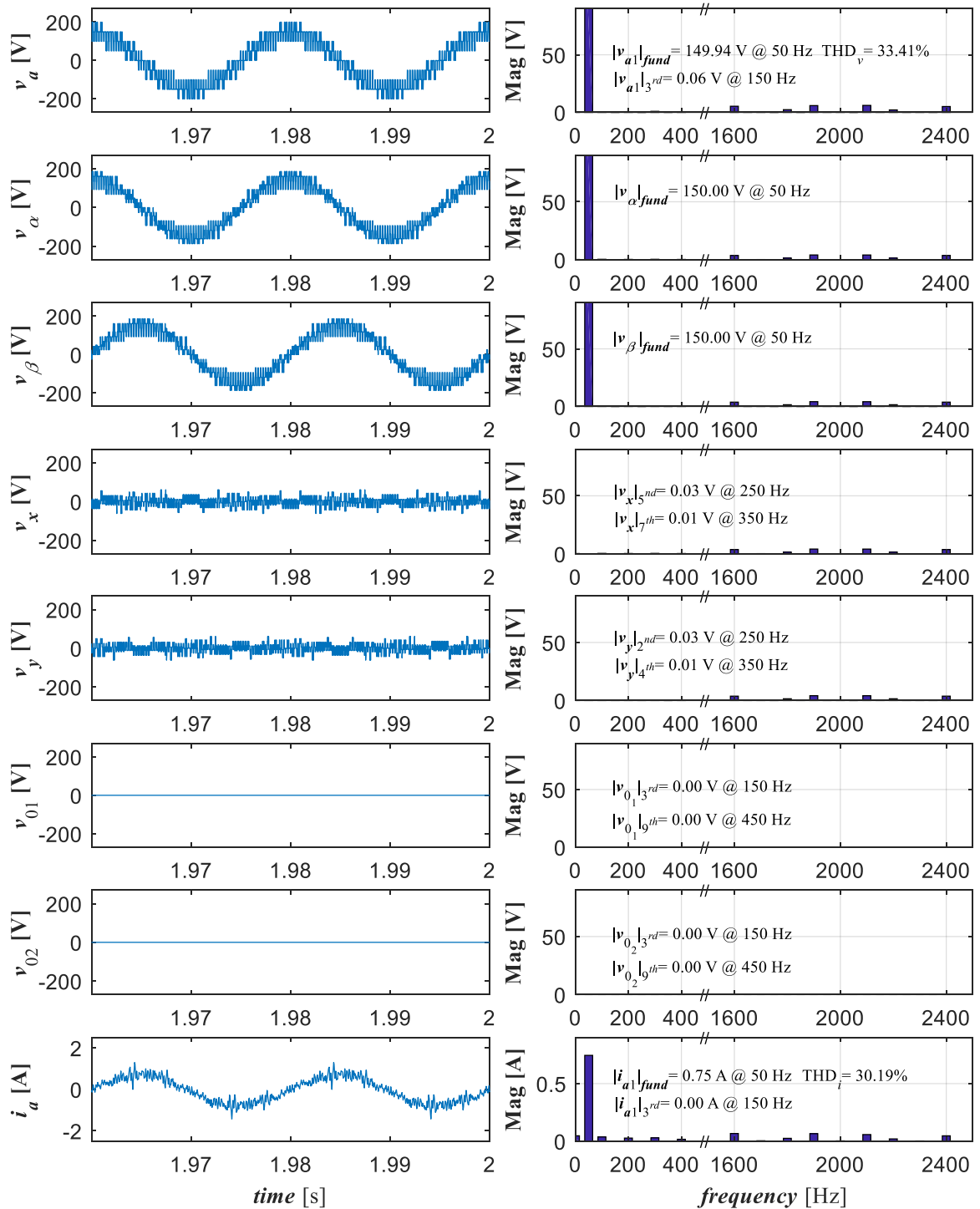


Figure 6.20: Phase 'a1' voltage, phase voltage components ( $v_a$ ,  $v_\beta$ ,  $v_x$ ,  $v_y$ ,  $v_{01}$  and  $v_{02}$ ), phase 'a1' current and corresponding spectra of D3P2CMI for the machine driven by ideal inverter at  $m_i = 1$ .

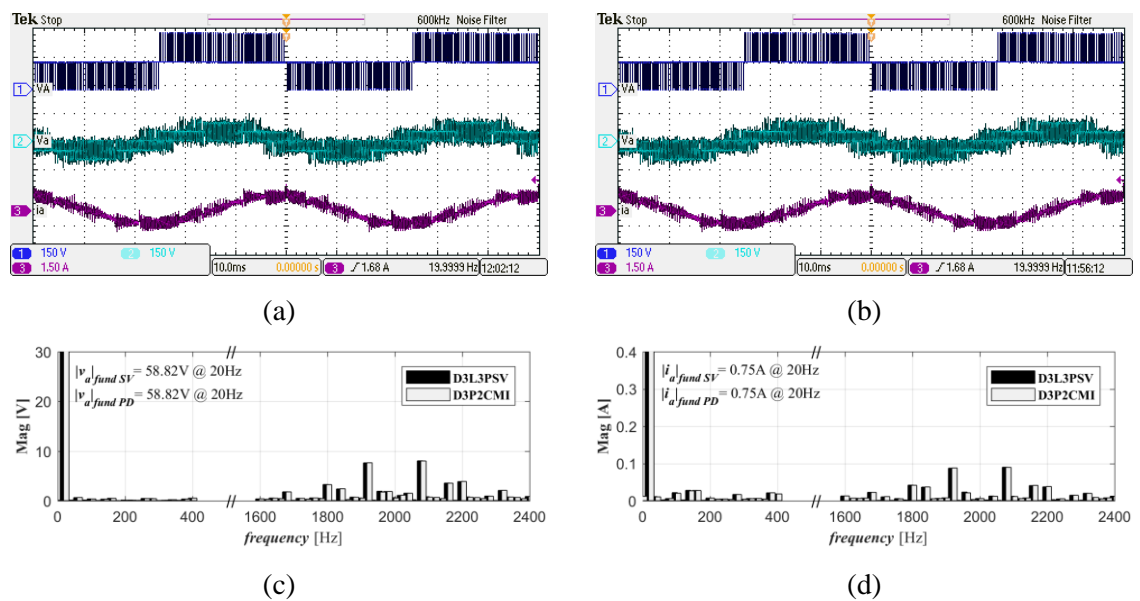


Figure 6.21: Oscilloscope capture of phase ‘ $a_1$ ’ leg and phase voltage and current at  $m_i=0.4$  for (a) D3L3PSV, (b) D3P2CMI, with corresponding (c) voltage and (d) current spectra.

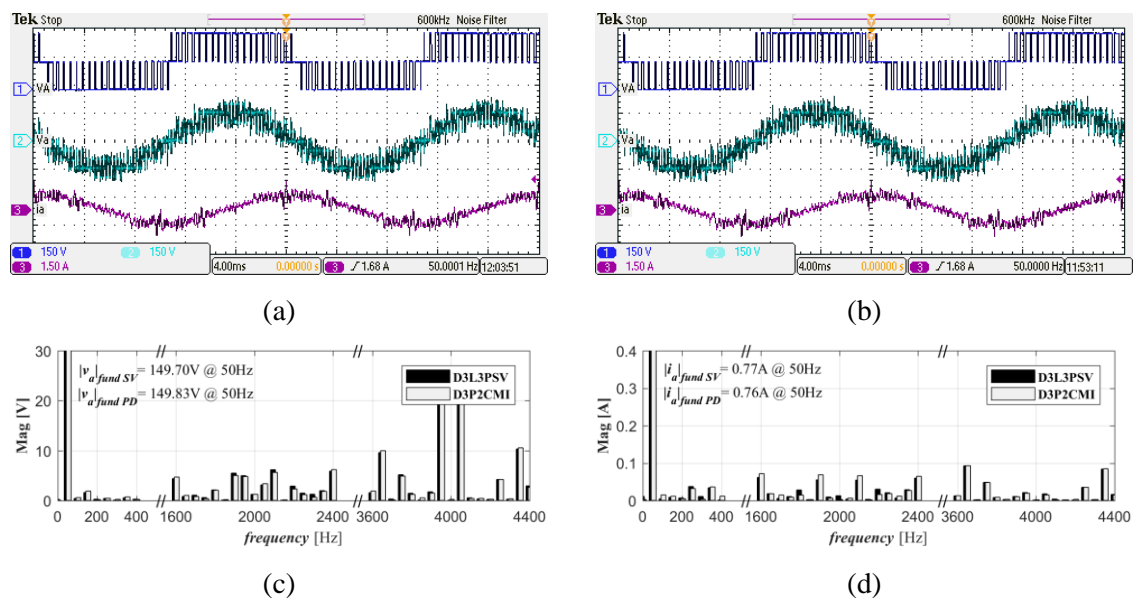


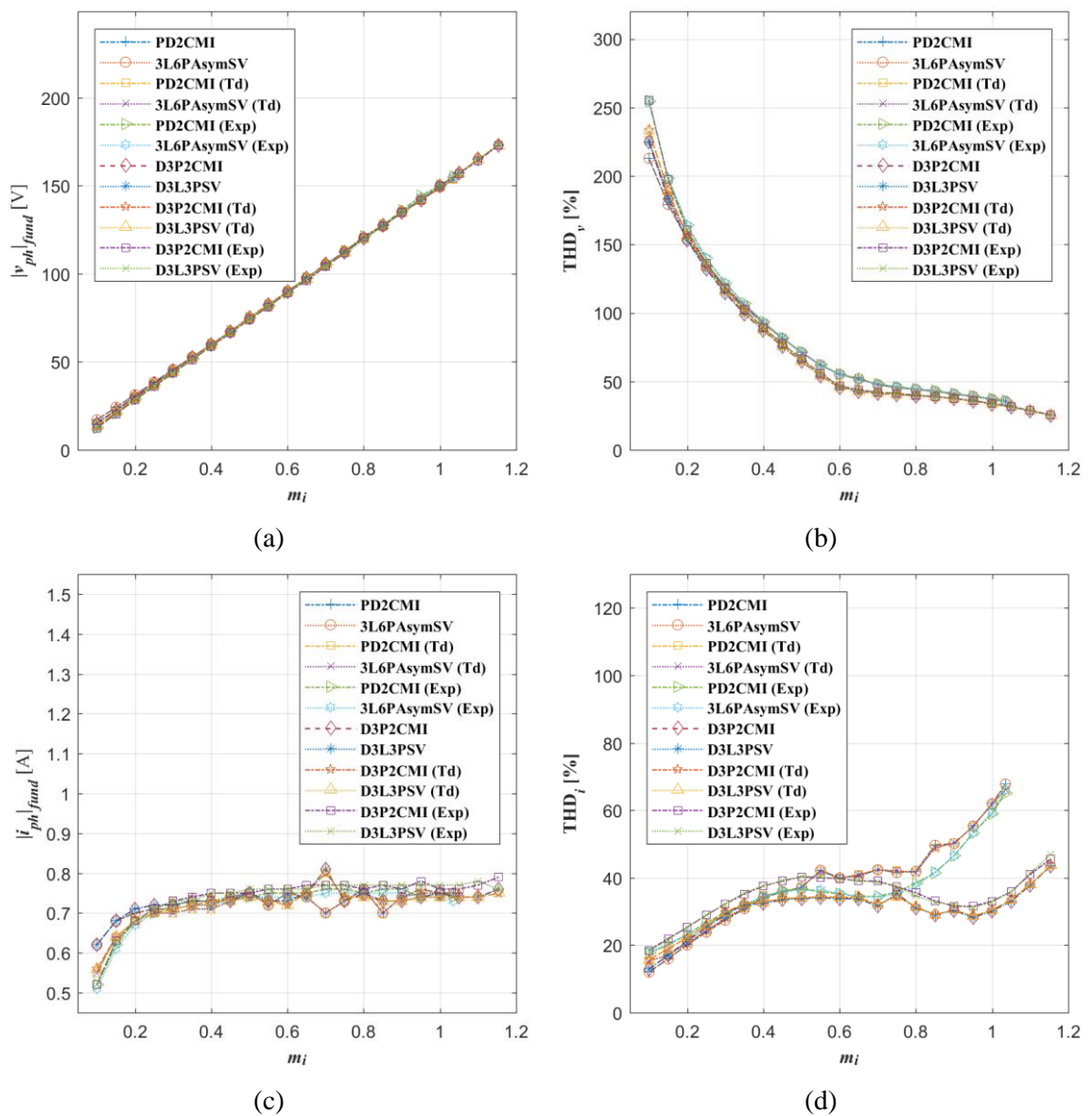
Figure 6.22: Oscilloscope capture of phase ‘ $a_1$ ’ leg and phase voltage and current at  $m_i = 1$  for (a) D3L3PSV, (b) D3P2CMI, with corresponding (c) voltage and (d) current spectra.

current spectra, Figure 6.23 and 6.24 sub-figures (c) and (d) are also the same. In addition, the measured fundamental phase voltage is close to the expected reference values of  $V_f^*$  from (3.19), i.e. 60 V and 150 V, at  $m_i = 0.4$  and  $m_i = 1$ , respectively. The presence of low order odd harmonics can also be seen in both the phase voltage and current spectra. However, they are relatively small in magnitude compared to the value of the fundamental phase voltage and current and, once again, the explanation for their existence lays with the non-ideal nature of the inverter.

### 6.5 Performance comparison between the modulation techniques of both neutral point configurations

The performance comparison of all presented modulation techniques is determined by their  $\text{THD}_v$  and  $\text{THD}_i$ , which are calculated using (3.20). Results for simulations that take into account the inverter dead time are also included for completeness and are denoted with (Td). The magnitudes of the obtained fundamental output phase voltage ( $|v_{ph}|_{fund}$ ), output phase current ( $|i_{ph}|_{fund}$ ), the calculated  $\text{THD}_v$  and  $\text{THD}_i$ , for the full linear modulation index range and for all presented modulation strategies, are shown in Figure 6.23. The validity of the presented modulation techniques can be seen from the characteristic of the obtained  $|v_{ph}|_{fund}$ , Figure 6.23(a), which is linear with respect to  $m_i$ . In other words, the obtained  $|v_{ph}|_{fund}$  is the same as the expected  $V_f^*$  for the full linear range of  $m_i$ . The magnitude of  $|i_{ph}|_{fund}$  is practically constant for whole modulation index range, because  $V/f = \text{const.}$  law was used (Figure 6.23(c)). The magnitude drops at low values or modulation index is the consequence of not compensated voltage drop across the stator (no voltage boost is used).

From the  $\text{THD}_v$  and  $\text{THD}_i$  characteristics of the analysed space vector algorithm and carrier-based PWM technique, either for the drive with single or two neutral points configuration, one can see that the performance of both modulation techniques is practically identical. Furthermore, one can also see that the  $|v_{ph}|_{fund}$ ,  $|i_{ph}|_{fund}$ ,  $\text{THD}_v$  and  $\text{THD}_i$  characteristics of the obtained simulation and experimental results are in a very good agreement, albeit with small discrepancies in values. Nevertheless, in terms of the performance between the drive with single and two isolated neutral points, one can clearly see from the  $\text{THD}_v$  and  $\text{THD}_i$  curves that the performance of the latter is better. This is the most obvious from  $\text{THD}_i$ , especially at higher values of  $m_i$ , Figure 6.23(d). Another important benefit of configurations with two isolated neutral points is in the increased value of maximum modulation index to 1.154, rather than 1.035 for a single neutral point.



Applied PWM techniques for single neutral point case:

PD2CMI	PD PWM with double common mode voltage injection
3L6PAsymSV	Space vector algorithm using time matrix approach

Applied PWM techniques for two neutral points case:

D3P2CMI	PD with double common mode voltage injection (dual three-phase modulators)
D3L3PSV	Three-level three-phase space vector algorithm (dual modulators)

Note: Td – denotes that the inverter dead-time is considered in the simulation  
Exp – denotes experiment results

Figure 6.23: The performance of applied modulation techniques for full linear range of  $m_i$  based on: (a) obtained  $|v_{ph}|_{fund}$  (b) calculated  $THD_v$  (c) obtained  $|i_{ph}|_{fund}$  and (d) calculated  $THD_i$ .

Table 6.3: Execution time of the applied modulation techniques.

Modulation techniques	Neutral point configuration	
	Single	Two
3L6PA <sub>sym</sub> SV	6.82 $\mu$ s	-
PD2CMI	1.16 $\mu$ s	-
D3L3PSV	-	2.36 $\mu$ s
D3P2CMI	-	1.18 $\mu$ s

The complexity of the proposed modulation techniques is compared. The execution time of each modulation techniques is measured using dSpace Profiler Tool and the values are listed in Table 6.3. It should be emphasised that the execution time of the 3L6PA<sub>sym</sub>SV has been significantly reduced by storing a significant amount of data (the switching sequences and corresponding pre-calculated inverse matrices of (5.4), for all 87 sub-sectors within S1 to S3) in the memory. Therefore, the memory usage of the 3L6PA<sub>sym</sub>SV is significantly higher than PD2CMI. In addition, the calculation of dwell times and determination of the correct sub-sector lead to a longer execution time for the space vector modulation method.

On the other hand, the difference in the execution time between the D3L3PSV and D3P2CMI is much smaller. This is because, unlike for 3L6PA<sub>sym</sub>SV, now a much smaller amount of data (the size of each stored switching sequences and corresponding pre-calculated inverse matrices are three by four and three by three matrices only) are necessary to be stored in the memory. In addition, the calculation of dwell times and the process of determining the corresponding sub-sector are much simpler, thus resulting in a shorter execution time.

## 6.6 Summary

In this chapter, four different PWM techniques, which are developed based on the space vector algorithm and carrier-based approach, for a three-level asymmetrical six-phase drive with single and two isolated neutral points configurations, are discussed. The process of developing the space vector algorithm for the three-level asymmetrical six-phase with single neutral point configuration, i.e. 3L6PA<sub>sym</sub>SV, is presented in detail.

In developing 3L6PA<sub>sym</sub>SV, the previously introduced rotational transformation in Chapter 5 is applied to the  $0^+-0^-$  plane, in order to make the realisation of sinusoidal output phase voltage waveforms through the chosen  $v_{LEG}$  space vectors possible. However, the

commonly used method of choosing the switching sequences in  $\alpha$ - $\beta$  plane cannot be applied due to the distribution of the projected space vectors. Thus, a permutation method is proposed, where all switching states are considered as potential subsequent switching states in the switching sequence. Last but not least, two additional small sectors located at each side of the odd sectors are also used in order to minimise the switching losses in the transitions between the sectors due to the absence of redundant switching sequences at certain sub-sectors.

The discussed modulation techniques are verified in PLECS and validated further in experimental testing for the full linear range of the modulation index in open loop. The obtained simulation and experimental results show that the modulation techniques based on space vector algorithms have identical performance as their equivalent carrier-based approaches. Therefore, PWM technique based on carrier-based approach is recommended if one only a simple PWM technique, without concerning the fundamental mechanism of how it works, is required. Moreover, by isolating the neutral points of the winding sets and then controlling them separately using dual three-phase modulators i.e. D3P2CMI, one can get better drive performance when compared to the topology with single neutral point configuration. Furthermore, a much higher dc-bus utilisation can also be achieved.



---

# CHAPTER 7

## Conclusion

---

### 7.1 Conclusion

This thesis presents the analysis and the development of several PWM techniques based on a space vector and carrier-based approach for two- and three-level, symmetrical and asymmetrical six-phase drives. Both, single and two isolated neutral points configuration have been considered. However, more emphasis is put on the analysis and development of modulation techniques for the single neutral point case. The stator windings are assumed to be sinusoidally distributed for all the considered machines. Thus, the aim of all the presented modulation techniques is focused towards obtaining sinusoidal output phase voltages. The modulation techniques are developed and verified through simulations using either PLECS or Matlab/Simulink software in open loop at no load for the full linear operating range of the modulation index. The simulations are done for ideal case as well as when the uncompensated inverter dead time is taken into account. In the three-level cases, the developed modulations techniques are further validated through experimental testing. Finally, appropriate comparisons between the obtained simulation and experimental results as well as their performances in terms of phase voltage and current THDs are provided.

The thesis starts by introducing a general description about multiphase machines and commonly used multilevel inverter topologies as well as the motivation for this research. The aim and objectives for successfully completing the research are also stated. Then, in Chapter 2, a broad review of the literature, which is relevant to the research topic, is presented. At first, literature related to multilevel three-phase drives is reviewed. This is followed by literature related to two-level multiphase drives covering machines with odd- and even-phase number. The available multilevel topologies and PWM techniques are also surveyed early in the literature review. As for the remaining parts, the focus is placed on the modelling of multiphase machines. Additionally, the modulation techniques for multiphase machines are also reviewed with the emphasis placed on the development of multilevel PWM techniques.

In Chapter 3, modulation techniques for two-level six-phase drives are discussed. The modulation techniques based on a space vector and carrier-based approach for both single and

two isolated neutral points configurations are discussed and verified. In the development of the space vector algorithm for single neutral point case, the potential switching sequences are chosen such that the  $x$ ,  $y$  and  $0^-$  space vector components in one switching period are zero on average. By satisfying the requirement, one can realise sinusoidal  $v_{ph}$  waveforms. In accordance to the space vectors in the chosen switching sequences, the equations to calculate the dwell times can then be derived. Furthermore, the dwell times can also be calculated using the dwell times matrix approach. As for the carrier-based approach, due to symmetry of the six-phase  $v_{ph}^*$  waveforms, a conventional carrier-based PWM technique is implemented. In the two isolated neutral points case there is the possibility of controlling each winding set separately. Therefore, dual two-level three-phase PWM modulators (based on either space vector algorithm or carrier-based approach with common mode voltage injection) are used. Obtained simulation results show that sinusoidal output waveforms are obtained. Moreover, it is shown that both the space vector algorithm and carrier-based approach yield identical performances.

In Chapter 4, modulation techniques for three-level symmetrical six-phase drives with both neutral point configurations are presented. However, more emphasis is given towards the development of new space vector algorithm for single neutral point configuration. Due to a much larger number of possible switching states compared to the two-level case, the process of choosing the potential switching sequences is more complex. Therefore, the order-per-sector law was used in order to reduce the number of considered switching states and hence simplify the analysis. In order to realise sinusoidal output waveforms, the potential switching sequences are chosen by meeting several requirements and conditions. By using graphical representation of space vector transitions in  $\alpha$ - $\beta$  and  $x$ - $y$  plane as well as  $0^-$  axis, the switching sequences whose transition patterns indicate that the  $x$ ,  $y$  and  $0^-$  space vector components are not able to produce zero on average, are eliminated. This results in only six switching sequences per sector. Finally, those switching sequences are applied in accordance to their corresponding sub-sectors. For the carrier-based approach, in-phase disposition technique, is used. One should note that double min-max injection was used in this case in order to obtain the same performance as the developed space vector modulation technique. The validity of the developed space vector algorithm is verified through simulation and experimental results.

In Chapter 5, modulation techniques for two-level asymmetrical six-phase drives with single and two isolated neutral points configuration are investigated. Similarly as the two isolated neutral points case, dual two-level three-phase modulators are used. Thus, the chapter is focused more towards the development of a space vector algorithm for the single neutral

point case. Although the VSD transformation matrix for two neutral points is also valid for the single neutral point case, the difference between the  $v_{LEG}$  and  $v_{ph}$  space vector projections in  $0^+0^-$  plane makes the realisation of the  $v_{ph}$  waveforms through  $v_{LEG}$  space vectors more difficult. Thus, a rotational transformation of  $0^+0^-$  plane is proposed. The switching sequences are chosen by meeting the same requirements and conditions as in previous chapters. However, an interesting occurrence can be observed. Unlike the symmetrical case, the chosen space vectors of the switching sequences are not located within the same sector in the  $\alpha\text{-}\beta$  plane. The obtained simulation results show the validity of the developed modulation techniques in obtaining sinusoidal  $v_{ph}$  waveforms and also show identical performance to the carrier-based approach.

Finally, modulation techniques for three-level asymmetrical six-phase drives with single and two isolated neutral points configuration are presented in Chapter 6. Here the new contribution is mainly the development of a novel space vector algorithm for the single neutral point configuration. The same modified transformation matrix as in the two-level case is applied to obtain the space vector projections. However, since the current drive is an extension of a two-level drive, the switching sequences of the latter become part of the potential switching sequences for the three-level drive. Therefore, the situation where the chosen space vectors of the potential switching sequences are not located within the sector is expected in this drive as well. As a result, a permutation method is proposed as a solution for choosing the potential switching sequences. Moreover, due to several of the sub-sectors lacking redundancy in the switching sequence, two additional small sectors are introduced at each side of the odd sectors. This results in the odd sectors having more than double the number of sub-sectors than the even sectors. Nevertheless, the obtained simulation and experimental results show the validity of the new space vector algorithm.

Since modulation techniques presented in this thesis cover both asymmetrical and symmetrical machine with two different neutral point configurations, a general comparison in terms of performance between those modulation techniques can be made. It should be noted that only comparison of  $\text{THD}_v$  is possible as different machines were used. The  $\text{THD}_v$  from the obtained experimental results i.e. for three-level modulation techniques are shown in Figure 7.1. It can be seen that for single neutral point case, the performance of the modulation techniques for asymmetrical six-phase machine do not differ that much from modulation techniques for symmetrical machine. Nevertheless, it does offer slightly higher (3.5% more) dc-bus utilisation than the latter. On the other hand, it is interesting to see that the performance of modulation techniques between the two machines for two neutral point case are the same. In

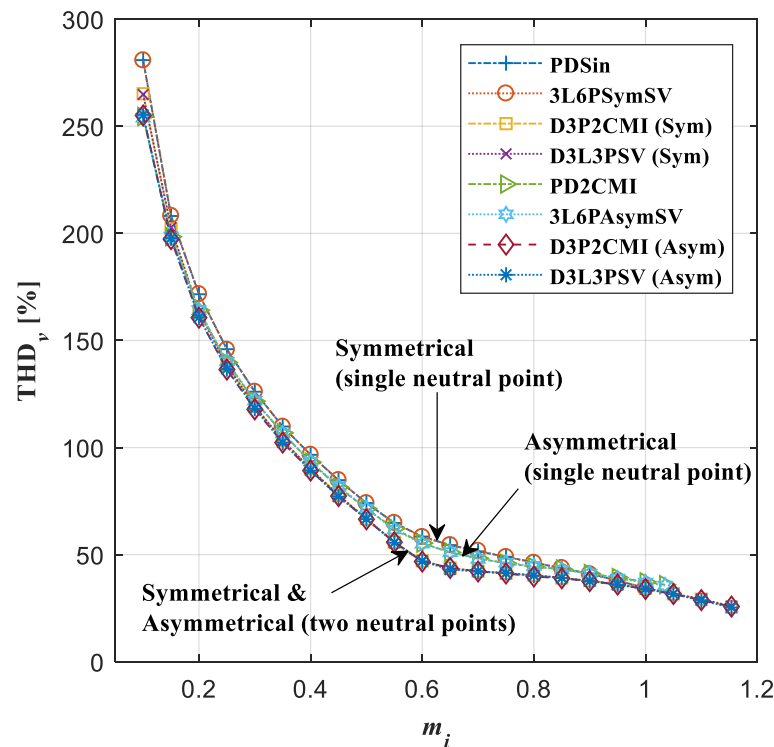


Figure 7.1: Calculated  $THD_v$  based on the obtained experimental result for three-level asymmetrical and symmetrical six-phase drive.

fact, the characteristic of  $THD_v$  is identical to three-phase case in (Dordevic et al., 2015). This is so since the implemented modulation techniques for this case are based on three-phase modulation techniques.

In conclusion, three new modulation techniques based on space vector algorithm are presented in this thesis. They are for two- and three-level asymmetrical and three-level symmetrical six-phase drives, all with single neutral point configuration. The new method for rotating the  $0^+-0^-$  plane for asymmetrical drive has been presented, reducing the order of the system to five, and allowing the leg voltage space vectors to be used for obtaining desirable phase voltage waveforms. In the three-level case a new permutation method for selecting the next switching state within a sequence was used. Although this method is coded with the aid of software, it is still universally applicable, allowing it to be applied to other topologies as well. The aim of the developed algorithms is to obtain sinusoidal  $v_{ph}$  waveforms based on the applied chosen switching sequences. It is shown from the simulation and experimental results that the developed algorithms have successfully realised sinusoidal  $v_{ph}$  waveforms. In addition, identical performance between the developed space vector algorithm and carrier-based

approaches can also be observed. However, in terms of performance comparison between single and two isolated neutral points case, the latter yields better performance from the perspective of lower current THD values, and better dc-bus voltage utilisation.

## 7.2 Future work

The research presented in this thesis is mainly focusing on understanding and process of space vector algorithms developing for two- and three-level symmetrical and asymmetrical six-phase drives. The machines are considered to have sinusoidal distribution of the windings. Furthermore, although it is adequate to verify and validate the developed modulation techniques for full linear range of modulation index in open loop with machine at no load, it will be interesting to see their performances under different kinds of testing. Moreover, the inverter dead time is also not compensated, which results in the obtained  $v_{ph}$  and  $i_{ph}$  waveforms containing undesirable low odd order harmonics. Therefore, it will be interesting to extend and broaden the scope of this research into topics as listed:

- Investigate the possibility of extending the presented modulation techniques into over-modulation range.
- Perform the experimental validation in closed loop.
- Compare the obtained experimental results when dead-time compensation is implemented with the results from the ideal case.
- Investigate the impact of lowering the switching frequency to sub kHz range for use in high power drives and devise new modulation strategies to mitigate the most troublesome low order harmonics.
- Investigate the possibility of enhancing the torque of asymmetrical six-phase machine by injecting the third harmonic, but with an additional i.e. the seventh inverter leg.
- Investigate the possibility of extending the proposed permutation method in determining the switching sequences towards the development of space vector algorithm for three-level nine- (symmetrical and asymmetrical) and eleven-phase drives.



---

## CHAPTER 8

### References

---

- Apsley, J. and Williamson, S. 2006. "Analysis of multiphase induction machines with winding faults". *IEEE Transactions on Industry Applications*, 42, p. 465-472.
- Aroquiadassou, G., Mpanda-Mabwe, A., Betin, F. and Capolino, G. A. 2009. "Six-phase induction machine drive model for fault-tolerant operation". IEEE International Symposium on Diagnostics for Electric Machines, Power Electronics and Drives, SDEMPED 2009, p. 1-6.
- Bakhshai, A. R., Joos, G. and Jin, K. 1998. "Space vector PWM control of a split-phase induction machine using the vector classification technique". 13th Annual Applied Power Electronics Conference and Exposition, APEC 1998, p. 802-808.
- Betin, F., Capolino, G. A., Casadei, D., Kawkabani, B., Bojoi, R. I., Harnefors, L., Levi, E., Parsa, L. and Fahimi, B. 2014. "Trends in electrical machines control: Samples for classical, sensorless, and fault-tolerant techniques". *IEEE Industrial Electronics Magazine*, 8, p. 43-55.
- Bodo, N. 2013. "*PWM strategies for open-end winding multiphase drives*". *PhD Thesis*, Liverpool John Moores University, Liverpool, UK.
- Bodo, N., Dordevic, O., Jones, M. and Levi, E. 2012. "A comparison of three-level single-sided and dual-inverter supply for a five-phase drive". 15th International Power Electronics and Motion Control Conference, EPE/PEMC 2012, p. LS1c.2-1-LS1c.2-6.
- Bodo, N., Jones, M. and Levi, E. 2011. "Multi-level space-vector PWM algorithm for seven-phase open-end winding drives". IEEE International Symposium on Industrial Electronics, ISIE 2011, p. 1881-1886.
- Bodo, N., Levi, E. and Jones, M. 2013. "Investigation of carrier-based PWM techniques for a five-phase open-end winding drive topology". *IEEE Transactions on Industrial Electronics*, 60, p. 2054-2065.
- Bojoi, R., Farina, F., Lazzari, M., Profumo, F. and Tenconi, A. 2003. "Analysis of the asymmetrical operation of dual three-phase induction machines". IEEE International Electric Machines and Drives Conference, IEMDC 2003, p. 429-435.
- Bose, B. K. 2009. "Power electronics and motor drives recent progress and perspective". *IEEE Transactions on Industrial Electronics*, 56, p. 581-588.
- Carrara, G., Gardella, S., Marchesoni, M., Salutati, R. and Sciutto, G. 1992. "A new multilevel PWM method: A theoretical analysis". *IEEE Transactions on Power Electronics*, 7, p. 497-505.
- Casadei, D., Dujic, D., Levi, E., Serra, G., Tani, A. and Zarri, L. 2008a. "General modulation strategy for seven-phase inverters with independent control of multiple voltage space vectors". *IEEE Transactions on Industrial Electronics*, 55, p. 1921-1932.
- Casadei, D., Grandi, G., Lega, A. and Rossi, C. 2008b. "Multilevel operation and input power balancing for a dual two-level inverter with insulated DC sources". *IEEE Transactions on Industry Applications*, 44, p. 1815-1824.
- Celanovic, N. and Boroyevich, D. 2001. "A fast space-vector modulation algorithm for multilevel three-phase converters". *IEEE Transactions on Industry Applications*, 37, p. 637-641.
- Che, H. S., Abdel-Khalik, A. S., Dordevic, O. and Levi, E. 2017. "Parameter estimation of asymmetrical six-phase induction machines using modified standard tests". *IEEE Transactions on Industrial Electronics*, 64, p. 6075-6085.

- Chen, K.-Y. and Hu, J.-S. 2014. "Multi-level multi-phase VSI control using multi-dimensional feedback quantization". International Conference on Intelligent Green Building and Smart Grid, IGBSG 2014, p. 1-4.
- Correa, M. B. R., Jacobina, C. B., da Silva, C. R., Lima, A. M. N. and da Silva, E. R. C. 2003. "Vector and scalar modulation for six-phase voltage source inverters". 34th IEEE Annual Power Electronics Specialist Conference, PESC 2003, p. 562-567.
- Dai, N. Y., Wong, M. C., Chen, Y. H. and Han, Y. D. 2005. "A 3-D generalized direct PWM algorithm for multilevel converters". *IEEE Power Electronics Letters*, 3, p. 85-88.
- Darijevic, M., Jones, M., Bodo, N. and Levi, E. 2013a. "Four-level five-phase open-end winding drive with unequal DC-link voltages". 15th European Conference on Power Electronics and Applications, EPE 2013, p. 1-10.
- Darijevic, M., Jones, M. and Levi, E. 2013b. "Analysis of dead-time effects in a five-phase open-end drive with unequal DC link voltages". 39th IEEE Annual Conference of Industrial Electronics Society, IECON 2013, p. 5136-5141.
- Dordevic, O. 2013. "*PWM strategies for multilevel multiphase AC drives*". *PhD Thesis*, Liverpool John Moores University, Liverpool, UK.
- Dordevic, O., Jones, M. and Levi, E. 2013a. "A comparison of carrier-based and space vector PWM techniques for three-level five-phase voltage source inverters". *IEEE Transactions on Industrial Informatics*, 9, p. 609-619.
- Dordevic, O., Jones, M. and Levi, E. 2015. "Analytical formulas for phase voltage RMS squared and THD in PWM multiphase systems". *IEEE Transactions on Power Electronics*, 30, p. 1645-1656.
- Dordevic, O., Levi, E. and Jones, M. 2013b. "A vector space decomposition based space vector PWM algorithm for a three-level seven-phase voltage source inverter". *IEEE Transactions on Power Electronics*, 28, p. 637-649.
- Dujic, D. 2008. "*Development of pulse-width-modulation techniques for multi-phase and multi-leg voltage source inverters*". *PhD Thesis*, Liverpool John Moores University, Liverpool, UK.
- Dujic, D., Iqbal, A. and Levi, E. 2007a. "A space vector PWM technique for symmetrical six-phase voltage source inverters". 12th European Power Electronics And Adjustable Speed Drives Conference, EPE 2007, p. 24-32.
- Dujic, D., Jones, M. and Levi, E. 2007b. "Continuous carrier-based vs. space vector PWM for five-phase VSI". International Conference on "Computer as a Tool", EUROCON 2007, p. 1772-1779.
- Dujic, D., Jones, M. and Levi, E. 2007c. "Space vector PWM for nine-phase VSI with sinusoidal output voltage generation: Analysis and implementation". 33rd IEEE Annual Conference of the Industrial Electronics Society, IECON 2007, p. 1524-1529.
- Dujic, D., Levi, E. and Jones, M. 2010. "Dc bus utilisation in multiphase VSI supplied drives with a composite stator phase number". IEEE International Conference on Industrial Technology, ICIT 2010, p. 1495-1500.
- Dujic, D., Levi, E., Jones, M., Grandi, G., Serra, G. and Tani, A. 2007d. "Continuous PWM techniques for sinusoidal voltage generation with seven-phase voltage source inverters". IEEE Power Electronics Specialists Conference, PESC 2007, p. 47-52.
- Duran, M. J., Barrero, F., Prieto, J. and Toral, S. 2010. "Predictive current control of dual three-phase drives using restrained search techniques and multi level voltage source inverters". IEEE International Symposium on Industrial Electronics, ISIE 2010, p. 3171-3176.

- Duran, M. J., Prieto, J., Barrero, F. and Toral, S. 2011. "Predictive current control of dual three-phase drives using restrained search techniques". *IEEE Transactions on Industrial Electronics*, 58, p. 3253-3263.
- Engku Ariff, E. A. R., Dordevic, O. and Jones, M. 2016. "Space vector PWM technique for a three-level six-phase drive". 8th IET International Conference on Power Electronics, Machines and Drives, PEMD 2016, p. 1-6.
- Engku Ariff, E. A. R., Dordevic, O. and Jones, M. 2017a. "A space vector PWM technique for a three-level symmetrical six phase drive". *IEEE Transactions on Industrial Electronics*, 64, p. 8396-8405.
- Engku Ariff, E. A. R., Dordevic, O. and Jones, M. 2018. "Space vector PWM technique for a two-level asymmetrical six-phase drive". 9th IET International Conference on Power Electronics, Machines and Drives, PEMD 2018, p. 1-6.
- Engku Ariff, E. A. R., Dordevic, O., Jones, M. and Levi, E. 2017b. "Space vector PWM technique for a three-level asymmetrical six-phase drive". 43rd IEEE Annual Conference of Industrial Electronics Society, IECON 2017, p. 3872-3877.
- Espinoza, M., Cárdenas, R., Díaz, M. and Clare, J. C. 2017. "An enhanced dq-based vector control system for modular multilevel converters feeding variable-speed drives". *IEEE Transactions on Industrial Electronics*, 64, p. 2620-2630.
- Fazel, S. S., Bernet, S., Krug, D. and Jalili, K. 2007. "Design and comparison of 4-kV neutral-point-clamped, flying-capacitor, and series-connected H-bridge multilevel converters". *IEEE Transactions on Industry Applications*, 43, p. 1032-1040.
- Franquelo, L. G., Rodriguez, J., Leon, J. I., Kouro, S., Portillo, R. and Prats, M. A. M. 2008. "The age of multilevel converters arrives". *IEEE Industrial Electronics Magazine*, 2, p. 28-39.
- Fukuda, S. and Suzuki, K. 1997. "Using harmonic distortion determining factor for harmonic evaluation of carrier-based PWM methods". 32nd IEEE Annual Meeting on Industry Applications Conference, IAS 1997, p. 1534-1541.
- Gao, L. and Fletcher, J. E. 2010. "A space vector switching strategy for three-level five-phase inverter drives". *IEEE Transactions on Industrial Electronics*, 57, p. 2332-2343.
- Gopakumar, K. 2011. "Recent trends in multilevel inverter - Ch 19", In: WILAMOWSKI, B. M. & IRWIN, J. D. (eds.) *The Industrial Electronics Handbook: Power Electronics and Motor Drives*. 2nd ed.: CRC Press.
- Grandi, G. and Loncarski, J. 2014. "Simplified implementation of optimised carrier-based PWM in three-level inverters". *Electronics Letters*, 50, p. 631-633.
- Grandi, G., Sanjeevikumar, P., Ostojic, D. and Rossi, C. 2010a. "Quad-inverter configuration for multi-phase multi-level AC motor drives". IEEE Region 8 International Conference on Computational Technologies in Electrical and Electronics Engineering, SIBIRCON 2010, p. 631-638.
- Grandi, G., Serra, G. and Tani, A. 2007. "Space vector modulation of a nine-phase voltage source inverter". IEEE International Symposium on Industrial Electronics, ISIE 2007, p. 431-436.
- Grandi, G., Serra, G. and Tani, A. 2008. "Space vector modulation of a six-phase VSI based on three-phase decomposition". International Symposium on Power Electronics, Electrical Drives, Automation and Motion, SPEEDAM 2008, p. 674-679.
- Grandi, G., Tani, A., Sanjeevikumar, P. and Ostojic, D. 2010b. "Multi-phase multi-level AC motor drive based on four three-phase two-level inverters". International Symposium on Power Electronics Electrical Drives Automation and Motion, SPEEDAM 2010, p. 1768-1775.

- Hadiouche, D., Baghli, L. and Rezzoug, A. 2006. "Space-vector PWM techniques for dual three-phase AC machine: Analysis, performance evaluation, and DSP implementation". *IEEE Transactions on Industry Applications*, 42, p. 1112-1122.
- Holmes, D. G. 1996. "The significance of zero space vector placement for carrier-based PWM schemes". *IEEE Transactions on Industry Applications*, 32, p. 1122-1129.
- Holmes, D. G. 1998. "A general analytical method for determining the theoretical harmonic components of carrier based PWM strategies". 33rd IEEE Annual Meeting on Industry Applications Conference Society, IAS 1998, p. 1207-1214.
- Honbu, M., Matsuda, Y., Miyazaki, K. and Jifuku, Y. 1983. "Parallel Operation Techniques of GTO Inverter Sets for Large AC Motor Drives". *IEEE Transactions on Industry Applications*, IA-19, p. 198-205.
- Hu, J.-S., Chen, K.-Y., Shen, T.-Y. and Tang, C.-H. 2011. "Analytical solutions of multilevel space-vector PWM for multiphase voltage source inverters". *IEEE Transactions on Power Electronics*, 26, p. 1489-1502.
- Iqbal, A. and Moinuddin, S. 2009. "Comprehensive relationship between carrier-based PWM and space vector PWM in a five-phase VSI". *IEEE Transactions on Power Electronics*, 24, p. 2379-2390.
- Islam, M. R., Youguang, G. and Jian Guo, Z. 2011. "Performance and cost comparison of NPC, FC and SCHB multilevel converter topologies for high-voltage applications". International Conference on Electrical Machines and Systems, ICEMS 2011, p. 1-6.
- Jae Hyeong, S., Chang Ho, C. and Dong-Seok, H. 2001. "A new simplified space-vector PWM method for three-level inverters". *IEEE Transactions on Power Electronics*, 16, p. 545-550.
- Jeong, S.-G. and Park, M.-H. 1991. "The analysis and compensation of dead-time effects in PWM inverters". *IEEE Transactions on Industrial Electronics*, 38, p. 108-114.
- Jones, M., Dujic, D., Levi, E., Prieto, J. and Barrero, F. 2011. "Switching ripple characteristics of space vector PWM schemes for five-phase two-level voltage source inverters - Part 2: Current ripple". *IEEE Transactions on Industrial Electronics*, 58, p. 2799-2808.
- Jones, M., Dujic, D., Levi, E. and Vukosavic, S. N. 2009a. "Dead-time effects in voltage source inverter fed multi-phase AC motor drives and their compensation". 13th European Conference on Power Electronics and Applications, EPE 2009, p. 1-10.
- Jones, M., Patkar, F. and Levi, E. 2013. "Carrier-based pulse-width modulation techniques for asymmetrical six-phase open-end winding drives". *IET Electric Power Applications*, 7, p. 441-452.
- Jones, M., Satiawan, I. N. W., Bodo, N. and Levi, E. 2012. "A dual five-phase space-vector modulation algorithm based on the decomposition method". *IEEE Transactions on Industry Applications*, 48, p. 2110-2120.
- Jones, M., Satiawan, W. and Levi, E. 2010. "A five-phase multilevel space-vector PWM algorithm for a dual-inverter supplied drive". 36th IEEE Annual Conference of Industrial Electronics Society, IECON 2010, p. 2461-2466.
- Jones, M., Vukosavic, S. N. and Levi, E. 2009b. "Parallel-connected multiphase multidrive systems with single inverter supply". *IEEE Transactions on Industrial Electronics*, 56, p. 2047-2057.
- Joos, G., Huang, X. G. and Ooi, B. T. 1998. "Direct-coupled multilevel cascaded series VAR compensators". *IEEE Transactions on Industry Applications*, 34, p. 1156-1163.
- Karwatzki, D. and Mertens, A. 2018. "Generalized control approach for a class of modular multilevel converter topologies". *IEEE Transactions on Power Electronics*, 33, p. 2888-2900.

- Kelly, J. W., Strangas, E. G. and Miller, J. M. 2003. "Multiphase space vector pulse width modulation". *IEEE Transactions on Energy Conversion*, 18, p. 259-264.
- Kouro, S., Malinowski, M., Gopakumar, K., Pou, J., Franquelo, L. G., Wu, B., Rodriguez, J., Perez, M. A. and Leon, J. I. 2010. "Recent advances and industrial applications of multilevel converters". *IEEE Transactions on Industrial Electronics*, 57, p. 2553-2580.
- Lai, J.-S. and Peng, F. Z. 1996. "Multilevel converters - A new breed of power converters". *IEEE Transactions on Industry Applications*, 32, p. 509-517.
- Lee, Y.-H., Kim, D.-H. and Hyun, D.-S. 2000. "Carrier based SVPWM method for multi-level system with reduced HDF [harmonic distortion factor]". 35th IEEE Annual Meeting and World Conference on Industrial Applications of Electrical Energy, IAS 2000, p. 1996-2003.
- Leon, J. I., Lopez, O., Franquelo, L. G., Doval-Gandoy, J., Vazquez, S., Alvarez, J. and Freijedo, F. D. 2010a. "Multilevel multiphase feedforward space-vector modulation technique". *IEEE Transactions on Industrial Electronics*, 57, p. 2066-2075.
- Leon, J. I., Portillo, R., Vazquez, S., Padilla, J. J., Franquelo, L. G. and Carrasco, J. M. 2008. "Simple unified approach to develop a time-domain modulation strategy for single-phase multilevel converters". *IEEE Transactions on Industrial Electronics*, 55, p. 3239-3248.
- Leon, J. I., Vazquez, S., Sanchez, J. A., Portillo, R., Franquelo, L. G., Carrasco, J. M. and Dominguez, E. 2010b. "Conventional space-vector modulation techniques versus the single-phase modulator for multilevel converters". *IEEE Transactions on Industrial Electronics*, 57, p. 2473-2482.
- Levi, E. 2008. "Multiphase electric machines for variable-speed applications". *IEEE Transactions on Industrial Electronics*, 55, p. 1893-1909.
- Levi, E. 2011. "Multiphase AC machines - Ch 3", In: WILAMOWSKI, B. M. & IRWIN, J. D. (eds.) *The Industrial Electronics Handbook: Power Electronics and Motor Drives*. 2nd ed.: CRC Press.
- Levi, E. 2013. "Multilevel multiphase drive systems - Topologies and PWM control". IEEE International Electric Machines & Drives Conference, IEMDC 2013, p. 1500-1508.
- Levi, E., Bojoi, R., Profumo, F., Toliyat, H. A. and Williamson, S. 2007. "Multiphase induction motor drives – A technology status review". *IET Electric Power Applications*, 1, p. 489-516.
- Levi, E., Jones, M. and Vukosavic, S. N. 2003. "Even-phase multi-motor vector controlled drive with single inverter supply and series connection of stator windings". *IEE Proceedings - Electric Power Applications*, 150, p. 580-590.
- Levi, E., Satiawan, I. N. W., Bodo, N. and Jones, M. 2012. "A space-vector modulation scheme for multilevel open-end winding five-phase drives". *IEEE Transactions on Energy Conversion*, 27, p. 1-10.
- Lopez, O., Alvarez, J., Doval-Gandoy, J., Freijedo, F., Nogueiras, A. and Penalver, C. M. 2008a. "Multilevel multiphase space vector PWM algorithm applied to three-phase converters". 34th IEEE Annual Conference on Industrial Electronics, IECON 2008, p. 3290-3295.
- Lopez, O., Alvarez, J., Doval-Gandoy, J. and Freijedo, F. D. 2008b. "Multilevel multiphase space vector PWM algorithm". *IEEE Transactions on Industrial Electronics*, 55, p. 1933-1942.
- Lopez, O., Alvarez, J., Doval-Gandoy, J. and Freijedo, F. D. 2009a. "Multilevel multiphase space vector PWM algorithm with switching state redundancy". *IEEE Transactions on Industrial Electronics*, 56, p. 792-804.
- Lopez, O., Levi, E., Freijedo, F. D. and Doval-Gandoy, J. 2009b. "Number of switching state vectors and space vectors in multilevel multiphase converters". *Electronics Letters*, 45, p. 524-525.

- Lu, S. and Corzine, K. 2005. "Multilevel multi-phase propulsion drives". IEEE Electric Ship Technologies Symposium, ESTS 2005, p. 363-370.
- Malinowski, M., Gopakumar, K., Rodriguez, J. and Perez, M. A. 2010. "A survey on cascaded multilevel inverters". *IEEE Transactions on Industrial Electronics*, 57, p. 2197-2206.
- Marouani, K., Baghli, L., Hadiouche, D., Kheloui, A. and Rezzoug, A. 2008. "A new PWM strategy based on a 24-sector vector space decomposition for a six-phase VSI-fed dual stator induction motor". *IEEE Transactions on Industrial Electronics*, 55, p. 1910-1920.
- McGrath, B. P. and Holmes, D. G. 2002. "Multicarrier PWM strategies for multilevel inverters". *IEEE Transactions on Industrial Electronics*, 49, p. 858-867.
- McGrath, B. P., Holmes, D. G. and Lipo, T. A. 2003. "Optimized space vector switching sequences for multilevel inverters". *IEEE Transactions on Power Electronics*, 18, p. 1293-1301.
- Moinoddin, S., Abu-Rub, H., Iqbal, A., Moin Ahmed, S., Dordevic, O. and Levi, E. 2015. "Space vector pulse-width modulation technique for an eleven-phase voltage source inverter with sinusoidal output voltage generation". *IET Power Electronics*, 8, p. 1000-1008.
- Nabae, A., Takahashi, I. and Akagi, H. 1981. "A new neutral-point-clamped PWM inverter". *IEEE Transactions on Industry Applications*, 17, p. 518-523.
- Nelson, R. H. and Krause, P. C. 1974. "Induction machine analysis for arbitrary displacement between multiple winding sets". *IEEE Transactions on Power Apparatus and Systems*, p. 841-848.
- Ogasawara, S., Akagi, H. and Nabae, A. 1990. "A novel PWM scheme of voltage source inverters based on space vector theory". *Archiv für Elektrotechnik*, 74, p. 33-41.
- Oleschuk, V., Gregor, R., Rodas, J. and Giangreco, A. 2013. "Dual three-phase system based on four neutral-point-clamped inverters with synchronized space-vector modulation". 15th European Conference on Power Electronics and Applications, EPE 2013, p. 1-10.
- Patkar, F. 2013. "*PWM techniques for control of dual-inverter supplied six-phase drives*". PhD Thesis, Liverpool John Moores University, Liverpool, UK.
- Patkar, F. and Jones, M. 2013. "Performance of an asymmetrical six-phase induction machine in single- and two-neutral point configurations". 48th International Universities' Power Engineering Conference, UPEC 2013, p. 1-6.
- Patkar, F., Levi, E. and Jones, M. 2012. "A six-phase multilevel space vector PWM algorithm for a dual-inverter supplied drive". 6th IET International Conference on Power Electronics, Machines and Drives, PEMD 2012, p. 1-5.
- Prats, M. M., Franquelo, L. G., Portillo, R., Leon, J. I., Galvan, E. and Carrasco, J. M. 2003. "A 3-D space vector modulation generalized algorithm for multilevel converters". *IEEE Power Electronics Letters*, 99, p. 110-114.
- Qingguo, S., Xiaofeng, Z., Fei, Y. and Chengsheng, Z. 2006. "Research on PWM techniques of five-phase three-level inverter". International Symposium on Power Electronics, Electrical Drives, Automation and Motion, SPEEDAM 2006, p. 561-565.
- Rodriguez, J., Bernet, S., Steimer, P. K. and Lizama, I. E. 2010. "A survey on neutral-point-clamped inverters". *IEEE Transactions on Industrial Electronics*, 57, p. 2219-2230.
- Sanmin, W., Bin, W., Fahai, L. and Congwei, L. 2003. "A general space vector PWM control algorithm for multilevel inverters". 18th IEEE Annual Applied Power Electronics Conference and Exposition, APEC 2003, p. 562-568.
- Schmitt, B. P. and Sommer, R. 2001. "Retrofit of fixed speed induction motors with medium voltage drive converters using NPC three-level inverter high-voltage IGBT based topology". IEEE International Symposium on Industrial Electronics, ISIE 2001, p. 746-751.

- Sivakumar, K., Das, A., Ramchand, R., Patel, C. and Gopakumar, K. 2009. "A three level voltage space vector generation for open end winding IM using single voltage source driven dual two-level inverter". *IEEE Region 10 Conference, TENCN 2009*, p. 1-5.
- Somasekhar, V. T., Gopakumar, K., Pittet, A. and Ranganathan, V. T. 2001. "A novel PWM inverter switching strategy for a dual two-level inverter fed open-end winding induction motor drive". *4th IEEE International Conference on Power Electronics and Drive Systems, 2001*, p. 196-202.
- Subotic, I., Levi, E., Jones, M. and Graovac, D. 2013. "Multiphase integrated on-board battery chargers for electrical vehicles". *15th European Conference on Power Electronics and Applications, EPE 2013*, p. 1-10.
- Tolbert, L. M., Peng, F. Z. and Habetler, T. G. 1999. "Multilevel converters for large electric drives". *IEEE Transactions on Industry Applications*, 35, p. 36-44.
- Toliyat, H. A. and Lipo, T. A. 1994. "Analysis of concentrated winding induction machines for adjustable speed drive applications-experimental results". *IEEE Transactions on Energy Conversion*, 9, p. 695-700.
- Toliyat, H. A., Lipo, T. A. and White, J. C. 1991a. "Analysis of a concentrated winding induction machine for adjustable speed drive applications. I. Motor analysis". *IEEE Transactions on Energy Conversion*, 6, p. 679-683.
- Toliyat, H. A., Lipo, T. A. and White, J. C. 1991b. "Analysis of a concentrated winding induction machine for adjustable speed drive applications. II. Motor design and performance". *IEEE Transactions on Energy Conversion*, 6, p. 684-692.
- Ueda, F., Matsui, K., Asao, M. and Tsuboi, K. 1995. "Parallel-connections of pulsewidth modulated inverters using current sharing reactors". *IEEE Transactions on Power Electronics*, 10, p. 673-679.
- van der Broeck, H. W., Skudelny, H. C. and Stanke, G. V. 1988. "Analysis and realization of a pulsewidth modulator based on voltage space vectors". *IEEE Transactions on Industry Applications*, 24, p. 142-150.
- Wang, F. 2002. "Sine-triangle versus space-vector modulation for three-level PWM voltage-source inverters". *IEEE Transactions on Industry Applications*, 38, p. 500-506.
- Ward, E. E. and Härer, H. 1969. "Preliminary investigation of an inverter-fed 5-phase induction motor". *Proceedings of the Institution of Electrical Engineers*, 116, p. 980-984.
- Wilkinson, R. H., Meynard, T. A. and Mouton, H. D. T. 2006. "Natural balance of multicell converters: The general case". *IEEE Transactions on Power Electronics*, 21, p. 1658-1666.
- Williamson, S. and Smith, S. 2003. "Pulsating torque and losses in multiphase induction machines". *IEEE Transactions on Industry Applications*, 39, p. 986-993.
- Zhao, Y. 1995. "Vector space decomposition modeling and control of multi-phase induction machine". *PhD Thesis*, University of Wisconsin, Wisconsin, USA.
- Zhao, Y. and Lipo, T. A. 1995. "Space vector PWM control of dual three-phase induction machine using vector space decomposition". *IEEE Transactions on Industry Applications*, 31, p. 1100-1109.
- Zoric, I., Jones, M. and Levi, E. 2016. "Phase voltage harmonic imbalance in asymmetrical multiphase machines with single neutral point". *42nd IEEE Annual Conference of Industrial Electronics Society, IECON 2016*, p. 4343-4348.



## APPENDIX A

### List of potential switching sequences – 3L6PSymSV

Table A1: List of all potential switching sequences for S1 for 3L6PSymSV developed in Chapter 4.

Ref. No.	Potential switching sequences for the S1 (only the first half of the switching period is covered)	
	Decimal	Ternary
1	0 - 243 - 324 - 325 - 355 - 355 - 364	000000 - 100000 - 110000 - 110001 - 111001 - 111011 - 111111
2	243 - 324 - 325 - 352 - 355 - 364 - 607	100000 - 110000 - 110001 - 111001 - 111011 - 111111 - 211111
3	243 - 324 - 325 - 352 - 355 - 598 - 607	100000 - 110000 - 110001 - 111001 - 111011 - 211011 - 211111
4	243 - 324 - 325 - 352 - 595 - 598 - 607	100000 - 110000 - 110001 - 111001 - 211001 - 211011 - 211111
5	243 - 324 - 325 - 568 - 595 - 598 - 607	100000 - 110000 - 110001 - 210001 - 211001 - 211011 - 211111
6	243 - 324 - 567 - 568 - 595 - 598 - 607	100000 - 110000 - 210000 - 210001 - 211001 - 211011 - 211111
7	243 - 486 - 567 - 568 - 595 - 598 - 607	100000 - 200000 - 210000 - 210001 - 211001 - 211011 - 211111
8	324 - 325 - 352 - 355 - 364 - 607 - 688	110000 - 110001 - 111001 - 111011 - 111111 - 211111 - 221111
9	324 - 325 - 352 - 355 - 598 - 607 - 688	110000 - 110001 - 111001 - 111011 - 211011 - 211111 - 221111
10	324 - 325 - 352 - 595 - 598 - 607 - 688	110000 - 110001 - 111001 - 211001 - 211011 - 211111 - 221111
11	324 - 325 - 568 - 595 - 598 - 607 - 688	110000 - 110001 - 210001 - 211001 - 211011 - 211111 - 221111
12	324 - 567 - 568 - 595 - 598 - 607 - 688	110000 - 210000 - 210001 - 211001 - 211011 - 211111 - 221111
13	324 - 325 - 352 - 355 - 598 - 679 - 688	110000 - 110001 - 111001 - 111011 - 211011 - 221011 - 221111
14	324 - 325 - 352 - 595 - 598 - 679 - 688	110000 - 110001 - 111001 - 211001 - 211011 - 221011 - 221111
15	324 - 325 - 568 - 595 - 598 - 679 - 688	110000 - 110001 - 210001 - 211001 - 211011 - 221011 - 221111
16	324 - 567 - 568 - 595 - 598 - 679 - 688	110000 - 210000 - 210001 - 211001 - 211011 - 221011 - 221111
17	324 - 325 - 352 - 595 - 676 - 679 - 688	110000 - 110001 - 111001 - 211001 - 221001 - 221011 - 221111
18	324 - 325 - 568 - 595 - 676 - 679 - 688	110000 - 110001 - 210001 - 211001 - 221001 - 221011 - 221111
19	324 - 567 - 568 - 595 - 676 - 679 - 688	110000 - 210000 - 210001 - 211001 - 221001 - 221011 - 221111
20	324 - 325 - 568 - 649 - 676 - 679 - 688	110000 - 110001 - 210001 - 220001 - 221001 - 221011 - 221111
21	324 - 567 - 568 - 649 - 676 - 679 - 688	110000 - 210000 - 210001 - 220001 - 221001 - 221011 - 221111
22	324 - 567 - 648 - 649 - 676 - 679 - 688	110000 - 210000 - 220000 - 220001 - 221001 - 221011 - 221111
23	325 - 352 - 355 - 364 - 607 - 688 - 689	110001 - 111001 - 111011 - 111111 - 211111 - 221111 - 221112
24	325 - 352 - 355 - 598 - 607 - 688 - 689	110001 - 111001 - 111011 - 211011 - 211111 - 221111 - 221112
25	325 - 352 - 595 - 598 - 607 - 688 - 689	110001 - 111001 - 211001 - 211011 - 211111 - 221111 - 221112
26	325 - 568 - 595 - 598 - 607 - 688 - 689	110001 - 210001 - 211001 - 211011 - 211111 - 221111 - 221112
27	325 - 352 - 355 - 598 - 679 - 688 - 689	110001 - 111001 - 111011 - 211011 - 221011 - 221111 - 221112

28	325 - 352 - 595 - 598 - 679 - 688 - 689	110001 - 111001 - 211001 - 211011 - 221011 - 221111 - 221112
29	325 - 568 - 595 - 598 - 679 - 688 - 689	110001 - 210001 - 211001 - 211011 - 221011 - 221111 - 221112
30	325 - 352 - 595 - 676 - 679 - 688 - 689	110001 - 111001 - 211001 - 221001 - 221011 - 221111 - 221112
31	325 - 568 - 595 - 676 - 679 - 688 - 689	110001 - 210001 - 211001 - 221001 - 221011 - 221111 - 221112
32	325 - 568 - 649 - 676 - 679 - 688 - 689	110001 - 210001 - 220001 - 221001 - 221011 - 221111 - 221112
33	325 - 352 - 355 - 598 - 679 - 680 - 689	110001 - 111001 - 111011 - 211011 - 221011 - 221012 - 221112
34	325 - 352 - 595 - 598 - 679 - 680 - 689	110001 - 111001 - 211001 - 211011 - 221011 - 221012 - 221112
35	325 - 568 - 595 - 598 - 679 - 680 - 689	110001 - 210001 - 211001 - 211011 - 221011 - 221012 - 221112
36	325 - 352 - 595 - 676 - 679 - 680 - 689	110001 - 111001 - 211001 - 221001 - 221011 - 221012 - 221112
37	325 - 568 - 595 - 676 - 679 - 680 - 689	110001 - 210001 - 211001 - 221001 - 221011 - 221012 - 221112
38	325 - 568 - 649 - 676 - 679 - 680 - 689	110001 - 210001 - 220001 - 221001 - 221011 - 221012 - 221112
39	325 - 352 - 595 - 676 - 677 - 680 - 689	110001 - 111001 - 211001 - 221001 - 221002 - 221012 - 221112
40	325 - 568 - 595 - 676 - 677 - 680 - 689	110001 - 210001 - 211001 - 221001 - 221002 - 221012 - 221112
41	325 - 568 - 649 - 676 - 677 - 680 - 689	110001 - 210001 - 220001 - 221001 - 221002 - 221012 - 221112
42	325 - 568 - 649 - 650 - 677 - 680 - 689	110001 - 210001 - 220001 - 220002 - 221002 - 221012 - 221112
43	352 - 355 - 364 - 607 - 688 - 689 - 716	111001 - 111011 - 111111 - 211111 - 221111 - 221112 - 222112
44	352 - 355 - 598 - 607 - 688 - 689 - 716	111001 - 111011 - 211011 - 211111 - 221111 - 221112 - 222112
45	352 - 595 - 598 - 607 - 688 - 689 - 716	111001 - 211001 - 211011 - 211111 - 221111 - 221112 - 222112
46	352 - 355 - 598 - 679 - 688 - 689 - 716	111001 - 111011 - 211011 - 221011 - 221111 - 221112 - 222112
47	352 - 595 - 598 - 679 - 688 - 689 - 716	111001 - 211001 - 211011 - 221011 - 221111 - 221112 - 222112
48	352 - 595 - 676 - 679 - 688 - 689 - 716	111001 - 211001 - 221001 - 221011 - 221111 - 221112 - 222112
49	352 - 355 - 598 - 679 - 680 - 689 - 716	111001 - 111011 - 211011 - 221011 - 221012 - 221112 - 222112
50	352 - 595 - 598 - 679 - 680 - 689 - 716	111001 - 211001 - 211011 - 221011 - 221012 - 221112 - 222112
51	352 - 595 - 676 - 679 - 680 - 689 - 716	111001 - 211001 - 221001 - 221011 - 221012 - 221112 - 222112
52	352 - 595 - 676 - 677 - 680 - 689 - 716	111001 - 211001 - 221001 - 221002 - 221012 - 221112 - 222112
53	352 - 355 - 598 - 679 - 680 - 707 - 716	111001 - 111011 - 211011 - 221011 - 221012 - 222012 - 222112
54	352 - 595 - 598 - 679 - 680 - 707 - 716	111001 - 211001 - 211011 - 221011 - 221012 - 222012 - 222112
55	352 - 595 - 676 - 679 - 680 - 707 - 716	111001 - 211001 - 221001 - 221011 - 221012 - 222012 - 222112
56	352 - 595 - 676 - 677 - 680 - 707 - 716	111001 - 211001 - 221001 - 221002 - 221012 - 222012 - 222112
57	352 - 595 - 676 - 677 - 704 - 707 - 716	111001 - 211001 - 221001 - 221002 - 222002 - 222012 - 222112
58	355 - 364 - 607 - 688 - 689 - 716 - 719	111011 - 111111 - 211111 - 221111 - 221112 - 222112 - 222122
59	355 - 598 - 607 - 688 - 689 - 716 - 719	111011 - 211011 - 211111 - 221111 - 221112 - 222112 - 222122
60	355 - 598 - 679 - 688 - 689 - 716 - 719	111011 - 211011 - 221011 - 221111 - 221112 - 222112 - 222122
61	355 - 598 - 679 - 680 - 689 - 716 - 719	111011 - 211011 - 221011 - 221012 - 221112 - 222112 - 222122
62	355 - 598 - 679 - 680 - 707 - 716 - 719	111011 - 211011 - 221011 - 221012 - 222012 - 222112 - 222122
63	355 - 598 - 679 - 680 - 707 - 710 - 719	111011 - 211011 - 221011 - 221012 - 222012 - 222022 - 222122
64	364 - 607 - 688 - 689 - 716 - 719 - 728	111111 - 211111 - 221111 - 221112 - 222112 - 222122 - 222222

---

## APPENDIX B

### Description of experimental setup

---

The description of the experimental setup used to validate the presented modulation techniques is given here. In general, there are six apparatuses, which are heavily used to conduct the experiments. The experimental setups for testing the presented modulation techniques for three-level symmetrical and asymmetrical six-phase drives are shown in Figure 4.15 and Figure 6.10, respectively.

#### **B.1 Computer with required software**

The modulators of the presented modulation techniques are developed in Matlab/Simulink software. Mainly, the modulators are constructed using the blocks provided in Simulink and several necessary blocks are also added for programming the PWM unit within the real-time platform dSpace. The model was loaded onto real-time platform through incremental build. In addition, the Matlab software is also used to communicate with the oscilloscope through VISA protocol and send the commands to retrieve the measured data, as well as to do a screen capture of the device. This conveniently reduces time needed to save the data compared to standard approach of manually saving the measurements directly from the oscilloscope.

Control Desk software is used to communicate with the processor board in real time. A custom control interface can be created using this software, which gives the user ability to visualise any signals generated by the programmed modulator and to remotely change the modulator variables or parameters accordingly. This offers flexibility to the user to properly test the presented modulation techniques whilst at the same time observe the changes due to different values set for the variables.

Another software that is being simultaneously used whilst conducting the experiments is dSpace Profiler Tool. The usage of this software is to observe the execution time of certain tasks that are being executed in real time by the processor board. By using certain command lines during the process of developing the modulator, the user can specify dSpace Profiler Tool

to display the time taken for the processor board to complete the task. The execution time is also used as the indicator to measure the complexity of the presented modulation techniques.

## B.2 Real-time platform

The modulators of the presented modulation techniques are programmed into real-time platform dSpace ds1006 in a standard way using Matlab/Simulink. In order to provide proper synchronisation between peripheral board ds5101 (which is in charge of generating the pulse width modulation signals i.e. switching signals for the inverter) and the main control board ds1006, ds5101 board is sending interrupt request to the main control board every 500  $\mu\text{s}$  (which is the switching period of the chosen switching frequency,  $f_s = 2 \text{ kHz}$ ). The processor board executes the code based on what the user currently sets in the user control interface in Control Desk. The data obtained, after the execution is complete, are then passed to ds5101 board where the generation of the switching signals is done locally. The source code for ds5101 board is written in a 'local' dSpace language and compiled using "DWOCOMP.exe" programme provided by dSpace. Additionally, other necessary signals (e.g. enable signal for enabling the inverter) can also be generated in the same way.

## B.3 Custom-built inverter

A custom-built three-level six-phase inverter based on neutral-point-clamp topology (see Figure 4.1) is used to drive the induction machine. The rating of the inverter is estimated to be 17.8 kVA. The dc-bus voltage can be supplied either from the three-phase mains or by an external dc source. The latter source is used here. The two dc-bus capacitors are of the same value  $C_1 = C_2 = 3 \text{ mF}$ . Each of the inverter legs has two Semikron SKM50GB12T4 IGBT modules. The module comprises of two transistors with back-to-back diodes as whole package and can be switched using two gating signals. Its maximum collector-emitter voltage is  $V_{CE} = 1200 \text{ V}$  and nominal current is 50 A. Although 24 different switching signals are needed in order to control all six inverter legs, half of the switching signals are complementary to the other half. They are generated internally by the inverter control board. Hence, only twelve switching signals are required from the ds5101 board (e.g.  $S_{A1}$  and  $S_{A2}$  for the first inverter leg shown in Figure 4.1). The inverter control board also introduces the dead time in the switching signals from the ds5101 board, as well as the generated complementary switching signals. The dead time is set internally to be 6  $\mu\text{s}$ .

#### **B.4 Dc power supply**

The dc-bus voltage of the inverter is supplied by an external dc source. A Sorensen SGI600-25 programmable power supply is used for this purpose. The rating of the power supply is 15 kW. The voltage can be set within the range of 0 to 600 V with maximum current at 25 A. The constant dc voltage of 200 V with overvoltage protection up to 220 V and overcurrent protection of 5 A, is set for symmetrical six-phase drive. As for asymmetrical six-phase drive, the power supply is set to supply a constant dc voltage of 300 V with overvoltage protection up to 320 V and overcurrent protection of 5 A.

#### **B.5 Induction machines**

The induction machines used in order to validate the presented modulation techniques are obtained by rewinding three-phase induction machines. The new estimated machine parameters are as listed in Table 3.1 for symmetrical six-phase induction machine and Table 5.1 for asymmetrical six-phase machine. The distribution of the stator windings of both machines is sinusoidal. Hence, it is desirable to drive the machine with sinusoidal output phase voltage waveforms, which is the aim of the presented modulation techniques. The machines are not connected to any load and the modulation techniques are validated in open loop.

#### **B.6 Measurement devices**

All necessary waveforms (e.g. inverter output leg voltage, machine output phase voltage and current) are measured using Tektronix P5205A differential voltage and TCP0030A AC/DC current probe, which are connected to Tektronix DPO2014B (100 MHz 4-channel) oscilloscope. The voltage probes are rated to measure voltage up to  $\pm 750$  V whilst the current probes are rated to measure current up to 30 A. The oscilloscope has a built-in variable low pass filter and it is set to filter out the noise signals above 600 kHz. It is also set up in such a way that it can receive the commands through VISA protocol from local PC running Matlab software. Generally, its settings can be changed and it can be triggered remotely. In addition, all measured data can be called and saved directly as Matlab formatted data i.e. in mat format. Furthermore, any signals or waveforms that are currently being displayed on its screen can be remotely captured and saved as picture format.

---

## APPENDIX C

### Publications from the thesis

---

#### C.1 Journal paper

Engku Ariff, E. A. R., Dordevic, O. and Jones, M. "A space vector PWM technique for a three-level symmetrical six phase drive". *IEEE Transactions on Industrial Electronics*, vol. 64, no. 11, pp. 8396-8405, Nov. 2017.

#### C.2 Conference papers

Engku Ariff, E. A. R., Dordevic, O. and Jones, M. "Space vector PWM technique for a three-level six-phase drive". 8th IET International Conference on Power Electronics, Machines and Drives, PEMD, pp. 1-6, 2016.

Engku Ariff, E. A. R., Dordevic, O., Jones, M. and Levi, E. "Space vector PWM technique for a three-level asymmetrical six-phase drive". 43rd IEEE Annual Conference of Industrial Electronics Society, IECON, pp. 3872-3877, 2017.

Engku Ariff, E. A. R., Dordevic, O. and Jones, M. "Space vector PWM technique for a two-level asymmetrical six-phase drive". 9th IET International Conference on Power Electronics, Machines and Drives, PEMD, pp. 1-6, 2018.